Two-Dimensional to Three-Dimensional

Global/Local Finite Element Analysis of

Laminated Composites

in Compression

by

Danniella Mellissa Muheim Thompson

Thesis submitted to the Faculty of the

Virginia Polytechnic Institute and State University

in partial fulfillment of the requirements for the degree of

Master of Science

in

Engineering Mechanics

APPROVED:

O. H. Griffin, Jr., Chairman

Z. Gurdal

N. F. Knight, Jr.

J. N. Reddy

May, 1990

Blacksburg, Virginia

LD
5655
V855
1990
T562
C.2

Two-Dimensional to Three-Dimensional

Global/Local Finite Element Analysis of

Laminated Composites

in Compression

by

Danniella Mellissa Muheim Thompson

O. H. Griffin, Jr., Chairman

Engineering Mechanics

(ABSTRACT)

A two-dimensional to three-dimensional global/local finite element approach was developed, verified, and applied to a laminated composite plate of finite width and length containing a central circular hole. The resulting stress fields for axial compression loads were examined in detail for several symmetric stacking sequences and hole sizes. Verification was based on comparison of the displacements and the stress fields with those accepted trends from previous free edge investigations and a complete three-dimensional finite element solution of the plate. Hole diameters of one, three, and six inches in plates 18 inches long, 12 inches wide, and 0.1 inches thick were considered. The laminates in the compression study included symmetric cross-ply, angle-ply and quasi-isotropic stacking sequences. The entire plate was selected as the global model and analyzed with two-dimensional finite elements. Displacements along a region identified as the global/local interface were applied in a kinematically consistent fashion to independent three-dimensional local models. Local areas of interest in the plate included a portion of the straight free edge near the hole, and the immediate area around the hole.

It was found that the global/local interface should not be placed inside or through any region where the stress field exhibits three-dimensional effects. Interlaminar stress results obtained from the global/local analyses compared well with previously reported trends, and some new conclusions about interlaminar stress fields in plates with different laminate orientations and hole sizes are pre-

sented for compressive loading. The effectiveness of the global/local procedure in reducing the computational effort required to solve these problems is clearly demonstrated through examination of the computer time required to formulate and solve the linear, static system of equations which result for the global and local analyses to those required for a complete three-dimensional formulation for a cross-ply laminate.

The Testbed, which is under continuing development by the Computational Structural Mechanics Group, now the Computational Mechanics Branch, was used throughout this investigation. Specific processors used during the analyses are described in general terms herein. The application of this global/local technique is not limited to this software system, and was developed and described in as general a manner as possible. The methodology developed is thus applicable to other large-scale structural analysis systems.

Acknowledgements

The author would like to thank several individuals who made the completion of this work possible, both professionally and personally. The patience of her committee chairman, Dr. O. Hayden Griffin, Jr., during this time was endless. His technical expertise and good-natured approach to advising, not doing, his students' work, allowed the author to continue to develop her analytical and communicative talents. Numerous hours spent by her NASA technical monitor, Dr. Norman F. Knight, Jr., in explaining aspects of the software system used, and general technical discussions about structural analysis, were both educating and motivating. The service of Dr. Zafer Gurdal and Dr. J. N. Reddy on the author's graduate committee was thankfully received.

The technical assistance and support of the Computational Structural Mechanics Group, now the Computational Mechanics Branch, at NASA-Langley Research Center through Grant NAG1-675 was invaluable throughout this effort. Allowing the author to perform finite element analyses on the Structural Mechanics Division's CONVEX computer at NASA Langley Research Center made the work swifter, smoother and more tractable. The individual contributions by many of the CSM group members were beyond their required support roles and very much appreciated.

On a more personal note, the support of the author's husband (Roger) and her parents (Fritz and Agnes Muheim) during this time was at times less thankfully received than it deserved. She would

also like to acknowledge those special close friends (D. Scott Norwood, Gina Novak-Ley, Andrea L. Ogden and others) and the staffs of the Lewis-Gale and Montgomery County Oncology Centers for their efforts.

Table of Contents

1.0 Introduction 1

2.0 Literature Review - Global/Local Analysis 4

3.0 Common Features of the Global/Local Finite Element Analysis Techniques 11

3.1 Assumptions and Limitations of the Global/Local Procedure 11

3.2 Finite Element Software System 14

3.3 Global Model Generation 18

3.4 Local Model Generation 22

3.5 Solution Procedure 24

3.6 Post-processing of Displacements and Stresses 25

4.0 Cross-ply Laminates Under Compression 26

4.1 Introduction 26

4.2 Problem Description and Approach 27

4.3 Results and Discussion 42

4.3.1 Two-Dimensional Global Model Results 51

4.3.2 Three-Dimensional Local Model Results 52
4.3.2.1 Verification of Global/Local Modeling Technique for the Straight Edge 52
4.3.2.2 Straight Free Edge Model Results 54
4.3.2.3 Verification of Global/Local Modeling Technique for Curved Edge 72
4.3.2.4 Curved Free Edge Model Results 78
4.4 Conclusions for In-Plane Compression of Cross-Ply Laminates 94

5.0 Angle-ply and Quasi-isotropic Laminates Under Compression 99
5.1 Introduction 99
5.2 Problem Description and Approach 100
5.3 Results and Discussion 123
5.3.1 Two-Dimensional Global Model Results 125
5.3.2 Three-Dimensional Local Model Results 126
5.3.2.1 Verification of Global/Local Modeling Technique for the Straight Edge 127
5.3.2.2 Straight Free Edge Model Results 130
5.3.2.3 Verification of Global/Local Modeling Technique for the Curved Edge 156
5.3.2.4 Curved Free Edge Model Results 158
5.4 Conclusions for In-Plane Compression of Angle-Ply and Quasi-Isotropic Laminates .. 191

6.0 Conclusions - Global/Local Analysis 196

7.0 References 200

Appendix A. Element Extrapolation Functions 208
A.1 Introduction 208
A.2 Development of Extrapolation Functions 209
A.3 Examples 212

Vita 242

List of Illustrations

Figure 1. Testbed Structural Methods Research 16

Figure 2. Three-Dimensional Elements Installed in Testbed 17

Figure 3. Boundary conditions applied to the global model for compression 19

Figure 4. Nodal distributions generated by "CSM1" and as modified for the straight edge for a six-inch hole model 21

Figure 5. Nodal distributions generated by "CSM1" and as modified for the curved edge region for a six-inch diameter hole 23

Figure 6. Global Grids for $[0_{2n}/90_{2n}]_s$ in Compression with Six-Inch Diameter Hole 29

Figure 7. Global Grids for $[0_{2n}/90_{2n}]_s$ in Compression with Three-Inch Diameter Hole ... 30

Figure 8. Global Grids for $[0_{2n}/90_{2n}]_s$ in Compression with One-Inch Diameter Hole 31

Figure 9. Local Full Straight Edge Model Displacement Application for Cross-plies in Compression 32

Figure 10. Reduced Local Straight Edge Model Displacement Application for Cross-plies in Compression 34

Figure 11. Local Curved Edge Model Displacement Application for Cross-plies in Compression 35

Figure 12. Complete Model Displacement Application for Cross-plies in Compression 38

Figure 13. Complete Models for $[0_{2n}/90_{2n}]_s$ viewing Straight Edge near Six-Inch Diameter Hole 39

Figure 14. Complete Models for $[0_{2n}/90_{2n}]_s$ viewing Straight Edge near Six-Inch Diameter Hole 40

Figure 15. Complete Models for $[0_{2n}/90_{2n}]_s$ viewing Curved Edge around Six-Inch Diameter Hole 41

Figure 16. Full Local Straight Edge Models for $[0_{2n}/90_{2n}]_s$ near Six-Inch Diameter Hole ... 43

Figure 17. Reduced Local Straight Edge Models for $[0_{2n}/90_{2n}]_s$ near Six-Inch Diameter Hole 44

Figure 18. Reduced Local Straight Edge Models for $[0_{2n}/90_{2n}]_s$ near Three-Inch Diameter Hole 45

Figure 19. Reduced Local Straight Edge Models for $[0_{2n}/90_{2n}]_s$ near One-Inch Diameter Hole 46

Figure 20. Local Curved Edge Models for $[0_{2n}/90_{2n}]_s$ with Six-Inch Diameter Hole 48

Figure 21. Local Curved Edge Models for $[0_{2n}/90_{2n}]_s$ with Three-Inch Diameter Hole 49

Figure 22. Local Curved Edge Models for $[0_{2n}/90_{2n}]_s$ with One-Inch Diameter Hole 50

Figure 23. Interlaminar Stresses for Complete and Reduced Local Model at Straight Edge . 55

Figure 24. Reduced Local Straight Edge Models for $[90_{2n}/0_{2n}]_s$ near Six-Inch Diameter Hole 57

Figure 25. Reduced Local Straight Edge Models for Dispersed Lay-up near Six-Inch Diameter Hole 58

Figure 26. σ_z for Reduced Straight Edge Model for $[0_{2n}/90_{2n}]_s$ 59

Figure 27. τ_{yz} for Reduced Straight Edge Model for $[0_{2n}/90_{2n}]_s$ 61

Figure 28. σ_z for Reduced Straight Edge Model for $[90_{2n}/0_{2n}]_s$ 62

Figure 29. τ_{yz} for Reduced Straight Edge Model for $[90_{2n}/0_{2n}]_s$ 63

Figure 30. σ_z for Reduced Straight Edge Model for Dispersed Lay-up 65

Figure 31. τ_{yz} for Reduced Straight Edge Model for Dispersed Lay-up 66

Figure 32. Interlaminar Stresses nearest Straight Edge for Different Laminate Orientations . 68

Figure 33. σ_z for Reduced Straight Edge Models for $[0_{2n}/90_{2n}]_s$ near Mid-plane with Smaller Holes 70

Figure 34. τ_{yz} for Reduced Straight Edge Models for $[0_{2n}/90_{2n}]_s$ at Interface with Smaller Holes 71

Figure 35. Interlaminar Stress Distributions at the Straight Free Edge for Different Holes .. 73

Figure 36. Interlaminar Stresses for Complete and Reduced Local Model at Curved Edge .. 76

Figure 37. Interlaminar Stresses for Complete and Reduced Local Model at Curved Edge .. 77

Figure 38. Local Curved Edge Models for $[90_{2n}/0_{2n}]_s$ around Six-Inch Diameter Hole 79

Figure 39. Local Curved Edge Models for Dispersed Lay-up around Six-Inch Diameter Hole 80

Figure 40. Interlaminar Stress Distributions Curved Edge Model for $[0_{2n}/90_{2n}]_s$ around Six-Inch Diameter Hole 82

Figure 41. σ_z Contours for Curved Edge Model for $[0_{2n}/90_{2n}]_s$ around Six-Inch Diameter Hole 83

Figure 42. $\tau_{\theta z}$ Contours for $[0_{2n}/90_{2n}]_s$ around Six-Inch Diameter Hole 85

Figure 43. τ_{rz} Contours for Curved Edge Model for $[0_{2n}/90_{2n}]_s$ around Six-Inch Diameter Hole 86

Figure 44. Stresses for Curved Edge Model for $[90_{2n}/0_{2n}]_s$ around Six-Inch Diameter Hole . 88

Figure 45. Stresses for Curved Edge Model for Dispersed Lay-up with Six-Inch Diameter Hole 89

Figure 46. Stresses for Curved Edge Model for Different Stacking Sequences Around Six-Inch Hole 92

Figure 47. Stresses for Curved Edge Model for Different Stacking Sequences Around Six-Inch Hole 93

Figure 48. σ_z for $[0_{2n}/90_{2n}]_s$ near Mid-plane Around Different Diameter Holes 95

Figure 49. Interlaminar Shear for $[0_{2n}/90_{2n}]_s$ at z = 0.025 in. Interface for Different Diameter Holes 96

Figure 50. Global Grids for $[\pm 15_{2n}]_s$ in Compression with Six-inch Diameter Hole 102

Figure 51. Global Grids for $[\pm 15_{2n}]_s$ in Compression with Three-Inch Diameter Hole . . . 103

Figure 52. Global Grids for $[\pm 15_{2n}]_s$ in Compression with One-Inch Diameter Hole 104

Figure 53. Global Grids for $[\pm 45_{2n}]_s$ in Compression with Six-Inch Diameter Hole 105

Figure 54. Global Grids for $[\pm 15_n/\pm 45_n]_s$ in Compression with Six-Inch Diameter Hole . 106

Figure 55. Global Grids for $[0_n/\pm 45_n/90_n]_s$ in Compression with Six-Inch Diameter Hole 107

Figure 56. Local Straight Edge Model Displacement Application for Laminates with Off-Axis Plies in Compression 108

Figure 57. Local Curved Edge Model Displacement Application for Laminates with Off-Axis Plies in Compression 109

Figure 58. Reduced Local Straight Edge Model Displacement Application for Laminates with Off-Axis Plies in Compression 112

Figure 59. Complete Model Displacement Application for Laminates with Off-Axis Plies in Compression 114

Figure 60. Reduced Straight Edge Models for $[\pm 15_{2n}]_s$ near Six-Inch Diameter Hole 115

Figure 61. Full Straight Edge Models for $[\pm 15_{2n}]_s$ near Six-Inch Diameter Hole 116

Figure 62. Straight Edge Models for $[\pm 15_{2n}]_s$ near Three-Inch Diameter Hole 117

Figure 63. Straight Edge Models for $[\pm 15_{2n}]_s$ near One-Inch Diameter Hole 118

Figure 64. Curved Edge Models for $[\pm 15_{2n}]_s$ with Six-Inch Diameter Hole 120

Figure 65. Curved Edge Models for $[\pm 15_{2n}]_s$ with Three-Inch Diameter Hole 121

Figure 66. Curved Edge Models for $[\pm 15_{2n}]_s$ with One-Inch Diameter Hole 122

Figure 67. Displacement Field Comparision Between Full and Reduced Models for $[\pm 15_{2n}]_s$ near a Six-Inch Diameter Hole 129

Figure 68. Through-the-Thickness Stresses for Local Straight Edge Model for $[\pm 15_{2n}]_s$ near Six-Inch Diameter Hole 132

Figure 69. τ_{xz} for Local Straight Edge Model for $[\pm 15_{2n}]_s$ near Six-Inch Diameter Hole . . 133

Figure 70. τ_{xz} at Straight Edge for $[\pm 15_{2n}]_s$ near Different Hole Diameters 135

Figure 71. Straight Edge Models for $[\pm 45_{2n}]_s$ near Six-Inch Diameter Hole 137

Figure 72. Through-the-Thickness Stresses at Straight Edge for $[\pm 45_{2n}]_s$ laminate near Six-Inch Diameter Hole 138

Figure 73. τ_{xz} at Straight Edge for $[\pm 45_{2n}]_s$ near Six-Inch Diameter Hole 140

Figure 74. Straight Edge Models for $[\pm 15_n/\pm 45_n]_s$ near Six-Inch Diameter Hole 141

Figure 75. Through-the-Thickness Stresses for Straight Edge Model for $[\pm 15_n/\pm 45_n]_s$ near Six-Inch Diameter Hole 144

Figure 76. Stress Distributions for $[\pm 15_n/\pm 45_n]_s$ near Six-Inch Diameter Hole 146

Figure 77. τ_{xz} for Straight Edge Model for $[\pm 15_n/\pm 45_n]_s$ near Six-Inch Diameter Hole .. 147

Figure 78. Straight Edge Models for $[0_n/\pm 45_n/90_n]_s$ near Six-Inch Diameter Hole 149

Figure 79. Through-the-Thickness Stresses for $[0_n/\pm 45_n/90_n]_s$ near Six-Inch Diameter Hole 151

Figure 80. σ_z for $[0_n/\pm 45_n/90_n]_s$ near Six-Inch Diameter Hole 153

Figure 81. τ_{yz} for $[0_n/\pm 45_n/90_n]_s$ near Six-Inch Diameter Hole 155

Figure 82. Interlaminar Stress Distributions for $[0_n/\pm 45_n/90_n]_s$ near Six-Inch Diameter Hole 157

Figure 83. Partial Curved Edge Models for $[\pm 15_{2n}]_s$ around Six-Inch Diameter Hole 161

Figure 84. Through-the-Thickness Stresses for Partial Curved Edge Model for $[\pm 15_{2n}]_s$ around Six-Inch Diameter Hole 162

Figure 85. σ_z Contours for Partial Curved Edge Model for $[\pm 15_{2n}]_s$ around Six-Inch Diameter Hole 163

Figure 86. $\tau_{\theta z}$ Contours for Partial Curved Edge Model for $[\pm 15_{2n}]_s$ around Six-Inch Diameter Hole 165

Figure 87. τ_{rz} Contours for Partial Curved Edge Model for $[\pm 15_{2n}]_s$ around Six-Inch Diameter Hole 167

Figure 88. σ_z around Hole for $[\pm 15_{2n}]_s$ for Different Holes Diameters 169

Figure 89. Interlaminar Shear Stress Distributions at the Curved Free Edge for Different Hole Diameters 170

Figure 90. Partial Curved Edge Models for $[\pm 45_{2n}]_s$ around Six-Inch Diameter Hole 173

Figure 91. Through-the-Thickness Stresses for Partial Curved Edge Model for $[\pm 45_{2n}]_s$ near Six-Inch Diameter Hole 174

Figure 92. σ_z Contours for Partial Curved Edge Model for $[\pm 45_{2n}]_s$ around Six-Inch Diameter Hole 175

Figure 93. $\tau_{\theta z}$ Contours for Partial Curved Edge Model for $[\pm 45_{2n}]_s$ around Six-Inch Diameter Hole 177

Figure 94. τ_{rz} Contours for Partial Curved Edge Model for $[\pm 45_{2n}]_s$ around Six-Inch Diameter Hole 178

Figure 95. Partial Curved Edge Models for $[\pm 15_n/\pm 45_n]_s$ around Six-Inch Diameter Hole 180

Figure 96. Stresses for Partial Curved Edge Model for $[\pm 15_n/\pm 45_n]_s$ around Six-Inch Diameter Hole 182

Figure 97. σ_z Contours for Partial Curved Edge Model for $[\pm 15_n/\pm 45_n]_s$ around Six-Inch Diameter Hole 183

Figure 98. $\tau_{\theta z}$ Contours for Partial Curved Edge Model for $[\pm 15_n/\pm 45_n]_s$ around Six-Inch Diameter Hole 184

Figure 99. τ_{rz} Contours for Partial Curved Edge Model for $[\pm 15_n/\pm 45_n]_s$ around Six-Inch Diameter Hole 186

Figure 100. Partial Curved Edge Model for $[0_n/\pm 45_n/90_n]_s$ around Six-Inch Diameter Hole 188

Figure 101. Stresses for Partial Curved Edge Model for Quasi-isotropic Laminate around Six-Inch Diameter Hole 189

Figure 102. σ_z Contours for Partial Curved Edge Model for Quasi-isotropic Laminate around Six-Inch Diameter Hole 190

Figure 103. $\tau_{\theta z}$ Contours for Partial Curved Edge Model for Quasi-isotropic Laminate around Six-Inch Diameter Hole 192

Figure 104. τ_{rz} Contours for Partial Curved Edge Model for Quasi-isotropic Laminate around Six-Inch Diameter Hole 193

Figure 105. Extrapolation functions for 2x2 and 2x3 integration sequences along z = constant 214

Figure 106. Extrapolation functions for 2x4 integration sequence along z = constant 215

Figure 107. Extrapolation functions for 3x3 integration sequence along z = constant 216

Figure 108. Extrapolation functions for 3x4 integration sequence along z = constant 217

Figure 109. Extrapolation functions for 4x4 integration sequence along z = constant 218

Figure 110. Extrapolation with 2x3 functions of xy^2 219

Figure 111. Extrapolation with 2x3 functions of x^2y^2 220

Figure 112. Extrapolation with 3x3 functions of x^2y^2 221

List of Tables

Table 1. Mechanical Properties of T300/5208 Graphite/Epoxy 12

Table 2. Two-Dimensional Cross-Ply Compression Global Model Characteristics 28

Table 3. Comparison of Complete and Global/Local Analyses for $[0_{2n}/90_{2n}]_s$ Laminate with Six-Inch Diameter Hole 37

Table 4. Three-Dimensional Cross-Ply Compression Local Straight Edge Model Characteristics 42

Table 5. Three-Dimensional Cross-Ply Compression Local Curved Edge Model Characteristics 47

Table 6. Two-Dimensional Angle-Ply and Quasi-isotropic Compression Global Model Characteristics 101

Table 7. Comparison of Complete and Global/Local Analyses for $[\pm 15_{2n}]_s$ Laminate with a Six-Inch Diameter Hole 113

Table 8. Three-Dimensional Angle-Ply and Quasi-isotropic Compression Local Straight Edge Model Characteristics 119

Table 9. Three-Dimensional Angle-Ply and Quasi-Isotropic Compression Local Curved Edge Models 123

Table 10. Extrapolation Functions for 2x2x2 Integration Rule 222

Table 11. Extrapolation Functions for 2x2x3 Integration Rule 223

Table 12. Extrapolation Functions for 3x3x2 Integration Rule for Integration Points along z = -g 224

Table 13. Extrapolation Functions for 3x3x2 Integration Rule for Integration Points along z = g 225

Table 14. Extrapolation Functions for 3x3x3 Integration Rule for Integration Points along z = -h 226

Table 15. Extrapolation Functions for 3x3x3 Integration Rule for Integration Points along z = 0 227

Table 16. Extrapolation Functions for 3x3x3 Integration Rule for Integration Points along z=h 228

Table 17. Extrapolation Functions for 3x3x4 Integration Rule for Integration Points along z=-m 229

Table 18. Extrapolation Functions for 3x3x4 Integration Rule for Integration Points along z=-n 230

Table 19. Extrapolation Functions for 3x3x4 Integration Rule for Integration Points along z=n 231

Table 20. Extrapolation Functions for 3x3x4 Integration Rule for Integration Points along z=m 232

Table 21. Extrapolation Functions for 4x4x2 Integration Rule for Integration Points along z=-g 233

Table 22. Extrapolation Functions for 4x4x2 Integration Rule for Integration Points along z=g 234

Table 23. Extrapolation Functions for 4x4x3 Integration Rule for Integration Points along z=-h 235

Table 24. Extrapolation Functions for 4x4x3 Integration Rule for Integration Points along z=0 236

Table 25. Extrapolation Functions for 4x4x3 Integration Rule for Integration Points along z=h 237

Table 26. Extrapolation Functions for 4x4x4 Integration Rule for Integration Points along z=-m 238

Table 27. Extrapolation Functions for 4x4x4 Integration Rule for Integration Points along z=-n 239

Table 28. Extrapolation Functions for 4x4x4 Integration Rule for Integration Points along z=n 240

Table 29. Extrapolation Functions for 4x4x4 Integration Rule for Integration Points along z=m 241

1.0 Introduction

Since their initial use by the aerospace industry, modern composite materials have been utilized in a wide range of applications. Extensive testing was done initially to establish the reliability and service limits of specific parts. As understanding and confidence in composite materials grew, it was desired to eliminate some of the time lag and expense of fabrication and testing by using analytical techniques. The inherent complexity of composite materials has meant that computer-implemented analysis techniques are required to predict the structural response of even simple components. Composite material constitutive relations are often highly coupled between extension, shearing, and bending, and not necessarily constant throughout a structure. Geometric discontinuities, large stress gradients, large displacements and rotations, and material nonlinearities may also be present. Different means of analysis exist for response prediction with varying levels of accuracy, capability, and efficiency. Available approaches include analytical, variational, finite difference methods, finite element methods, and boundary element methods. Each approach has advantages and disadvantages. Some of the more computationally expensive techniques have very broad modeling capabilities, while other less complex techniques work well only for specific problems with simple geometries. The analyst is required to select, or possibly develop, an analysis strategy which best suits the problem at hand.

To analyze general problems, many have turned to the finite element method. The initial approach adopted was to use the computationally least demanding means possible: two-dimensional elements. For composite laminates of finite size subjected to external loads, application of a two-dimensional finite method can yield accurate results at locations away from traction-free edges and discontinuities where the stress states are more complex.

Stress fields in composite laminates, in general, consist of six components which can be divided into two groups: intralaminar stresses (σ_x, σ_y, τ_{xy}) and interlaminar stresses (σ_z, τ_{xz}, τ_{yz}). Intralaminar stresses are the in-plane components, while interlaminar stresses arise during the transition from the internal in-plane stress state to that near a traction-free edge or discontinuity. The character of the stress distribution is dependent not only on the type of loading and the geometry involved, but also on the Poisson's ratio mismatch or shear coupling that may exist between adjacent material layers. All six components of stress can have large gradients during the transition from the internal stress state to the traction-free edge condition (Renieri and Herakovich, 1976), (Wang and Crossman, 1977). Two-dimensional elements have been applied extensively during the study of a straight free edge of a laminated plate subjected to uniaxial tension or compression (Salamon, 1980). However, near a circular hole the transition from the internal stress state to the traction-free edge of the hole is considerably more complicated, and a two-dimensional finite element solution cannot necessarily capture this effect (Dana, 1974), (Salamon, 1980). As limitations of two-dimensional analyses became known and more powerful computers became available, the use of three-dimensional finite elements for detailed stress analysis of composite structures increased (Rybicki, 1971), (Dana, 1974), (Dana and Barker, 1974), (Barker et al, 1974), (Renieri and Herakovich, 1976), (Stanton et al, 1977), (Griffin, 1983), (Griffin, 1989), (Thompson and Griffin, 1990), (Thompson et al, 1990). For many applications, however, a full three-dimensional analysis may be inefficient or even intractable. It is logical to streamline the analysis so that adequate response predictions are obtained with minimum computational and analyst effort.

A simplified analysis on the entire body, or global region, is done here with two-dimensional finite elements. A more detailed and independent analysis is then performed on a local region of interest

with three-dimensional finite elements. In particular, this two-dimensional to three-dimensional global/local finite element analysis technique is applied to a finite laminated composite plate with a central circular hole, with the local regions of interest being the area around the hole and a portion of the straight free edge near the hole. The interlaminar stress state in these regions is examined in detail for several stacking sequences and three different hole sizes under compressive loading. Cross-ply, angle-ply and quasi-isotropic laminates in compression are considered herein. All plates had dimensions of 18 inches in length, 12 inches in width, a thickness of 0.1 inch, with one-, three-, and six-inch diameter holes centrally located. The results obtained are compared to known information about interlaminar stress states and to complete three-dimensional finite element solutions, whenever available. The development and verification of global/local finite element analysis was considered to be the primary focus of this particular work, and the interlaminar stress states were examined during the verification of this technique. In addition, the effectiveness of this computationally more efficient method of analysis was demonstrated.

2.0 Literature Review - Global/Local Analysis

Although the concept of global/local analysis is not new, little work has been published which explains the development and verification of specific techniques, especially as applied to stress analysis of composite structures. Recently, more analysts have been addressing the issue of reducing the computational effort associated with nonlinear and transient structural analysis. It is believed that a considerable amount of global/local analysis has been utilized in the aircraft industry. The majority of this information, however, is proprietary and does not appear in the open literature. This fact complicates the transfer of technical information about global/local analysis techniques and hinders careful development and verification of the methods.

The definition of global/local analysis varies from one analyst to another, and a wide range of such analyses can be performed in the analysis and design of various structural components of an airplane. For example, the fuselage, skin, stiffeners, and fasteners would require different levels of modeling detail and analysis. Concurrent work on several areas of a complex problem could occur more readily with global/local analyses. However, before any global/local analysis technique is used, development and verification of that method must be complete. Reddy (1985) gives several candidate problem areas that lend themselves to global/local analysis and may be used in the development of a particular global/local analysis technique. These include free-edge stress and contact stress problems, impact, fracture mechanics, and unbounded domains. All of these problems share

some of the following features: stress concentrations which require detailed modeling, often three-dimensional in character; large rotations/strains which require a nonlinear analysis; local discontinuities, either geometric or material in nature; and possible material nonlinearities. Some of these may affect a small section of the structure in question, and attempting to incorporate all of the details in a single model of the entire domain can lead to large, prohibitively expensive models. It is proposed to perform an accurate global model which determines the local effect on a gross scale, and then subsequently perform as many local analyses as required. These local analyses would account for the local effects either by further refinement of the global theory or by applying a new theory in the local region. Reddy (1985) and Noor (1986) identify several problem areas that need to be addressed for the development and use of global/local analyses. These include the selection of the regions and the method to be used in those regions, interfacing between the regions and the possibly different methods while maintaining displacement compatibility and traction equilibrium, and how to best compensate for local regions that are transient and may change in geometry or the required analytical technique during the course of the analysis.

Various combinations of methods have been proposed for global/local techniques and for both the global and local areas, including analytical, variational, finite difference, finite element, and boundary elements (Reddy, 1985). The combination of different methods has been termed hybrid global/local analysis methods. Substructuring is the reduction of a complex structure to smaller parts which will allow for more detailed analysis of the localized effect. This substructuring can involve the use of different methods between the regions or merely a refinement of the smaller regions. Zooming is a type of substructuring when a more refined local model is generated from a coarse global model. As can readily be seen, global/local analysis techniques can be created which fall into more than one category. A comprehensive literature review of global/local analyses can be found in Ransom (1989). Discussion of some of the techniques applicable to structural analysis of laminated composites with holes will be presented herein.

Bradford et al (1976) and Dong (1983,1985) have developed a hybrid technique, which they call Global Local Finite Element Method (GLFEM). This particular method focuses on sets of

problem-dependent analytical functions to model the global response. The resulting displacement and rotation field is applied to a local two-dimensional finite element model. Several problems have been solved using GLFEM with success: the axisymmetric scattering of elastic waves, determining the frequency of simply-supported, rectangular, isotropic plates with and without holes, and crack tip analysis in fracture mechanics. However, this method is highly dependent on the global functions and requires that the selected functions model the global behavior accurately. In addition, the solutions of these global and local models are coupled, requiring a reanalysis for each problem parameter change. This method lends itself well to problems of regular geometry, but not to problems whose geometry or response cannot be described readily in a functional manner, such as composite laminates with discontinuities.

The linear constraint method is attributed to Schwartz (1981) and was used by Kelley (1982) to impose the displacement field from a coarse structural model on a refined local model of a discontinuity. To apply displacements at nodes which are not in the global model, interpolation of the global displacements from nearby nodes was done with the global element shape functions, which were linear. Depending on the refinement level, the linear constraints on the additional local nodes could over-constrain the model and introduce errors into the displacement field. These small errors in the displacements could result in more substantial errors in the stress field; particularly, if stress gradients were present. Another problem with this method is that re-analyses are required for changes in the local area of interest, and that foreknowledge of the extent of the localized area is required prior to the global solution.

Hirai and colleagues (1984) have developed "an efficient zooming technique." A coarse finite element mesh was analyzed, and zones of interest were identified and subdivided further. The displacements from the coarse mesh are applied as input to the finer mesh, but the effect of the refined region is ignored in the overall response of the coarse model. Static condensation is then performed, and exact structural reanalysis methods are used to analyze the new system. Successive application of this technique requires the information from all of the previous levels of zooming in order to generate the solution, and thus this method may become rather unwieldy. Further developments

led to the "exact zooming method" (Hirai,1985). The improvements eliminated some of the information required for each zoom level since successive zooms involved the previous level. The expanded stiffness matrix contains information from all of the previous levels in the stiffness of the boundary of the local area, and is used to solve only for the information at the desired location contained within the final refinement. Only an isotropic plate with a hole was considered.

Global/local modeling was done by Knight and colleagues (1989) to calculate the detailed stresses around discontinuities in a buckled composite component with analytical failure prediction techniques. Two-dimensional finite elements were used for a coarse global model, and the displacements and rotations at the global/local interface were applied to a refined two-dimensional model created with a zooming technique. It was noted that a three-dimensional modeling capability would be required in order to determine through-the-thickness state of stress for this particular case. Four-node quadrilateral elements were used throughout the modeling process.

Ransom et al (1989a, 1989b) used a two-dimensional global model to model the overall behavior of an isotropic panel with finite-width effects, and a composite blade-stiffened panel with a discontinuous stiffener. The local models are two-dimensional, but are more refined to determine the local detailed stress states for specific regions. Application of the displacements and rotations to the local model was done with interpolation splines. The coefficients of the splines were determined from the global-displacement field, and so this technique does not require à priori knowledge of the location of the local region. In this approach, those nodes in the local model which are not in the global model will have the displacements determined from the appropriate interpolated displacement field. The out-of-plane strain and stress components were not presented.

The specified boundary stiffness/force method (Jara-Almonte and Knight, 1988) uses the stiffnesses and forces from the global model at the nodes of the local model. This approach is like substructuring, but discards the information from the old region. Stiffnesses and forces represent the effect of the rest of the structure on the subregion through the incorporation of the global stiffness terms in the local stiffness matrix of the subregion model, and the application of the forces as external

loads on the local area. Global/local analysis was performed, and it was found that for the problem considered, their method was more accurate than specifying displacements, and was an improvement over the linear constraint and the zooming techniques developed by others.

The development of a two-dimensional to three-dimensional global/local finite element analysis was reported by Vidussoni (1988). A global two-dimensional finite element analysis using 4-node quadrilateral elements was followed by a three-dimensional finite element analysis using 20-node displacement-based brick elements. Interfacing between the models was done by applying in-plane displacement from the global model to the independent local models. The effect of the presence of a circular hole on the straight free-edge stresses, and of the stress states around holes was considered. A limitation of this work was the version of the software system and the available computational power. Part of the current work repeats some of the analyses performed by Vidussoni, using quadratic elements and extends the technique to other laminates. Studies done by Vidussoni for acceptable element aspect ratio limits, the number of elements per material layer for a given element integration scheme, and the straight edge nodal distribution were used in the present work.

A natural extension of two-dimensional to three-dimensional analysis is to use transition elements between the two models. Surana (1980) presented information about a family of transition finite elements between two-dimensional shell elements and three-dimensional isoparametric solid elements. Linear elastic isotropic applications were initially considered, with further work being published by Surana (1982) which included a geometrically-nonlinear formulation for the family of elements. Liao et al (1988) investigated both linear and geometrically-nonlinear static and transient analysis of laminated anisotropic shell-type structures. Comparison was done between models built of degenerated shell elements, three-dimensional continuum elements, and the transition elements. Gong (1988) also derived a family of transition elements of variable number of nodes enabling three-dimensional finite elements to be joined to two-dimensional finite elements. Applications examined included an aircraft hatch door with a polymethyl-methacrylate shell. Because of the formulation of the transition elements, their use is appropriate only in regions where out-of-plane stresses, (σ_z, τ_{yz}, τ_{xz}) are negligible, and gradients are relatively low.

Several global/local techniques have been developed specifically to reduce the time and effort associated with solving nonlinear problems. Clough and Wilson (1979) reported work in applying a global/local substructuring approach to a structure with a materially nonlinear response region. Most of the structure was assumed to be linear with only small areas of nonlinearity. Subdivision of the structure into independent linear and nonlinear areas was based on the assumption that each nonlinear section was also independent of other nonlinear sections. During each step of the analysis the nonlinear subsystem stiffnesses were updated, while the evaluation of the linear stiffness occurred at the first load step, and then these were assembled to determine the total system stiffness. Specific examples were mentioned, but the focus of this paper was on development of the method. None of the examples mentioned, however, were composite structures. Noor and Peters (1980) presented a global/local approach to perform nonlinear finite element analysis applied to large deflections of isotropic clamped beams and shallow arches. The discretized area was limited to a small number of deformation modes which were described by functions commonly used in static perturbation methods. Rayleigh-Ritz approximations were used to reduce the vectors of unknown nodal forces and displacements with these functions, and therefore to reduce effort required to solve the nonlinear analysis.

Han and Abel (1985) developed and used an adaptive hybrid substructuring technique where the entire body was initially modeled with three-dimensional linear elastic superelements. As the loading increases and localized stresses approach a user-specified critical stress, then those areas are modeled with nonlinear elements. While automatic mesh refinement was implemented, provisions for user-interfaced refinement were made. The stiffness matrix was updated whenever a linear portion developed nonlinearities, and for each load step in any nonlinear portion of the model. Static condensation was done to eliminate degrees of freedom. While this method appears advantageous, as more of the structure develops nonlinearities its tractability may decrease. Examples presented were metallic structural components using the yield stress as the user-defined critical stress.

Division of a structural component into localized areas which could be considered in parallel with global/local analyses techniques appears to be a viable way to take advantage of increasingly more common and powerful parallel computers. Sun and Mao (1988) have implemented such a technique which exploits the rapid convergence of displacement fields for finite element analyses. A coarse global finite element two-dimensional solution is generated, and its displacements are applied to the local refined models of interest. Application of the displacements is done directly or with the shape functions of the global model when nodal correspondence is not exact. Because quadratic elements were used, the local model is not constrained linearly. Each local 'zoomed' two-dimensional region then had a processor devoted to its solution.

3.0 Common Features of the Global/Local Finite Element Analysis Techniques

The problems analyzed in the present study include: a) cross-ply plates under compression, b) angle-ply plates under compression, and c) quasi-isotropic plates under compression. The interlaminar stress states for a portion of the straight free edge near a central circular hole and the region near the hole itself were examined. Common features of the problem description and approach for these cases and some special considerations are presented in the following section.

3.1 Assumptions and Limitations of the Global/Local Procedure

The two-dimensional to three-dimensional global/local finite element analysis used in the present study has certain limitations which cannot be overcome. Some of these limitations are generally found within two-dimensional or three-dimensional finite element analysis, while others are attrib-

utable to the global/local analysis technique itself. At all times, it must be remembered that the finite element method is an approximate solution to a set of differential equations governing the elastic response of a medium. An elasticity solution, for example, would satisfy compatibility and equilibrium over the entire domain exactly, while the finite element method may satisfy these conditions in a piecewise manner (Reddy, 1984, 1989), (Zienkiewicz, 1986), (Kardestuncer, 1987). Such approximations are necessary when no exact solution is available. The limitations of the global/local finite element analysis are discussed later.

The material properties used for the global and local finite element analyses are the elastic moduli and Poisson's ratios presented in Table 1. The U.S. Customary units values were used during the analyses. Most experimental procedures used to determine material properties involve testing laminates of a specific layup, applying a known load, and backcalculating the properties of the fiber/matrix system from the strain state. This approach assumes that the laminated composite is comprised of perfectly bonded laminae with no mechanical property variations within a particular lamina. These properties are smeared: the fibers and matrix are assumed to be an homogenous and orthotropic system. These must be converted to oriented layer-by-layer constitutive properties for use in determining the mechanical response of a laminated composite with a three-dimensional finite element analysis, while classical two-dimensional plate/shell finite element analyses require a stiffness quantity.

Table 1. Mechanical Properties of T300/5208 Graphite/Epoxy

E_1	E_2	E_3	G_{12}	G_{13}	G_{23}	ν_{12}	ν_{13}	ν_{23}
19.2 Msi	1.56 Msi	1.56 Msi	0.82 Msi	0.82 Msi	0.54 Msi	0.239	0.239	0.45
132.3 GPa	10.7 GPa	10.7 GPa	5.65 GPa	5.65 GPa	3.72 GPa	0.239	0.239	0.45

The conversion of material properties for a system to the stiffness quantities required by the two-dimensional finite element analyses is done by integrating the effect of each layer through the thickness as done for classical lamination theory. Thus, the stiffness of different plies and their

orientations are combined, generally, by the constitutive processors of the finite element software system selected. Assumptions in classical lamination theory include: the laminate is assumed to be thin, made of perfectly bonded individual orthotropic laminae, each of which obeys Hooke's Law, and is linear elastic in its response, as laminae and as a laminate. These bonds are assumed to be infinitesimally thin, and not shear-deformable. The reference surface of a laminate is usually considered to be a laminate mid-surface, and a straight line drawn perpendicular to this surface will remain straight, normal and its original length throughout the deformation. All interlaminar strains and stresses are therefore assumed to be negligible, and all through-the-thickness variation is lost. Thus, the global model displacement values for a particular node are an 'average' of the actual response for the laminate. Because of the method to determine the the stiffness quantities used in two-dimensional finite element analysis, displacement or strain fields from the global model cannot, in general, determine effects of the individual material layers (Jones, 1975), (Reddy, 1984, 1989), (Zienkiewicz, 1986).

Isoparametric elements can accurately determine the displacement field for a given converged model by using a polynomial description of the displacement field. Equilibrium is enforced through the static equations between the internal forces generated throughout the model and the applied external forces. The strain field at the integration points is determined on an element-by-element basis as a derivative of the element displacement field. Nodal point strains, however, may be discontinuous. This method of strain determination has been accepted by finite element users since the initial use of finite element analysis. However, the strains, and ultimately the stresses which are found by multiplying the strains by an elasticity matrix, are determined by derivatives of displacements and are not as accurate as when equations governing their behavior are included in the element stiffness matrix formulation, as in the formulation of hybrid elements.

The technique of enforcing conditions on the strains and stresses inside an element creates a new class of elements called hybrid- and mixed-formulation elements, which are often problem specific, more expensive, and less versatile (Zienkiewicz, 1986), (Kardestuncer, 1987). With displacement-based elements, stresses determined along traction-free edges are not identically zero. A traction-

free hybrid element has been developed to overcome this difficulty (Spilker and Chou, 1980). Even though these elements are available, the use of displacement-based finite elements has not diminished noticeably. If a global/local modeling technique is to be general in its application, then the workhorse elements used by most analysts should be used, not special elements which may be of limited availability. The stress field, as determined by these models, will therefore be limited in its accuracy and should not be taken as absolute, but rather as a strong indicator of the distribution and relative magnitude.

The global/local finite element method developed in this thesis requires that displacements from the global model be applied to the local model in a consistent fashion. As with most computer-based applications, when the displacements are calculated in the global model and then applied to the local model, there is a limit in the accuracy involved. The global displacement field has a finite number of accurate digits, which are then applied to a system of equations which may encounter further accuracy limitations because of computer round-off errors to determine the local model displacement field. When the strains are determined as gradients of these displacements, small inaccuracies can result in spurious strains. In addition, should repeated zooming be desired from the global model to the local model, and then to another local model, care must be taken that the displacements which are applied are still significant and not compromised by the displacement application of the previous step. The inherited errors from previous models may grow and dominate the solution and lead the analyst astray.

3.2 Finite Element Software System

All of the analyses reported herein were done on the CONVEX C220 computer in the Structural Mechanics Division at the NASA Langley Research Center, and all computation times reported are from batch jobs submitted on the CONVEX. The finite element software system used is under

continuing development by the Computational Mechanics Branch (CMB, formerly the Computational Structural Mechanics Group) at NASA Langley Research Center and is called the Testbed (Knight, 1989), (Stewart, 1989). The Testbed is a set of multi-purpose modular processors which allows for the study of computational and structural analysis methods under a common framework. The hierarchy inherent in the Testbed is represented in the pyramid shown in Figure 1. A user executes or customizes procedures which interact with and invoke processors. A user of the Testbed requires no more detailed knowledge about the processors than would be required to use a commercially available software package. Installation of elements into the Testbed is relatively straightforward through the generic element processor (Stanley and Nour-Omid, 1990). Once implemented, benchmarking and performance evaluations of an element can be conducted. The architecture of the Testbed data structure is independent of the operating systems and the computer itself. Some processors exploit the architecture of the individual systems, but most do not. Research in structural analysis methods can take place in a cooperative environment at the procedure or processor level, while computational methods research often delves deeper toward the base of the pyramid.

The EX97 element of processor "ES1" implemented through the generic element processor was used to solve all of the global models. This two-dimensional element is a nine-node assumed natural-coordinate strain element installed in the Testbed by Lockheed Palo Alto Research Laboratories. The local model was analyzed with classical 20-node displacement-based Serendipity elements. A family of these elements was installed in the Testbed using the generic element processor by the author, and is presented in Figure 2. Mesh studies were done by Vidussoni (1988) for the cross-ply compression loading case with an earlier version of the Testbed, and it was determined that two 20-node elements, with a full 3x3x3 Gauss point rule to integrate the element stiffness matrices, per material layer were sufficient to capture the desired information. This was assumed to be correct for the other families of loading conditions considered here.

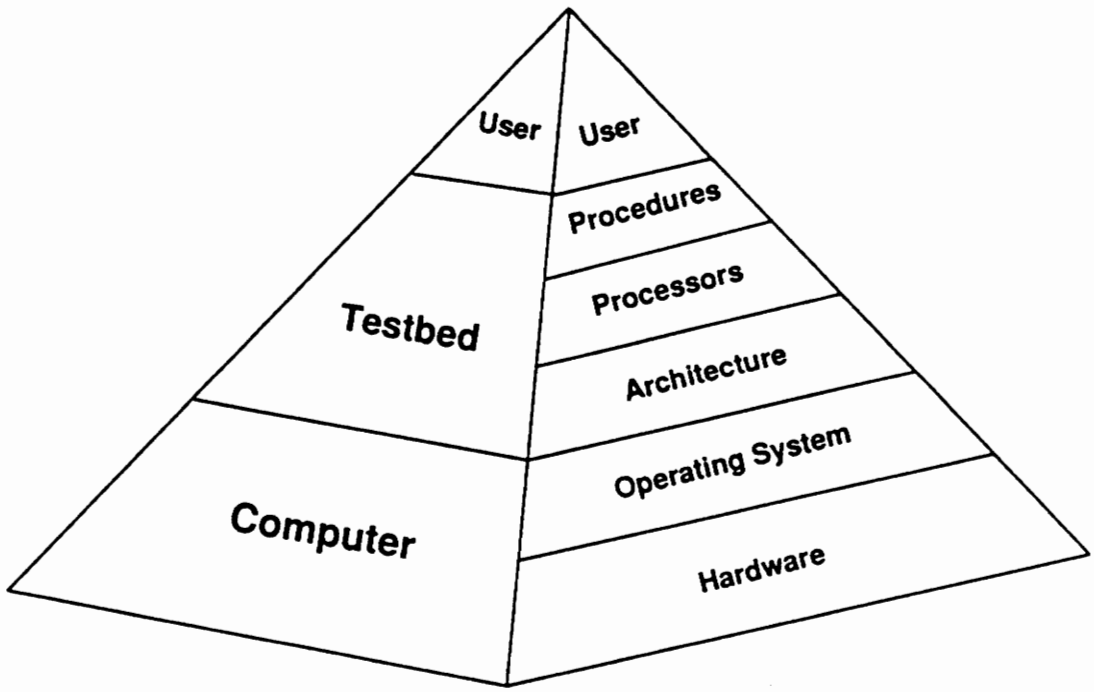

Figure 1. Testbed Structural Methods Research

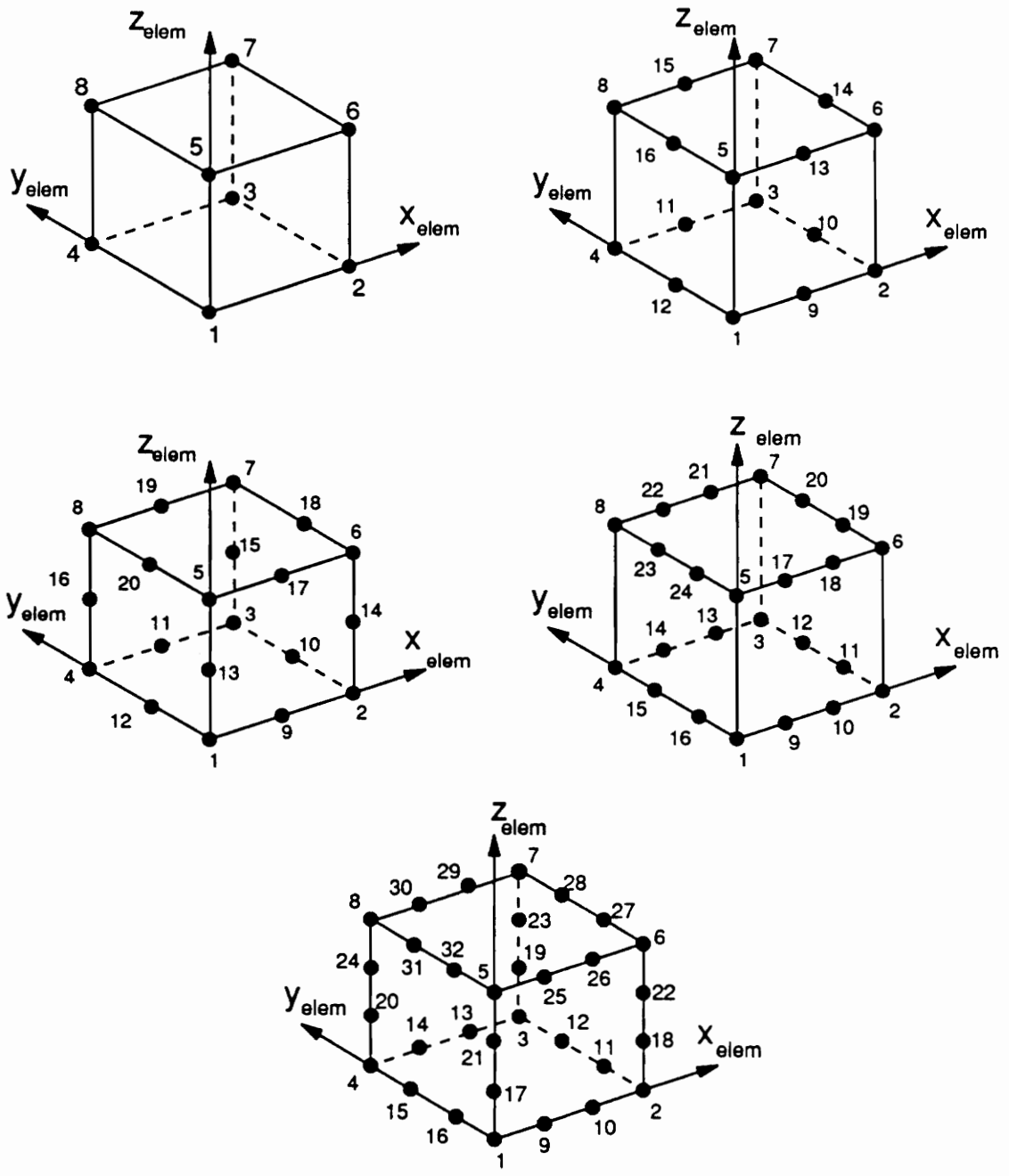

Figure 2. Three-Dimensional Elements Installed in Testbed

3.3 *Global Model Generation*

The global model was initially generated using processor "CSM1" of the Testbed (Version 1.2), which produces a grid of plate elements. Each plate had a total thickness of 0.1 inch and planar dimensions of 18x12 inches. Three different hole diameters were considered: one, three, and six inches. Figure 3 is a schematic of the plate with a hole and the prescribed uniform x-displacement of 0.1 inches at the global $x = 0$ edge imposed as boundary conditions. This edge was restrained from movement in the y-direction, the z-direction, and all rotations, while the opposing edge was fixed for all degrees of freedom. No other displacement or rotation conditions were applied. This corresponds to having the loaded ends perfectly clamped as for a compression test.

It has been shown previously that interlaminar effects are generally confined to one laminate thickness from a straight free edge (Pagano, 1974). A fine mesh was generated in this region with "CSM1." Three elements were distributed equally by "CSM1" across two laminate thicknesses (0.2 in.) of width. The line two laminate thicknesses from and parallel to the straight edge along the maximum y-dimension of the plate thus became the global/local interface for the straight free edge models. A mesh study was done by Vidussoni (1988) to determine a distribution of elements in this zone to model accurately the interlaminar effects in cross-ply laminates under in-plane compression. The three rows of elements generated by "CSM1" for all of the global models were modified to have the distribution used by Vidussoni (1988), as shown in Figure 4, for a portion of the six-inch hole global model. The row nearest the global/local boundary is one laminate thickness in width and provides a zone between this boundary and the area affected by the free edge of the laminate. The next row was two-thirds of the laminate thickness, with the remaining row being one-third of the laminate thickness in width. This modification was performed so that all of the models had a one-to-one nodal correspondence along global/local interfaces. This two-dimensional to three-dimensional global/local analysis method is not restricted to having such a nodal correspondence to succeed, but to demonstrate the validity of this modeling technique it was so limited for the

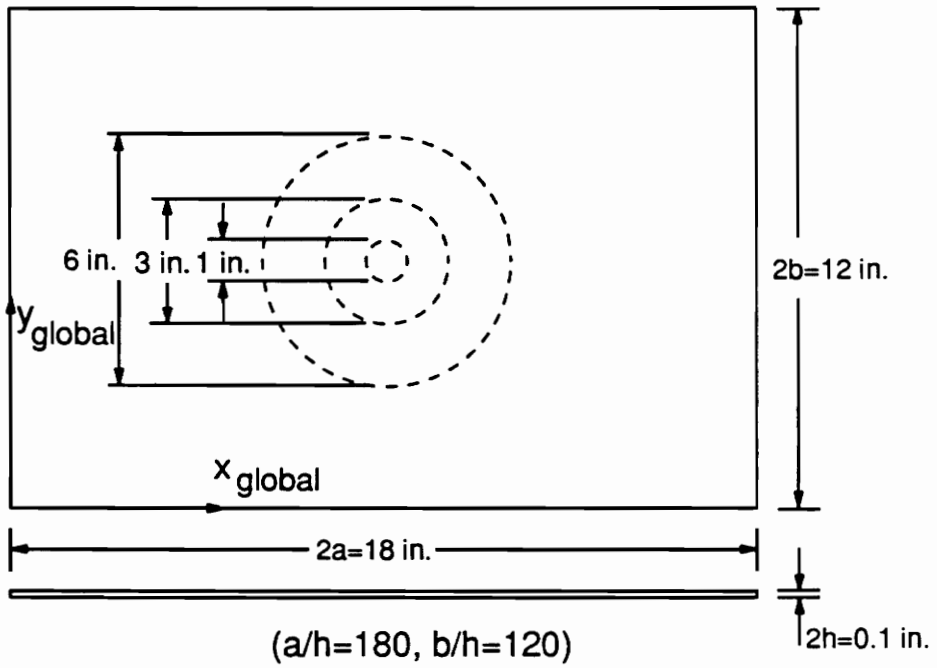

(a/h=180, b/h=120)

Compression

along edge x =0 in.
allow only displacement in x
along edge x =18 in.
allow no movement
along edge y =0 in.
completely free
along edge y =12 in.
completely free

x =0 in., y =0 in.
allow only displacement in x
x =0 in., y =12 in.
allow only displacement in x
x =18 in., y =0 in.
allow no movement
x =18 in., y =12 in.
allow no movement

Figure 3. Boundary conditions applied to the global model for compression

present study. The determination of the in-plane displacement values at those nodes which do not exist in the global model can be done in a number of ways. Previous work has used interpolation splines over a critical region of the global model (Ransom, 1989), or the global element shape functions (Schwartz, 1981), (Kelley, 1982), (Sun and Mao, 1988). The concentration of this thesis is on the methodology of the extraction of accurate global two-dimensional displacement fields and their application in three-dimensions to the local models.

Vidussoni (1988) also examined the interlaminar effects around holes of different sizes. For the plate with a six-inch hole, it was determined that if the global/local boundary was a minimum of five laminate thicknesses (0.5 in.) away from the hole, the local analysis could determine accurately the stress field around the hole. During his study the global/local interfaces remained at the same global nodal locations, and the smaller holes were consequently farther from the global/local interface than the larger ones. Generally a large hole in a finite width plate is considered to have a more severe impact on the global response than a smaller hole, and because Vidussoni (1988) had success with this distance from the six-inch hole, the minimum distance from the global/local interface to the hole edge was selected to be five laminate thicknesses for all of the hole diameters. No attempt was made in the present study to further minimize this distance. To provide an ample buffer zone between the displacement application region of the local model and the hole edge, five rings of elements of equal distribution were placed around the central circular hole for all of the hole sizes, as seen in Figure 5. The number of radial spokes emanating from the hole was varied to obtain elements with comparatively low in-plane aspect ratios and curvatures, with the larger holes having a higher number of spokes and a greater number of elements around the hole region. The square of nodes around the holes, in this figure, was identified as the global/local boundary for all laminates. This identification was done à priori, but this type of global/local analysis is not restricted to foreknowledge of the exact extent of the three-dimensional stress field. However, the global/local interface selected should not intersect the three-dimensional effect, as will be demonstrated. The global model was then analyzed for the angle-ply and quasi-isotropic laminates. Cross-ply laminates contain additional planes of symmetry, so that the in-plane modeling requirement is one-

a)

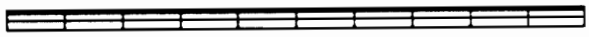

b)

Figure 4. Nodal distributions generated by "CSM1" and as modified for the straight edge for a six-inch hole model: a) Original b) As modified

quarter of the global model. In order to maintain a one-to-one nodal correspondence along the global/local boundaries, additional modifications to the nodal distributions were required. The rings of elements around the hole region had their nodal distributions altered so four concentric rings of circular elements were obtained. These rings are the same as those used in the local hole models for all of the laminates, and are described in detail in the following section.

3.4 Local Model Generation

The local straight edge model had the same modified in-plane nodal distribution as the global model. Three 20-node elements with full integration, resulting in nine integration points in the y-direction, were used across the local model width. For laminates with off-axis plies, the global model had an in-plane nodal distribution inside the global/local boundary which was not coincident with the local curved edge model. To generate these distributions, the grid provided by "CSM1" was modified slightly to produce concentric rings of elements with specified widths around the hole (Figure 5). Because interlaminar stresses are often limited to a region which is approximately equal to the laminate thickness, two element rings of equal width were placed within one laminate thickness of the hole edge. The next two rings were specified to be one and two laminate thicknesses in width, respectively, along any radial line extending outward from the curved edge. The final ring of elements was allowed to vary in its planar dimensions in order to mate the curved elements of the hole region with the surrounding rectangular elements maintaining a minimum element width of 0.1 inches throughout this matching region.

The modified in-plane nodal distribution produced by "CSM1" was then expanded through the thickness for both the straight edge and the curved edge models. Half of the laminate thickness is sufficient for each local model due to the symmetry of the geometry and loading conditions about the laminate mid-plane. A total of eight elements was used through the thickness for each of the

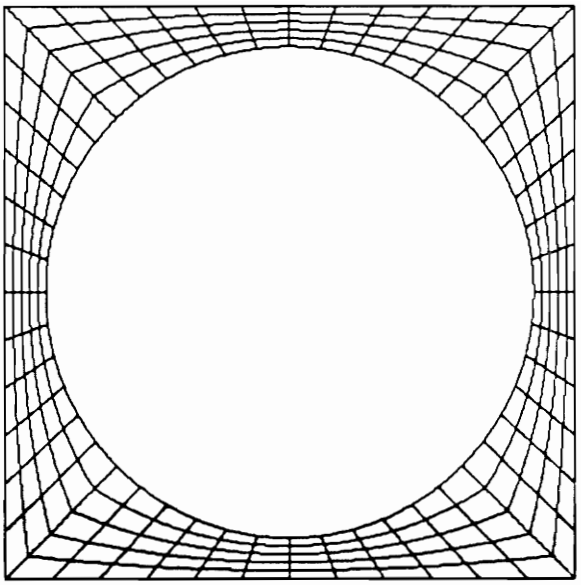

a)

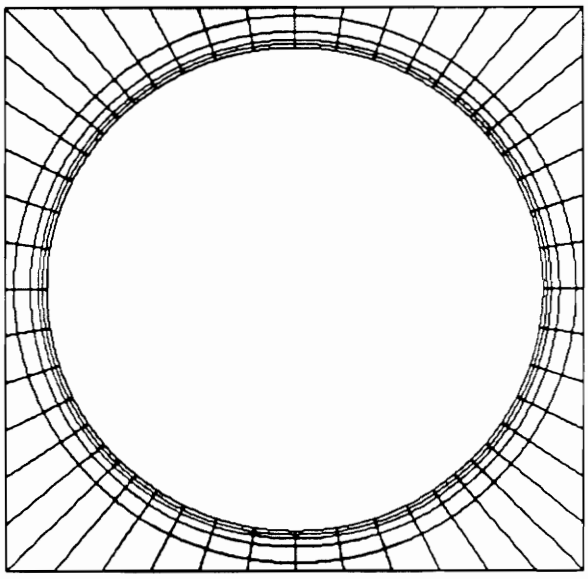

b)

Figure 5. Nodal distributions generated by "CSM1" and as modified for the curved edge region for a six-inch diameter hole: a) Original b) As modified

local models. Each local model was bounded by the prescribed global/local interfaces, appropriate symmetry planes, and the traction-free edges.

3.5 *Solution Procedure*

The nodal point locations, element connectivities, material property data, and stacking sequence are input to the Testbed. Element-level stiffness matrices are formed within the generic element processor and then assembled into a global stiffness matrix for a given model. With the applied displacements as constraints on the global matrix, a set of static, linear equations is solved. Several of the equation solvers available in the Testbed exploit the vector computer architecture of the CONVEX computer. A processor called "ITER," which contains several preconditioned conjugate gradient iterative methods, was used for each global solution, all angle-ply local models, and any complete three-dimensional models. Another solver called "BAND," which contains a direct Choleski solver designed for matrices stored in a novel variable-band format, was used only for the cross-ply local models. "BAND" is restricted, by the amount of available incore memory for a given computer, in the total number of equations that can be solved and could not be used for all of the models. The solution rate for iterative solvers is dependent on the speed of the solver and the rate of convergence, both of which are dependent on the method selected, and the parameters governing the initial guess from which the iteration technique proceeds (Stewart, 1989), (Poole and Overman, 1989). For the present work, no effort was made to minimize the solution time, and the first set of parameters for which the solution converged was used, with an incomplete Choleski preconditioned conjugate gradient (ICCG) iterative method selected. A noteworthy point is that all of these analyses were performed while the author was physically at Virginia Polytechnic Institute and State University with results transmitted, via the Internet, to university computer systems for post-processing.

3.6 *Post-processing of Displacements and Stresses*

Interlaminar stresses near the straight free edge in proximity to the hole and around the hole were examined. All of the stress results for the straight and curved edge models were normalized by the absolute value of the far-field in-plane stress (σ_x) as predicted by classical lamination theory for a plate without a hole. This value is 57,861 psi for all of the cross-ply laminates. The angle-ply stresses range in value due to their varying in-plane constitutive properties: 88,088 psi for $[\pm 15_{2n}]_s$, 15,821 psi for $[\pm 45_{2n}]_s$, and 51,992 psi for $[\pm 15_n/\pm 45_n]_s$. The quasi-isotropic normalization constant is 42,152 psi for the $[0_n/\pm 45_n/90_n]_s$ stacking sequence. All of the in-plane displacements are scaled by a factor of 20 for viewing, while the z-direction displacements are scaled by the in-plane scaling factor multiplied by ten for the local models, unless noted otherwise.

Integration point stresses are generally considered to be most accurate (Barlow, 1976) but are often at inconvenient locations, thus nodal stress values were obtained by extrapolating from the integration point stresses when presentation of the integration point values is precluded. Information about the extrapolation functions which were used, including their origin, derivation, and several sets of examples are presented in Appendix A. All figures which contain stress contours required the nodal stress values, because the software system used to present this information allowed either elemental values from an element centroid or nodal values to be imported, not integration point values. Whenever multiple values for the nodal stresses occurred for those nodes connected to several elements, those which were known to be continuous, were input to the software, as the average of the values. Intralaminar stresses are continuous on an element-to-element basis in-plane and out-of-plane for a given material layer, but exhibit jumps in values through a laminate when layer properties or orientation differ. Interlaminar stresses are continuous out-of-plane, regardless of changes in layer characteristics through the thickness.

4.0 Cross-ply Laminates Under Compression

4.1 Introduction

The relative success of this two-dimensional to three-dimensional analysis technique will be judged based on its ability to determine the localized three-dimensional displacement, strain, and stress fields in a more efficient manner, given only information from a global two-dimensional displacement field, than a complete three-dimensional analysis. All of the laminates considered are symmetric, and thus no coupling exists between the applied uniaxial compression loads and bending. The lamination sequences under consideration have an equal number of 0° and 90° plies, but are either clustered, reversed, or dispersed. Because integration through the laminate thickness of the material properties of the individual laminae is performed in order to determine the laminate stiffnesses required for the global finite element solution, the global displacement field for these stacking sequences will be indistinguishable. The influence of the different stacking sequences on the interlaminar response will be determined by the local analyses. The effect of stacking sequence change and varying hole diameter on the interlaminar stress distributions is studied. A complete three-dimensional finite element analysis is completed for one of the plates and used to demonstrate the accuracy and efficiency of the global/local analysis technique.

4.2 *Problem Description and Approach*

A family of plates with planar dimensions of 18x12 inches and 0.1 inch thickness is under study. These plates consist of laminated cross-plies with a central circular hole, and the following laminate orientations: $[0_{2n}/90_{2n}]_s$, $[90_{2n}/0_{2n}]_s$, and $[0_n/90_n/0_n/90_n]_s$ with n equal to one. These laminates will be referred to as clustered, reversed, and dispersed, respectively. Comparison of the stress fields for the stacking sequences is completed for the plates with a six-inch diameter hole. In order to determine the effect of different hole diameters, three were considered: one, three, and six inches. For validation purposes, a complete three-dimensional analysis was completed for the $[0_{2n}/90_{2n}]_s$ laminate with a six-inch diameter hole.

Since the in-plane response of the laminates for each hole size is identical, only one global analysis was performed for each hole size, while the local models were considered individually. The global model contains four concentric circular rings of elements with an additional ring of quadrilateral elements within the central square region of the plate surrounding the hole, and a graded element distribution along the straight free edge with the maximum y-dimension. This nodal distribution is described in detail in the Common Features Section. Because of the in-plane loading and the cross-ply stacking sequences, analysis of one-quarter of the global model would have been sufficient, but the analysis was performed on the entire global model because of the way it was generated by the "CSM1" processor. Table 2 contains information about the characteristics of the global model for each of the three hole sizes, and the undeformed grids are presented in Figure 6a), Figure 7a), and Figure 8a) for the plates with six-, three-, and one-inch diameter holes, respectively. Table 2 includes information about the size of the hole in the plate, the number of nodes in the model, the total number of degrees of freedom, the number of elements in the entire model and around the hole area, the number of spokes around the hole, and the total computer analysis time for the model in question.

Table 2. Two-Dimensional Cross-Ply Compression Global Model Characteristics

Hole Dia. (in.)	Nodes	Degrees of Freedom	Elements		Spokes Around Hole	Global Solution Time (CPU seconds)
			Total	Hole		
1.0	3,208	19,248	768	160	64	488.9
3.0	2,824	16,944	672	200	80	435.2
6.0	2,440	14,640	576	240	96	242.2

A local coordinate system with its origin at the geometric center of the plate was chosen and used for the straight and curved edge models with an angle theta (θ) defined as a rotation about the z-axis from the local x-axis toward the local y-axis. These axes are coincident with the global x-, y-, and z-symmetry planes, as can be seen in Figure 9. The laminates consist of only 0° and 90° layers; and therefore, two additional planes of symmetry exist through the geometric center of the plate. These are aligned with the local coordinate system and are identified by their local location. These planes affect both local areas of interest: the straight edge model extends from the local $x = 0$ symmetry plane to the load application edge, while the local model for the curved edge was reduced to one-quarter of the square region around the hole between the local $x = 0$ and $y = 0$ symmetry planes. It should be noted that these symmetry planes do not necessarily exist for more general ply orientations or loading conditions, and this must be considered before the application of this global/local modeling technique. A more general class of laminates is considered in the following chapter.

In-plane displacement components were applied directly to each local model along the global/local interfaces as applied motions. Because the assumptions inherent in classical lamination theory are valid in this region, there was no predicted rotation or distortion of the normal lines to the mid-plane, and the in-plane displacements could be applied constant through the laminate half-thickness. The placement of the global/local interfaces in areas where the normals were not distorted and where the in-plane stress gradients are low was deliberate. These exact locations were

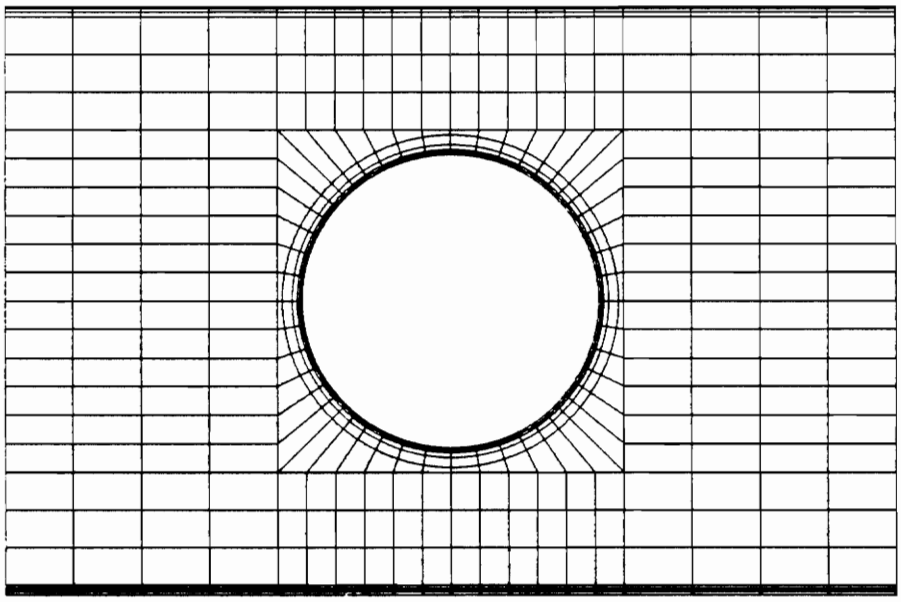

a)

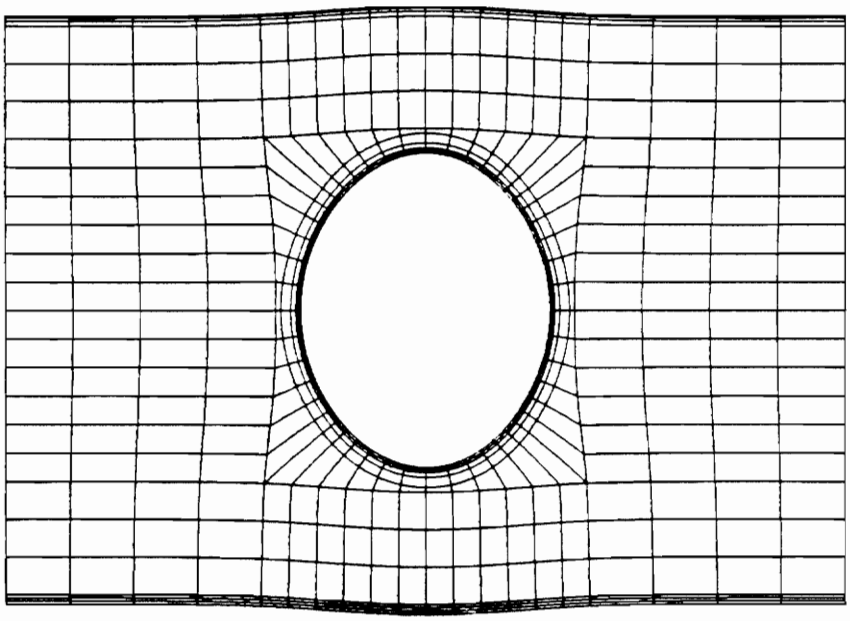

b)

Figure 6. **Global Grids for $[0_{2n}/90_{2n}]_s$ in Compression with Six-Inch Diameter Hole:** a) Undeformed b) Deformed

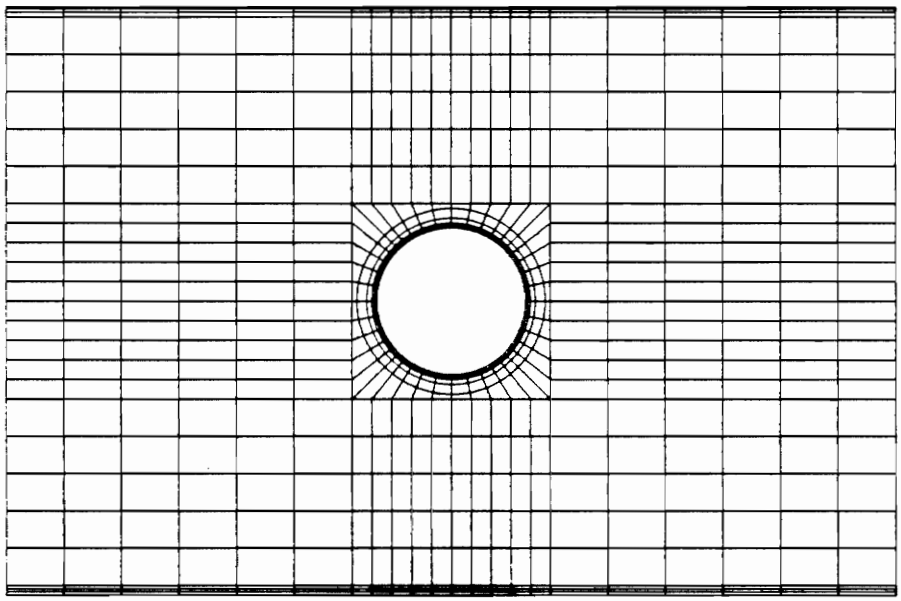

a)

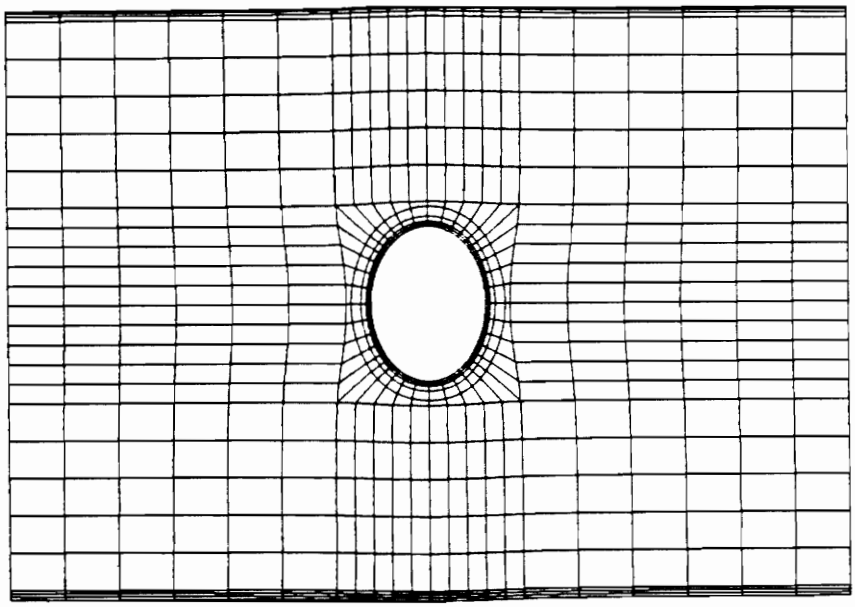

b)

Figure 7. **Global Grids for $[0_{2n}/90_{2n}]_s$ in Compression with Three-Inch Diameter Hole:** a) Undeformed b) Deformed

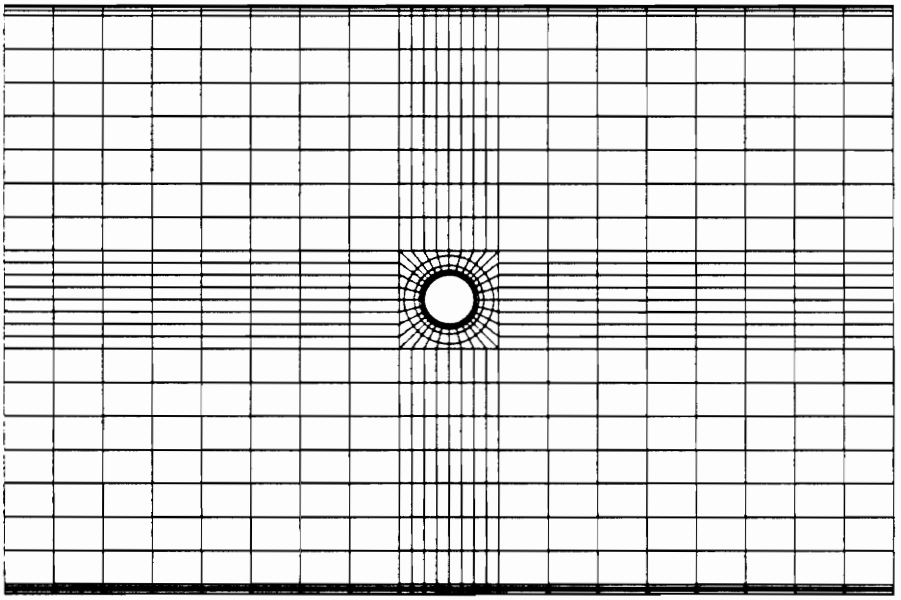

a)

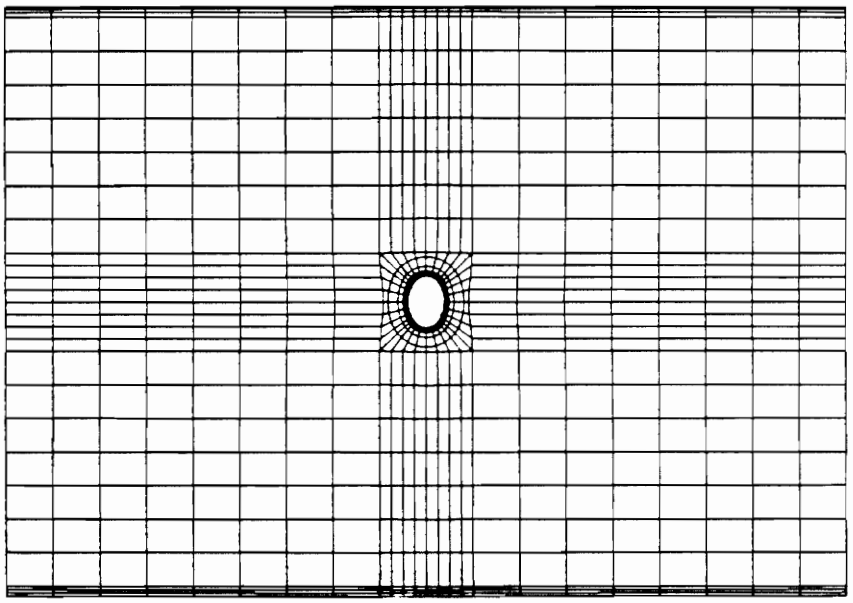

b)

Figure 8. **Global Grids for $[0_{2n}/90_{2n}]_s$ in Compression with One-Inch Diameter Hole:** a) Undeformed b) Deformed

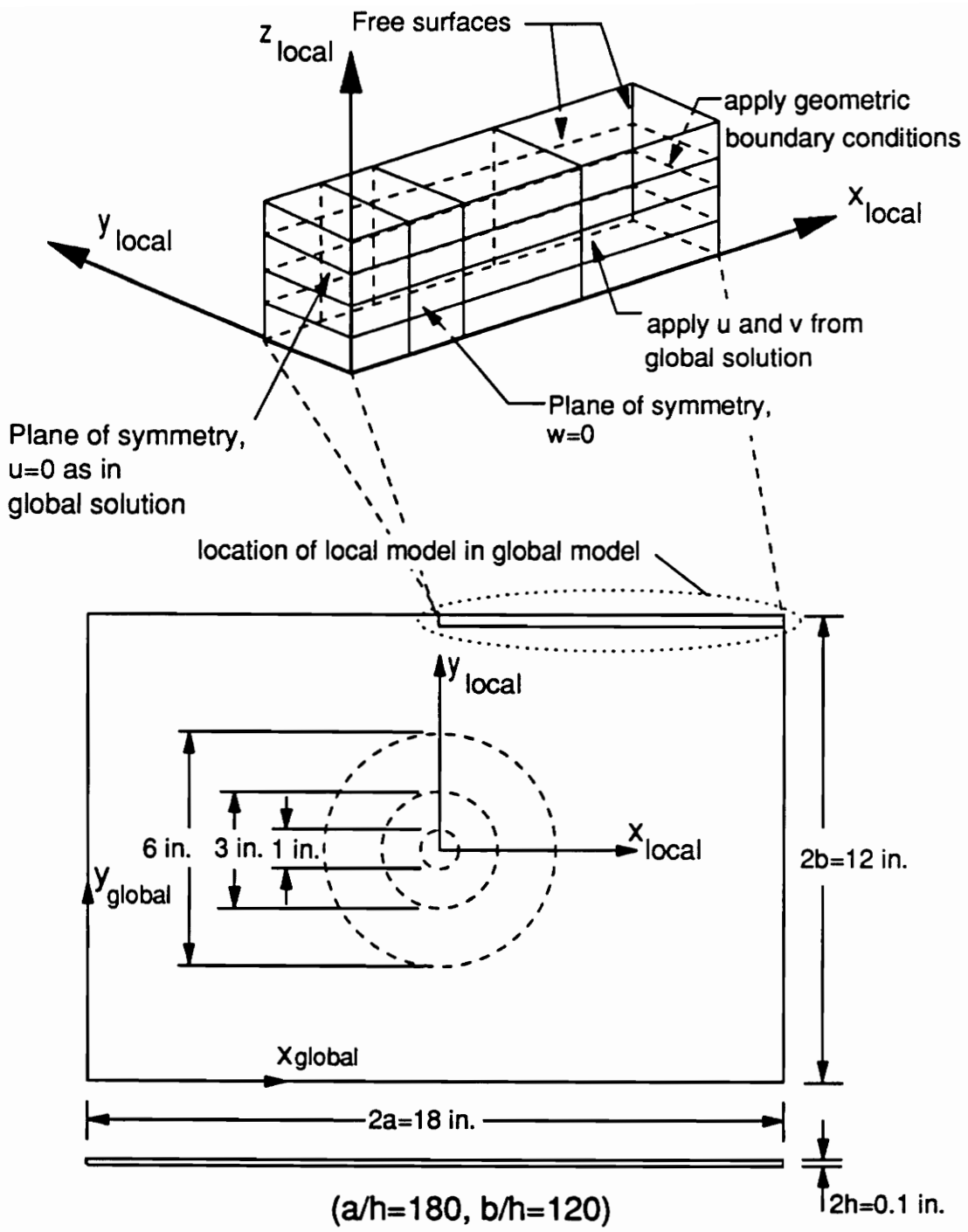

Figure 9. Local Full Straight Edge Model Displacement Application for Cross-plies in Compression

described in the Common Features Section and can be seen in Figure 9, Figure 10, and Figure 11. Whenever x-direction displacements (u) were applied, the x-direction rigid body translation of the local $x = 0$ symmetry plane was removed. Along the local $x = 0$ symmetry plane for all of the local models, only the x-direction displacement ($u = 0$, because of removal of the rigid body motion) was applied constant through the thickness. No y-direction displacements (v) were applied, because the local $x = 0$ symmetry plane passes through boundary layers and the application of constant y-direction displacements would inhibit the development of the interlaminar stress field. Along the local $y = 0$ symmetry plane which is a boundary for the curved edge local models, only the y-direction displacements from the global model were applied constant through the thickness, and these displacements are all zero from the global solution. No x-direction displacements were applied here for the same reason as no y-direction displacements were applied along the local $x = 0$ symmetry plane. The local $z = 0$ symmetry plane is at the mid-plane of the laminate. This plane was fixed in the z-direction for all of the local models and was the only location throughout the local model with applied z-direction (w) displacements. There were no applied conditions at any of the nodes along any of the free edges of the local models which did not coincide with the global/local interfaces or the symmetry planes. The end of the full straight edge model which is coincident with the load application region for the global model is constrained to move only in the x-direction 0.05 in., after removal of the rigid body translation of the local $x = 0$ symmetry plane.

In-plane loading of a cross-ply laminate results in two interlaminar stress components, a normal stress (σ_z) and a shear stress (τ_{yz}), during the transition from the internal stress state to the traction-free edge. The existence of the interlaminar shear stress component (τ_{yz}) in the three-dimensional stress state precludes the application of y-direction displacements through the boundary layer since no predictions can be made from the global model about the exact character of these displacements. Constant displacements should not be applied to any three-dimensional element in any direction where the displacements cannot be expected to be constant. Along straight edges in cross-ply laminates under in-plane compressive loading, no interlaminar shearing occurs in the x-z plane ($\gamma_{xz} = 0$). Therefore, the application of constant x-direction displacements in the z-direction

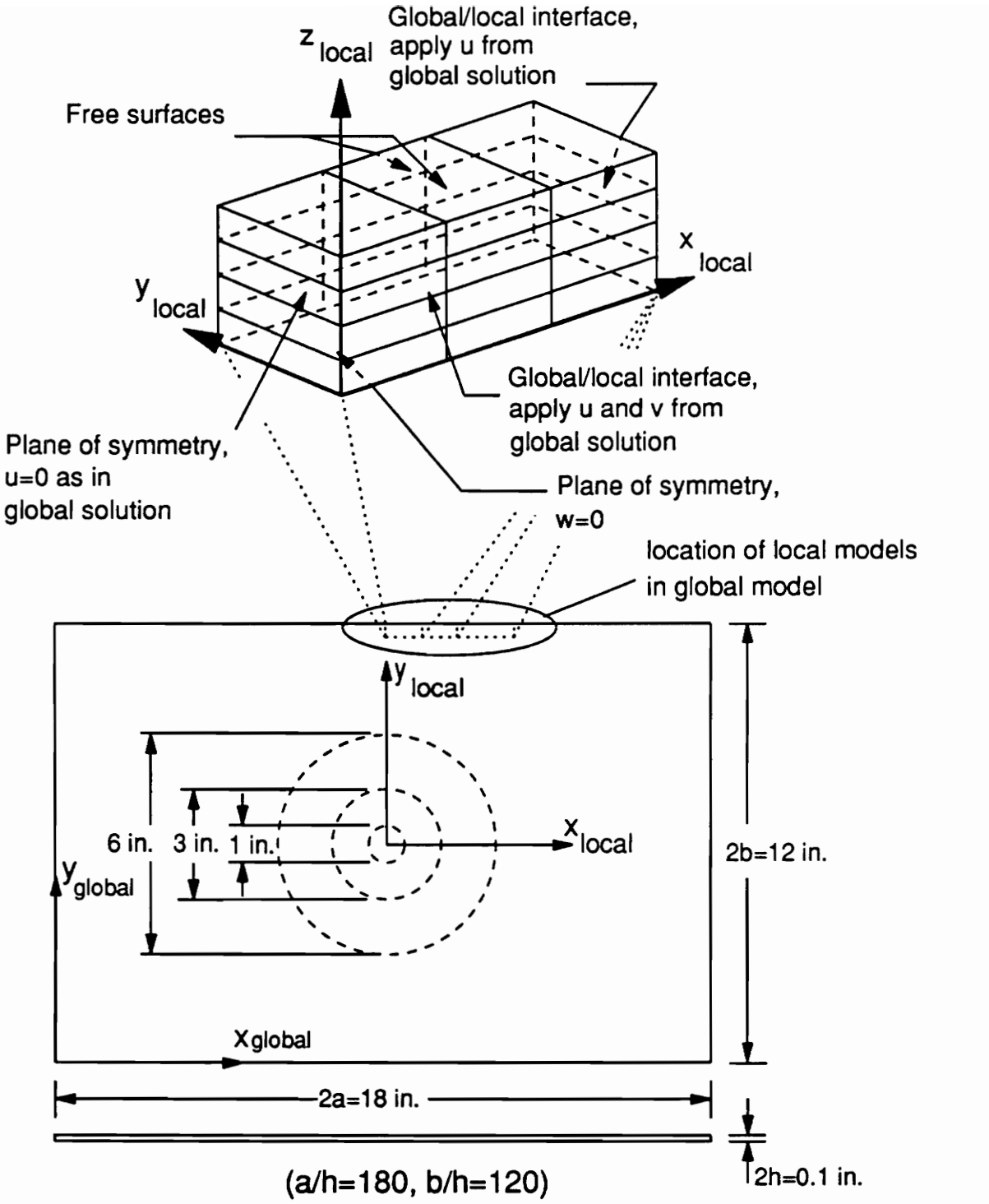

Figure 10. Reduced Local Straight Edge Model Displacement Application for Cross-plies in Compression

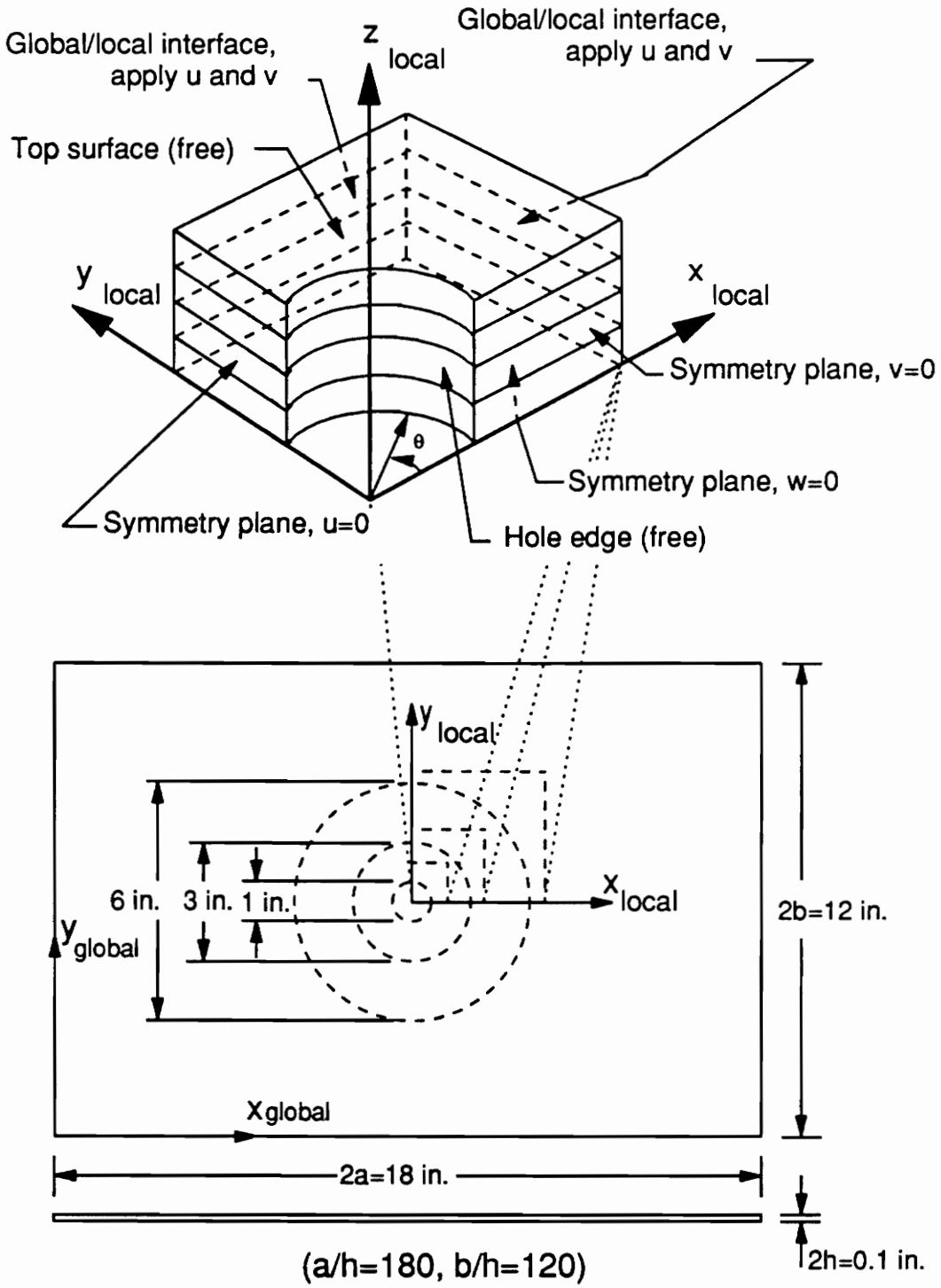

Figure 11. Local Curved Edge Model Displacement Application for Cross-plies in Compression

would not violate any kinematic conditions inherent in the three-dimensional solution of the boundary layer. A cut was made through the boundary layer region to form the reduced local straight edge models with the same x-direction dimension as their corresponding local curved free edge models. This tremendously reduced the modeling effort for the straight free edge region. The displacement application procedure for these reduced local straight edge models, shown schematically in Figure 10, is similar to the full local straight edge models except for the treatment of the cut itself. Since the cut is parallel to the local $x = 0$ symmetry plane, it has the same rule of of displacement application: only the global x-direction displacements, with the rigid body translation of the symmetry plane removed, are applied constant through the thickness. A comparison of the interlaminar stress fields between the complete three-dimensional model and the local models is presented in the following sections and demonstrates that using a reduced local model for this particular loading and stacking sequence will yield accurate answers.

The complete three-dimensional model consisted of one-quarter of the in-plane area of the plate and one-half of the plate thickness. The common regions modeled by the complete and local models were designed to have identical nodal distributions so that the stress fields could be compared at exactly the same locations. The displacement application procedure considered only the x-, y-, and z-symmetry planes, and the clamped plate ends (Figure 12). The undeformed three-dimensional meshes for the $[0_{2n}/90_{2n}]_s$ laminate with the six-inch diameter hole are shown in Figure 13a) and b), Figure 14a), and Figure 15a). Both an unscaled and a scaled undeformed model are shown in Figure 13. To see the detail of the model through its thickness, its presented z-dimensions were multiplied by ten for the remainder of this study. The unscaled plate shows the relative dimensions of the model that is being analyzed: a thin laminate with a large hole. Hole-radius to laminate-thickness ratios are 60, 30 and 10. The length to laminate-thickness ratio is 180. The width to laminate-thickness ratio is 120. Information presented in Table 3 indicates the resources required for the complete three-dimensional model, and the global/local solutions for the full and reduced straight edge models, and the curved edge model for the $[0_{2n}/90_{2n}]_s$ laminate with a six-inch diameter hole.

Table 3. Comparison of Complete and Global/Local Analyses for $[0_{2n}/90_{2n}]_s$ Laminate with Six-Inch Diameter Hole

Model Type	Nodes	Degrees of Freedom	Elements	Local/Total Solution Time (CPU seconds)
Complete 3-D	5,759	17,277	1,152	--/2,302.6
Global 2-D	2,440	14,640	576	--/242.2
Full Straight	1,405	4,215	240	162.5/404.7
Reduced Straight	881	2,643	144	99.8/342.0
Curved	2,559	7,677	480	436.0/678.2

The full straight edge local model is presented in Figure 16a). The smaller elements near the local $x = 0$ symmetry plane form the reduced local model pictured in Figure 17a). Forty percent of the full straight edge model contains elements away from the curved free edge of the hole, which are not the focus of this study. Should the global/local analysis be successful without these elements, then they need not be included in future analyses. Quantitative information about each reduced local model is presented in Table 4. The local x-direction was modeled with six elements for the local model near the six-inch diameter hole, five elements for the three-inch case, and four elements for the one-inch case as shown in Figure 17a), Figure 18a), and Figure 19a), respectively. Each of the reduced local models has a length equal to the hole radius plus five laminate thicknesses in the local x-direction, matching the x-direction dimension for the corresponding curved free edge model. Because the stress gradients away from the edge are small and increase with proximity to the edge, it was advantageous to grade the mesh accordingly so that the element density increased closer to the free edge. The grading employed was that determined by Vidussoni (1988), as described in the Common Features Section, modeling the local y-direction with three elements.

Another view of the complete three-dimensional model is presented in Figure 15a). Not including the elements in the straight edge region, nearly half of the model is outside the area of interest around the hole. The undeformed local curved edge models for the three hole sizes are presented in Figure 20a), Figure 21a), and Figure 22a), in order of decreasing hole diameter. The relative

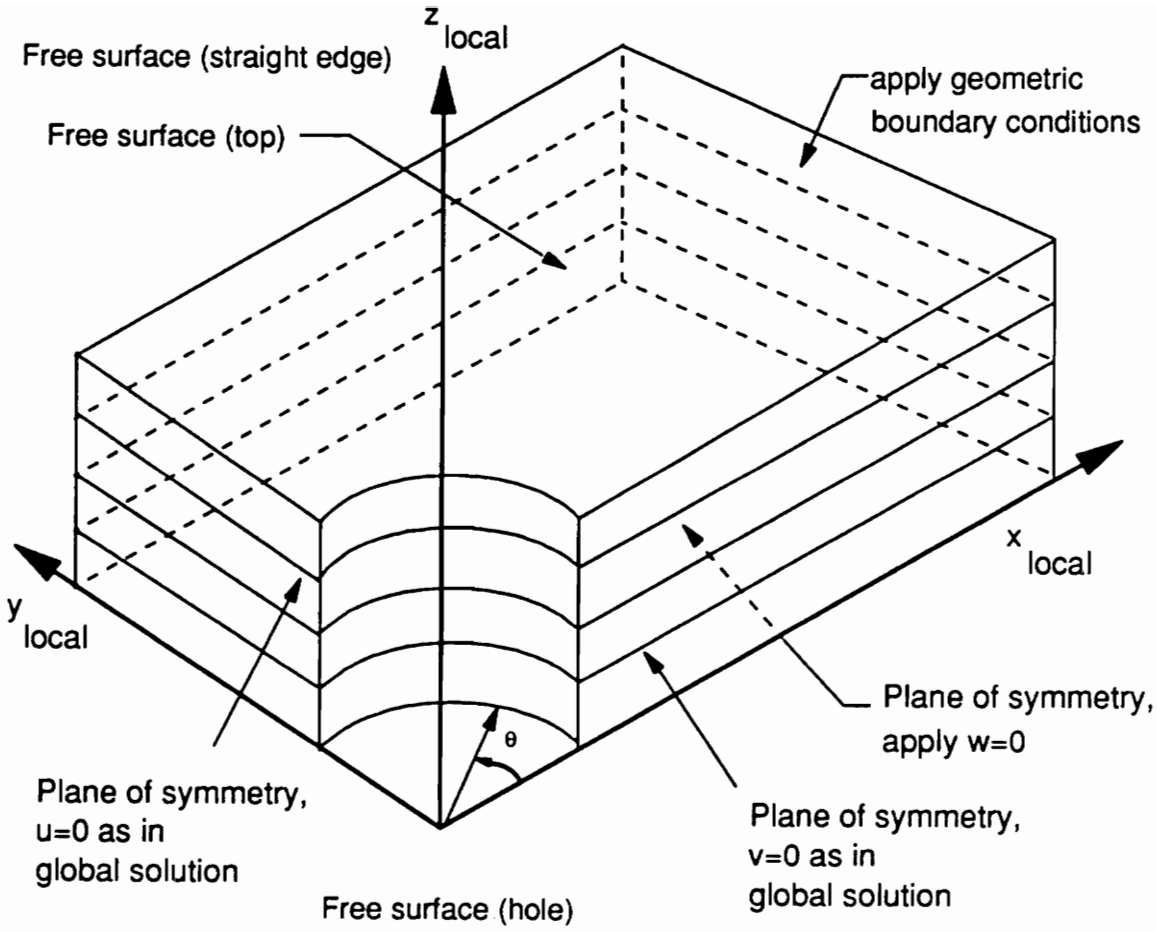

Figure 12. Complete Model Displacement Application for Cross-plies in Compression

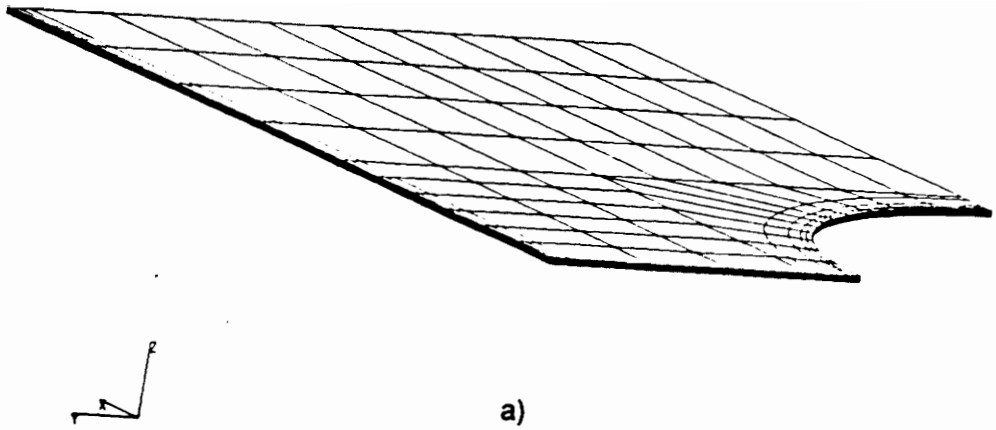

a)

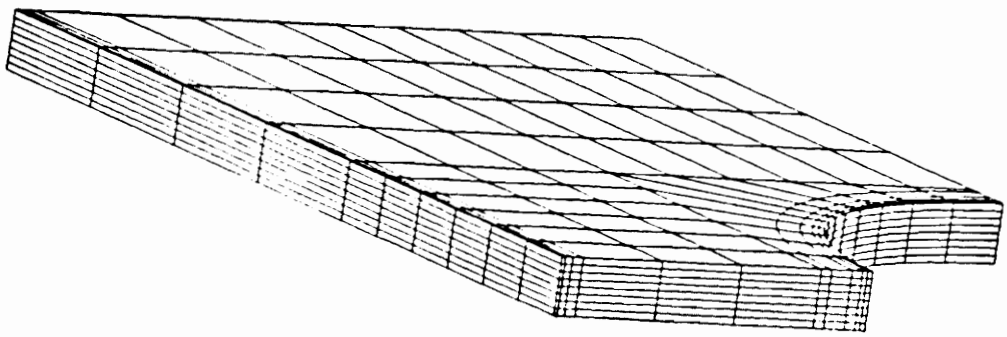

b)

Figure 13. Complete Models for $[0_{2n}/90_{2n}]_s$ viewing Straight Edge near Six-Inch Diameter Hole: a) Actual Model b) Scaled Model

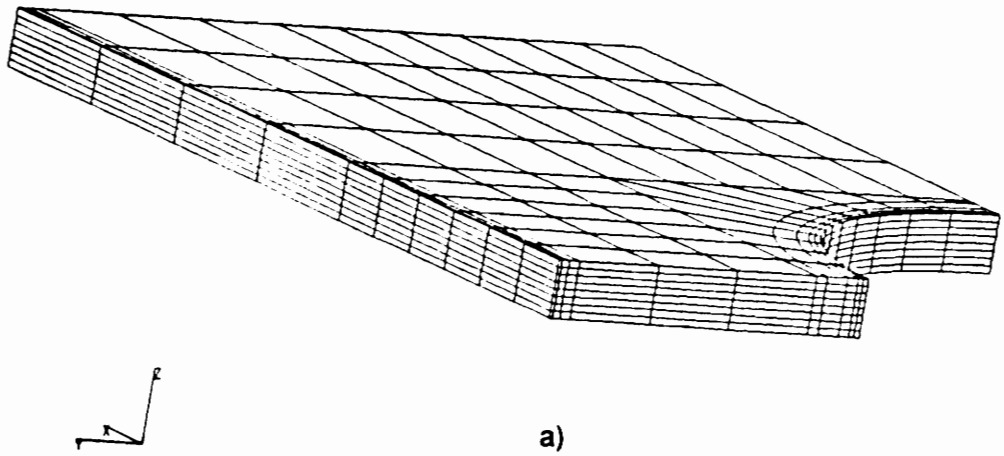

a)

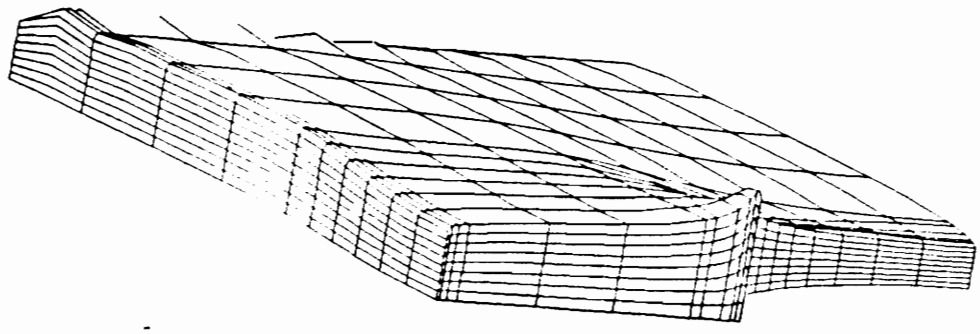

b)

Figure 14. **Complete Models for $[0_{2n}/90_{2n}]_s$ viewing Straight Edge near Six-Inch Diameter Hole:** a) Undeformed b) Deformed

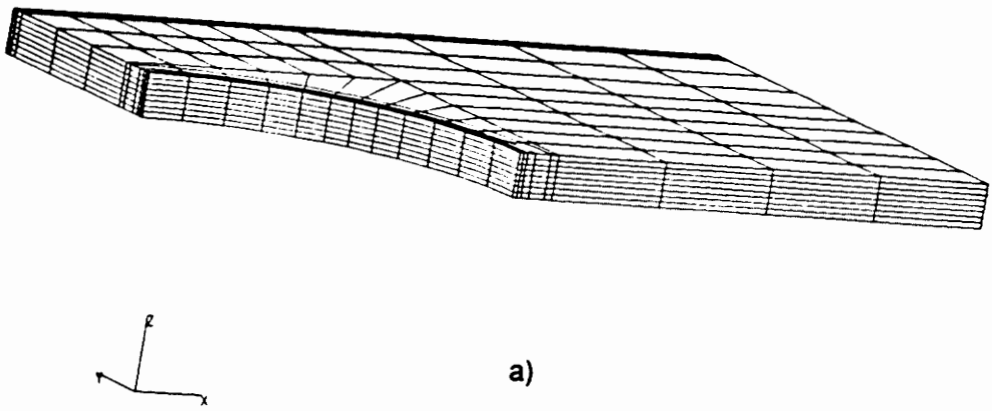

a)

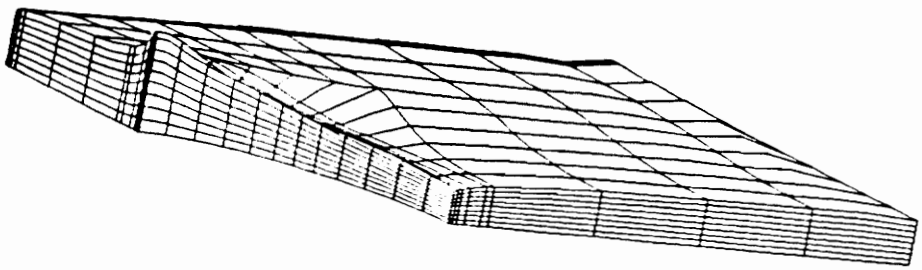

b)

Figure 15. Complete Models for $[0_{2n}/90_{2n}]_s$ viewing Curved Edge around Six-Inch Diameter Hole: a) Undeformed b) Deformed

Table 4. Three-Dimensional Cross-Ply Compression Local Straight Edge Model Characteristics

Hole Dia. (in.)/ Lay-up	Nodes	Degrees of Freedom	Elements	Local/Total Solution Time (CPU seconds)
1.0/ $[0_{2n}/90_{2n}]_s$	619	1,857	96	70.8/559.7
3.0/ $[0_{2n}/90_{2n}]_s$	750	2,250	120	84.5/519.7
6.0/ $[0_{2n}/90_{2n}]_s$	881	2,643	144	99.8/342.0
$[90_{2n}/0_{2n}]_s$				99.4/341.6
$[0_n/90_n/0_n/90_n]_s$				94.2/336.4

dimensions of the rings around each of the holes can be seen in these figures. Further information is provided in Table 5. In-plane curvature of the elements was kept low, with a larger number of spokes for the larger hole diameters. Element arc lengths along a constant radial distance from the hole were varied to generate radial nodal lines from the hole edge to the global/local boundary around the hole. Care was taken to ensure that the mid-side nodes for a given element in the revised grid were exactly at the mid-point between the corner nodes, since this is an inherent assumption behind the governing equations of the displacement-based elements. Incorrect placement of the nodes will affect the solution.

4.3 Results and Discussion

The two-dimensional global model was analyzed, and its appropriate displacements were applied to the three-dimensional local models. After determining the local nodal displacements, the strains and stresses at the integration points were calculated. Examination of solution times presented in

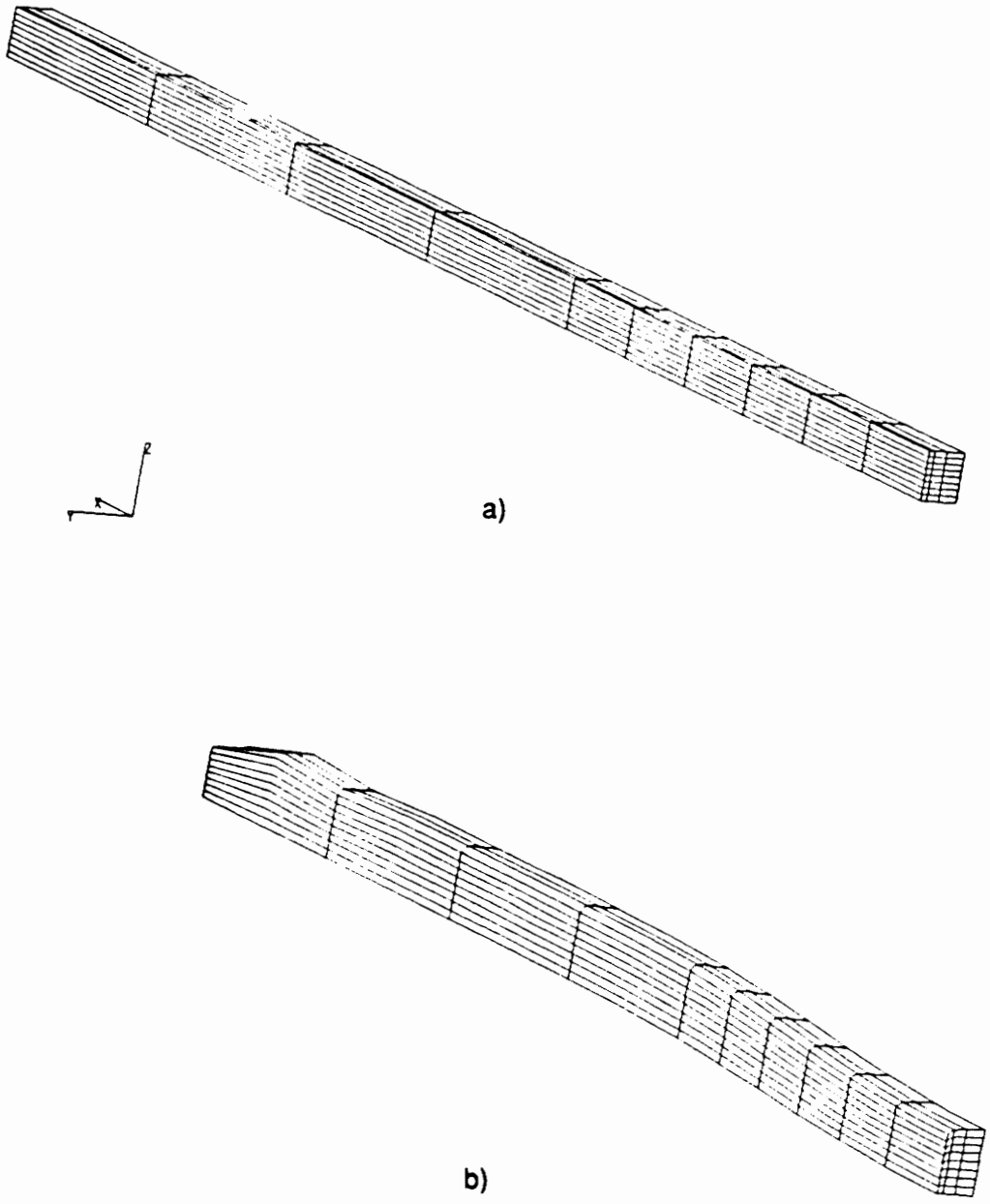

Figure 16. Full Local Straight Edge Models for $[0_{2n}/90_{2n}]_s$ near Six-Inch Diameter Hole: a) Undeformed b) Deformed

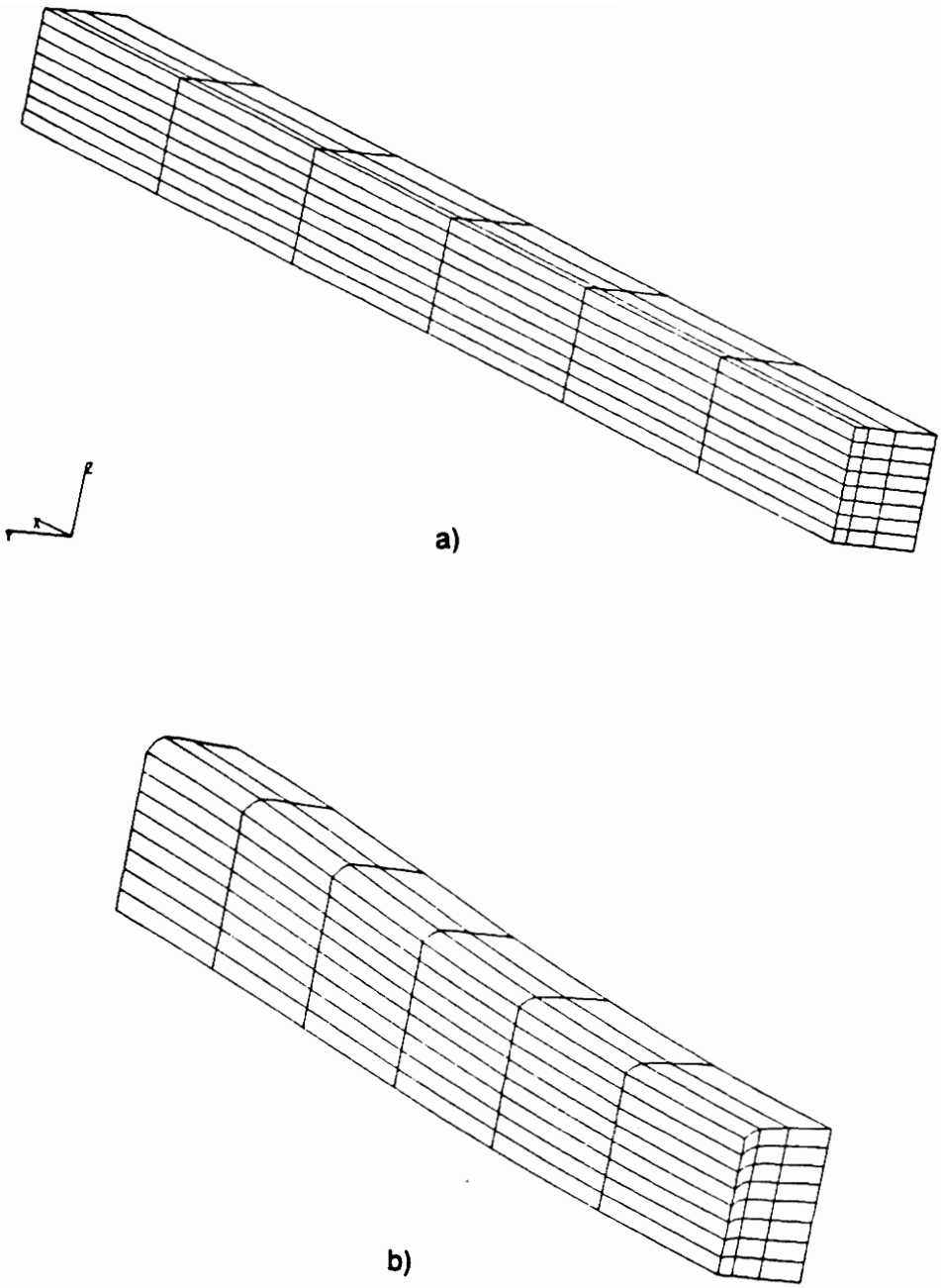

Figure 17. **Reduced Local Straight Edge Models for $[0_{2n}/90_{2n}]_s$ near Six-Inch Diameter Hole:** a) Undeformed b) Deformed

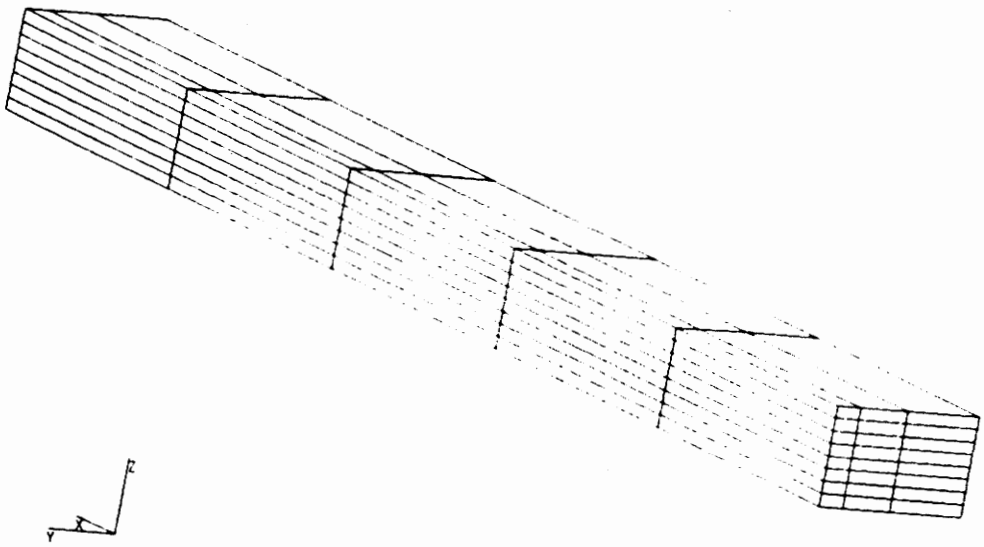

a)

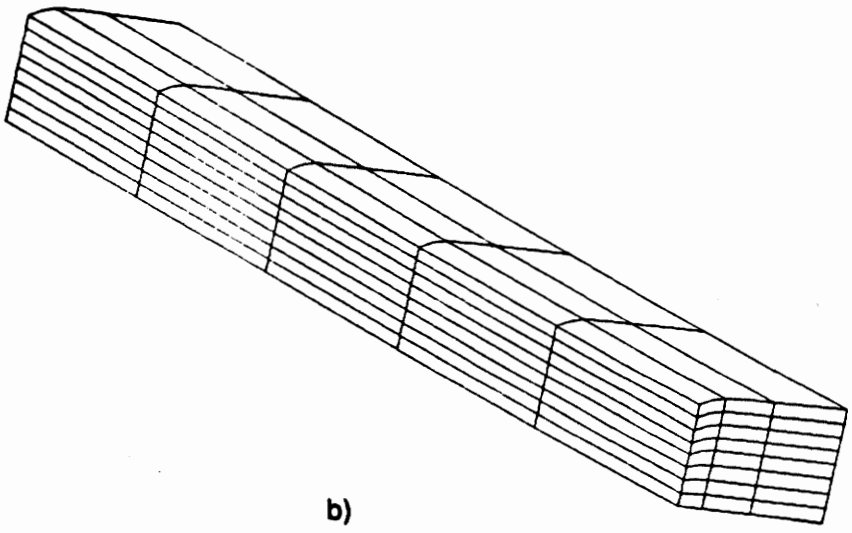

b)

Figure 18. Reduced Local Straight Edge Models for $[0_{2n}/90_{2n}]_s$ near Three-Inch Diameter Hole: a) Undeformed b) Deformed

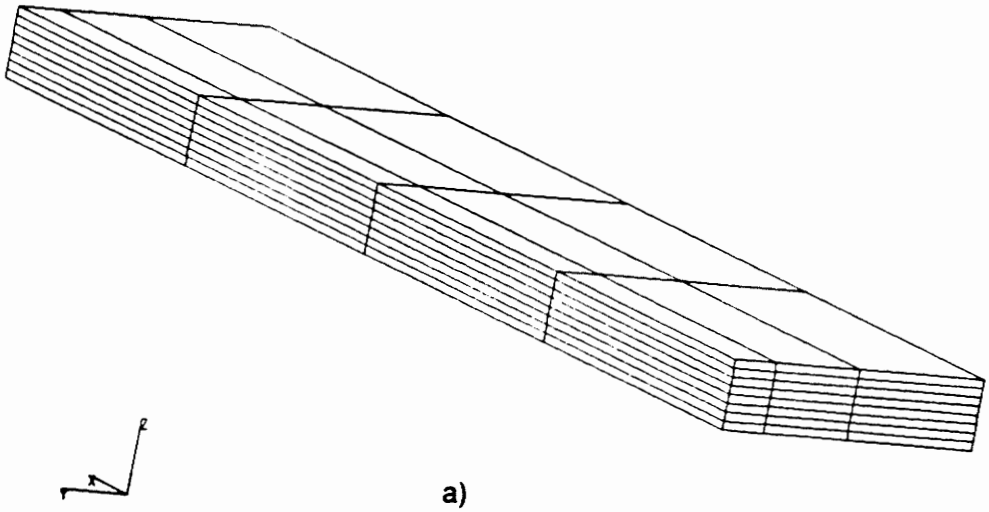

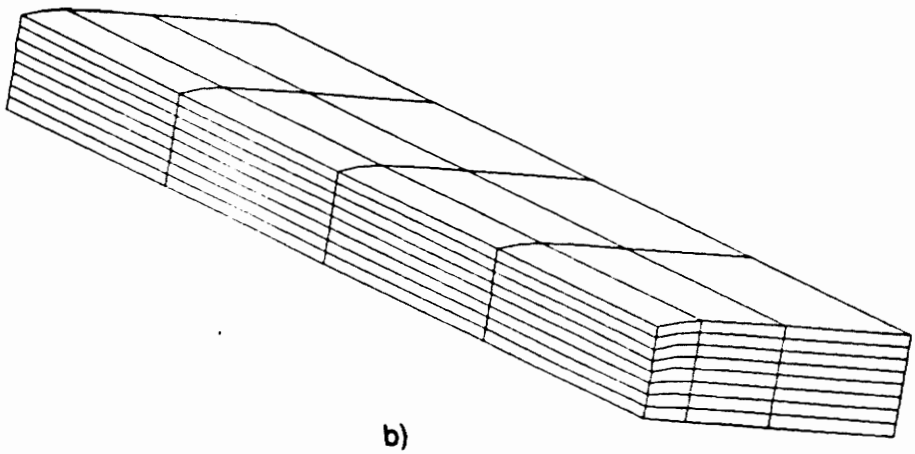

Figure 19. Reduced Local Straight Edge Models for $[0_{2n}/90_{2n}]_s$ near One-Inch Diameter Hole: a) Undeformed b) Deformed

Table 5. Three-Dimensional Cross-Ply Compression Local Curved Edge Model Characteristics

Hole Dia. (in.)/ Layup	Nodes	Degrees of Freedom	Elements	Model/Total Solution Time (CPU seconds)
1.0 $[0_{2n}/90_{2n}]_s$	1,755	5,265	320	245.4/487.6
3.0/ $[0_{2n}/90_{2n}]_s$	2,157	6,471	400	326.5/568.7
6.0/ $[0_{2n}/90_{2n}]_s$	2,559	7,677	480	436.0/678.2
$[90_{2n}/0_{2n}]_s$				443.0/685.2
$[0_n/90_n/0_n/90_n]_s$				440.1/682.3

Table 3 indicates that the two-dimensional to three-dimensional global/local finite element analyses presented were accomplished with a reasonable expenditure of computer resources.

There is a wide range of information available in the open literature about the interlaminar stress state in composite structures, and an excellent review was written by Salamon (1980). Most of the previous investigations have concentrated on the stress state for laminates with no internal cutouts, under uniaxial tension or compression. Among those who have completed work for cross-ply laminates are (Pipes and Pagano, 1970), (Wang and Crossman, 1977). Along straight free edges of cross-ply laminates under in-plane loading away from the load application region, the interlaminar normal stress (σ_z) is maximum at the mid-plane. Considering z-locations closer to the top free edge, the in-plane stress character is unchanged but diminishes in magnitude. The interlaminar shear stress (τ_{yz}) is zero at the mid-plane and top free surface, and has local maxima and minima at the 0° and 90° ply interfaces. Its character is dependent on the relative positions of the ply orientations at each interface. The remaining interlaminar shear stress (τ_{xz}) is zero throughout the laminate. At the straight free edge, the interlaminar stress state that develops for cross-ply laminates is dependent on the Poisson's ratio mismatch between the layers at a particular interface. Because the 0° and 90° plies have different Poisson's ratio values, they tend to distort in

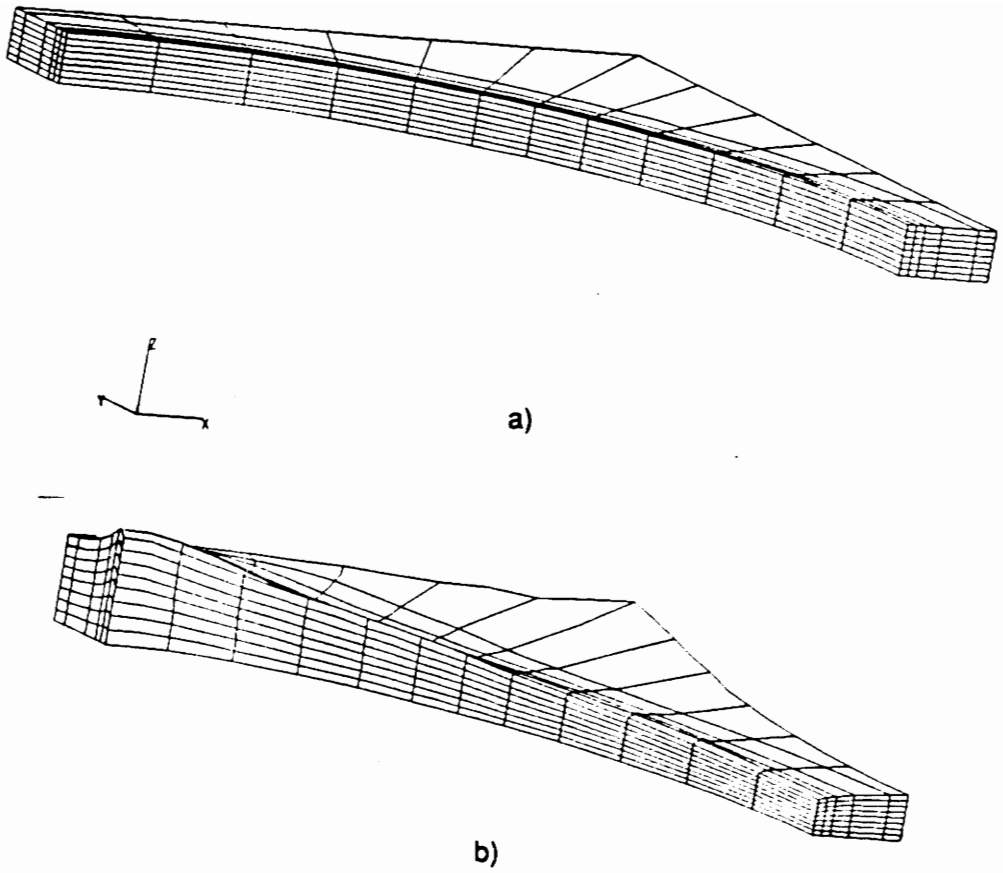

Figure 20. **Local Curved Edge Models for $[0_{2n}/90_{2n}]_s$ with Six-Inch Diameter Hole:** a) Undeformed b) Deformed

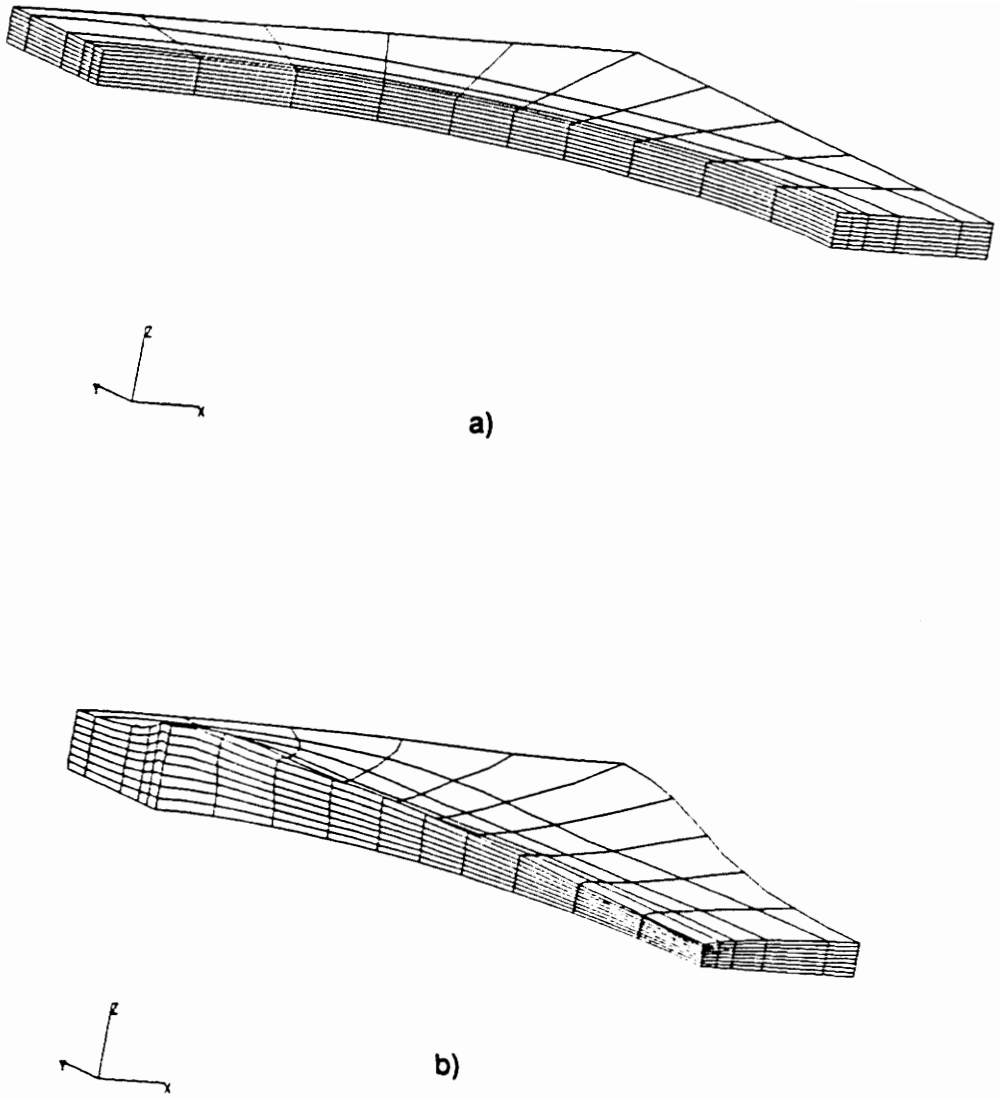

Figure 21. **Local Curved Edge Models for $[0_{2n}/90_{2n}]_s$ with Three-Inch Diameter Hole:** a) Undeformed b) Deformed

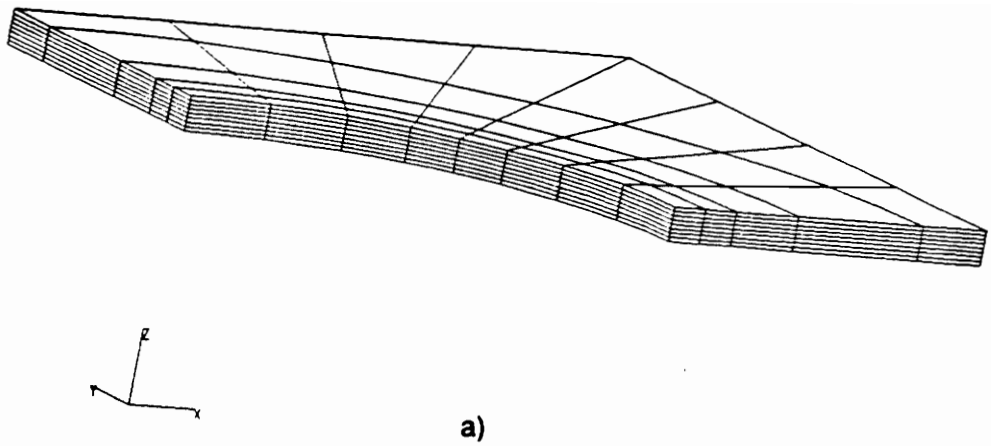

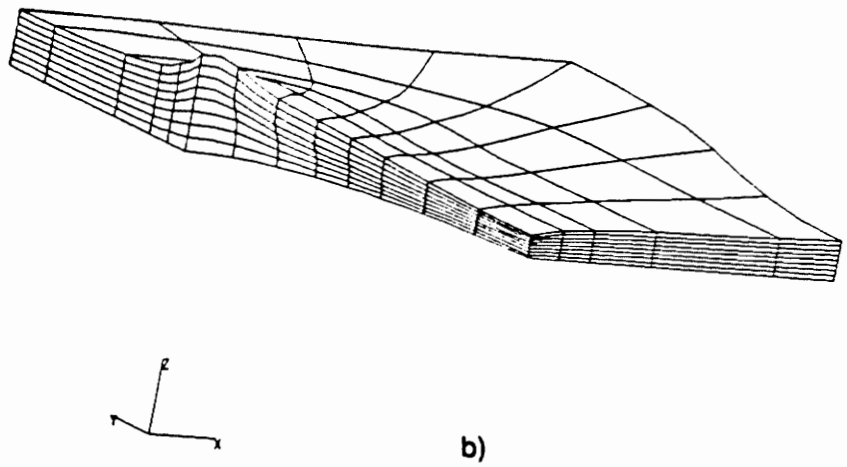

Figure 22. **Local Curved Edge Models for $[0_{2n}/90_{2n}]_s$ with One-Inch Diameter Hole:** a) Undeformed b) Deformed

different directions under loading. This stress component develops to enforce compatibility of the displacement field, while the distribution of σ_z provides a countering moment so that there is no net moment at the edge. The 0° and 90° layers exhibit no shear coupling in the x-z plane.

Consideration of the deformation, and hence the stress, state around the hole, however, is more complex. While the global cross-ply stacking sequence is fixed, subsequent angular positions around the hole will experience a change in the local stacking sequence. For different angular positions around the curved edge, the 0° and 90° plies experience a different local effective stiffness. Thus, the local Poisson's ratio mismatch and shear coupling between the plies will change as a function of the angular location around the hole. This fact, coupled with the change in load around the hole and through the laminate half-thickness ensures that the character of the interlaminar stress components around holes in cross-ply laminates is complex to predict, and three-dimensional in nature (Dana, 1974), (Rybicki and Schmueser, 1978), (Salamon, 1980). Along the mid-plane at the hole edge, the interlaminar normal stress is a maximum and reduces in magnitude through the laminate thickness for a given angular location. The two shear stress components ($\tau_{\theta z}$, and τ_{rz}) are both zero at the mid-plane and top of the laminate and exhibit peaks at interfaces of the 0° and 90° layers. For the purpose of this study, only those stress components which are significant are presented for a given interface.

4.3.1 Two-Dimensional Global Model Results

The deformed global grid for the plate with a six-inch diameter hole and a $[0_{2n}/90_{2n}]_S$ stacking sequence is shown in Figure 6b), the plate with three-inch hole in Figure 7b), and the plate with one-inch hole in Figure 8b). All displacements were scaled by a factor of 10 for viewing. Note that the ends (vertical edges) of each plate remained straight and their original length as specified by the boundary conditions. The circular holes became noncircular, and there was a bulging of the previously straight edges of the plates. As expected, the deformations and influence due to the hole

extend farther into the plate with larger holes. The line of nodes two laminate thicknesses from the maximum global y-dimension is the global/local interface for the straight edge models. The curvature at this location is transferred to the local model through the displacement application procedure described earlier. The square of nodes around each hole exhibits concavity on its vertical sides and convexity on its horizontal sides. These are the global/local interfaces for the curved edge models, and its distortion will be transferred to the local curved free edge model.

4.3.2 Three-Dimensional Local Model Results

The straight free edge local analyses shall be presented prior to those of the curved free edge. The success of the global/local analysis technique shall be determined by the comparing the interlaminar stress fields from the full and reduced local finite element models to the complete three-dimensional model. Comparison of the local stress fields for different ply orientations for a plate with a single hole diameter and the effect of hole size for a given layup were completed. The curved free edge results follow the same format: verification of the global/local model results with respect to the complete model, the ply orientation study for the largest hole, and finally determination of the influence of different diameter holes for one of the stacking sequences in a finite-width plate.

4.3.2.1 Verification of Global/Local Modeling Technique for the Straight Edge

If the two-dimensional to three-dimensional global/local analysis results are indistinguishable from those of the complete three-dimensional analysis and determined with less effort, then this technique can be considered both verified and successful. Specific information about the different models is presented in Table 3 on page 37 The combined computer time to solve the global model and the straight and curved edge local models is less than two-thirds the complete three-dimensional model. However, since all of the existing planes of symmetry were not exploited for the two-

dimensional global model, its solution time could have been reduced further. The presented two-dimensional to three-dimensional global/local analysis methodology is more efficient than a complete three-dimensional analysis, because only those areas of interest are included in the three-dimensional model(s). Parallel computation schemes become attractive since the local models are independent of one another, but are not explored here.

The undeformed and deformed complete models for the $[0_{2n}/90_{2n}]_s$ laminated quarter plate with a six-inch diameter hole are presented in Figure 14a) and b) and Figure 15a) and b). In-plane deformations were scaled by a factor of twenty, while the z-direction displacements were multiplied by 200. The plate is visibly thicker because of a through the thickness Poisson effect over the entire plate, and most noticeably near the hole. The local full straight edge and the complete models are indistinguishable through visual inspection over the straight free edge region. Because of the boundary conditions, those elements nearest the plate ends have large deformation gradients in the transition from the free z-direction expansion over the whole plate to the enforced no z-direction expansion region at the clamped ends. Nearest the hole along the straight edge, elements are bowed away from the hole, as in the global model. Along the local $x = 0$ symmetry plane, the deformation state changes from z-directional expansion due to the far-field loading conditions to z-directional contraction because of the free edge effects. It can also be seen that this change is confined to the elements within one laminate thickness of the free edge, as found previously by others (Salamon, 1980). Visual comparison between the reduced local model and the complete model is more difficult because of the difference in scale between the models. The reduced model exhibits Poisson deformation and the element bowing found in the full and complete models.

The comparison of the stress field along the straight edge as determined by the two approaches is encouraging. The interlaminar normal stress (σ_z) distributions for the integration points nearest the mid-plane and free edge for the complete model and the reduced local model are presented in Figure 23a) for the entire length of the plate. For this stress component, the complete model has extreme values at the clamped ends because the no expansion is allowed in this region. At those integration points common to both models, the σ_z distributions are indistinguishable. The

interlaminar shear stress (τ_{yz}) distribution at the interface between the 0° and 90° layers at the integration points nearest the free edge for the complete three-dimensional and the reduced local model are shown in Figure 23b). Again, the stress values for these two models are coincident. Both of the models correctly determined that the interlaminar shear stress (τ_{xz}) is zero for this laminate. The two-dimensional to three-dimensional global/local finite element analysis produced developed for cross-ply laminates along a straight free edge near a hole may be considered valid, verified, and more efficient than a complete three-dimensional finite element analysis since the same results were determined with less computational effort.

The imposition of the constant x-direction and y-direction displacements from the global model on the local straight edge model at the global/local interfaces was an integral assumption of the global/local modeling technique. However, examination of the complete model displacement field in this area reveals that there is some variation through the half-thickness, but that this variation is less than 1%. The imposed global displacements on the local three-dimensional model are smeared through the thickness, and therefore, are not identical to the three-dimensional displacement field. However, since the global/local interface was close but outside the boundary layer, the local model could develop the correct three-dimensional displacement field at the free edge, and thus, determine the free edge stress field correctly.

4.3.2.2 Straight Free Edge Model Results

The deformed reduced local six-inch hole models for the different stacking sequences are presented in Figure 17b), Figure 24b), and Figure 25b). Each local model is visibly compressed in the x-direction. Also noticeable is an in-plane bowing of the global/local interface, as expected when the applied displacement conditions contain such curvature effects. In Figure 17b) the elements modeling the 90° plies are seen to restrain those elements modeling the 0° plies from movement away from the center of the plate. Because of the clustering of plies with common orientation, this interlaminar effect is more pronounced. The free edge becomes noticeably thinner for this stacking

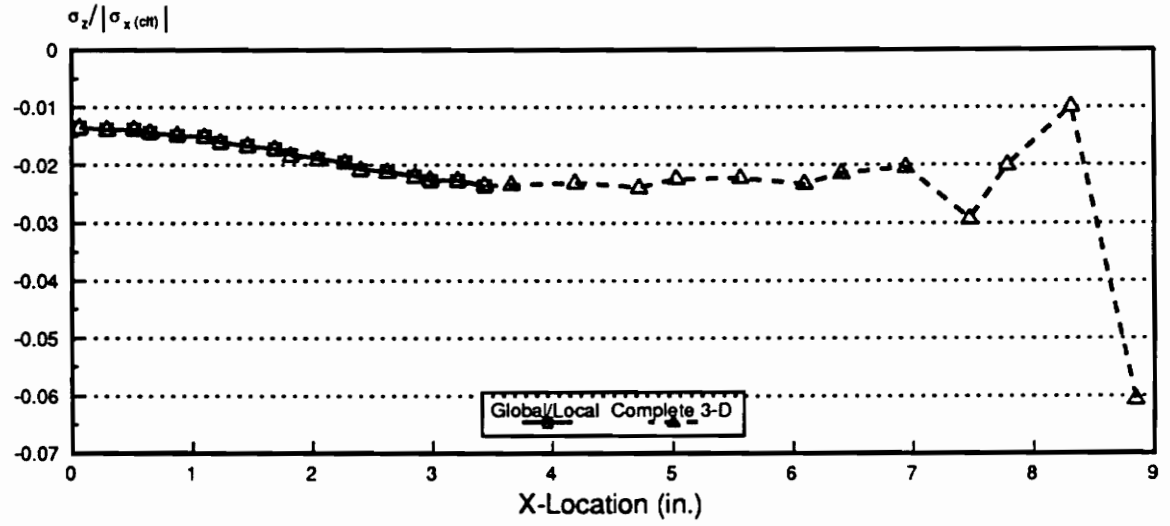

a)

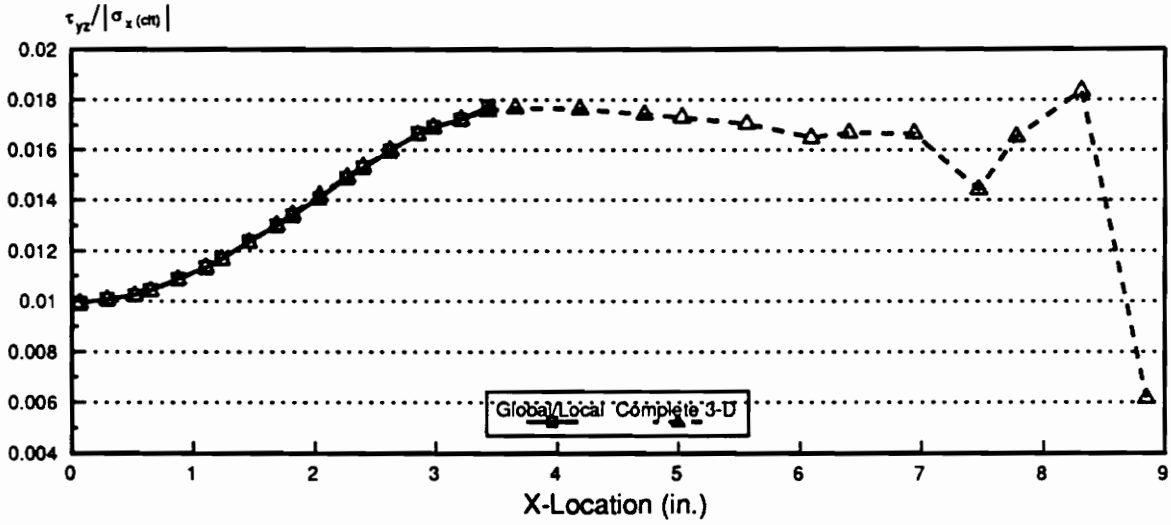

b)

Figure 23. Interlaminar Stresses for Complete and Reduced Local Model at Straight Edge: a) σ_z near Mid-plane b) τ_{yz} at $z = 0.025$ in.

sequence. By comparing Figure 17b) and Figure 24b), the effect of reversing the order of the plies can be seen with the $[90_{2n}/0_{2n}]_S$ local model having the opposite distortion at the free edge, because of the reversal of order of the plies at the interface. By comparing Figure 17b) and Figure 25b), its is determined that the dispersed plies in the $[0_n/90_n/0_n/90_n]_S$ laminate have the same type of deformation as the $[0_{2n}/90_{2n}]_S$ plate, but reduced in magnitude, because the alternating layers temper the effect of the Poisson's ratio mismatch between the plies.

From the through-the-thickness stress distribution in Figure 26a), the maximum interlaminar normal stresses are found at the integration points near the mid-plane of the laminate. The characteristic shape determined by others for this stress component is maintained for each x-location within the local model, as seen in Figure 26b). In the deformed view of the global model there is displacement in this area, indicating that the hole is influencing the displacement field of the previously straight edge, and thus the stress state. This is reflected in Figure 26b) because with increasing distance from the centerline of the hole, the absolute magnitudes of the stress increase. For the $[0_{2n}/90_{2n}]_S$ orientation, the values ranged from 1.4% of the far-field stress at the local $x = 0$ symmetry plane to a maximum magnitude of 2.24% away from the hole.

The through-the-thickness distribution of the interlaminar shear stress (τ_{yz}) is presented in Figure 27a) at the $z = 0.025$ in. interface for each x-location in the local model. Because there are no integration points at the element boundaries, all interfacial stress values are an average of the integration point stresses on either side of the interface. From stress-reporting studies completed by the author, it was determined that this approach was sufficiently accurate for the nodal distributions used here (Barlow, 1976, 1989). This stress is maximum at the interface of the 90° and 0° layers and zero at the mid-plane and top free edge of the laminate. As with σ_z, the character of both its through-the-thickness and in-plane distribution becomes more exaggerated farther from the hole, shown in Figure 27a) and b), respectively. The range in stress values from the centerline of the plate to the farthest local model integration point is from 1% to 1.8% of the classical lamination theory in-plane normal stress, demonstrating that the effect of the large hole in proximity to the free edge is to reduce the absolute magnitude of the stress. τ_{yz} has an in-plane distribution that is gen-

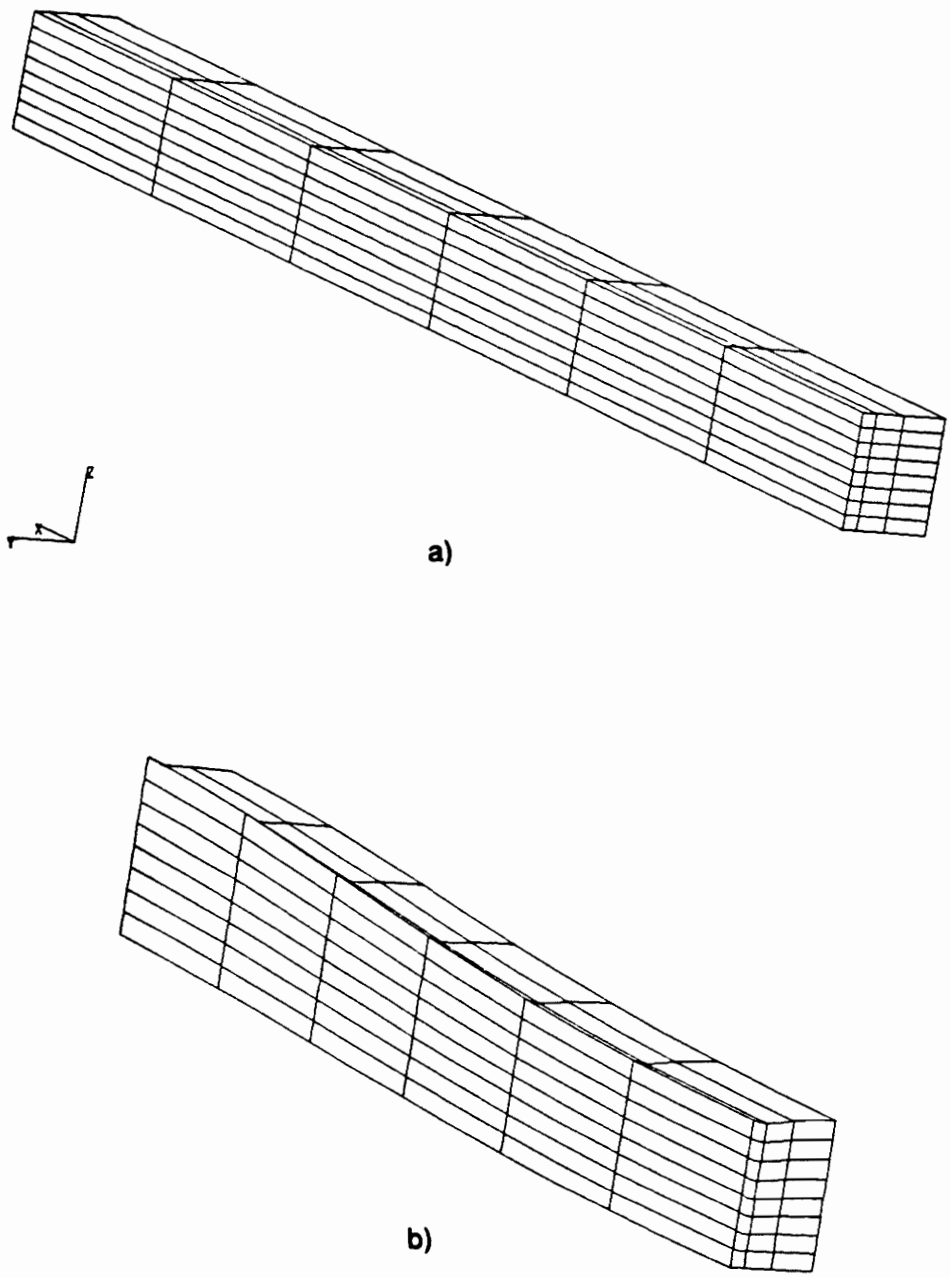

Figure 24. Reduced Local Straight Edge Models for $[90_{2n}/0_{2n}]_s$ near Six-Inch Diameter Hole: a) Undeformed b) Deformed

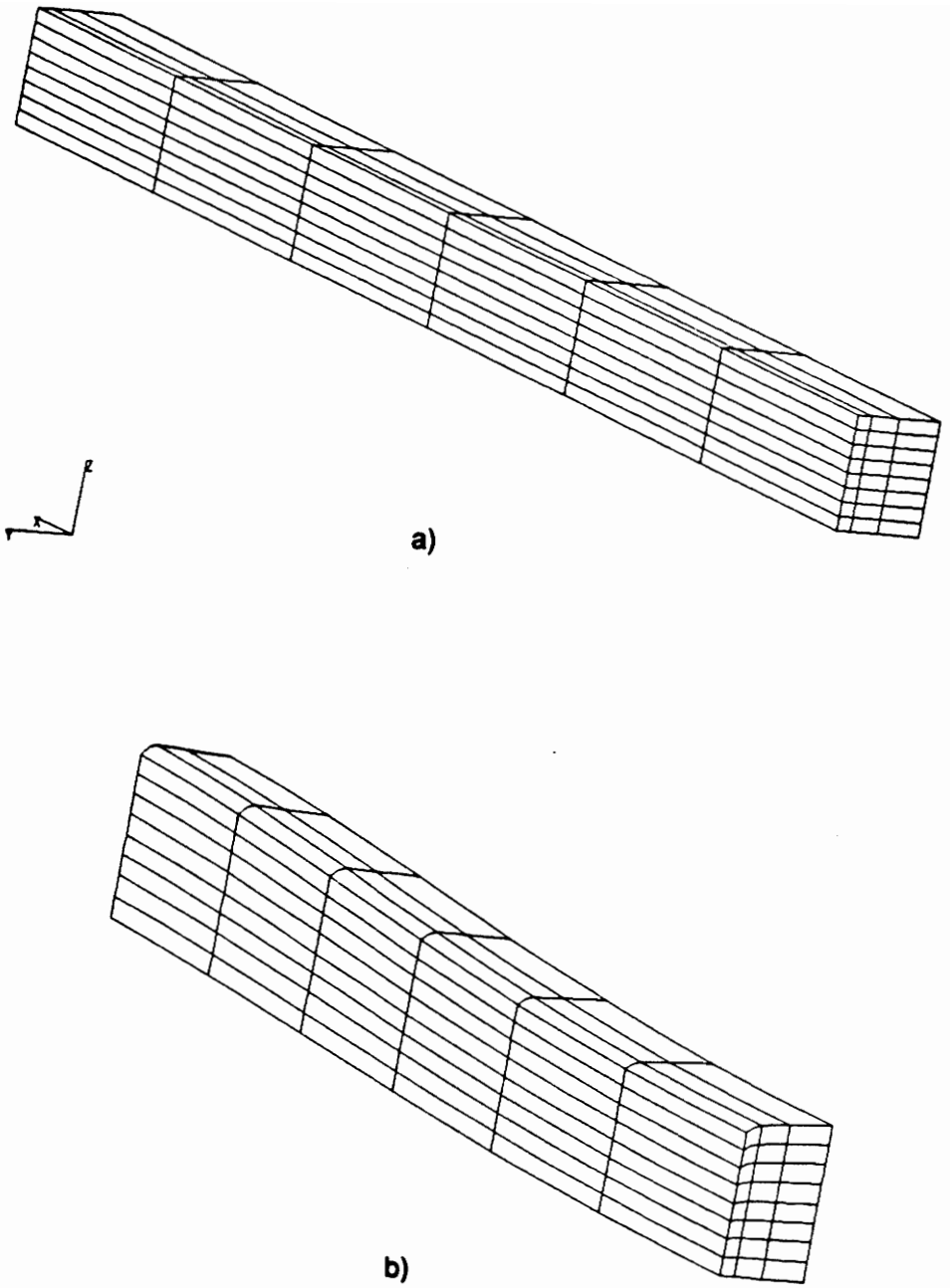

Figure 25. Reduced Local Straight Edge Models for Dispersed Lay-up near Six-Inch Diameter Hole: a) Undeformed b) Deformed

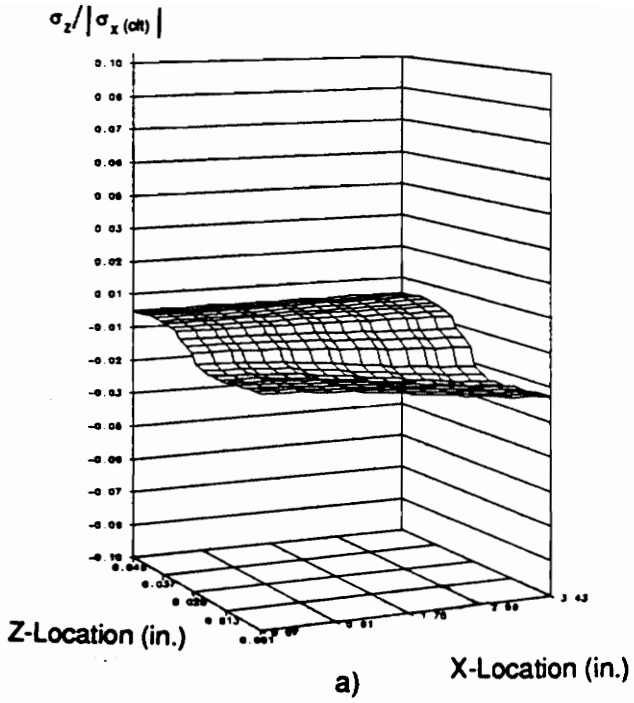

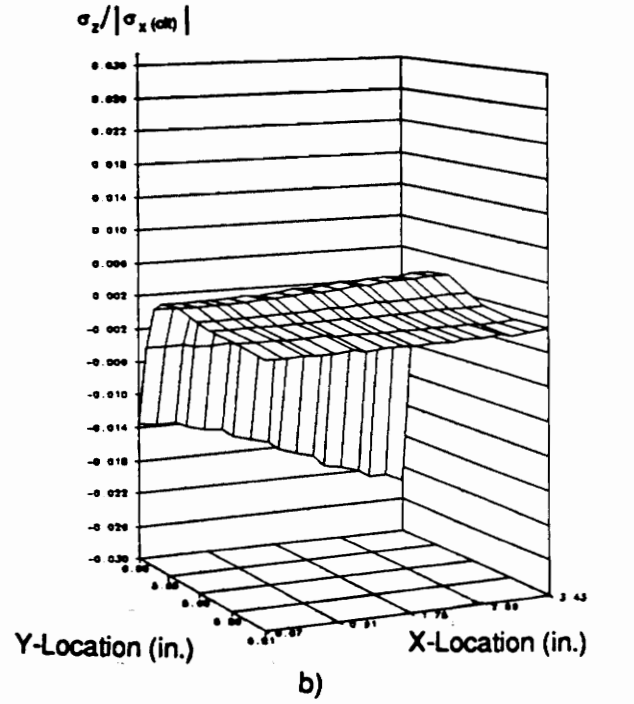

Figure 26. σ_z **for Reduced Straight Edge Model for** $[0_{2n}/90_{2n}]_s$**:** a) Through-the-thickness b) Near Mid-plane

erally zero, but rises sharply near the free edge. As these gradients are within one quadratic element, further refinement or higher order elements may yield different values at the free edge. In the limit, however, the exact stress value is unattainable, because displacement-based elements do not satisfy the traction-free condition exactly (Salamon, 1980), and (Spilker and Chou, 1980).

Figure 28a) is the through-the-thickness distribution, while Figure 28b) is the mid-plane distribution of σ_z at a straight edge for the $[90_{2n}/0_{2n}]_s$ lamination sequence near a six-inch hole. As for the previous lamination sequence, the maximum values are found along the mid-plane in Figure 28a). The change in stacking sequence causes a change in sign of this stress component. However, reversing the stacking sequence does not produce a mirror image of the in-plane distribution, seen by comparing Figure 26b) and Figure 28b). The $[90_{2n}/0_{2n}]_s$ lay-up produces maximum tensile values (2.8%) which are greater in magnitude than those compressive values for the $[0_{2n}/90_{2n}]_s$ laminate (2.4%). Again, the larger absolute magnitudes are found at the farthest integration points from the hole centerline. At the integration point nearest the centerline of the plate, the absolute value of this stress component is larger for the $[90_{2n}/0_{2n}]_s$ laminate, 1.6% versus 1.4%. The influence of the nearby hole is to reduce the magnitude of σ_z along the free edge from a value of 2.8% to 1.6% of the in-plane normal stress in the same pattern as that for the $[0_{2n}/90_{2n}]_s$ laminate.

As for the interlaminar normal stress component, reversing the order of the plies in the laminate changes the sign of the through-the-thickness distribution of the interlaminar shear stress, as seen in Figure 29a). The peak values for this stress component are again at the interface between the 0° and 90° layers. The result of reversing the lamination sequence on the in-plane distribution of τ_{yz} is to produce a stress distribution that is a mirror image of that for the $[0_{2n}/90_{2n}]_s$ sequence, with the same minimum and maximum absolute magnitudes as before. Once again, as the integration points are farther from the hole along the free edge and thus, the effect of the hole is lessened, the absolute magnitude of τ_{yz} becomes larger.

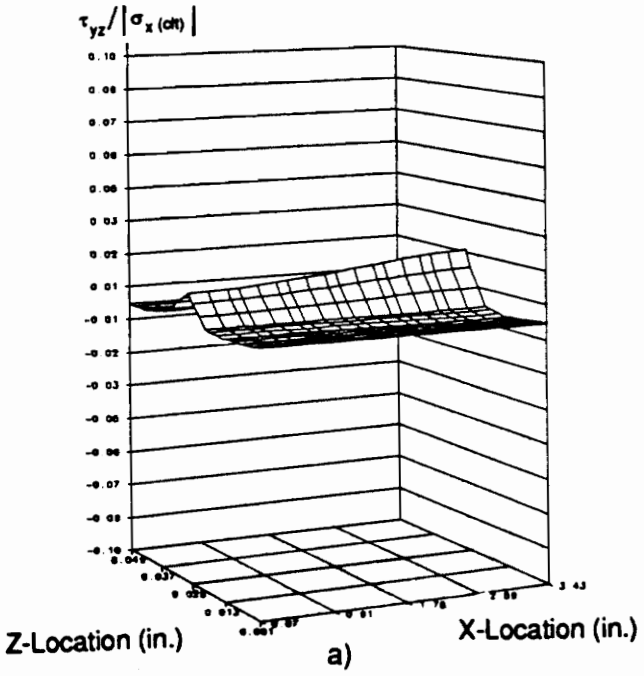

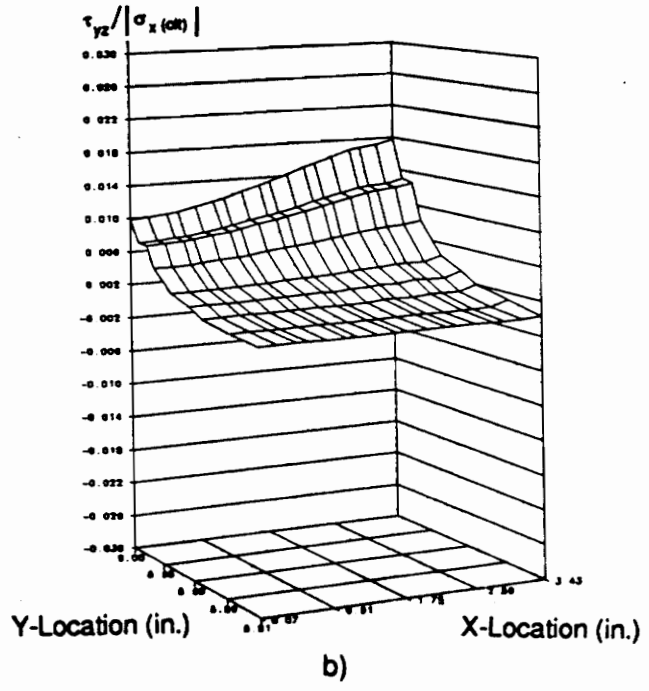

Figure 27. τ_{yz} **for Reduced Straight Edge Model for** $[0_{2n}/90_{2n}]_s$**:** a) Through-the-thickness b) At $z = 0.025$ in.

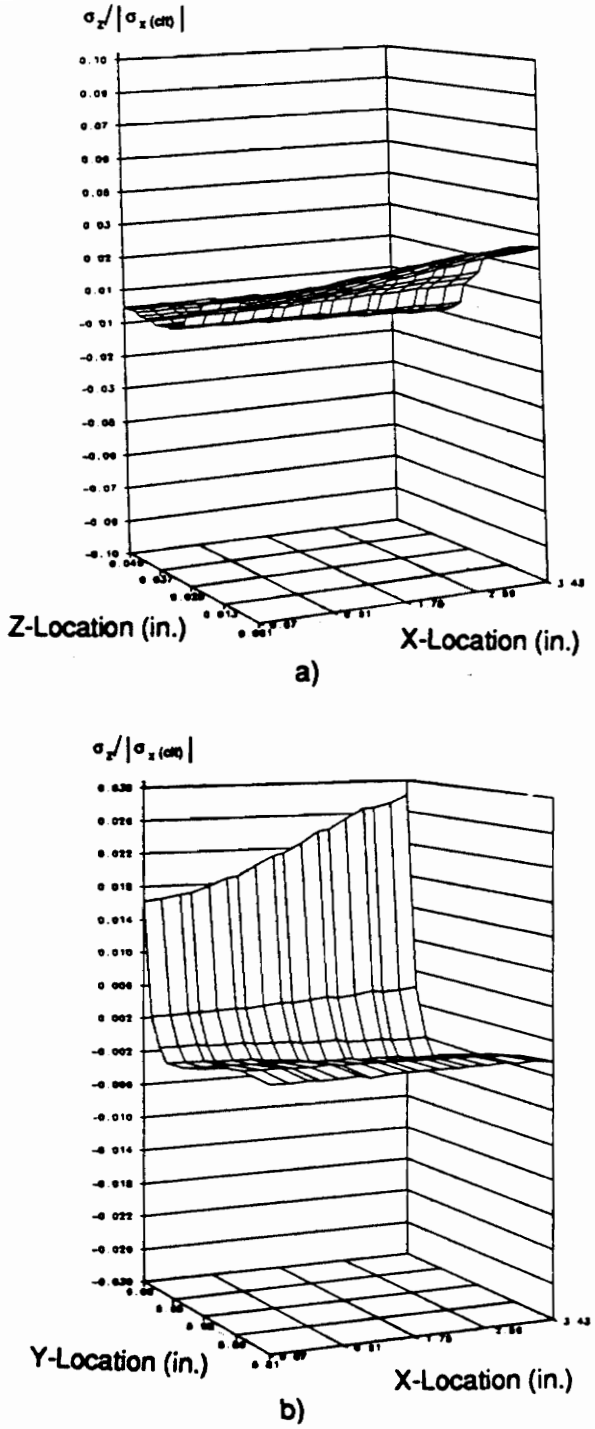

Figure 28. σ_z **for Reduced Straight Edge Model for** $[90_{2n}/0_{2n}]_s$: a) Through-the-thickness b) Near Mid-plane

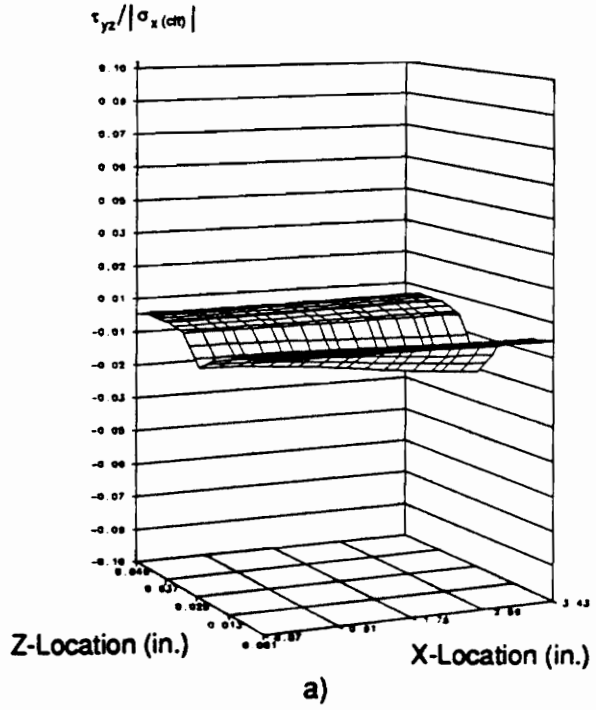

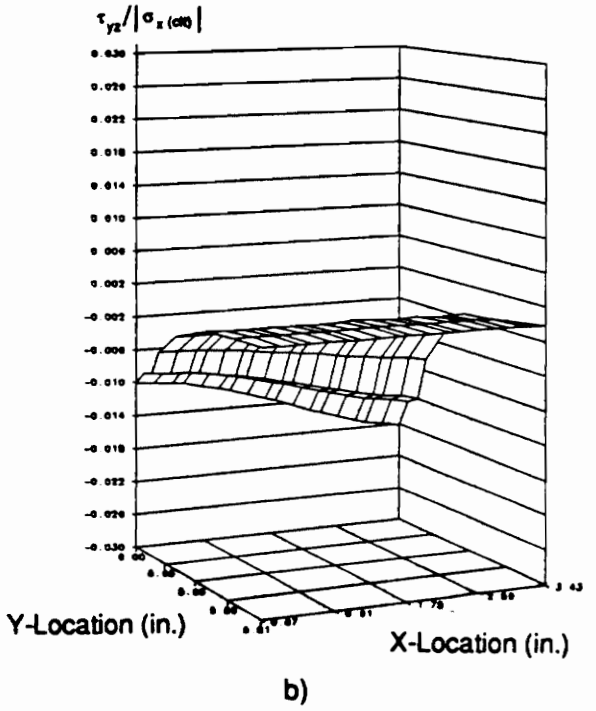

Figure 29. τ_{yz} **for Reduced Straight Edge Model for** $[90_{2n}/0_{2n}]_s$**:** a) Through-the-thickness b) At $z=0.025$ in.

Unlike the other cross-ply laminates, the $[0_n/90_n/0_n/90_n]_s$ laminate has several interfaces between 0° and 90° plies. As a result, its through-the-thickness interlaminar normal stress distribution exhibits more sign reversals and a reduction in overall magnitude than the clustered stacking sequences (Figure 30a). Because of the dispersal of the 0° and 90° layers, the influence of the Poisson's ratio mismatch between the layers is not as concentrated as with the clustered stacking sequences, and exists at more locations through the laminate thickness. The in-plane distribution at the integration points nearest the mid-plane of σ_z, as shown in Figure 30b), is similar in nature to the $[0_{2n}/90_{2n}]_s$ laminate, however, its magnitude is lowered. Again, the effect of the large hole in proximity to the free edge alters the values for the stress values but not the character of its distribution for a given x-location in the local model.

The through-the-thickness interlaminar shear stress distribution, in Figure 31a), exhibits more variation than the clustered lamination sequences, as expected. Peaks exist at the 90°/0° ($z = 0.025$ in.) interface, with valleys at the 0°/90° ($z = 0.0125$ in. and $z = 0.0375$ in.) interfaces. The fact that the effect of the Poisson's ratio mismatch between the different layers is dependent on the order of the plies about a particular interface is shown clearly in this figure. To date, the interface of interest in this work has been the $z = 0.025$ in. location, which is the only interface common to all three laminates. Because the order of the ply orientations from the mid-plane above the $z = 0.025$ in. location is 0° and then 90°, its in-plane distribution should resemble the $[90_{2n}/0_{2n}]_s$ laminate and not the $[0_{2n}/90_{2n}]_s$ laminate. Since the dispersal of the plies lessens the effective Poisson's ratio mismatch, the stress magnitudes at this location should be less than that for the clustered lamination sequence. Examination of Figure 31b) supports both of these statements.

The effect of clustered, reversed, and dispersed laminate orientations along the integration points nearest the free edge for cross-ply laminates with a six-inch diameter hole for both of the stress components of interest is found in Figure 32. First the interlaminar normal stress at those integration points nearest the mid-plane is shown in Figure 32a). Dispersal of the 0° and 90° layers in the $[0_n/90_n/0_n/90_n]_s$ laminate reduces the stress values by 50% from the $[0_{2n}/90_{2n}]_s$ laminate over this region. The fact that the $[90_{2n}/0_{2n}]_s$ laminate does not have a mirror-image stress distribution

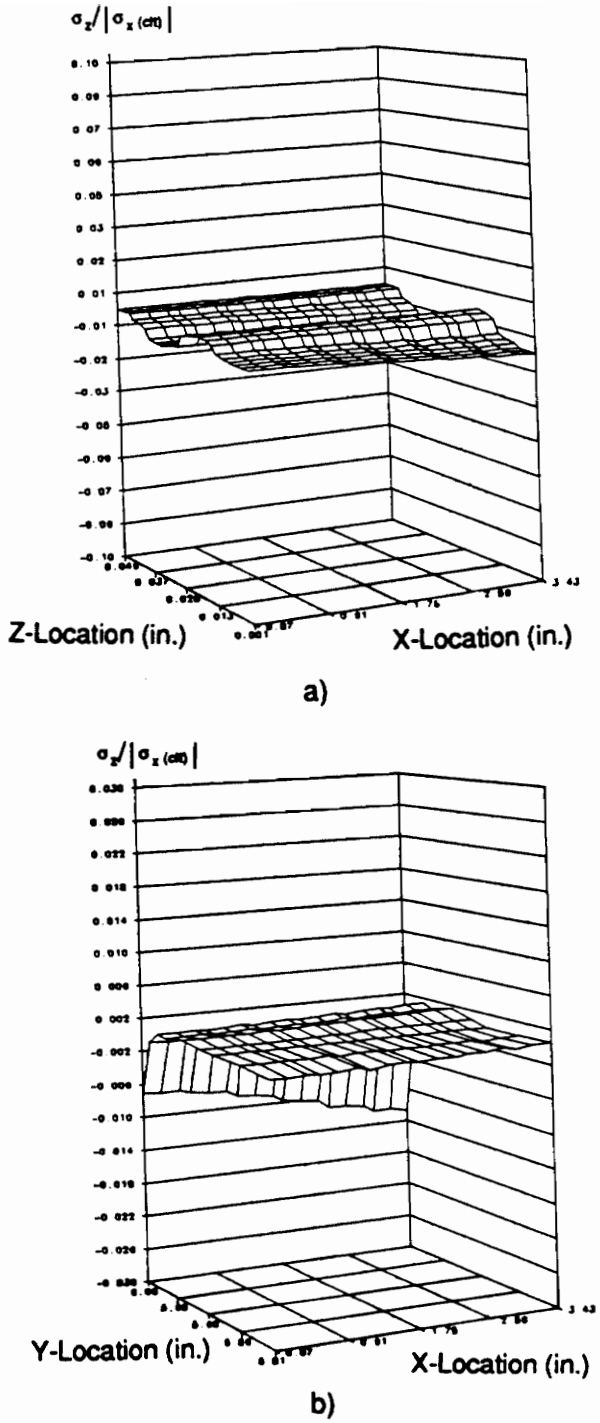

Figure 30. σ_z **for Reduced Straight Edge Model for Dispersed Lay-up:** a) Through-the-thickness b) Near Mid-plane

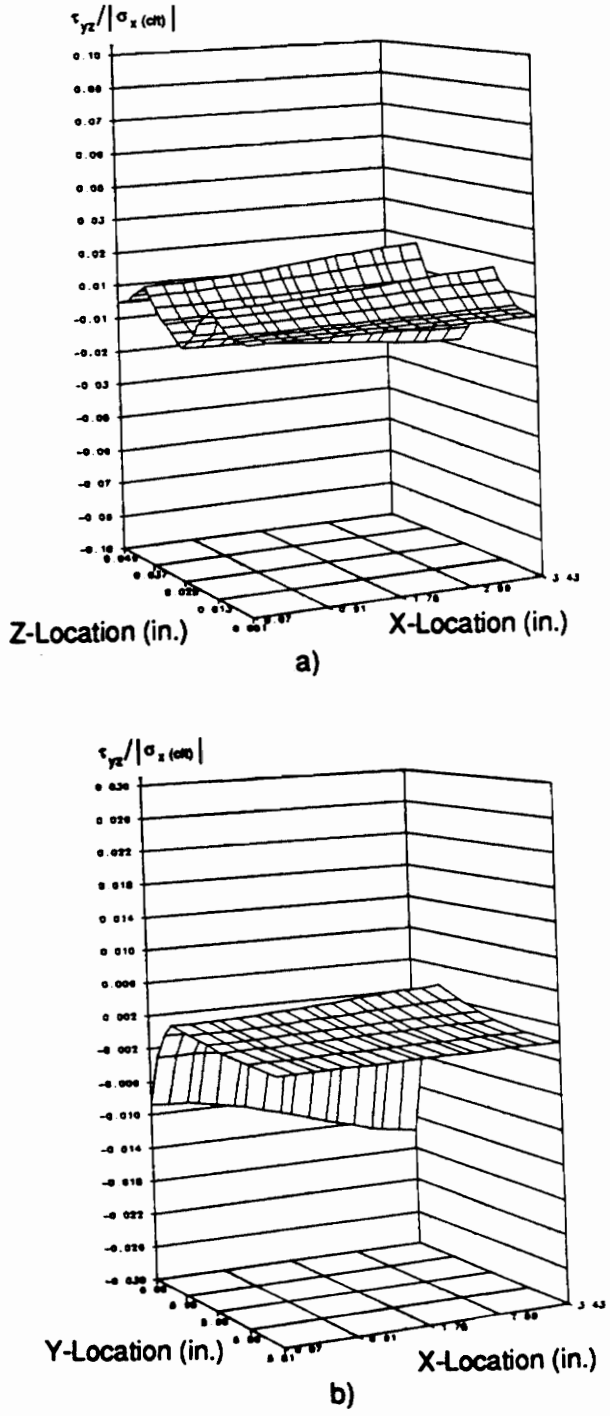

Figure 31. τ_{yz} **for Reduced Straight Edge Model for Dispersed Lay-up:** a) Through-the-thickness b) At z = 0.025 in.

of the $[0_{2n}/90_{2n}]_s$ laminate is clearly visible in this figure, since throughout the local model near the free edge its magnitude is clearly larger. For all of these stacking sequences, the presence of the six-inch diameter hole reduces the magnitude of the stresses. Within each local model, the peak free edge stress is at the farthest integration point from the hole.

The effect of altering the order of the plies on τ_{yz} is shown in Figure 32b) for the $z = 0.025$ in. interface. As was noted in previous discussions about this component, τ_{yz} for the $[0_n/90_n/0_n/90_n]_s$ laminate will more closely resemble the $[90_{2n}/0_{2n}]_s$ laminate than the $[0_{2n}/90_{2n}]_s$ laminate at this interface, because of the order of the plies immediately above and below it. The magnitude for the dispersed laminate is reduced in magnitude from its corresponding clustered laminate by nearly 10%, which is not as large a reduction as found for the interlaminar normal stress. An exact reversal in the sign of the stress distributions for the two opposing clustered sequences is shown in this figure. As found for the interlaminar normal stress distributions, the integration points farthest from the hole in the local model had the largest magnitude of stress. This suggests again that the six-inch diameter hole relieves the stress field in all of the laminates considered.

While the six-inch hole has a considerable effect on the straight free edge stress distributions for all of the stacking sequences, the effect of different hole diameters in a finite width plate remains to be considered. Examination of the deformed local straight free edge meshes for the $[0_{2n}/90_{2n}]_s$ laminate for the different diameter holes in Figure 17b), Figure 18b), and Figure 19b) reveals the trend. The influence of the hole on the local straight free edge was most pronounced near the six-inch diameter hole, which caused a bulging outward of the model away from the center of the plate (Figure 17b). This phenomenon was observed for the model of the straight edge near the three-inch diameter hole, but to a lesser degree (Figure 18b). As expected, there is little in-plane curvature along the edge near the plate, with a one-inch diameter hole (Figure 19b). This hole is one-twelfth of the plate width and is not expected to influence the previously straight free edge as strongly as the holes which are one-quarter (three-inch diameter), and one-half of the plate (six-inch diameter) width. The same trend was noticed earlier with the deformed views of the global models for the plates.

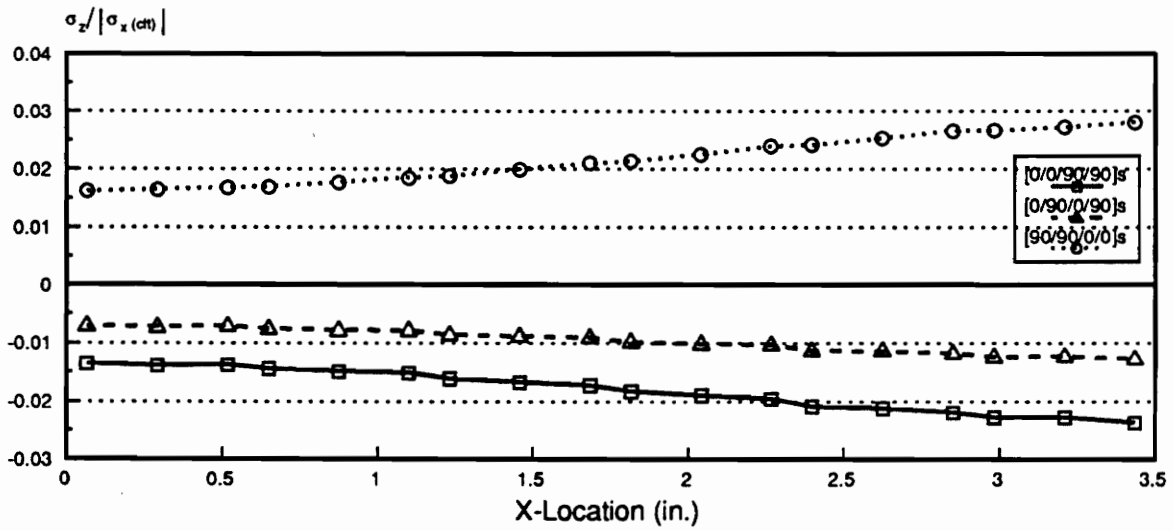

a)

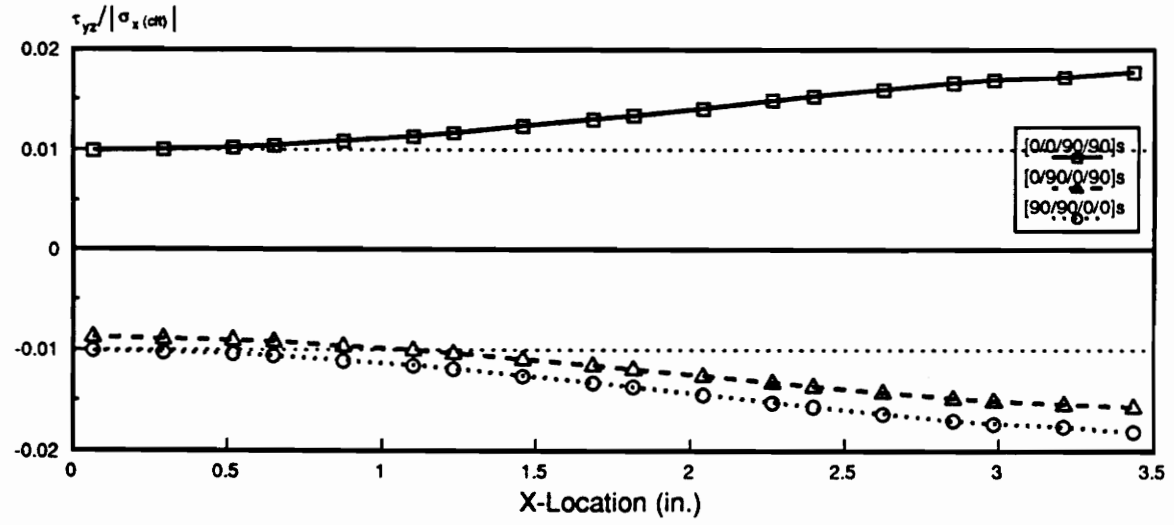

b)

Figure 32. Interlaminar Stresses nearest Straight Edge for Different Laminate Orientations: a) σ_z near Mid-Plane b) τ_{yz} at z = 0.025 in.

The trend found for increasing hole diameter in a finite-width plate on the deformation state of the local models will undoubtedly be reflected in the interlaminar stress distributions, and is considered next. The interlaminar normal stress distributions near the mid-plane for the $[0_{2n}/90_{2n}]_S$ laminates with three- and one-inch holes is shown in Figure 33a) and b), respectively. As found for the plate with a six-inch diameter hole, the characteristic shape of this stress component is maintained for each x-location in the local model for plate, regardless of the hole diameter. As expected, the straight edge near the three-inch hole is affected, but not as strongly as the straight edge near the six-inch diameter hole. The variation in the stress, as seen in Figure 33a), ranges from 1.7% to nearly 2.2% of the reference stress. The model near the one-inch hole exhibits a nearly uniform distribution across the x-dimension of the model, and most closely resembled the distributions found in the literature for plates without holes (Figure 33b). The peak stress value found was 2% of the in-plane normal stress predicted by classical lamination theory for plates without holes.

In Figure 34, the interlaminar shear stress distributions at the $z = 0.025$ in. interface are presented for the plates with the two smaller holes. Like the straight edge near the six-inch diameter hole, there is a steep rise in the stress as it nears the free edge for each of the straight edges near the smaller holes. From Figure 34a), it can be noted that the influence of the three-inch diameter hole on the straight edge alters the magnitude of the peak stress from 1.3% to 1.6% of the reference value. As found for the other lamination sequences and hole diameters, the largest absolute magnitude of stress exists along the straight edge farthest from the hole region. As seen in Figure 34b), the one-inch diameter hole appears to have no effect on this stress component, since its distribution is uniform across the x-dimension of the local model with a value of 1.5%.

Direct comparison of σ_z at the integration points nearest the mid-plane and free edge for all three hole sizes is presented in Figure 35a) for the $[0_{2n}/90_{2n}]_S$ laminate, while in Figure 35b), the same comparison is presented for τ_{yz} at the $z = 0.025$ in. interface. As the diameter of the hole increases in a finite width plate, the effect of the hole on the stress state along the straight free edge near the hole increases. The presence of the nearby hole reduces the magnitudes of all of the stress components, both intralaminar and interlaminar, nearest the hole centerline. The largest reduction in

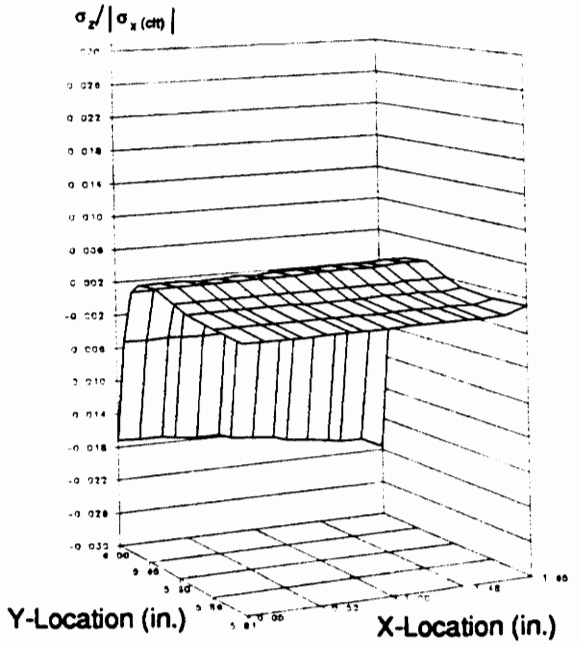

a)

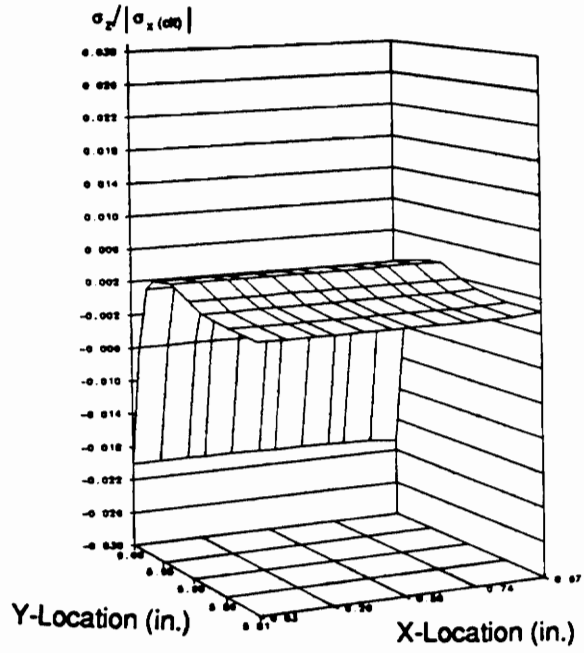

b)

Figure 33. σ_z **for Reduced Straight Edge Models for** $[0_{2n}/90_{2n}]_s$ **near Mid-plane with Smaller Holes:** a) Three-Inch Hole b) One-Inch Hole

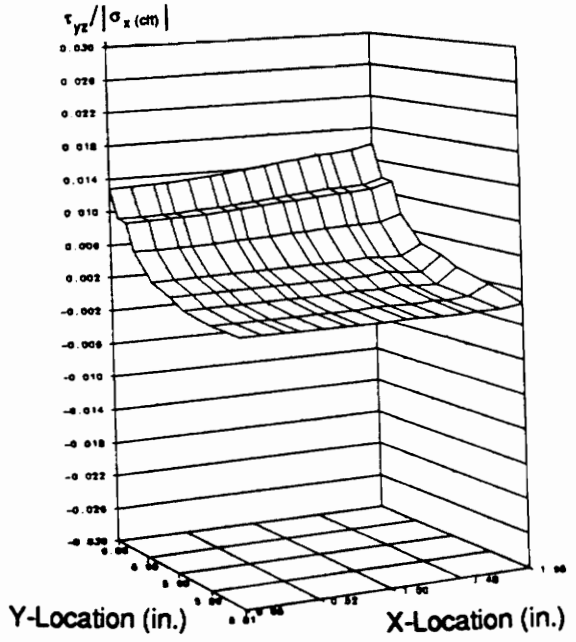

a)

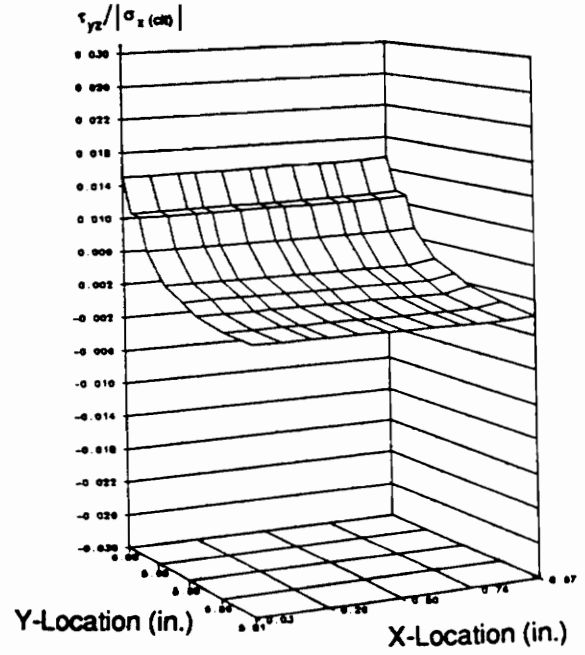

b)

Figure 34. τ_{yz} **for Reduced Straight Edge Models for** $[0_{2n}/90_{2n}]_s$ **at Interface with Smaller Holes:** a) Three-Inch Hole b) One-Inch Hole

free edge stresses in proximity to the hole was found for the plate with a six-inch diameter hole, as was the greatest change in absolute magnitude of the stress for both of these stress components. Regardless of the hole diameter, the same end-shortening displacement condition was applied to all of the plates. The relative stiffness of each plate will vary, however, because of the reduction in net section and hence the ability to resist the load because of the presence of the hole. The larger holes will reduce the stiffness of the 18x12 inch plate to a higher degree than the one-inch diameter hole, and higher intralaminar and interlaminar stresses will result. Each figure reveals that the stress values for the local model near the larger holes overshoots that determined for the one-inch diameter hole at the end of the local models, verifying the above statements.

4.3.2.3 Verification of Global/Local Modeling Technique for Curved Edge

As with the straight edge, validation of the two-dimensional to three-dimensional global/local modeling technique was done by comparing the displacement and stress fields of a local model to those from a complete three-dimensional finite element model. Information about the models is presented in Table 3 on page 37. For all of the characteristics presented in this table, the technique of analyzing a global two-dimensional model (an inefficient one, at that) and then a local three-dimensional model is clearly more efficient than a complete three-dimensional analysis, but the issue of accuracy remains.

The undeformed and deformed views of the complete model of the $[0_{2n}/90_{2n}]_s$ laminated quarter plate with a six-inch diameter hole are presented in Figure 15a) and b), respectively. From this viewing angle, the variation in the thickness of the plate with angular position around the hole is readily visible. The portion of the plate near the local $y = 0$ symmetry plate exhibits z-direction contraction of the elements near the hole edge, while near the local $x = 0$ symmetry plane, the elements undergo expansion. Near the local $x = 0$ symmetry plane, the extent of the hole effect is approximately 0.5 in. into the plate, which is the same distance from the boundary of the local curved edge model to the hole edge. In the two-dimensional global model, the compressive load

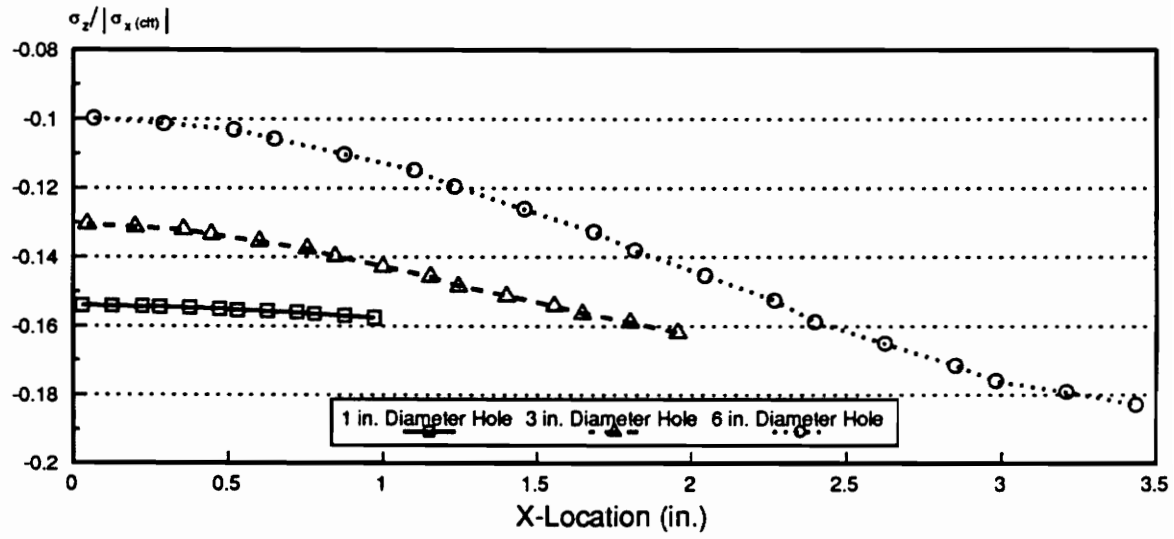

a)

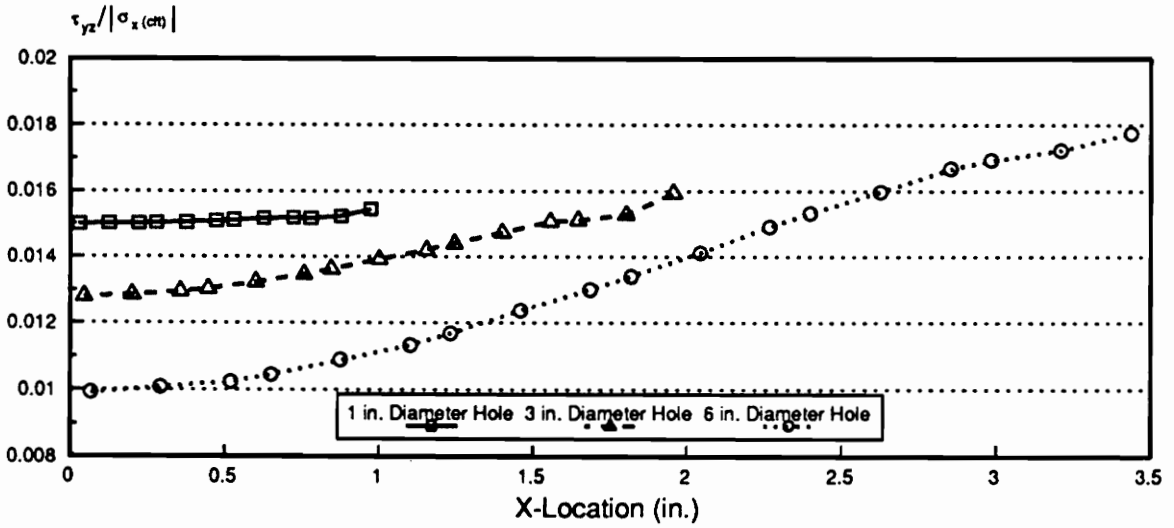

b)

Figure 35. Interlaminar Stress Distributions at the Straight Free Edge for Different Holes: a) σ_z near Mid-plane b) τ_{yz} at Interface

resulted in the development of a noncircular hole, and no hint of these thickness changes existed. In the three-dimensional models, the in-plane change from a circular hole to a noncircular hole affects the out-of-plane response. The area near the hole at the local $x = 0$ symmetry plane is compressed in-plane, and must bulge out-of-plane to compensate, while the area near the local $y = 0$ symmetry plane expanded in-plane and contracted out-of-plane. While the in-plane loading is causing expansion through the laminate thickness at angular positions near 90°, the combined effect of the local strain and Poisson's ratio mismatch is to reduce this growth, as seen in Figure 15b), along the both local axes for the two rows of elements within one laminate thickness of the edge. The same influence is seen for the curved edge local model in Figure 20b). Because of the difference in the scaling between these two figures, these appear erroneously to be more pronounced for the local model.

Comparison of the stress fields for the curved edge model and the complete three-dimensional model was completed for the interlaminar normal stress near the laminate mid-plane, and the interlaminar shear stress components ($\tau_{\theta z}$ and τ_{rz}) at the $z = 0.025$ in. interface of the laminate, and is presented in Figure 36 and Figure 37a) and b), respectively. The stresses are identical in value for these models for the interlaminar normal stresses outside the region between $\theta = 35°$ and $\theta = 50°$. The difference in the stresses in this region is small, however, less than 0.25% of the in-plane normal stress as determined by classical lamination theory, but its presence casts a shadow on the global/local analysis method. Examination of the undeformed two- and three-dimensional models showed that between the global/local boundary and the rings of circular elements around the hole, there are elements which are long, tapered, and skewed. While displacement-based elements generally determine displacement fields accurately, whenever distorted elements are used, the displacement field can degrade rapidly (Reddy, 1989). Thus, the two-dimensional displacements from 'questionable' elements in the global model, are applied to 'questionable' three-dimensional local elements. The complete three-dimensional finite element model contains these element geometries as well, but in contrast to the local model, well-behaved elements surround these elements so that their collective stiffness buffers the effect of the distorted elements. Examination of the in-

plane displacements in this region between those applied to the local model and those determined by the three-dimensional model, revealed slight variations along the global/local interfaces. The greatest variation was found near the same angular locations where the stress states for the local and complete models did not coincide, precluding the determination of the identical stress field in this area. The fact that local model was able to determine the three-dimensional stress field identically in the other regions around the hole is encouraging; there appears a certain robustness in the global/local analysis technique, but the application of displacements that are not necessarily accurate in the global sense will adversely affect the local solution.

Examination of the interlaminar shear stresses for the local and complete models at the $z = 0.025$ in. interface is more encouraging. The $\tau_{\theta z}$ distribution for both of these models is presented in Figure 37a) and is coincident. The global/local analysis technique determined the character and magnitude of this stress component correctly for all of the angular positions. Note that magnitude of this component is large in comparison to the normalization stress. This is because of the changing local lamination sequence, and hence local material properties in the laminae, and the load path around the hole. The remaining stress component (τ_{rz}), in Figure 37b), is smaller in magnitude than the other stress components. While this stress component reaches a value of zero at the hole edge, it is presented here at the same radial distance from the hole as the nearest integration points, which is in an area of large stress gradients. A slight difference between the complete and local three-dimensional model results was found in the same region as found for the interlaminar normal stress, which was less than 0.1% of the normalization stress. It is acknowledged that a wiser element selection process could have improved the global/local results, but the relative success of the global/local procedure is considered to be excellent. Within limits, the local model can compensate for the fact that the displacements are accurate, or nearly so, in the global sense but not locally accurate. The two-dimensional to three-dimensional global/local procedure used to determine the stress state around a curved edge for cross-ply laminate in compression can be considered a valid and viable modeling technique.

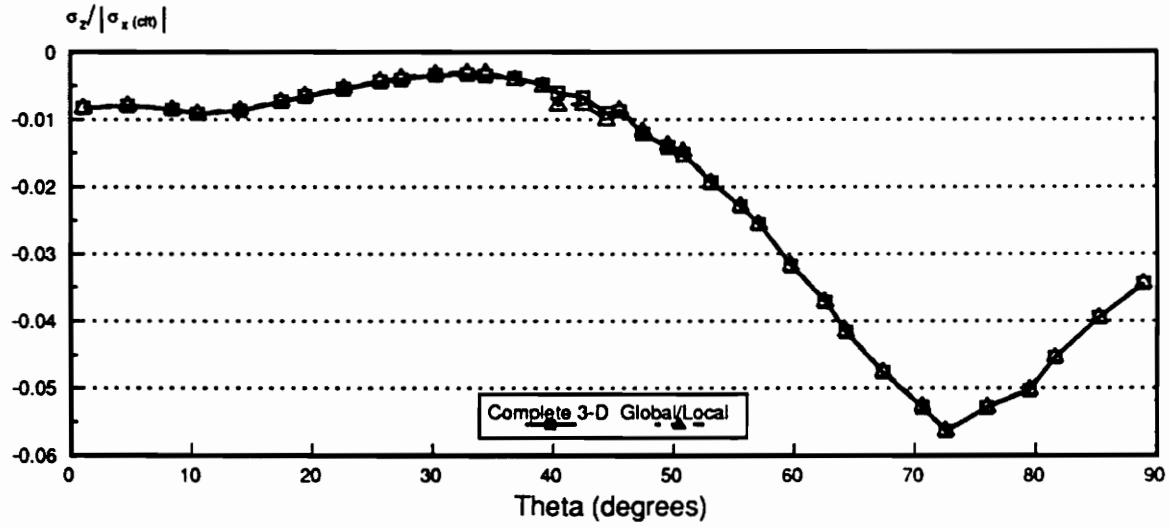

Figure 36. Interlaminar Stresses for Complete and Reduced Local Model at Curved Edge: a) σ_z near Mid-plane

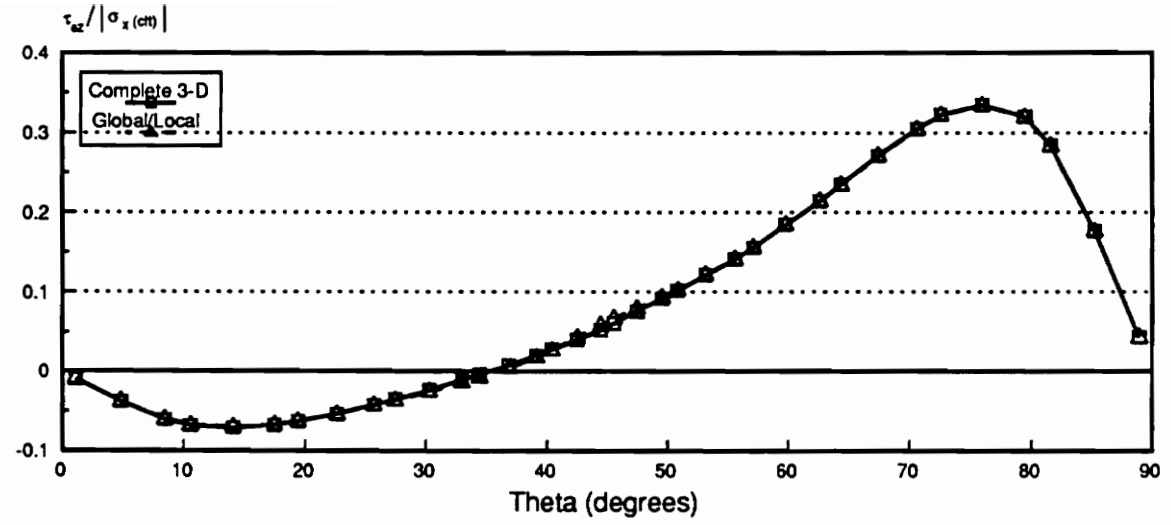

a)

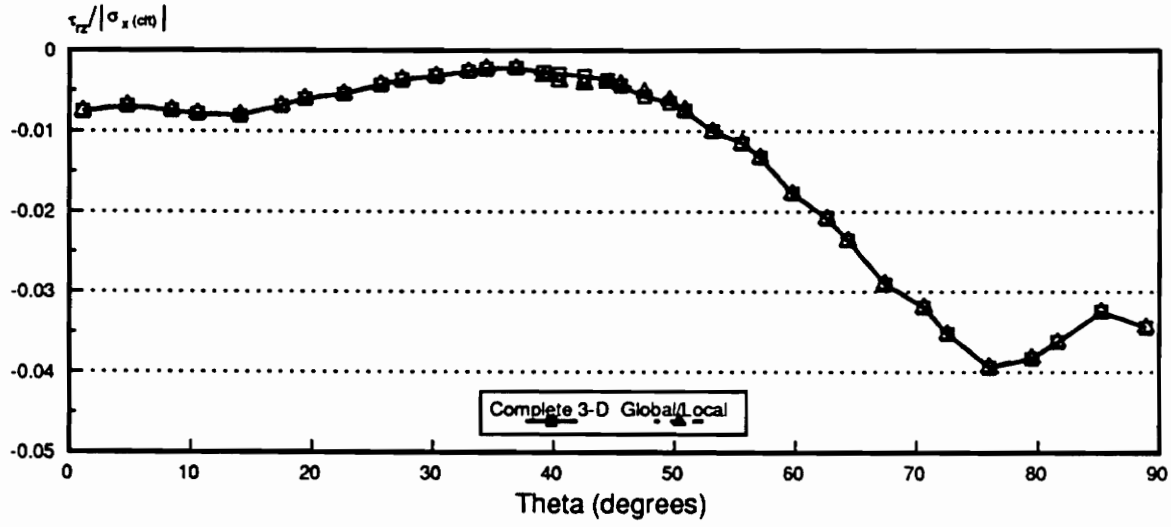

b)

Figure 37. Interlaminar Stresses for Complete and Reduced Local Model at Curved Edge: a) $\tau_{\theta z}$ at z = 0.025 in. b) τ_{rz} at z = 0.025 in.

4.3.2.4 Curved Free Edge Model Results

The undeformed and deformed local curved edge meshes for the different stacking sequences around a six-inch diameter hole are shown in Figure 20a) and b), Figure 38a) and b), and Figure 39a) and b). Each of the local models are compressed in the x-direction and the holes became noncircular, as it did for the global models. There is a noticeable nonuniform thickening of the local models around the hole. Each local model, regardless of the stacking sequence, exhibited thickening near the local $x = 0$ symmetry plane and contraction near the local $y = 0$ symmetry plane, which is attributable to the applied load on the plate. The effect of the laminate stacking sequence manifested itself in the rows of elements nearest the curved free edge. For the $[0_{2n}/90_{2n}]_s$ laminate, those rows contracted more toward the mid-plane of the laminate than the $[0_n/90_n/0_n/90_n]_s$ laminate near the local $x = 0$ symmetry plane. Because the $[0_n/90_n/0_n/90_n]_s$ plate has an alternating ply sequence, some of the rows of elements modeling the plies contracted while others expanded, and the effect of the local Poisson's ratio mismatch and shear coupling was not as concentrated (Figure 20b) and Figure 39b). In contrast, the $[90_{2n}/0_{2n}]_s$ model had regions of noticeable element expansion near the local $x = 0$ and local $y = 0$ symmetry planes away from the laminate mid-plane (Figure 38). From the viewing angle selected, it is difficult to see that there is a difference in the hole diameter through the laminate half-thickness for each of these stacking sequences, but the existence of τ_{rz} inside the hole edge suggests that hole diameter reduction is not constant. It is obvious that the deformation states between the different lamination sequences vary and not necessarily in an intuitive manner.

The displacements were post-processed to determine the stress fields around the hole near the mid-plane and at the interface of the plies. For the integration points nearest the curved edge, through-the-thickness stress distributions were generated for all lamination sequences and interlaminar stress components and are considered in detail. No distributions parallel to the mid-plane of the laminate or those in the r-z plane for a given angular position are presented in the interest of brevity, not as a limitation of the global/local modeling technique.

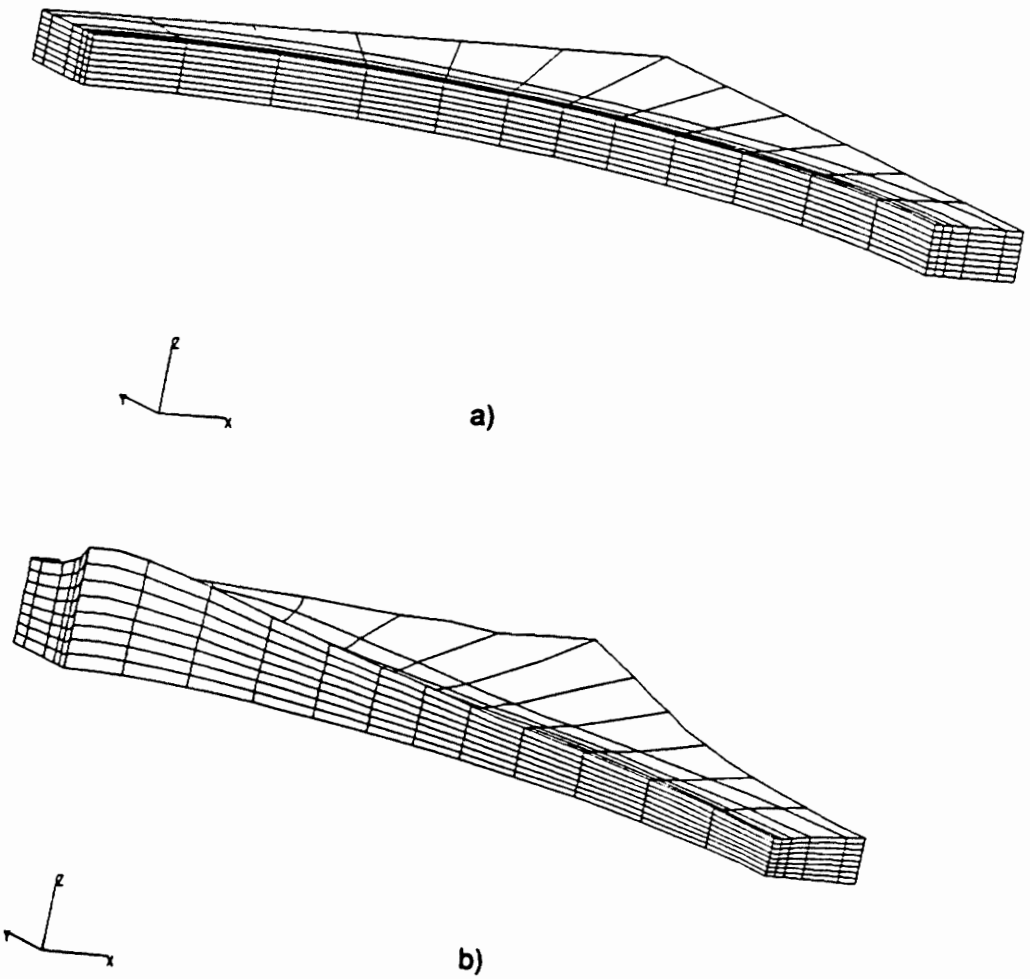

Figure 38. Local Curved Edge Models for $[90_{2n}/0_{2n}]_s$ around Six-Inch Diameter Hole: a) Undeformed b) Deformed

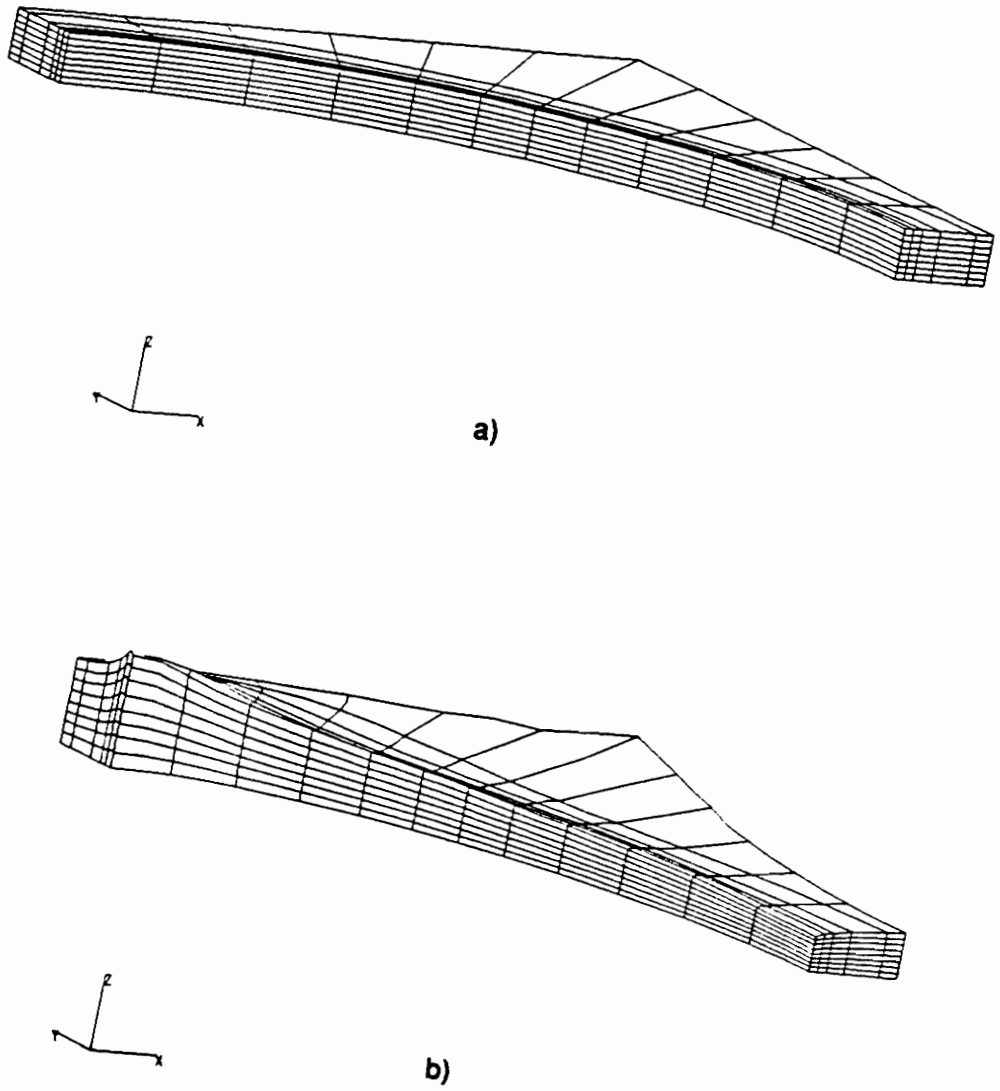

Figure 39. Local Curved Edge Models for Dispersed Lay-up around Six-Inch Diameter Hole: a) Undeformed b) Deformed

The interlaminar normal stress distribution around the hole and through the laminate thickness is presented in Figure 40a), while the stress contours superimposed on a deformed view of the local model are in Figure 41. The stress contours were produced from stress values extrapolated to the nodes from the integration point stresses by the extrapolation technique described in detail in Appendix A. From these figures, it can be determined that σ_z is largest and negative along the mid-plane and diminishes in magnitude through the laminate, becoming zero at the top free edge. At the interface between the 90° and 0° plies, the stress gradients change rather abruptly, and diminish more rapidly. At approximately $\theta = 72°$, its maximum is attained, and there are considerable gradients both through the thickness and in the angular direction. The existence of high in-plane displacement gradients in this region coupled with the the local Poisson's ratio mismatch between the layers affects the character and the magnitude of the stress component. In Figure 41, the stress contours are seen to be concentrated in those angular positions nearest the local $x = 0$ symmetry plane and within one laminate thickness of the curved free edge. The negative values of σ_z are found in the region of the curved edge model that is contracted toward the mid-plane, and are concentrated in the 90° ply. Those elements in the 0° ply, while contracted toward the mid-plane, experience no interlaminar normal stress and appear to follow those elements within the 90° ply toward the mid-plane.

The interlaminar shear stress ($\tau_{\theta z}$) through-the-thickness stress distribution and contours are found in Figure 40b), and Figure 42. With Figure 40b), it was determined that consideration of this component is significant only at the interface between the plies. At $\theta = 75°$, this shear stress reaches a maximum and at $\theta = 10°$ a minimum. The growth and decay of this component through the laminate is immediate, even, and centered about a particular angular location. This is due to the larger gradients in the in-plane stress in this region caused by the redistribution of the deformation and stress state around the hole: greater interlaminar stresses must exist to enforce the displacement boundary conditions. This stress component indicates the degree of slippage of the elements past one another around the hole. Those elements with large positive stress values moving in one direction and those with negative values in opposition. Examination of the stress contours on the

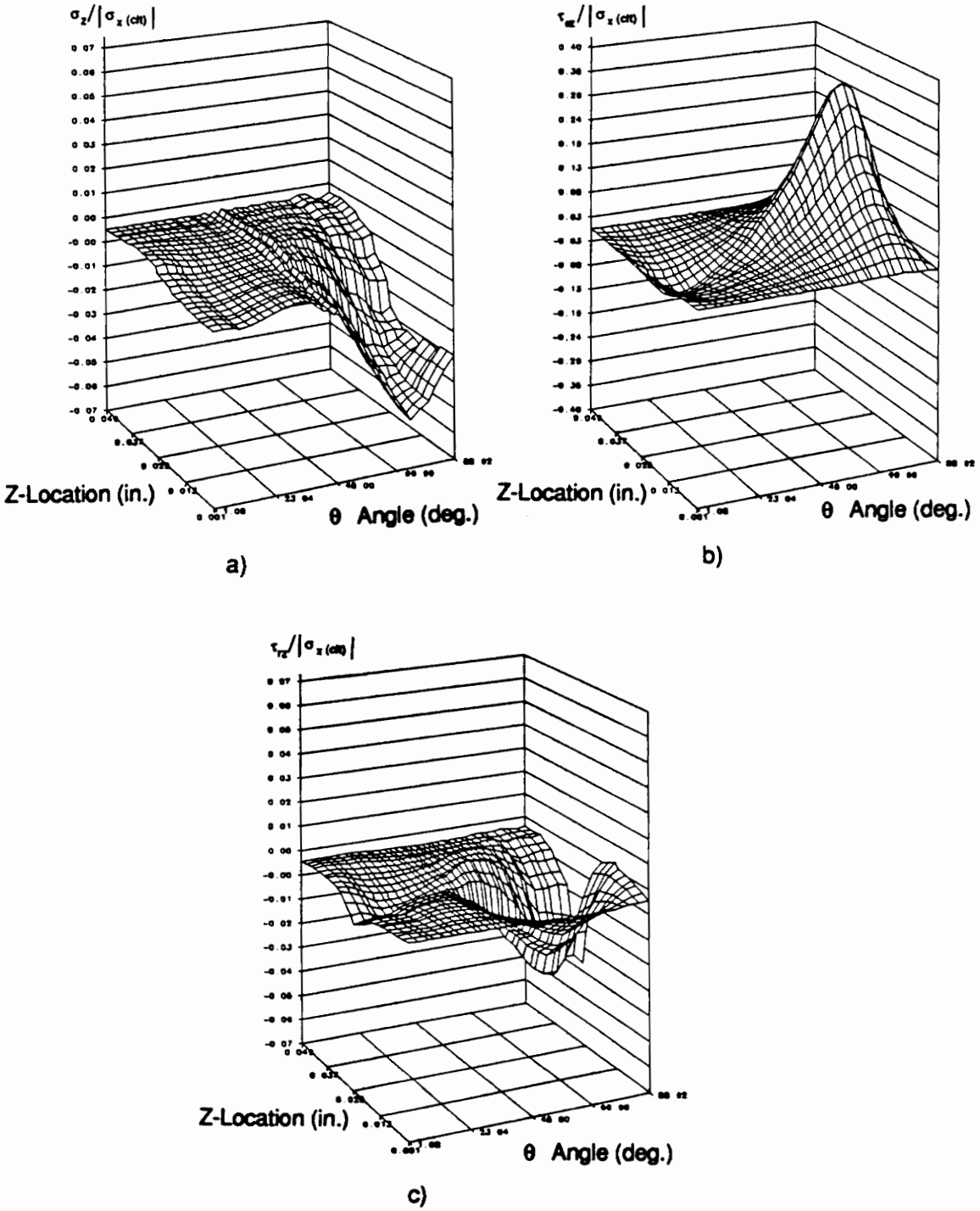

Figure 40. Interlaminar Stress Distributions Curved Edge Model for $[0_{2n}/90_{2n}]_s$ around Six-Inch Diameter Hole: Through-the-Thickness a) σ_z b) $\tau_{\theta z}$ c) τ_{rz}

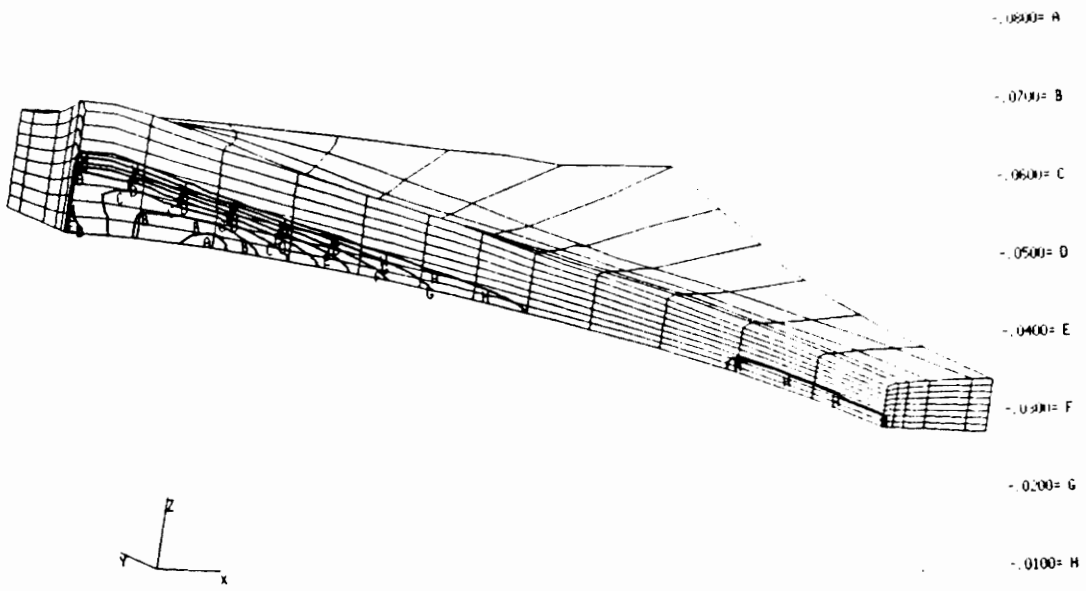

Figure 41. σ_z **Contours for Curved Edge Model for** $[0_{2n}/90_{2n}]_s$ **around Six-Inch Diameter Hole**

deformed model does not reveal much information with the selected viewing angle, however, the elements in the 90° ply are noticeably moving upward and away from the mid-plane, while those in the 0° ply are slipping toward the mid-plane in the region between $\theta = 60°$ and $\theta = 90°$.

Through-the-thickness distributions and stress contours around the hole for the the remaining interlaminar stress component (τ_{rz}) are in Figure 40c), and Figure 43. Its distribution exhibits large gradients near the interface. Unlike the other shear stress component, large opposing gradients exist on either side of the 0°/90° interface. In Figure 40c), the concentration of this stress nearer to the local $x = 0$ symmetry plane is noticed. Again, the region of the hole with a larger normal stress and greater degree of shear coupling is where the stresses are larger in magnitude. In Figure 43 along the local $x = 0$ and $y = 0$ symmetry planes, these stresses are shown to be nonzero only within one laminate thickness of the curved free edge. The 90° and 0° plies will tend to distort the hole in a different direction under the same load, and since those elements at the ply interface are constrained to remain in contact, interlaminar stresses arise to enforce this and generate gradients on either side of the interface.

Reversing the stacking sequence of the laminate has a pronounced effect on the interlaminar response around the hole. Presented in Figure 44a) is the through-the-thickness distribution of the interlaminar normal stress at the integration points nearest the hole for a $[90_{2n}/0_{2n}]_s$ plate with a six-inch diameter hole. Comparing this distribution with that for the $[0_{2n}/90_{2n}]_s$ laminate in Figure 40a), it was found that these distributions are not mirror images as an inexperienced analyst might assume. The decay of the magnitude of σ_z through the laminate is expected. At the locations nearing the local $x = 0$ symmetry plane, the mid-plane magnitude of σ_z for the $[0_{2n}/90_{2n}]_s$ laminate is considerably reduced from its peak at $\theta = 72°$, while for the $[90_{2n}/0_{2n}]_s$ laminate there is no significant reduction in value. Those elements nearest the hole edge for this laminate would be expected to move in the opposite fashion to those for the $[0_{2n}/90_{2n}]_s$ laminate, and comparison of Figure 20b) and Figure 38b) shows this to be true. For all of the angular positions around the hole, the interlaminar stress (σ_z) is negative for the $[0_{2n}/90_{2n}]_s$ laminate and positive for the $[90_{2n}/0_{2n}]_s$ laminate. Those elements within one laminate thickness of the curved free edge for the

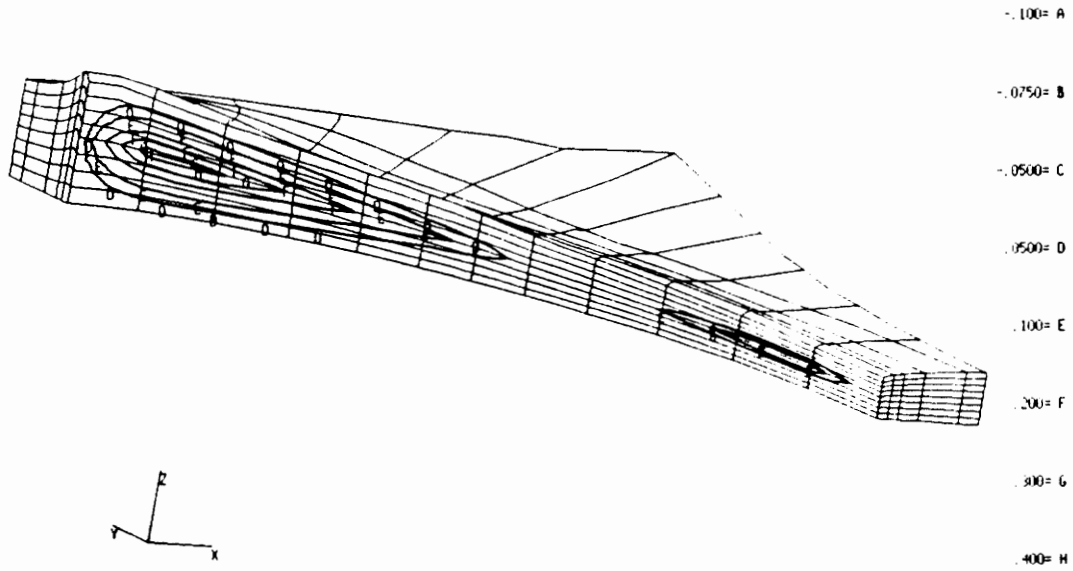

Figure 42. τ_{oz} **Contours for** $[0_{2n}/90_{2n}]_s$ **around Six-Inch Diameter Hole**

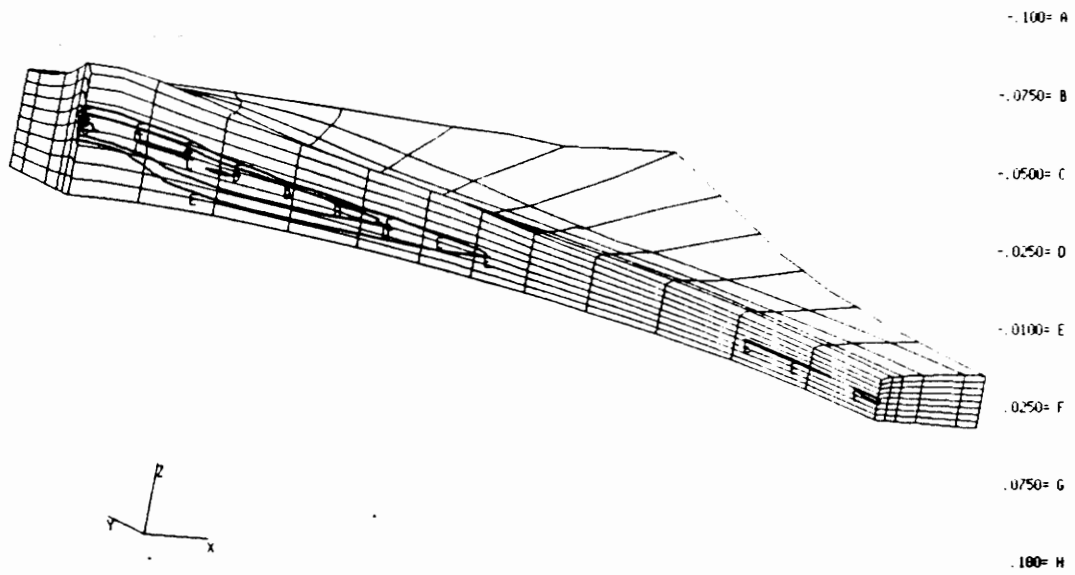

Figure 43. τ_{rz} **Contours for Curved Edge Model for** $[0_{2n}/90_{2n}]_s$ **around Six-Inch Diameter Hole**

$[0_{2n}/90_{2n}]_s$ laminate contracted toward the laminate, in the opposite direction to those elements under the influence of the global loading alone. Those same elements for the $[90_{2n}/0_{2n}]_s$ laminate expanded away from the mid-plane, further increasing the thickness of the plate.

In Figure 44b), the through-the-thickness distribution of $\tau_{\theta z}$ is presented for $[90_{2n}/0_{2n}]_s$ stacking sequence. As for the $[0_{2n}/90_{2n}]_s$laminate, this stress component changes shape and value smoothly through the laminate thickness and with angular position for a $[90_{2n}/0_{2n}]_s$ laminate, and, unlike the other stress component, is opposite in sign. Scrutinizing Figure 20b) and Figure 38b) closely reveals that the element boundaries immediately above and below the interface for these two models, which were initially perpendicular to the interface, have opposite slopes in their deformed state. The layers at the interface are sliding past each other in these two laminates, but in the opposite direction.

The interlaminar shear stress (τ_{rz}), is complex in nature. Large opposing gradients on either side of the interface are noticeable for both laminates (Figure 44c). From the difference in the sign of this stress for the stacking sequence reversal, the hole diameter changes would be expected to be different through the laminate thickness.

When the plies are dispersed, the interlaminar stresses were found to be lower in magnitude with a more complex distribution through the laminate thickness than for the straight free edge models. The curved edge models reflect this fact. All of the interlaminar stress distributions through the laminate thickness are presented in Figure 45. The interlaminar normal stress, in Figure 45a), for this laminate exhibits negatives values both at the mid-plane and at the interface at $z = 0.025$ in. As for the $[0_{2n}/90_{2n}]_s$ laminate, the $[0_n/90_n/0_n/90_n]_s$ laminate has its maximum magnitude near $\theta = 72°$. The 0° layers have low (near zero) σ_z values through the thickness of the laminate. The character of σ_z for $[0_n/90_n/0_n/90_n]_s$ laminate around the hole at the mid-plane is similar to the $[0_{2n}/90_{2n}]_s$ laminate, but reduced in magnitude.

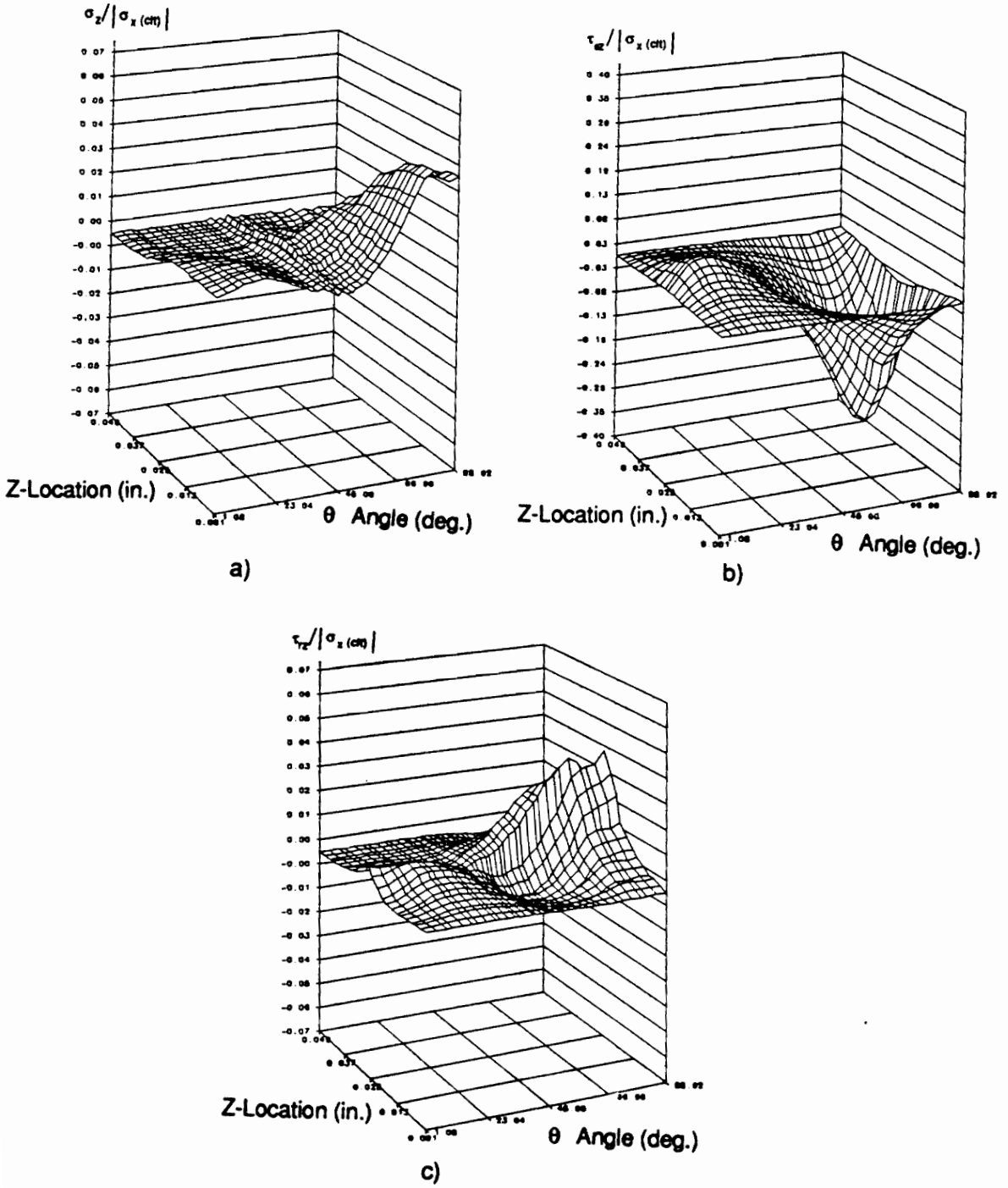

Figure 44. Stresses for Curved Edge Model for $[90_{2n}/0_{2n}]_s$ around Six-Inch Diameter Hole: Through-the-Thickness a) σ_z b) $\tau_{\theta z}$ c) τ_{rz}

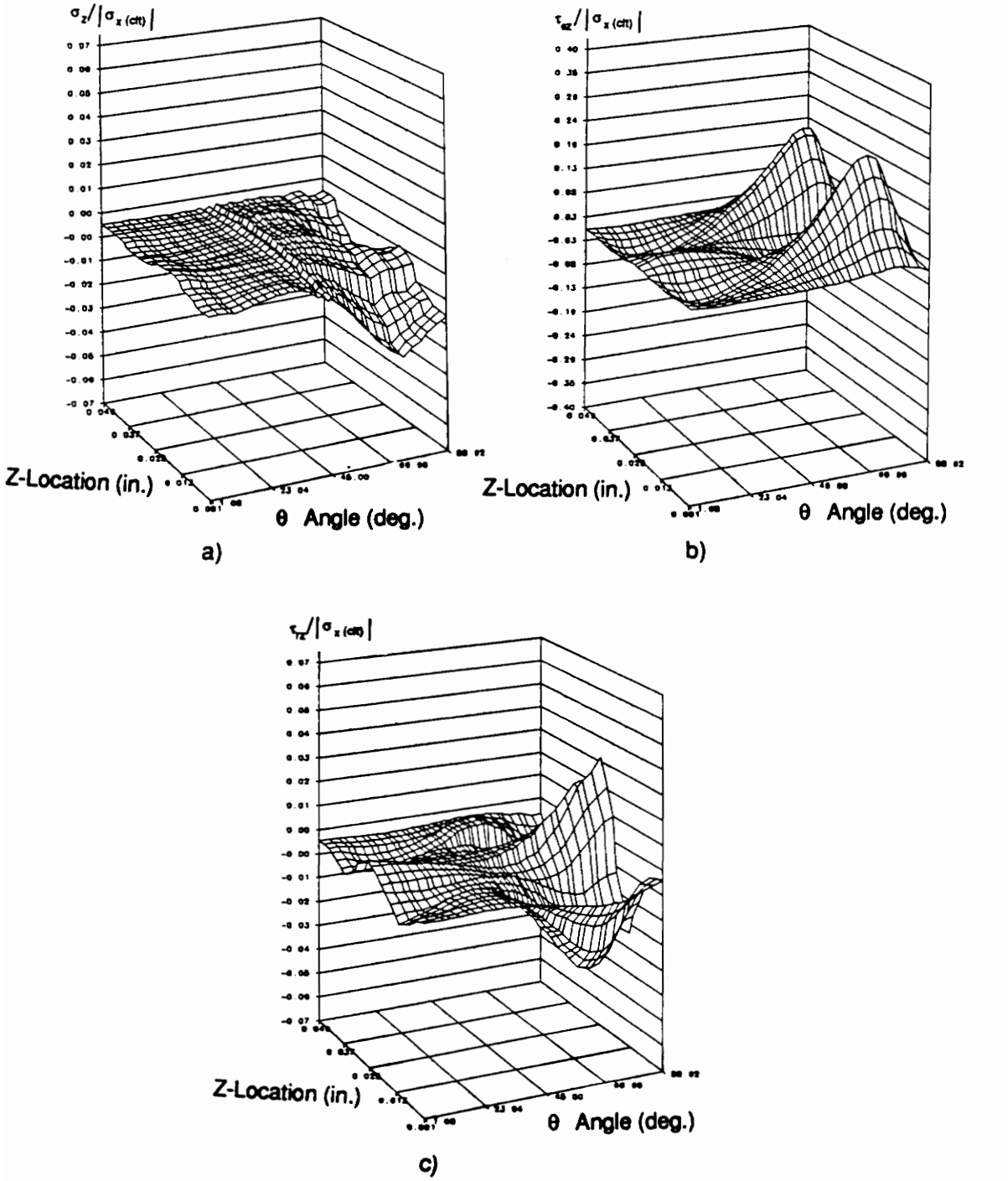

Figure 45. Stresses for Curved Edge Model for Dispersed Lay-up with Six-Inch Diameter Hole: Through-the-Thickness a) σ_z b) $\tau_{\theta z}$ c) τ_{rz}

Due to the dispersal of the 0° and 90° layers, two distinctive peaks can be found at z = 0.0125 in. and z = 0.0375 in. for the interlaminar shear stress ($\tau_{\theta z}$) with an obscured valley at the z = 0.025 in. interface (Figure 45b). Those 0°/90° interfaces exhibit peaks similar to the $[0_{2n}/90_{2n}]_s$ laminate, while the one with the 90°/0° interface, as expected, has valleys like the $[90_{2n}/0_{2n}]_s$ laminate. Reduction in the magnitudes of this stress component are noticeable for each of the interfaces, in comparison to the clustered laminate, while the deformed view of the local model in Figure 39b) reveals that the element boundaries, which were originally perpendicular to the interfaces, have different slopes at the interfaces.

The remaining interlaminar shear stress (τ_{rz}) has a more complex through-the-thickness stress distribution around the hole because of the larger number of interfaces through the thickness than the other laminates studied. The peak positive value is lowered slightly for this laminate, when compared to that for the $[90_{2n}/0_{2n}]_s$ laminate, while there is little difference in the peak negative value from Figure 45c). Hole diameter change through the laminate thickness for $[0_n/90_n/0_n/90_n]_s$ is lower in magnitude but with several sign reversals.

Direct comparison of the interlaminar normal stress for changing stacking sequence at those integration points near the mid-plane is presented in Figure 46. While the stress distributions for the $[0_{2n}/90_{2n}]_s$ and $[90_{2n}/0_{2n}]_s$ laminates are opposite in sign, their absolute magnitudes are not identical. There is a reduced peak absolute magnitude for $[90_{2n}/0_{2n}]_s$ at a slightly larger value of θ than for the $[0_{2n}/90_{2n}]_s$ laminate. In addition, while the stresses nearest the local x = 0 symmetry plate decay in magnitude from the peak stress for the $[0_{2n}/90_{2n}]_s$ laminate, this laminate does not have the same degree of decay. As expected, the dispersed laminate stress distribution is reduced in magnitude, but with the same character as the $[0_{2n}/90_{2n}]_s$ laminate for this stress component near the laminate mid-plane.

Since the only interface common to all three laminates is at z = 0.025 in., direction comparison between the laminates is determined at that location for the interlaminar shear stresses ($\tau_{\theta z}$ and τ_{rz}). These are presented in Figure 47a) and b). For $\tau_{\theta z}$, reversing the stacking sequence produces

an exact reversal in sign of the stresses. At $z = 0.025$ in. the 90° ply is above the interface, while the 0° ply is below for the dispersed laminate, so the stress distribution is expected to resemble the $[90_{2n}/0_{2n}]_S$ laminate, but with reduced magnitudes. This reduction is found to be nearly two-thirds at the peak stress location as presented in Figure 47a).

Figure 47b) contains the information for the three lamination sequences about the remaining interlaminar shear stress (τ_{rz}) at the $z = 0.025$ in. interface. Recall that these stresses were originally calculated at the integration points on either side of the interface, and that average of these values are presented. As for the other interlaminar shear stress, the reversal in the stacking sequence produces a mirror image distribution about $\tau_{rz} = 0$. While the dispersal of plies reduced the magnitude of the distribution of the $[90_{2n}/0_{2n}]_S$ laminate, unlike the other shear stress, its character was not identical. τ_{rz} for the $[0_n/90_n/0_n/90_n]_S$ laminate continued to increase in magnitude at the larger angular positions until it reached $[90_{2n}/0_{2n}]_S$ laminate distribution.

For the different hole sizes, presentation of the through-the-thickness distributions of the stress components will be omitted since they closely resemble those for the six-inch diameter hole. Instead, direct comparison of the stresses is presented next. The interlaminar normal stress near the mid-plane of the laminate is presented in Figure 48 for the $[0_{2n}/90_{2n}]_S$ stacking sequence and all three hole diameters. The location of the largest magnitude stress moves toward the local $x = 0$ symmetry plane with increasing hole size. The six-inch hole exhibits a lower stress magnitude than either of the hole cases, with the one-inch hole largest. Stress relief due to hole size in a finite width plate is believed to cause this phenomenon. Since the straight free edge does not strongly resist the outward bowing because of the hole, the in-plane stress components around the hole are redistributed, and hence, lower interlaminar stresses result. While there is some stress relief with the three-inch hole, there is none for the one-inch hole, which explains the shift in peak stress location and value. The lack of stress relief for the one-inch hole appears to further manifest itself in this distribution since there are both positive and negative stresses, while those for the other holes are all negative. The one-inch diameter hole is unable to resist the out-of-plane expansion of the plies at

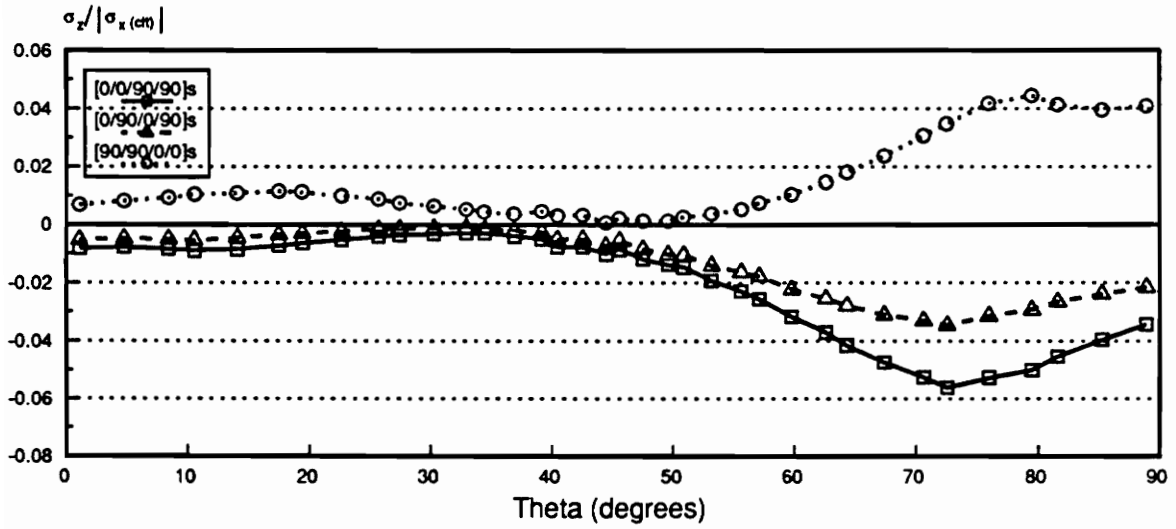

Figure 46. Stresses for Curved Edge Model for Different Stacking Sequences Around Six-Inch Hole: a) σ_z at Mid-plane

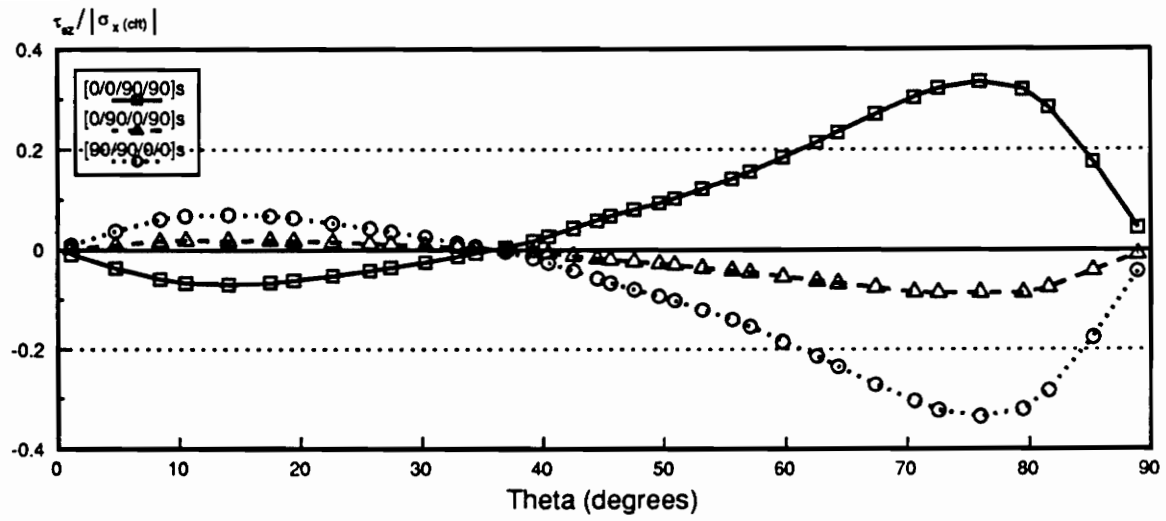

a)

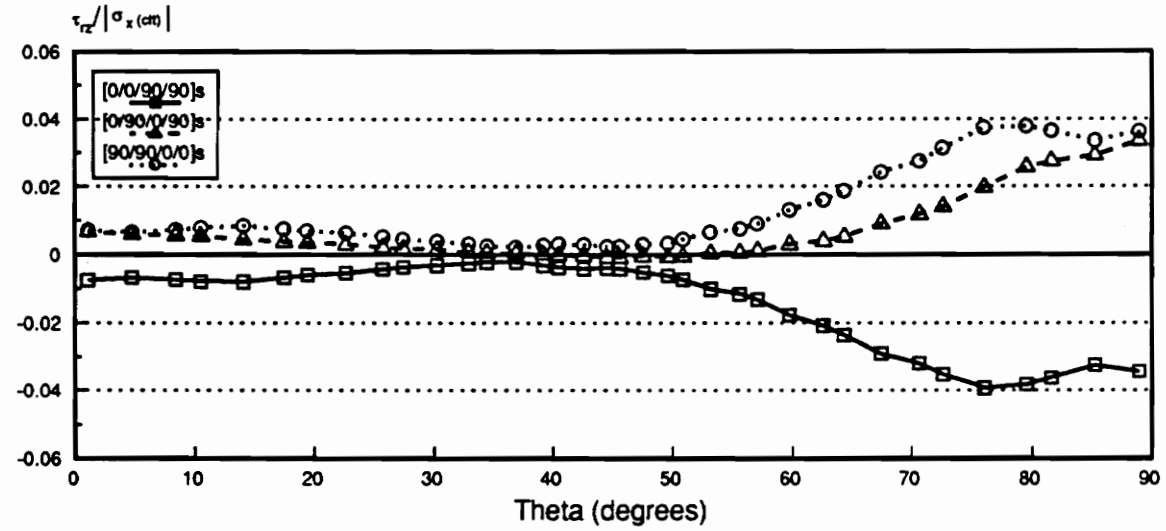

b)

Figure 47. **Stresses for Curved Edge Model for Different Stacking Sequences Around Six-Inch Hole:** a) $\tau_{\theta z}$ at z = 0.025 in. b) τ_{rz} at z = 0.025 in.

the local $x = 0$ symmetry plane through the interlaminar strain state. A closer examination of the deformed model for this case corroborates this.

The influence of decreasing hole diameter in a finite width plate on the interlaminar shear stresses is presented at at the $z = 0.025$ in. interface in Figure 49. From Figure 49a), all three hole diameters exhibit the same character for $\tau_{\theta z}$, with the location of the maximum absolute value of the stress moving closer to the $\theta = 90°$ as the hole diameter increases. The maximum magnitude for the three-inch diameter hole model is slightly greater than the other holes, and this suggests that there is a critical hole size in the laminate in a finite width plate. The results for the remaining interlaminar stress component, (τ_{rz}) are found in Figure 49b). The peak locations move toward the local $x = 0$ symmetry plane with increasing hole diameter. The three-inch diameter hole is larger in absolute magnitude than the six-inch diameter hole for all angular positions except those greater than 75° and less than 90°. Once again the one-inch diameter hole exhibits both positive and negative shearing values suggesting that there is no stress relief for this hole size. Indeed, its character does not resemble the larger holes as closely as the other stresses. Between $\theta = 20°$ and 70°, its absolute magnitude is larger than other holes.

4.4 Conclusions for In-Plane Compression of Cross-Ply Laminates

A number of conclusions can be drawn from the analyses discussed, both relative to the state of stress around large holes in thin laminates and to the application of two-dimensional to three-dimensional global/local stress analysis in laminated cross-ply composites. The global/local conclusions will be presented in a later following the development and application of a global/local technique on laminates with off-axis plies.

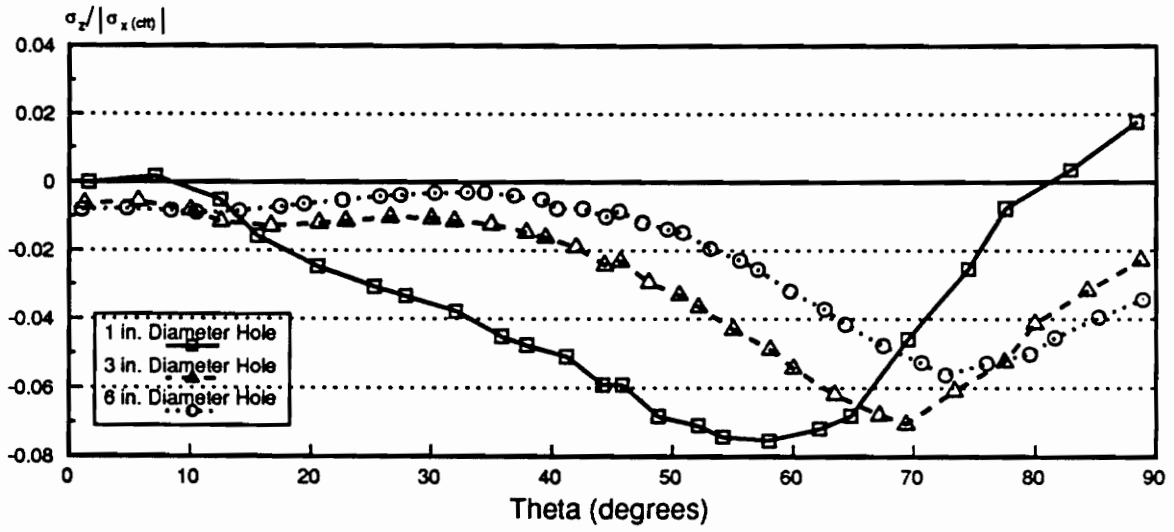

Figure 48. σ_z for $[0_{2n}/90_{2n}]_s$ near Mid-plane Around Different Diameter Holes

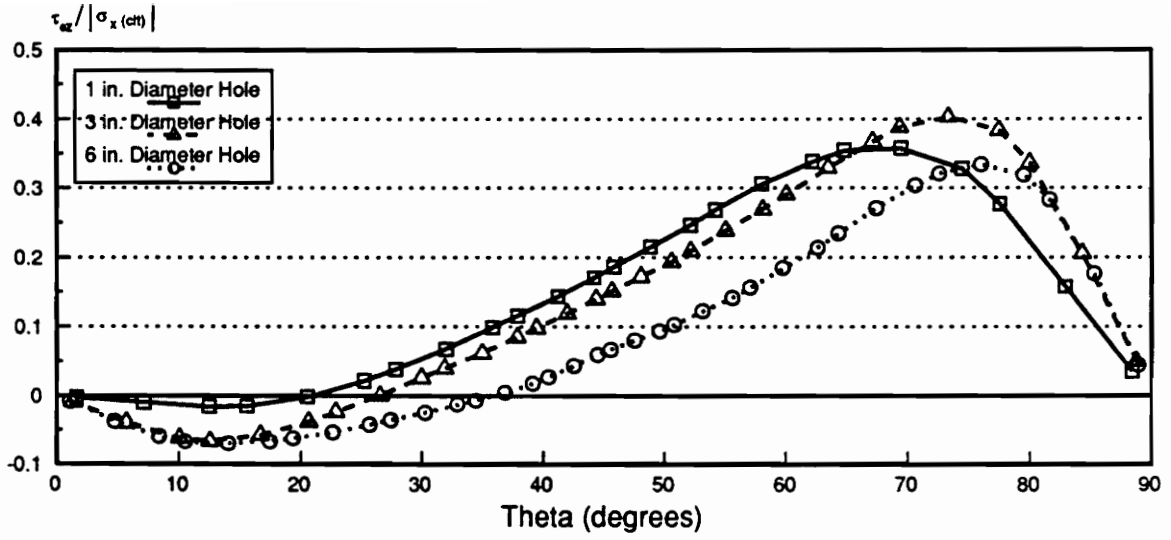

a)

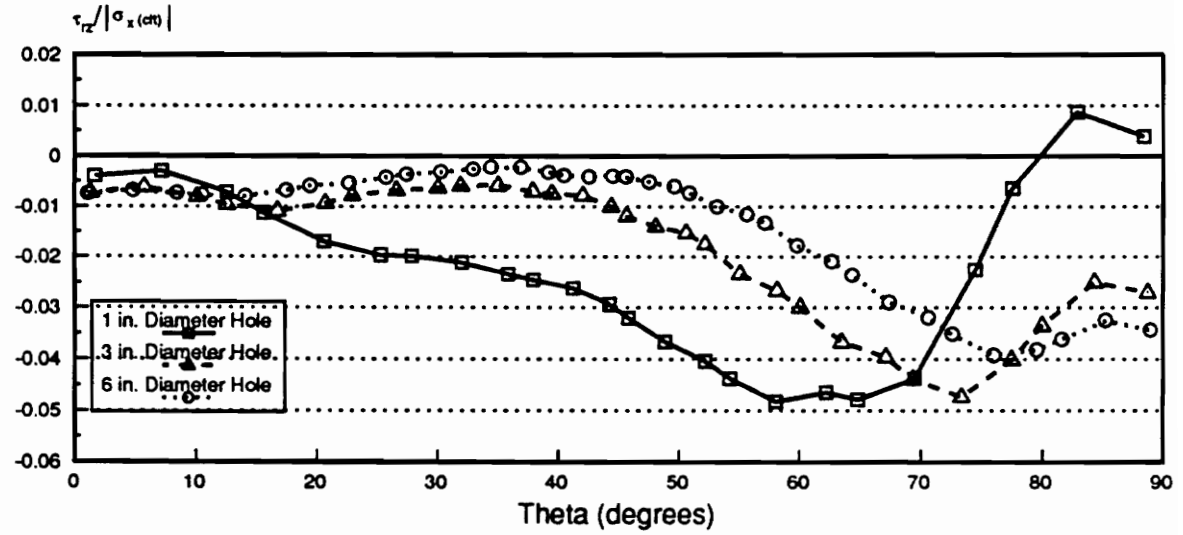

b)

Figure 49. Interlaminar Shear for $[0_{2n}/90_{2n}]_s$ at z = 0.025 in. Interface for Different Diameter Holes: a) $\tau_{\theta z}$ b) τ_{rz}

Interlaminar effects at straight free edges for plates without holes have been considered extensively in the past. A comparative study done by Vidussoni (1988) on the effect of hole size on the interlaminar stress state at the straight free edge and around a hole for plates with holes was hampered by a lack of computer resources. Both the effect of stacking sequence for a large hole at the free edge and hole size for a particular laminate were studied in this thesis in detail.

When considering different plates with large holes, it was found that dispersing the 0° and 90° layers in cross-ply laminates lowered the overall magnitude of the interlaminar normal and shear stresses, but did not alter the overall shape of the stress distribution for a particular interface along the straight free edge. At the mid-plane the $[0_n/90_n/0_n/90_n]_s$ laminate resembled the $[0_{2n}/90_{2n}]_s$ laminate, as expected, while the $[90_{2n}/0_{2n}]_s$ distribution was not an exact reversal in sign for the interlaminar normal stress. At the $z = 0.025$ in. interface, the staggered laminate has a 90°/0° interface and thus its shear stress distribution at this interface was like the $[90_{2n}/0_{2n}]_s$ laminate and reduced in magnitude. Reversing the stacking sequence produced an exact reversal in sign of the interlaminar shear stress at the interface.

At the straight free edge, the effect of increasing hole diameter reduced the magnitude of the stress, but not its in-plane distribution for a particular z-location. The six-inch diameter hole in a 12-in. wide plate exhibits a large stress reduction at the centerline of the hole, but increases the interlaminar stresses at the far edge of the local model. The one-inch diameter hole exhibited no effect on the straight edge nearby, while the influence attributable to the three-inch hole was between those of the other hole diameters.

The investigation of the curved edge region was also completed by Vidussoni (1988) for both stacking sequence and hole size, but concern was expressed about the computer resources. Considerable refinement around the hole was done for the present study, and the global/local interface was moved closer to the curved free edge for plates with smaller holes. A stacking sequence study for the largest hole size, and a hole size study for one of the laminates was completed. Thickening of laminates with holes in compression was not constant around the hole, for all of the stacking

sequences. The degree of thickening varied with layup, hole diameter, and position around the hole. For applications when laminate thickness is constrained, as in the case of rivets which are set into the laminate, this is a source of potential damage.

Reversal of stacking sequence for interlaminar stress components produced a reversal in sign over the laminate, but whether this is an exact reversal is dependent on the location in the laminate and the stress component in question. The interlaminar normal stress at the integration points nearest the mid-plane were not exactly reversed. The interlaminar shear stresses were a mirror image for the z = 0.025 in. interface. While "dispersion" of plies with different ply angles reduces the absolute value of certain stress components, its distribution is directly dependent on the order of the layers about the z-location in question.

For the interlaminar normal stress around holes near the mid-plane, the effect of hole size is clear. Stress values around the hole for large holes are reduced in magnitude, and peak stresses are shifted in location. Stress relief at the straight free edge is believed to be responsible, because the one-inch diameter hole which has no effect on the stress field at the straight edge, experienced both a positive and negative stress around the hole. There appears to be a "critical" hole size in this laminate, where the interlaminar shear stress ($\tau_{\theta z}$) around the hole is maximized, as evidenced by the larger stresses for a three-inch diameter hole as compared to a one- or a six-inch diameter hole in the laminates presented. The hole effect for the remaining interlaminar shear stress (τ_{rz}) is less clear. Examination of three-dimensional results indicates that the reduction in hole diameter for laminates loaded in compression is not constant for all plies. Should the hole contain a fastener, this could result in bearing failures and fiber crushing in the plies tending to have larger displacements.

5.0 Angle-ply and Quasi-isotropic Laminates Under Compression

5.1 Introduction

The global/local analysis technique discussed and presented for symmetric cross-ply laminates in the previous chapter is a specific implementation of a general analysis tool. Development and demonstration of this method as applied to laminates with off-axis plies, e.g. angle-ply and quasi-isotropic laminates, will be presented in this chapter. The lamination sequences considered include several $[\pm\Theta]_S$ laminates, one $[\pm\Theta_1/\pm\Theta_2]_S$ laminate and one quasi-isotropic laminate. Several of the assumptions used in the global/local procedure for the cross-ply laminates are invalid for off-axis ply laminates. There are fewer symmetry planes to exploit, and the global strain state affects the local model geometry differently than the cross-ply laminates. An example of erroneously modeling the straight edge is compared to a correct local straight edge model to demonstrate the need to understand this global/local two-dimensional to three-dimensional finite element analysis procedure and its limitations. The interlaminar response for the different stacking sequences is then determined for a finite-width plate with the large hole, followed by a study of the influence of the size

of a hole in a finite-width plate. Attempts to verify this technique with a complete three-dimensional analysis were unsuccessful, because the size of the resulting model was intractable. Verification of the technique is done on a qualitative basis by comparing the interlaminar response determined with this technique to that determined by other methods for laminates with off-axis plies.

5.2 *Problem Description and Approach*

The plates under consideration include laminated angle-ply and quasi-isotropic laminates with a central circular hole, and the following ply orientations: $[\pm 15_{2n}]_s$, $[\pm 45_{2n}]_s$, $[\pm 15_n/\pm 45_n]_s$, and $[0_n/\pm 45_n/90_n]_s$ with n equal to one. All were 18 in. long, 12 in. wide and 0.1 in. thick. An investigation of the interlaminar stress fields for a constant width plate with different hole diameters was performed for the $[\pm 15_{2n}]_s$ laminate. Three different hole diameters were considered: six, three, and one inches. The $[\pm 15_{2n}]_s$ laminate with a six-inch diameter hole was modeled with a complete three-dimensional model and also used to demonstrate the correct and incorrect way to apply this global/local analysis method to the straight free edge region.

Each plate was analyzed with a global model which contains five equal-sized rings of elements within the central square region of the plate surrounding the hole, and a graded element distribution along the straight edge with the maximum y-dimension. This has been described in detail in the Common Features Section. Table 6 contains information about the characteristics of each global model, including the diameter of the hole, the number of nodes, the total number of degrees of freedom, the number of elements in the entire model and around the hole area, the number of radial lines of nodes around the hole (spokes), and the total computational time for the model in question. The undeformed and deformed global grids for the $[\pm 15_{2n}]_s$ stacking sequence are presented in Figure 50a) and b), Figure 51a) and b), and Figure 52a) and b) for the plates with six-, three-, and

one-inch diameter holes, respectively. The undeformed and deformed global grids for the $[\pm 45_{2n}]_s$, $[\pm 15_n/\pm 45_n]_s$, and the $[0_n/\pm 45_n/90_n]_s$ laminates with a six-inch diameter hole are in Figure 53a) and b), Figure 54a) and b), and Figure 55a) and b), respectively.

Table 6. Two-Dimensional Angle-Ply and Quasi-isotropic Compression Global Model Characteristics

Hole Dia. (in.)/ Layup	Nodes	Degrees of Freedom	Elements		Spokes Around Hole	Global Solution Time (CPU Seconds)
			Total	Hole		
1.0/ $[\pm 15_{2n}]_s$	3,208	19,248	768	160	64	439.9
3.0/ $[\pm 15_{2n}]_s$	2,824	16,944	672	200	80	437.7
6.0/ $[\pm 15_{2n}]_s$	2,440	14,640	576	240	96	304.0
$[\pm 45_{2n}]_s$						351.0
$[\pm 15_n/\pm 45_n]_s$						309.3
$[0_n/\pm 45_n/90_n]_s$						429.2

A local coordinate system with its origin at the center of the plate was chosen and used for all the two-dimensional and three-dimensional models with an angle (θ) defined as a rotation about the z-axis from the local x-axis toward the y-axis (Figure 56). The local $z = 0$ plane was coincident with the laminate mid-plane. Because of the symmetry of the lamination sequences and the applied global loading about the mid-plane, this is a plane of symmetry for all models. The full straight edge model extends between both ends of the plate, while the elements bounded by the rectangular elements surrounding the hole form the local curved edge model, as shown in Figure 56 and Figure 57.

The displacement application procedures for these local models are different from the cross-ply models. There are no local $x = 0$ and local $y = 0$ symmetry planes, so the ends of the local straight edge model are coincident with the load application regions for the global model for laminates with off-axis plies. These ends are clamped and undergo compressive loading by displacing the global

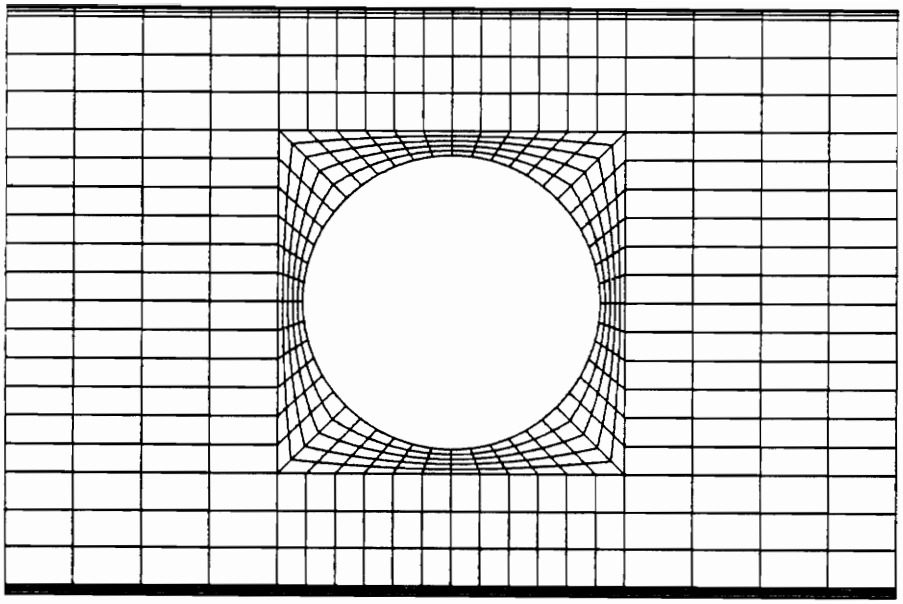

a)

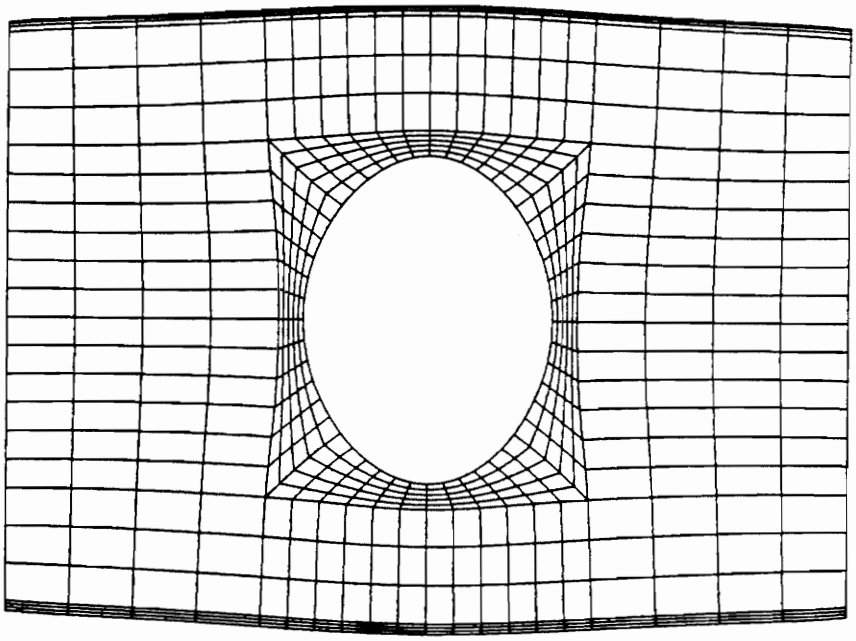

b)

Figure 50. Global Grids for $[\pm 15_{2n}]_s$ in Compression with Six-inch Diameter Hole: a) Undeformed b) Deformed

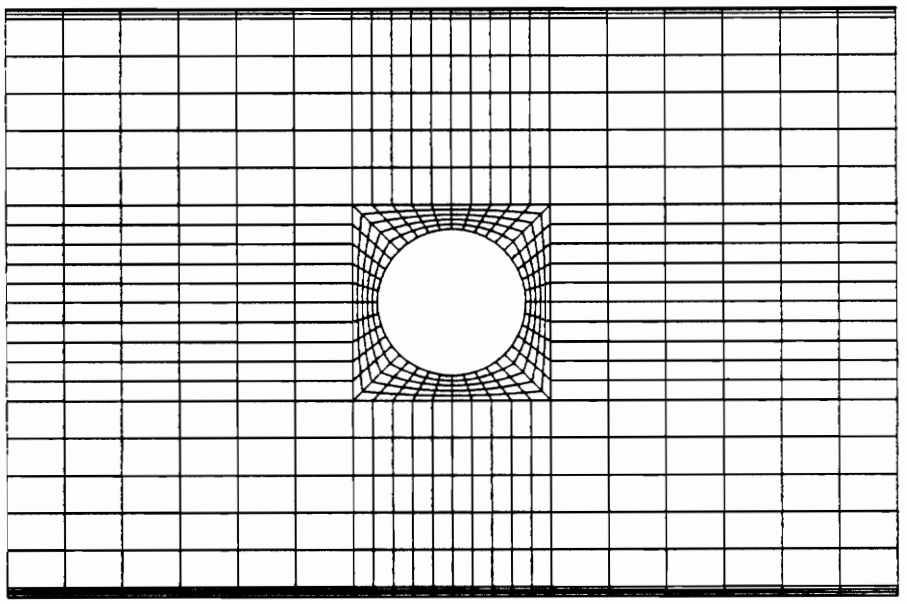

a)

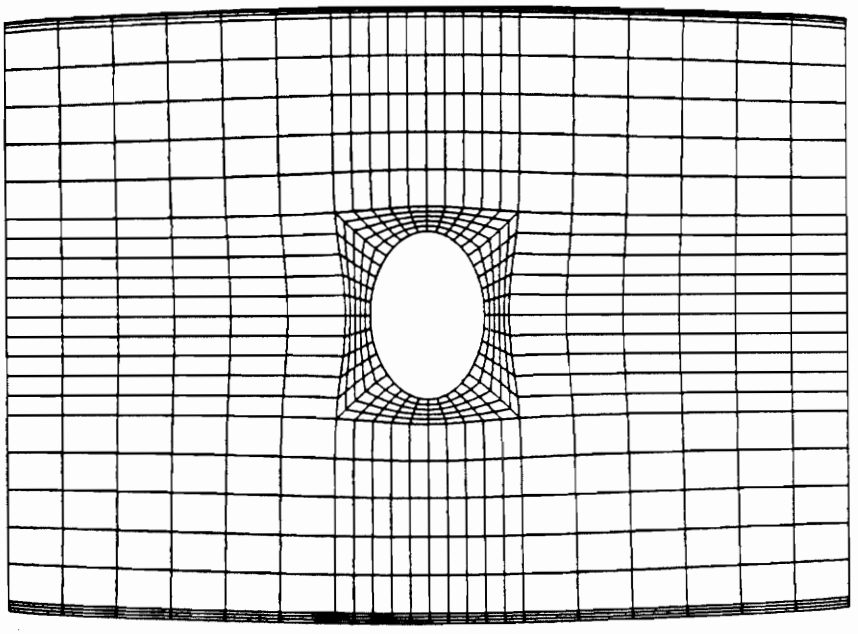

b)

Figure 51. Global Grids for $[\pm 15_{2n}]_s$ in Compression with Three-Inch Diameter Hole: a) Undeformed b) Deformed

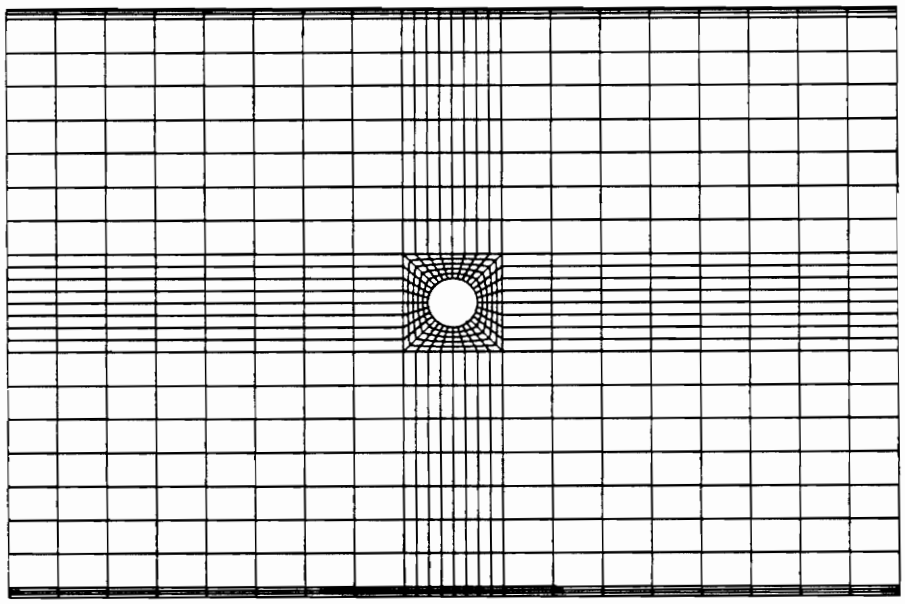

a)

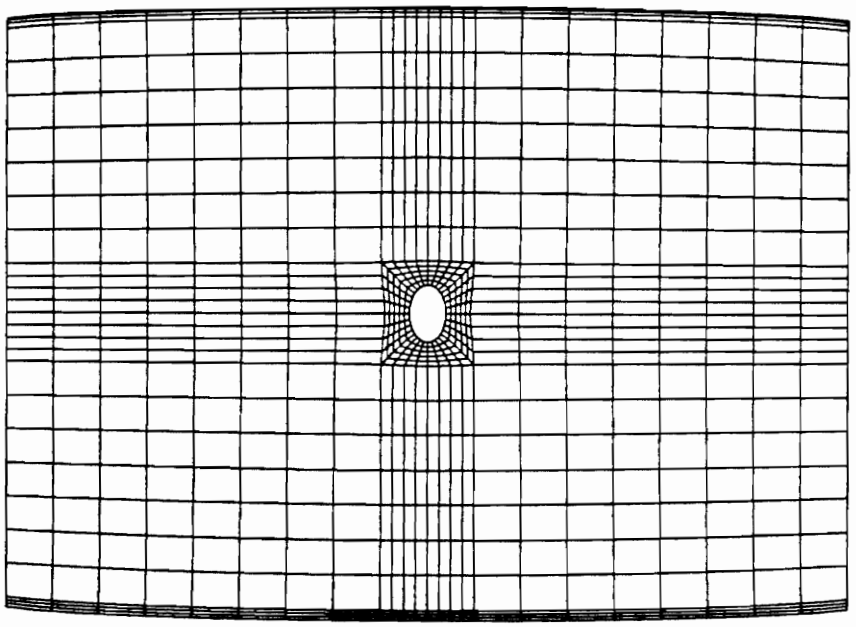

b)

Figure 52. Global Grids for $[\pm 15_{2n}]_s$ in Compression with One-Inch Diameter Hole: a) Undeformed b) Deformed

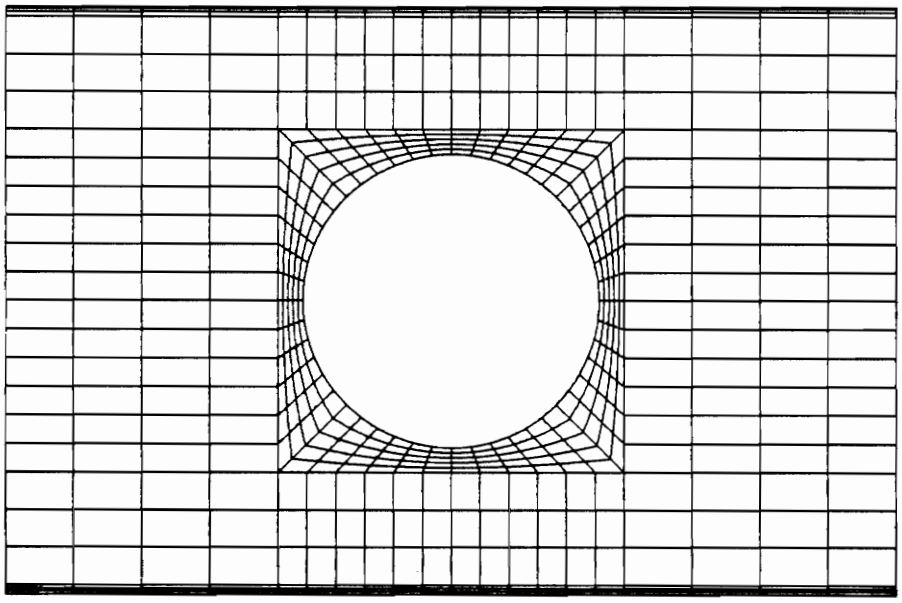

a)

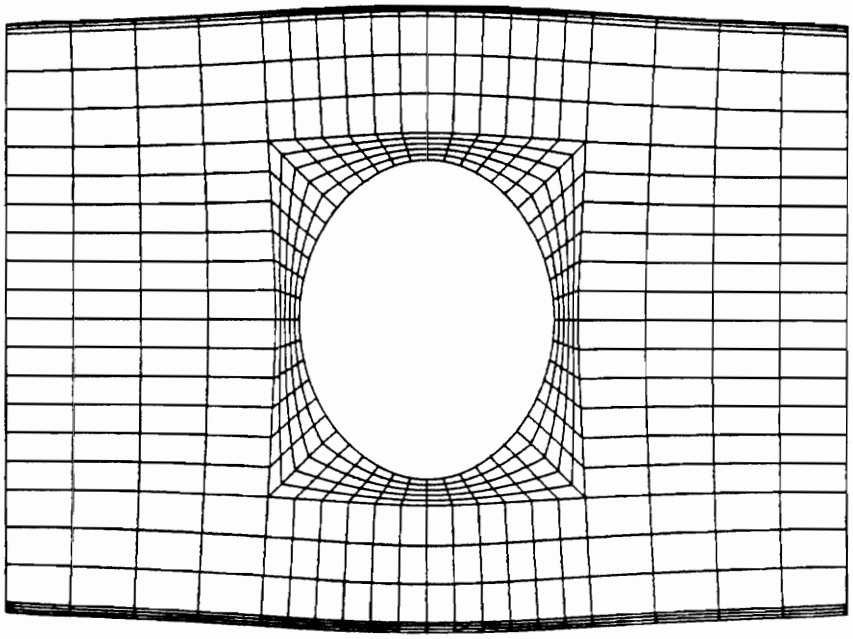

b)

Figure 53. Global Grids for $[\pm 45_{2n}]_s$ in Compression with Six-Inch Diameter Hole: a) Undeformed b) Deformed

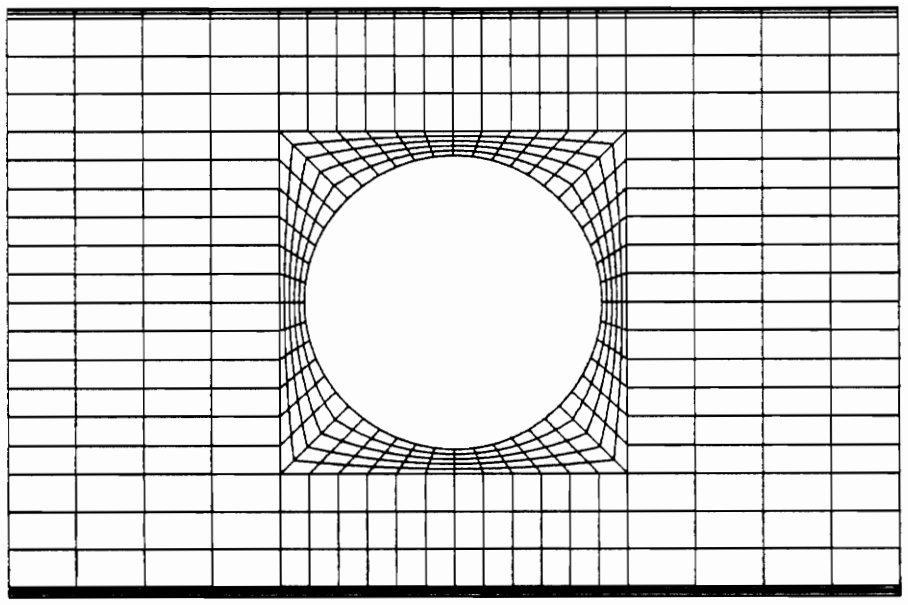

a)

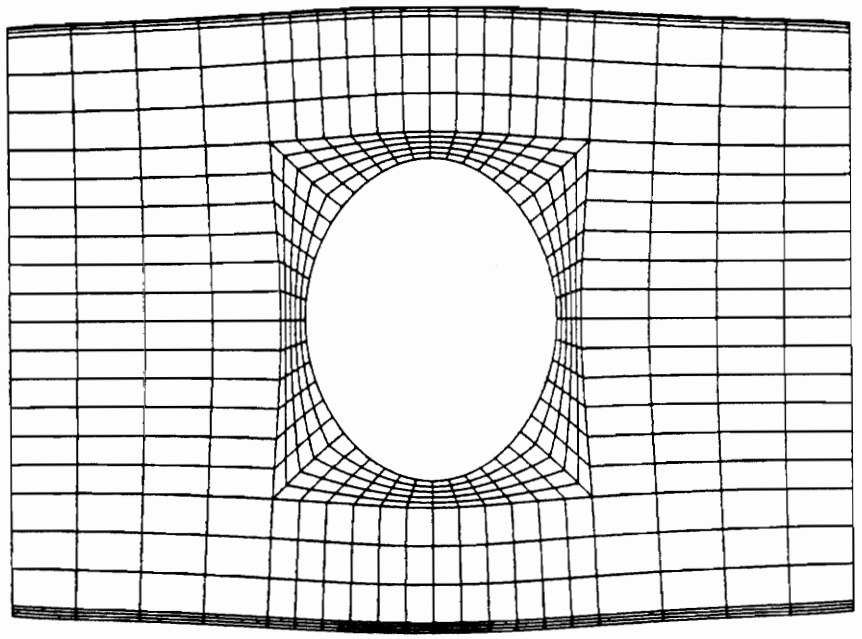

b)

Figure 54. Global Grids for $[\pm 15_n/\pm 45_n]_s$ in Compression with Six-Inch Diameter Hole: a) Undeformed b) Deformed

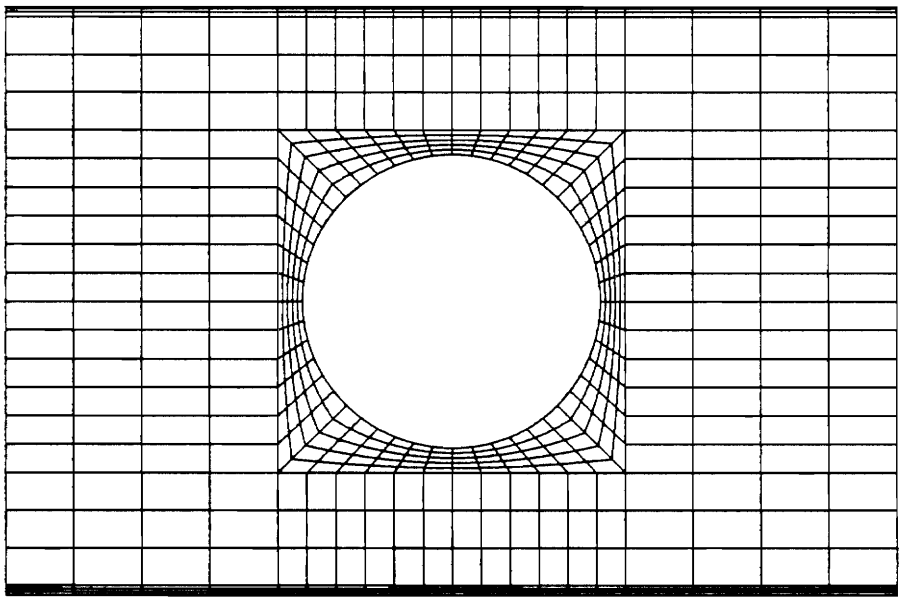

a)

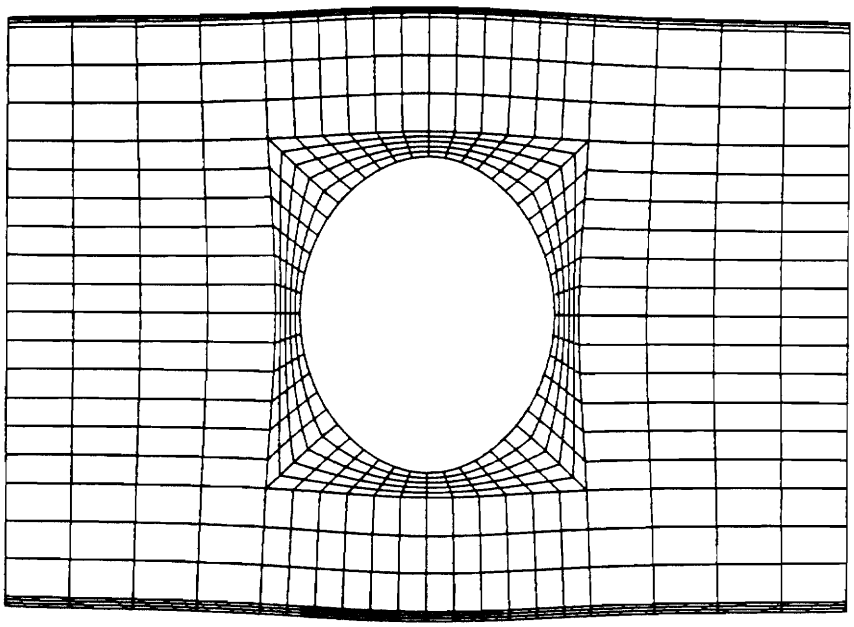

b)

Figure 55. Global Grids for $[0_n/\pm 45_n/90_n]_s$ in Compression with Six-Inch Diameter Hole: a) Undeformed b) Deformed

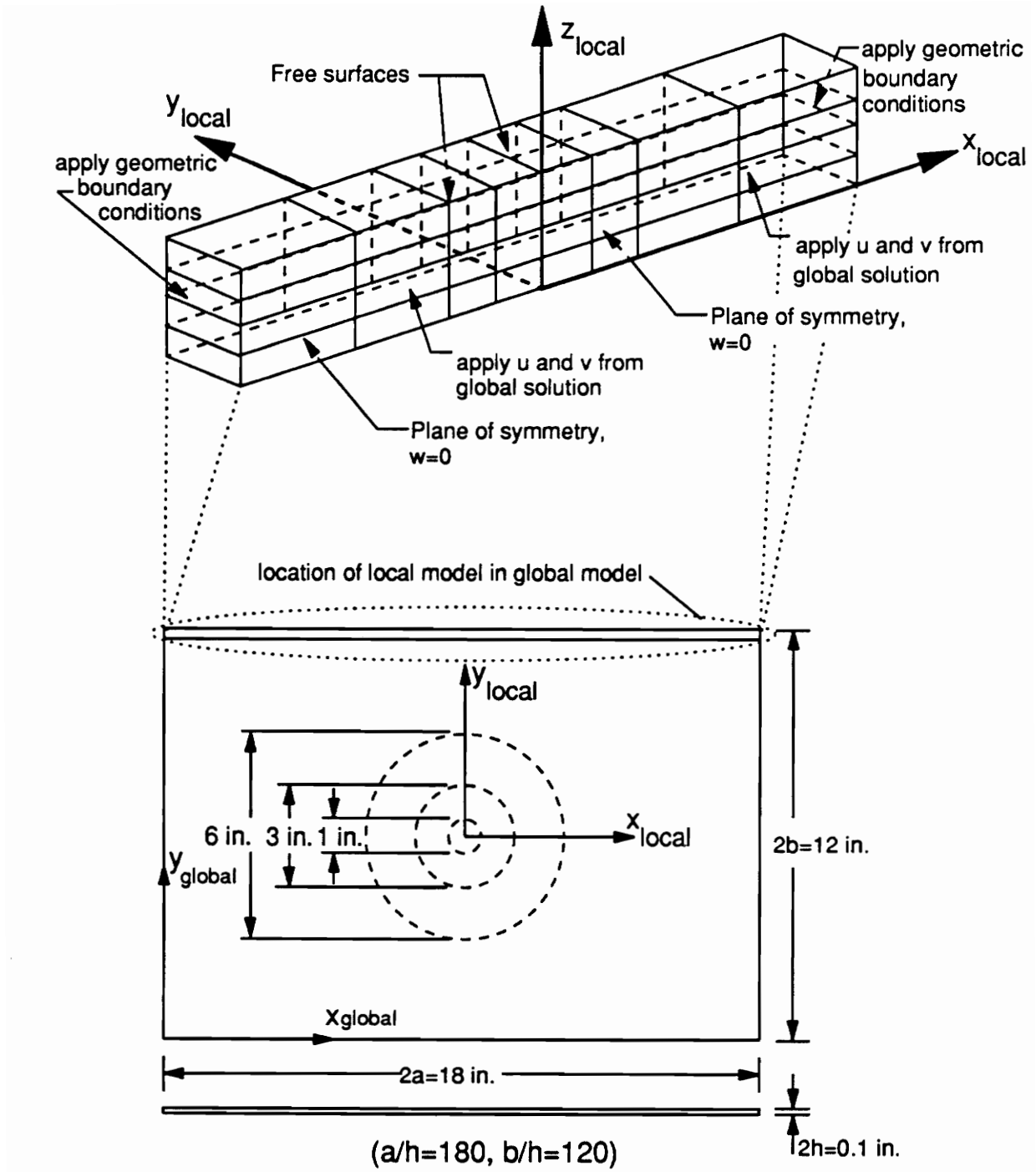

Figure 56. Local Straight Edge Model Displacement Application for Laminates with Off-Axis Plies in Compression

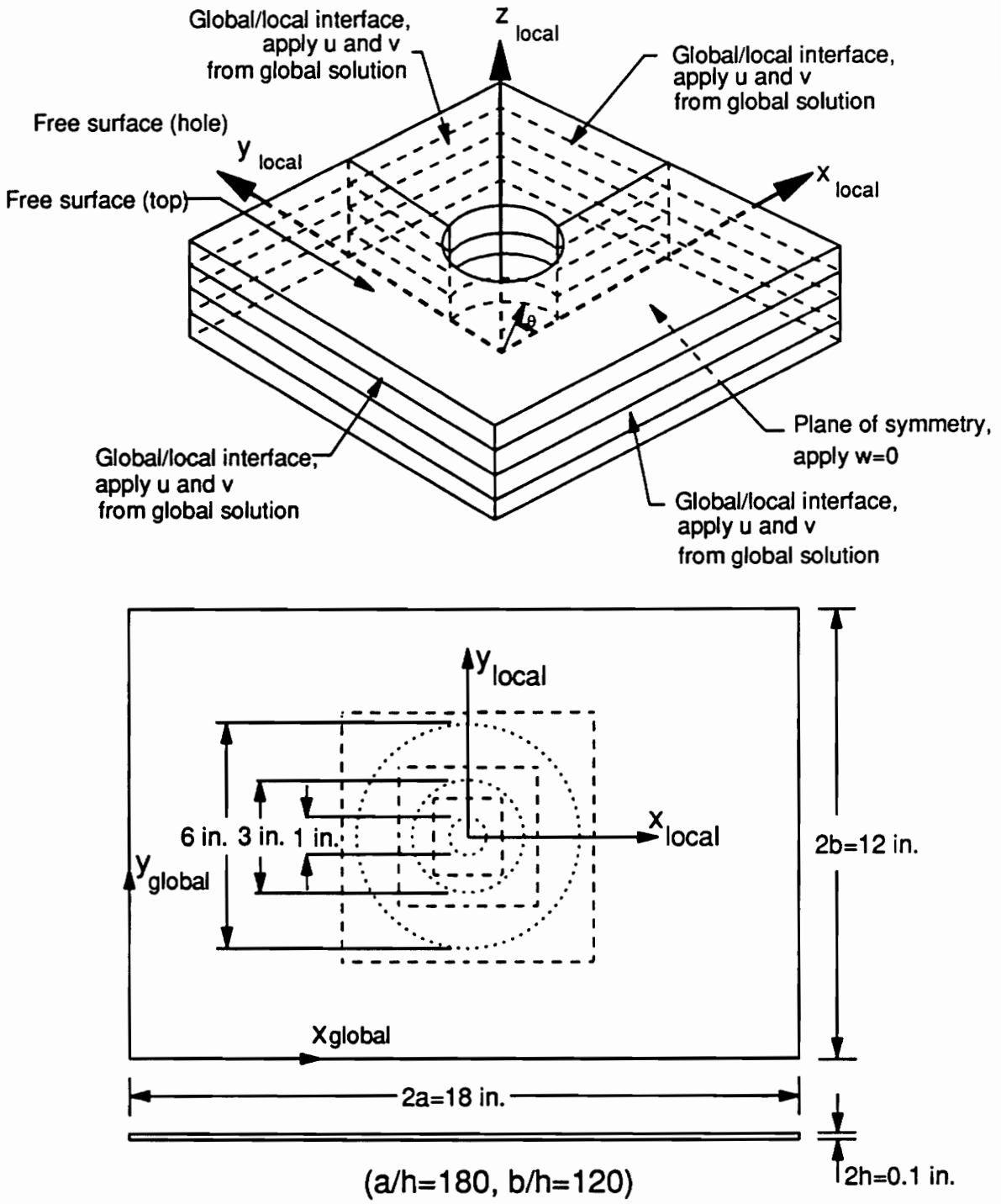

Figure 57. Local Curved Edge Model Displacement Application for Laminates with Off-Axis Plies in Compression

x = 0 in. end toward the global x = 18 in. end by 0.01 in. as in the global model. Along the global/local interfaces, the in-plane global displacement components were applied constant through the thickness directly to each local straight edge model. Like the cross-ply local models, the in-plane stress gradients were low and there was no expected rotation or distortion of the normal lines to the mid-plane in the regions where the global/local interfaces were located. These locations were described in the Common Features Section and are identified in Figure 56 and Figure 57 for both areas of interest. The local z = 0 symmetry plane was fixed in the z-direction for all of the models. There were no applied conditions at any nodes along any of the free edges of the local models which did not coincide with the global/local boundaries or the local z = 0 symmetry plane.

For cross-ply laminates under in-plane loading, the only interlaminar stress components which arise during the transition from the internal stress state to the traction-free straight edge are the interlaminar normal stress (σ_z) and interlaminar shear stress (τ_{yz}). With no shear in the x-z plane, ($\gamma_{xz} = 0$), the application of constant x-displacements through the thickness in the boundary layer region would not violate any three-dimensional kinematic conditions. Therefore, an arbitrarily located cut through the boundary layer could be made. This allowed the analyst to limit the local models to only the region of interest and is not true for any laminates with off-axis plies, like angle-ply or quasi-isotropic laminates, or any loading situation which would cause shearing in a plane where constant displacements are applied. The error in arbitrarily locating a global/local interface through such a region to create a reduced local model is demonstrated for a $[\pm 15_{2n}]_s$ laminate with a six-inch diameter hole.

As with the cross-ply models, the reduced straight edge model was designed to have the same x-direction dimension as its corresponding local curved edge model. The displacement application procedure for these reduced models is similar to the full straight edge models, except for the treatment of the interfaces cutting through the boundary layer. The procedure is presented schematically in Figure 58. This is the same displacement application procedure used for the cuts through the boundary layer for the cross-ply laminates in compression. Since the two-dimensional global model yields no information about the through-the-thickness behavior of the laminate, only an 'averaged'

response at the laminate mid-plane and to enforce the clamped end condition, these displacements must be applied constant through the thickness. At each end of the reduced local model, planes of nodes pass through the boundary layer and the applied x-direction displacements were constant through the thickness. On the other hand, y-direction displacements were not applied along the cut, to avoid inhibiting the three-dimensional interlaminar effect. A comparison of the displacements for the full (correct) and reduced (incorrect) local straight edge models is presented in the Results and Discussion section.

Because of the existence of off-axis plies, the entire in-plane area of the plate must be modeled globally, since the only plane of symmetry is at the laminate mid-plane. This was also true for the complete three-dimensional model. To allow stress field comparison at the same locations, the common region modeled by the complete and local models had identical nodal distributions. Figure 59 is a schematic representation of the complete three-dimensional model displacement application procedure. Presented in Table 7 is the computer resources required for the complete three-dimensional model, and the global/local solutions for the full straight edge, the incorrect straight edge, and the curved edge for the $[\pm 15_{2n}]_S$ laminate with a six-inch diameter hole. Table 7 contains the information that quantitatively demonstrates that the global/local modeling technique will undoubtedly be more efficient than a complete three-dimensional analysis, since there are nearly two-thirds more nodes in it than the largest local model. Its solution is currently intractable, and the global/local modeling procedure provides an attractive alternative.

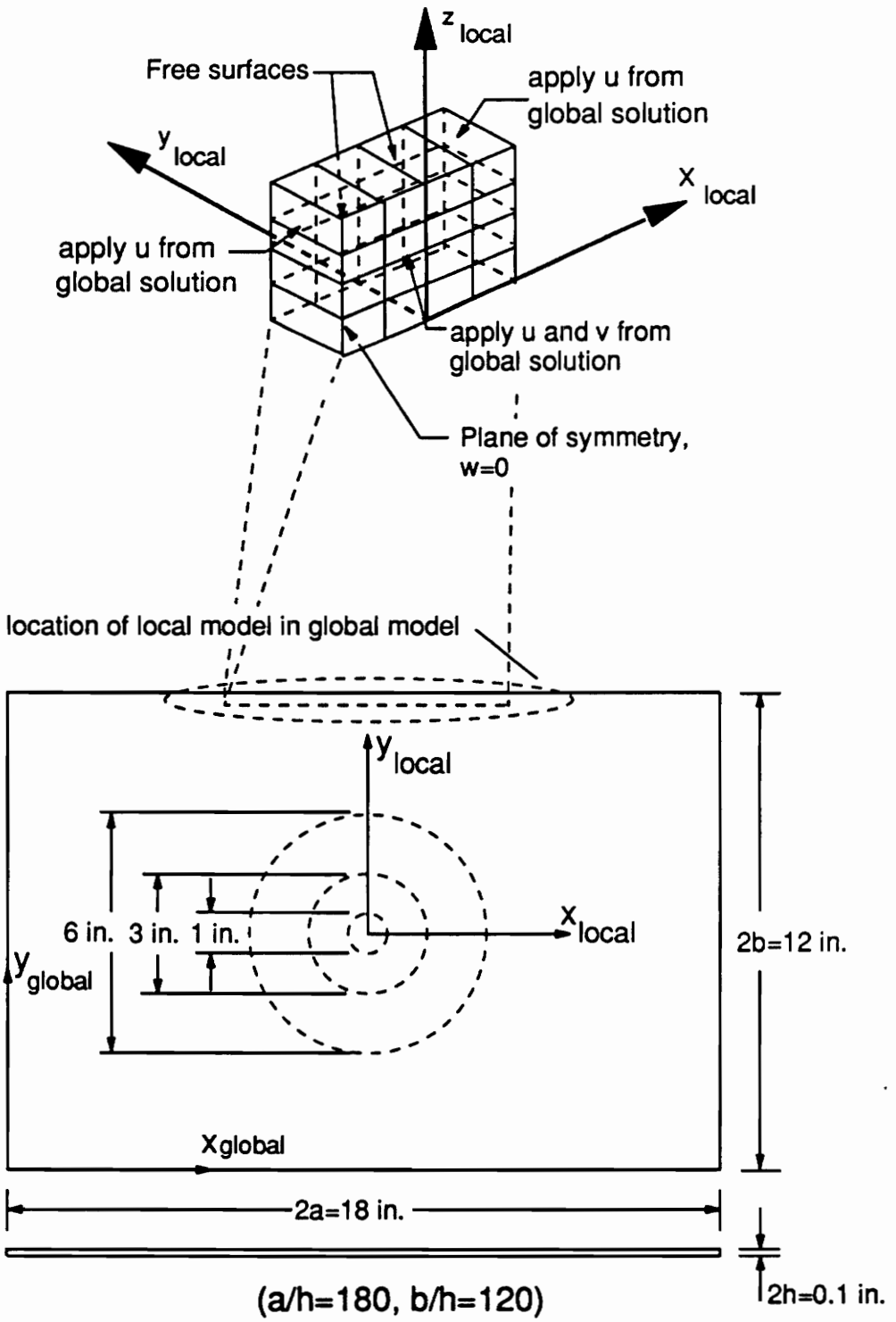

Figure 58. Reduced Local Straight Edge Model Displacement Application for Laminates with Off-Axis Plies in Compression

Table 7. Comparison of Complete and Global/Local Analyses for $[\pm 15_{2n}]_s$ Laminate with a Six-Inch Diameter Hole

Model Type	Nodes	Degrees of Freedom	Elements	Local/Total Solution Time (CPU seconds)
Complete 3-D	27,112	81,336	4,608	--/ +
Global 2-D	2,440	14,640	576	304.0/--
Reduced Straight	1,667	5,001	288	223.0/527.0
Straight	2,715	8,145	480	344.6/648.6
Curved	9,648	28,944	1,920	2,330.3/2,634.3

+model was not solved satisfactorily

The reduced and full straight edge undeformed and deformed models are shown for the $[\pm 15_{2n}]_s$ laminate with a six-inch diameter hole in Figure 60a) and b), and Figure 61a) and b). The full straight edge model is larger, with 65% more nodes than the reduced straight edge model. Figure 62a) and b), and Figure 63a) and b) are the undeformed and deformed local straight edge models for the $[\pm 15_{2n}]_s$ laminates with three- and one-inch diameter holes, respectively. Since all of the plates had the same global dimensions, these full local straight edge models had the same x-, y- and z-dimensions, while the number of nodes changed as a function of the diameter of the hole. The plates with the larger holes had a had a greater number of nodes around the hole, which affected the nodal distribution along the straight edge in proximity to the hole. Visual inspection of the local straight edge models reveals that greater number of nodes in the models near the smaller holes, since more nodes were needed between the finely discretized hole region and the ends of the plate. This information is presented quantitatively in Table 8.

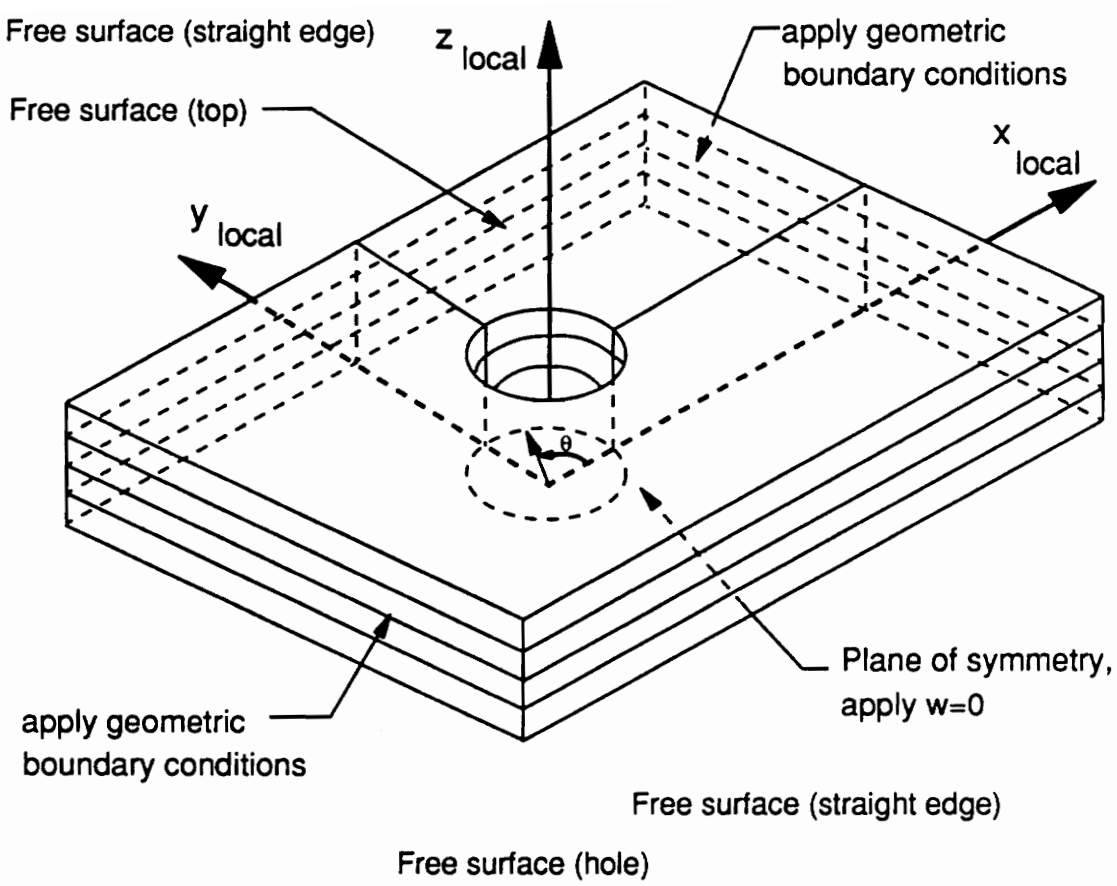

Figure 59. Complete Model Displacement Application for Laminates with Off-Axis Plies in Compression

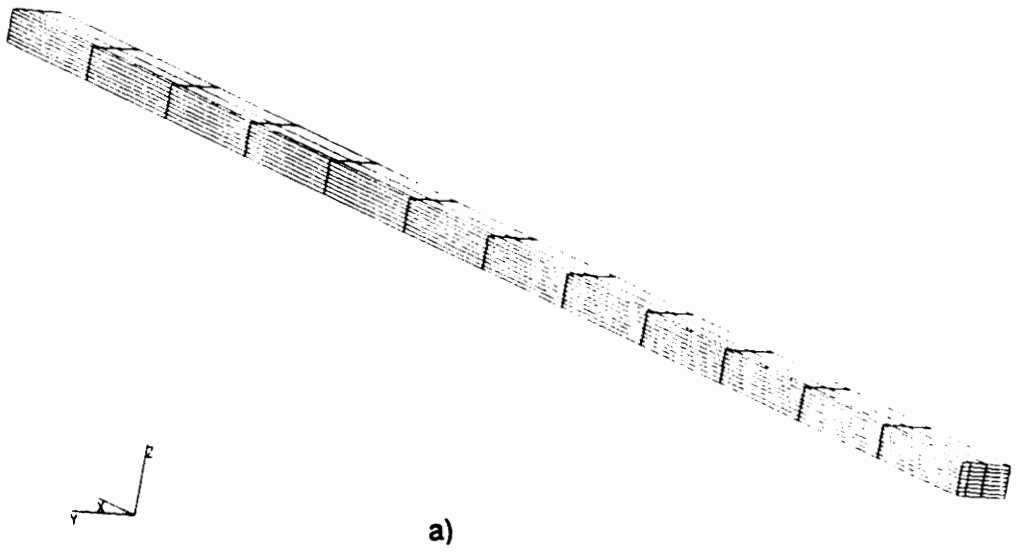

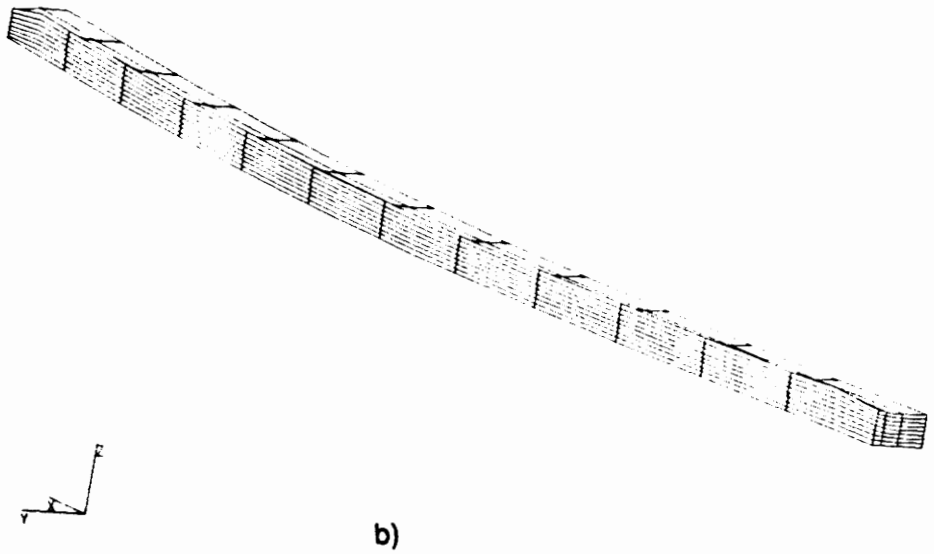

Figure 60. Reduced Straight Edge Models for $[\pm 15_{2n}]_s$ near Six-Inch Diameter Hole: a) Undeformed b) Deformed

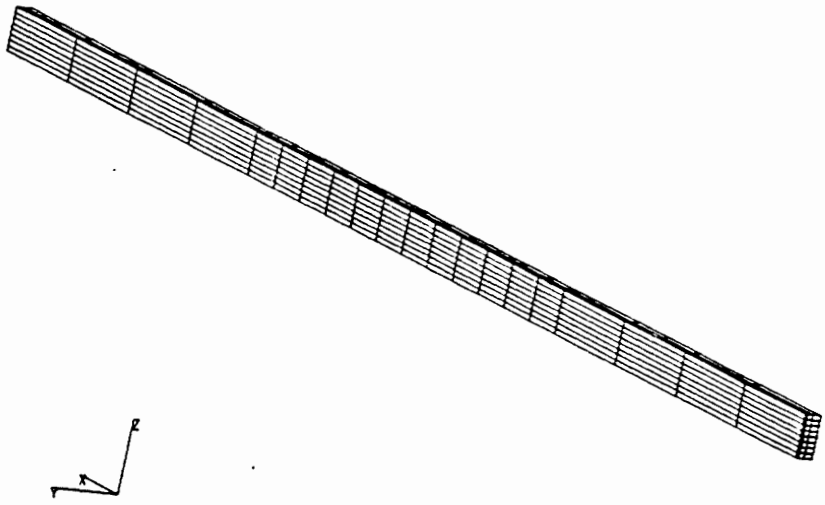

a)

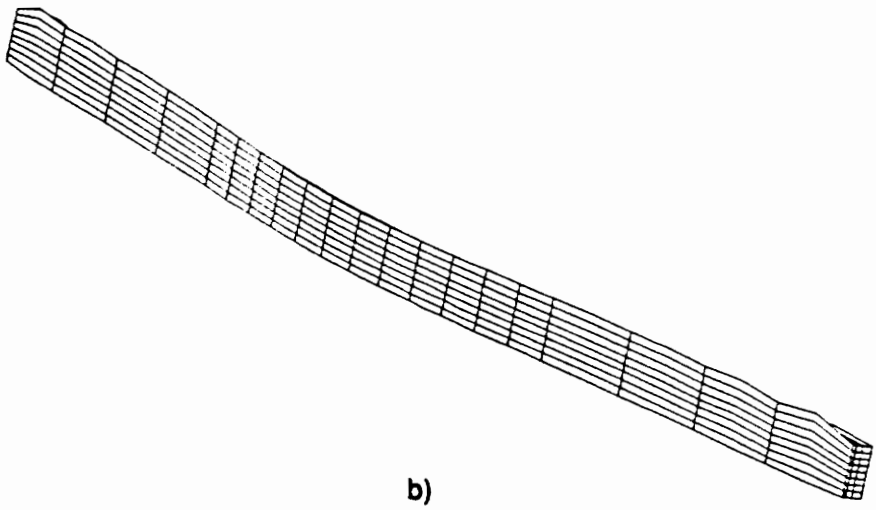

b)

Figure 61. Full Straight Edge Models for $[\pm 15_{2n}]_s$ near Six-Inch Diameter Hole: a) Undeformed b) Deformed

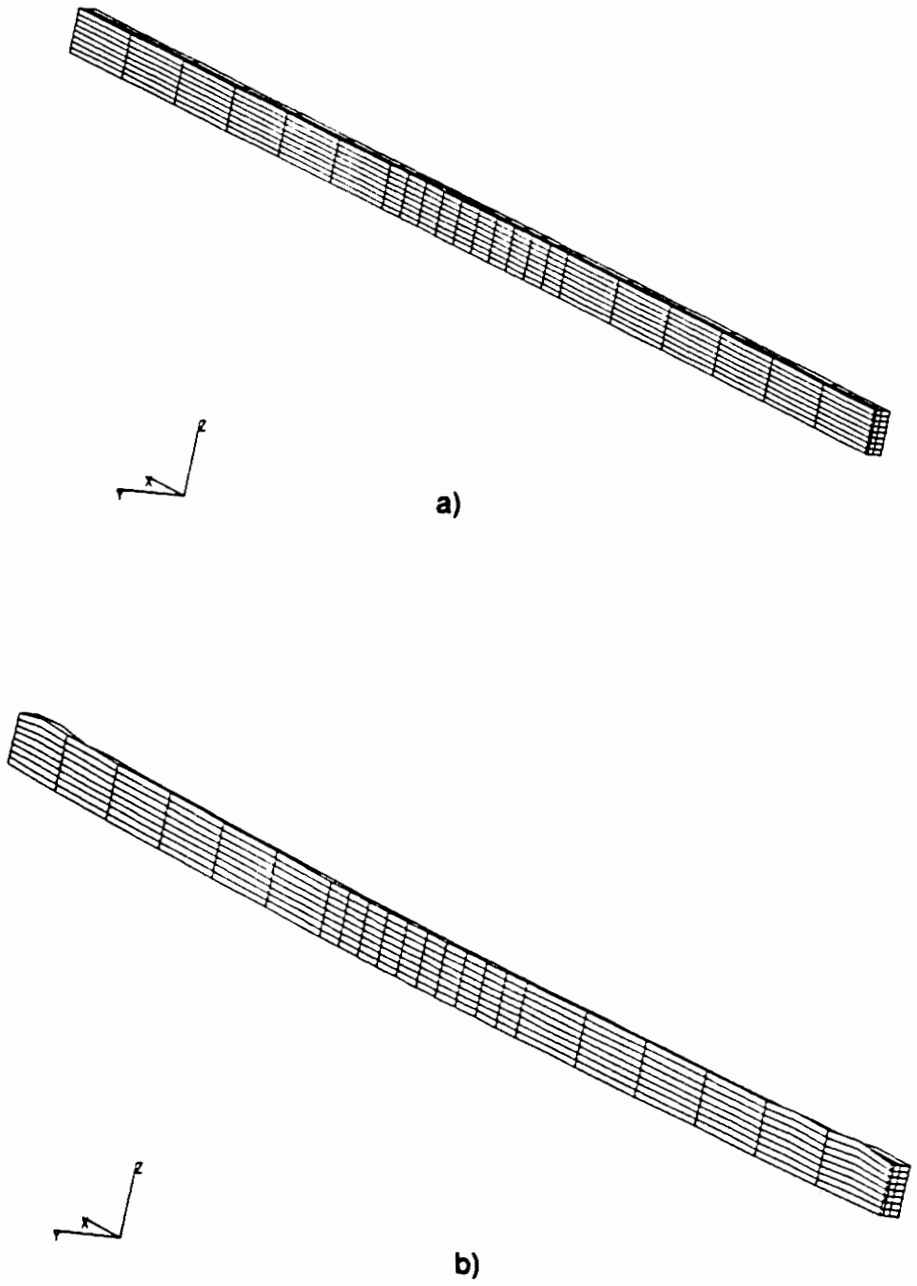

Figure 62. **Straight Edge Models for $[\pm 15_{2n}]_s$ near Three-Inch Diameter Hole:** a) Undeformed b) Deformed

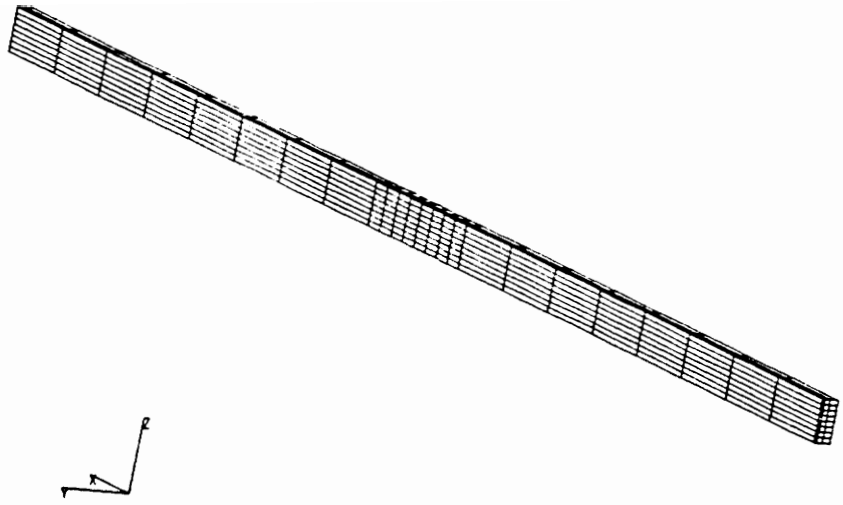

a)

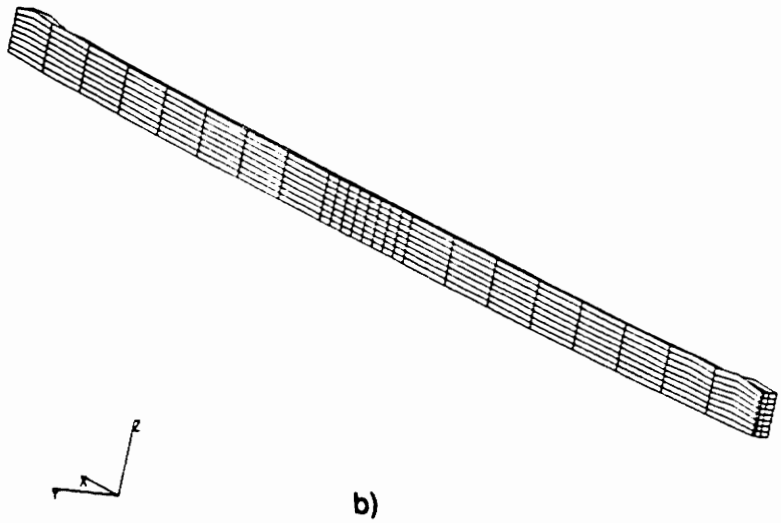

b)

Figure 63. Straight Edge Models for $[\pm 15_{2n}]_s$ near One-Inch Diameter Hole: a) Undeformed b) Deformed

Table 8. Three-Dimensional Angle-Ply and Quasi-isotropic Compression Local Straight Edge Model Characteristics

Hole Dia. (in.)/ Layup	Nodes	Degrees of Freedom	Elements	Local/Total Solution Time (CPU seconds)
1.0/ $[\pm 15_{2n}]_s$	3,239	9,717	576	501.0/940.9
3.0/ $[\pm 15_{2n}]_s$	2,977	8,931	528	488.1/925.8
6.0/	2,715	8,145	480	
$[\pm 15_{2n}]_s$				344.6/648.6
$[\pm 45_{2n}]_s$				342.0/693.0
$[\pm 15_n/\pm 45_n]_s$				344.2/653.5
$[0_n/\pm 45_n/90_n]_s$				347.0/776.2

A concern associated with modeling curved geometries with finite elements is to have a sufficient number of elements in that region to reduce the amount of in-plane curvature modeled by the individual elements. Through the selection of a greater number of spokes for the larger hole diameters, and thus more nodes, the in-plane curvature of the elements was kept low. Although more nodes were required in-plane around the local curved edge region for the larger hole sizes, there were fewer nodes required for the entire global model. The undeformed local curved edge models for the three different hole diameters are shown in Figure 64a), Figure 65a), and Figure 66a), while Table 9 contains quantitative information about the local models. Element arc lengths at a constant radial distance from the hole were varied to generate radial nodal lines from the hole edge to the global/local boundary around the hole. As with the cross-ply laminate models, the new locations of the mid-side nodes for the elements were carefully selected to be exactly at the mid-point between the corner nodes. The resulting in-plane nodal distribution did not have the same angular distance between the individual nodes around the hole.

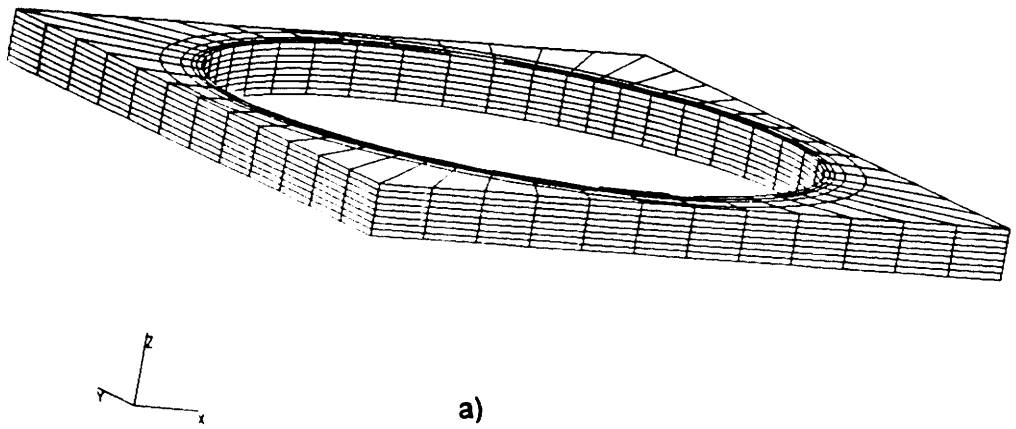

a)

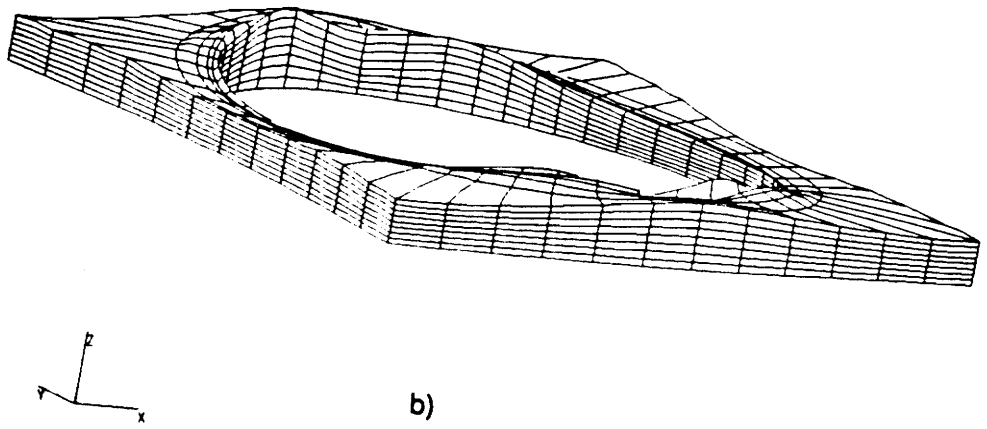

b)

Figure 64. Curved Edge Models for $[\pm 15_{2n}]_s$ with Six-Inch Diameter Hole: a) Undeformed b) Deformed

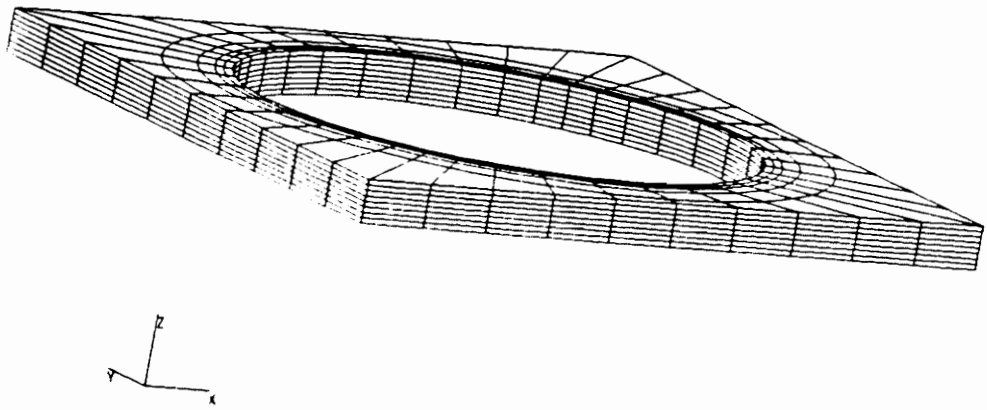

a)

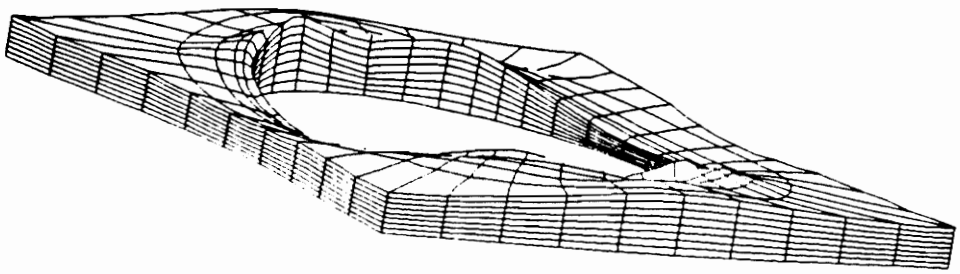

b)

Figure 65. Curved Edge Models for $[\pm 15_{2n}]_s$ with Three-Inch Diameter Hole: a) Undeformed b) Deformed

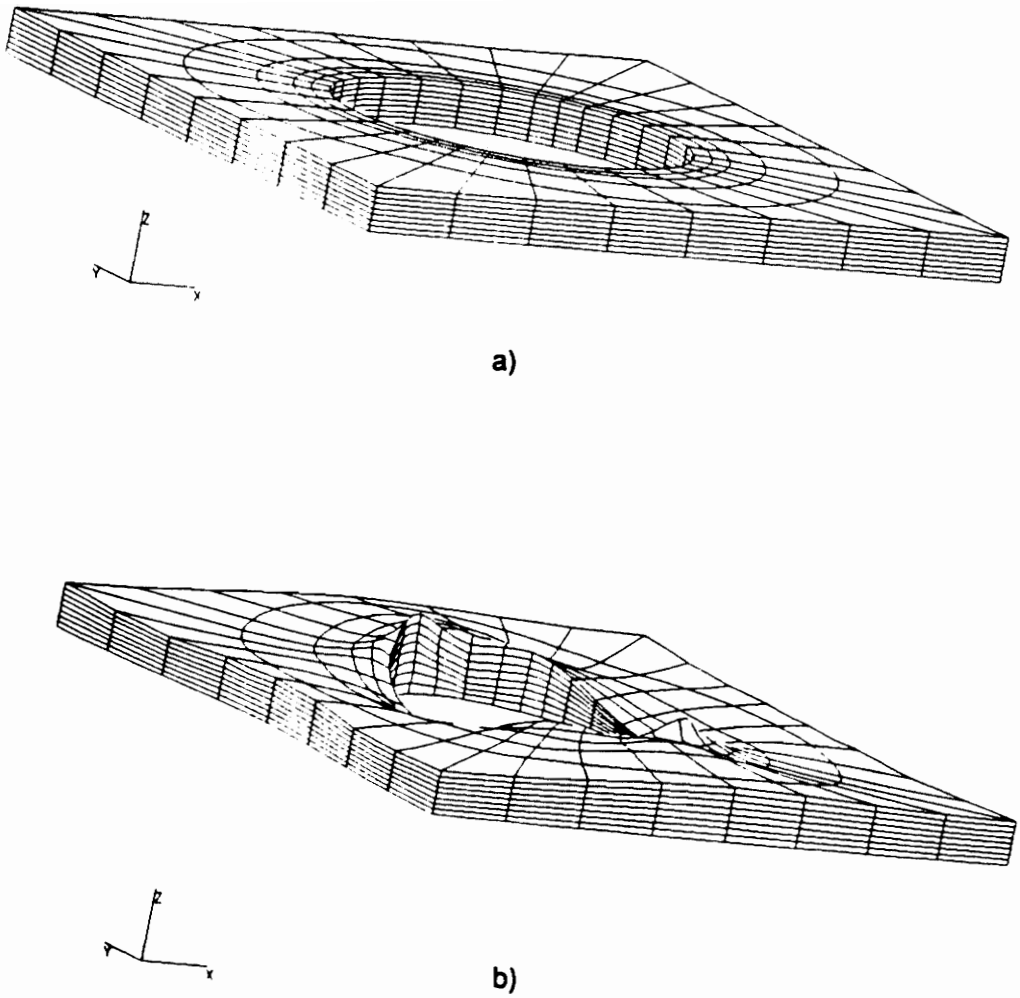

Figure 66. Curved Edge Models for $[\pm 15_{2n}]_s$ with One-Inch Diameter Hole: a) Undeformed b) Deformed

Table 9. Three-Dimensional Angle-Ply and Quasi-Isotropic Compression Local Curved Edge Models

Hole Dia. (in.)/ Layup	Nodes	Degrees of Freedom	Elements	Local/Total Solution Time (CPU seconds)
1.0/ $[\pm 15_{2n}]_s$	6,432	19,296	640	1,115.7/1,555.6
3.0/ $[\pm 15_{2n}]_s$	8,040	24,120	800	1,571.3/2,009.0
6.0/	9,648	28,944	1,920	
$[\pm 15_{2n}]_s$				2,330.3/2,634.3
$[\pm 45_{2n}]_s$				2,071.4/2,422.2
$[\pm 15_n/\pm 45_n]_s$				2,090.3/2,399.6
$[0_n/\pm 45_n/90_n]_s$				1,984.5/2,413.7

5.3 *Results and Discussion*

The two-dimensional global model was analyzed, and selected in-plane displacements were applied to the three-dimensional local models along the global/local interface. After determining the local nodal displacements, the strains and stresses at the integration points were calculated. Examination of solution times presented in Table 7 indicates that the two-dimensional to three-dimensional global/local finite element analyses presented were accomplished with a moderate amount of computer resources.

The processor used to determine the displacement fields for all of these models was an iterative solver. The amount of computer resources needed by iterative solvers is often substantially less than those which contain conventional solution techniques. The time required for a solution with iterative techniques is dependent on the iterative method selected, the initial guess, and the condition of the coefficient matrix, which is the system stiffness matrix. Since each two-dimensional

global model had a different stiffness matrix, models with the same total number of degrees of freedom required different amounts of computer time (Table 6 on page 101). No attempt was made to minimize the time to solve these systems, and the first set of parameters input to processor "ITER" which yielded a solution with the correct accuracy level was used. The complete three-dimensional model for the $[\pm 15_{2n}]_S$ laminate with a six-inch diameter hole did not converge to an admissible solution during repeated attempts to solve the system. Examination of the reported displacement field revealed that the elements were displaced in a manner inconsistent with the applied load. It is believed that the stiffness matrix was strongly ill-conditioned, so that the tests for convergence incorrectly reported that the model was converged. With no available complete three-dimensional finite element solution, validation of the global/local modeling technique was completed, on a qualitative basis, by comparison to known information about the interlaminar stress fields in composite laminates.

Angle-ply laminates whose stacking sequence is of the form $[\pm\Theta]_S$ generate interlaminar stress fields through a different mechanism than cross-ply laminates. There is no Poisson's ratio mismatch between these laminae, while there is shear coupling at the interface. The strength and direction of the shear coupling is dependent on the magnitude and sign of the orientation angle of the plies. Unconstrained off-axis laminae with different ply angles tend to shear in different directions under uniaxial loading, but are constrained from doing so when in a laminate. Compatibility is enforced through the development of an interlaminar shear (τ_{xz}) at the interface between the laminae. τ_{xz} has been shown previously to be dominant and seemingly without bound at this location (Salamon, 1980). Previous studies of the interlaminar stress distributions for $[\pm\Theta]_S$ laminates concentrate on this component (Pipes and Pagano, 1970), (Pagano and Pipes, 1971), (Dana, 1974), (Pagano, 1974), (Hsu and Herakovich, 1977), (Rybicki and Schmueser, 1978), (Salamon, 1980), (Burns et al, 1985), (Kassapoglou and Lagace, 1987). Most of these have focused on stresses at the straight free edge, but some did consider the interlaminar stress state around holes.

More complex laminates formed with off-axis plies could take the form of a $[\pm\Theta_1/\pm\Theta_2]_S$ stacking sequence, for example, or may be quasi-isotropic. Because these laminates include laminae of dif-

ferent angles, there may be Poisson's ratio mismatch or shear coupling or both at the ply interfaces, resulting in complex interlaminar stress fields to enforce compatibility and equilibrium through the laminate. However, certain general statements can be made about the character of these stress fields. The interlaminar normal stress was found previously to be maximum along the mid-plane for the $[\pm 15_n/\pm 45_n]_s$ and $[0_n/\pm 45_n/90_n]_s$ laminates. The interlaminar shear stresses (τ_{yz}) is maximum at the interface nearest the mid-plane for these stacking sequences, while the interlaminar shear stress (τ_{xz}) exhibits maxima or minima at interfaces where it dominates. In addition, because the interlaminar stress field distribution is truly three-dimensional in character, the in-plane distributions of each of these stresses change shape as well as magnitude for each ply interface. Such trends are reflected successfully in the interlaminar stress fields generated with the presented two-dimensional to three-dimensional global/local analysis method.

5.3.1 Two-Dimensional Global Model Results

The deformed grids for each hole diameter are shown in Figure 50b) through Figure 52b) for the $[\pm 15_{2n}]_s$ laminate. The deformed $[\pm 45_{2n}]_s$ plate with a six-inch diameter hole is found in Figure 53b), while the $[\pm 15_n/\pm 45_n]_s$ and the $[0_n/\pm 45_n/90_n]_s$ deformed global models are in Figure 54b) and Figure 55b). All in-plane displacements were scaled by a factor of 10. Note that the vertical ends of each plate remained straight and their original length as specified by the global boundary conditions. The circular holes became noncircular, and there is a bulging of the previously straight edges of the plates. The line of nodes two laminate thicknesses from the maximum global y-dimension is the global/local interface for the straight edge models, as it was for the cross-ply straight edge models. This boundary is curved outward from the hole region, and this curvature is transferred from the global model to the local through the applied displacement conditions. The square of nodes around each hole exhibits concavity on its vertical sides and convexity on its horizontal sides. These are the global/local interfaces for the local curved free edge model, and this deformation state will be applied to the local model.

For a uniform end displacement, the reduced in-plane stiffness of those laminates with larger holes is reflected in the global deformation field, where the influence of the hole is experienced over a greater portion of the plate. Because the in-plane stiffnesses are also dependent on stacking sequence, each lamination sequence will have a different in-plane displacement field for the same end-shortening displacement. Since the $[\pm 15_{2n}]_s$ laminate has a higher x-direction in-plane stiffness than the $[\pm 45_{2n}]_s$ laminate, the same end-displacement deformed the $[\pm 15_{2n}]_s$ plate less than the $[\pm 45_{2n}]_s$. Because the stiffness of the $[\pm 15_n/\pm 45_n]_s$ laminate is between these other laminates, the same end-displacement will cause more deformation than the $[\pm 15_{2n}]_s$ laminate and less than the $[\pm 45_{2n}]_s$ laminate. By examining the global deformed grids in Figure 50b) through Figure 54, this is seen to be the case. No direct comparison between the interlaminar stress states are made because of the change in the in-plane laminate stiffness with stacking sequence.

5.3.2 Three-Dimensional Local Model Results

The straight free edge results shall be presented prior to those of the curved free edge. The success of the global/local analysis method shall be determined by comparing the trends of the interlaminar stress fields determined with the global/local finite element procedure to those from previous studies, since the complete three-dimensional model could not be solved. Preceding the straight edge model interlaminar stress results, two different methods of determining the straight edge displacement fields are presented and compared for the $[\pm 15_{2n}]_s$ plate with a six-inch diameter hole. One model was formed by selecting a smaller region of interest in the global model than the other, and it is this reduced model that will be compared to a full model for the straight edge region. Once it is established which model is preferable and why, the interlaminar stress fields at the straight edges near the different diameter holes will be considered. The effect of decreasing hole diameter in a finite-width plate for the $[\pm 15_{2n}]_s$ lamination sequence is examined. The straight edge interlaminar stress fields for a plate with a six-inch hole and for the $[\pm 45_{2n}]_s$, $[\pm 15_n/\pm 45_n]_s$, and $[0_n/\pm 45_n/90_n]_s$ laminates, respectively, are then studied. Since the region of interest for the straight

free edge is that nearest the hole, all of the presented information for the local models will be limited to that region. For this particular study that region is $-3.5 < x < 3.5$ in., where x is the local coordinate dimension. The in-plane displacements in the local straight edge models were scaled by a factor of 10, and the out-of-plane displacements by 100. In addition, their z-direction dimensions were multiplied by 5 to allow clearer viewing of the through-the-thickness effects. The curved free edge results will follow the same format: verification of the global/local model results, determination of the influence of different hole diameters for the $[\pm 15_{2n}]_S$ lamination sequence, and then the effect of different laminate orientations on the interlaminar stress field. While the entire region around the hole was modeled, only information at those angular positions between $0° < \theta < 180°$ are presented since the data will be cyclic over the entire hole boundary. These are the integration points nearest the straight edge under examination and closest to the hole edge.

5.3.2.1 Verification of Global/Local Modeling Technique for the Straight Edge

The primary feature of global/local finite element analysis methods is the option of selecting only those areas of interest for further discretization. With the two-dimensional to three-dimensional finite element analysis technique under consideration, the selection of this region and the displacement application procedure is not as straightforward as some analysts would prefer. Undeformed and deformed models for the two $[\pm 15_{2n}]_S$ local straight edge models near a six-inch diameter hole, reduced and full, are in Figure 60a) and b) and Figure 61a) and b). Visual comparison of these deformed models suggests that there is a marked difference in the displacement of the free edges. Focusing in Figure 67b) on the displacements along the local $x = 3.5$ in. plane in the full model, and on the ends of the reduced model, dramatically reveals the error in using a reduced model for this laminate and loading. The application of constant x-direction displacements along this model boundary inhibited shearing in the x-z plane, which is the dominant interlaminar effect for laminates with only off-axis plies. Because the global model cannot predict the exact through-the-thickness nature of the displacements and the application of constant displacements in the x-z plane is clearly

incorrect, local models of laminates with off-axis plies should not penetrate the free edge boundary layer. Furthermore, this will impact global/local stress analysis techniques for any application where the interlaminar stress state includes either x-z or y-z shearing: the local model may encompass, but not partition, any region where shearing will be present. As a result, the local models along the straight free edge for any laminate with off-axis plies must be more extensive than those of cross-ply laminates under compression or tension. Further discussion of the straight edge stress analyses for laminates with off-axis plies will focus on the full local model, since the reduced local model displacement field is incorrect.

Several attempts were made to verify the local straight edge stress fields with those found for a complete three-dimensional model for the plate with a six-inch diameter hole and a $[\pm 15_{2n}]_S$ orientation. To allow comparison of the stresses at the same locations, the complete model had the same level of discretization as the local models. Attempts to solve the system with the Testbed were numerous, computationally intensive, lengthy, and unsuccessful. However, the degree of effort required to attempt this analysis proves the point that with a careful global/local analysis solution of otherwise intractable problems is a reality. Over 14 million coefficients form the complete three-dimensional system matrix with 4,608 elements, while the total number of nine-node plate elements for the global model was 576 and a total of 2,410 20-node brick elements were used for two local models. This represents a substantial saving of computational resources with this global/local technique over a complete three-dimensional finite element analysis. The validity of the global/local analysis is determined by comparing to previous studies in the open literature. Since finite element analyses using classical elements do not satisfy the traction-free conditions exactly, this precludes attempting to compare to stress field values generated from other methods. While there has been work which used finite elements in the past, close comparison to their results was not possible because of modeling differences between these and the current work. Since the global/local method and not the use of the finite element method is under scrutiny, until a complete three-dimensional analysis with the same discretization is completed, only the trends of the stress field can be validated.

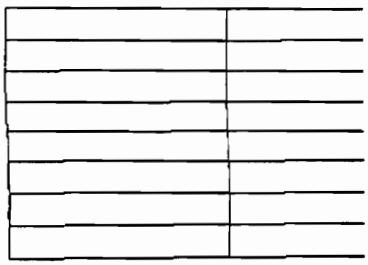

a) x=-3.5 in. edge, correct boundary conditions

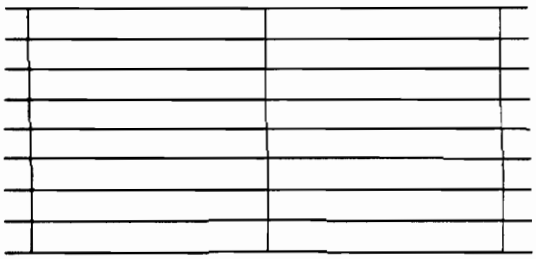

b) center of model, correct boundary conditions

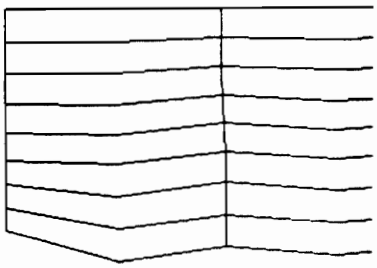

c) x=-3.5 in. edge, incorrect boundary conditions

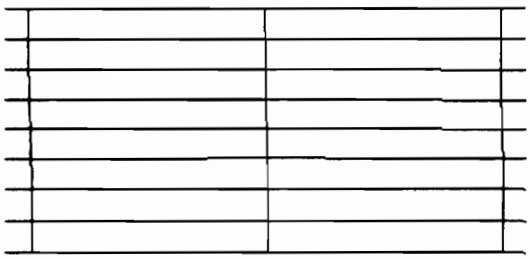

d) center of model, incorrect boundary conditions

Figure 67. Displacement Field Comparision Between Full and Reduced Models for $[\pm 15_{2n}]_s$ near a Six-Inch Diameter Hole

Previous investigations have concentrated on the straight free edge of a $[\pm 45_{2n}]_S$ laminate without holes, under uniaxial tension. Pipes and Pagano (1970) used a reduced exact elasticity formulation with a finite difference solution for a $[\pm 45_{2n}]_S$ laminate under uniaxial tension. The through-the-thickness distribution of the interlaminar shear stress (τ_{xz}) was reported to approach a singular value at the interface between the layers. Values for the other interlaminar stress components (σ_z and τ_{yz}) were presented along that interface with noticeably smaller magnitudes. The character of the stress distributions determined in their investigation is similar to that found with the current study. Wang and Crossman (1977) presented some results found with the finite element method, but not all of the trends between their study and the current one match exactly. However, some of their results do not match those of other researchers. Using a perturbation approach to solve the exact elasticity solution, Hsu and Herakovich (1977) found similar distributions to those in the current study. Rybicki and Schmueser (1978) modeled the $\pm\theta$ layers as a single orthotropic layer, which eliminated the possibility of comparing stresses at the interface. Kassapoglou and Lagace (1987) presented a closed form solution for interlaminar stresses at a straight free edge which enforced a zero interlaminar normal stress at the interface. Both the in-plane and the through-the-thickness distributions at the interface were similar to those found by others, including this work. The global/local analysis technique determines the proper character of the interlaminar stresses along the straight edge for a particular x-location in the local model, and can be considered valid.

5.3.2.2 Straight Free Edge Model Results

The undeformed and deformed straight edge models for the $[\pm 15_{2n}]_S$ plate with a six-inch hole are shown in Figure 60a) and b). From the deformed view of the model, the expansion of elements away from the laminate mid-plane along the straight free edge is seen to be confined within one laminate thickness of the free edge. Bowing of the elements nearest the hole away from the center of the plate is predicted, illustrating the influence of the nearby hole on the in-plane and out-of-plane displacement field. Careful examination of the deformed view confirms that the elements in

the center of the local model also are expanding less through the laminate thickness. It is expected that these changes in the deformation field due to the hole will be reflected in the interlaminar stress distributions. The through-the-thickness distributions for the interlaminar normal stress (σ_z) and interlaminar shear stress (τ_{yz}) for this laminate are presented in Figure 68a) and b). From Figure 68a), the maximum interlaminar normal stress is near the laminate mid-plane, but comparatively low in magnitude. The maximum stress for τ_{yz} is found at the $z = 0.025$ in. interface in Figure 68b) which is the interface between the 15° and -15° layers. Both of these figures underscore the fact that for a $[\pm 15_{2n}]_S$ laminate these do not warrant further study because of their low magnitudes.

The through-the-thickness and in-plane distributions at the interface for the dominant interlaminar stress component (τ_{xz}) are presented in Figure 69a) and b) along the straight free edge in the $[\pm 15_{2n}]_S$ plate with nearby a six-inch diameter hole. This stress component increases in value from zero at the mid-plane to a maximum at the ply interface, and decays to zero at the top free surface. Its character suggests that the interfacial values could continue to increase with further refinement of the model, indicating the possible presence of a stress singularity. The nearby six-inch diameter hole lowers the peak magnitude of this stress at the ply interface for a given x-location, but does not affect its in-plane character. Along the free edge, the lowest magnitude of τ_{xz} is predicted to be at the centerline of the hole. As the distance from the straight free edge to the hole increases, and thus the effect of the hole is lessened, the the stress reduction becomes less prevalent. The expected limitation of the boundary layer to one laminate thickness in distance from the straight free edge is shown in the in-plane stress distribution in Figure 69b).

General comments about the deformation and stress stress states at the straight edge for plates with three- and one-inch diameter holes follow, while the undeformed and deformed local models are presented in Figure 62a) and b), and Figure 63a) and b). In each of the deformed views of the local models, a thickening along those rows of elements nearest the straight free edge can be seen, with the greatest expansion across the final row of elements. Visual comparison of the undeformed and deformed meshes for all the hole diameters in the central area of the models reveals the diminished

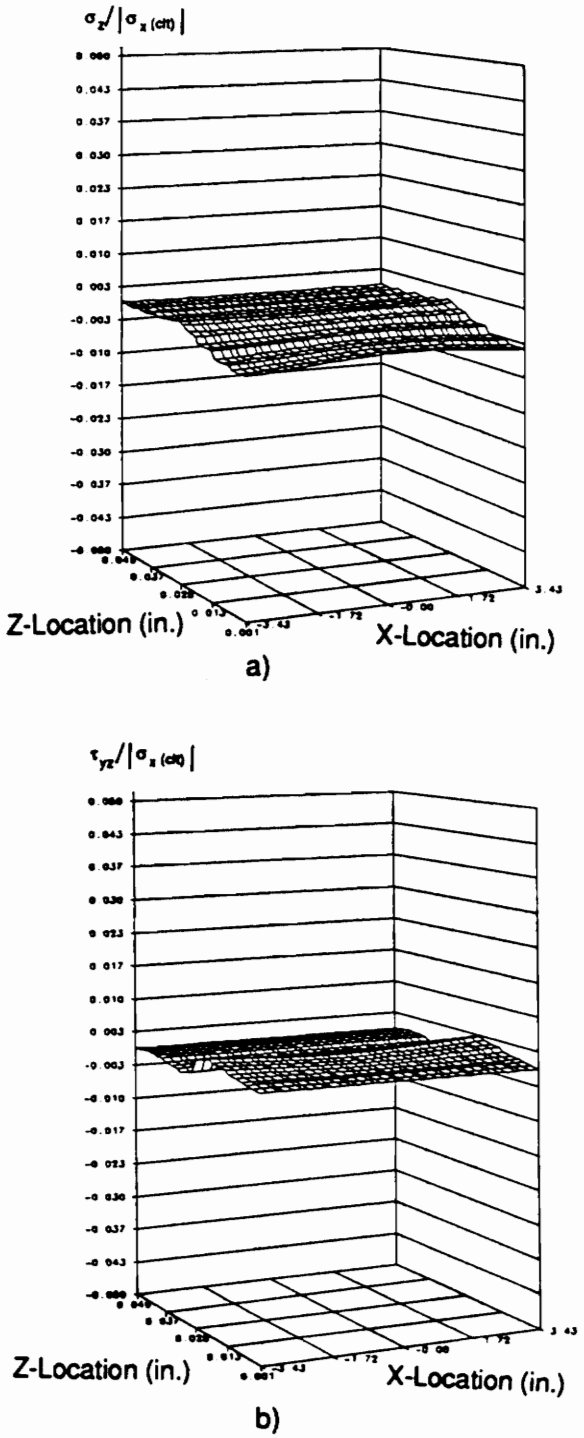

Figure 68. Through-the-Thickness Stresses for Local Straight Edge Model for $[\pm 15_{2n}]_s$ near Six-Inch Diameter Hole: a) σ_z b) τ_{yz}

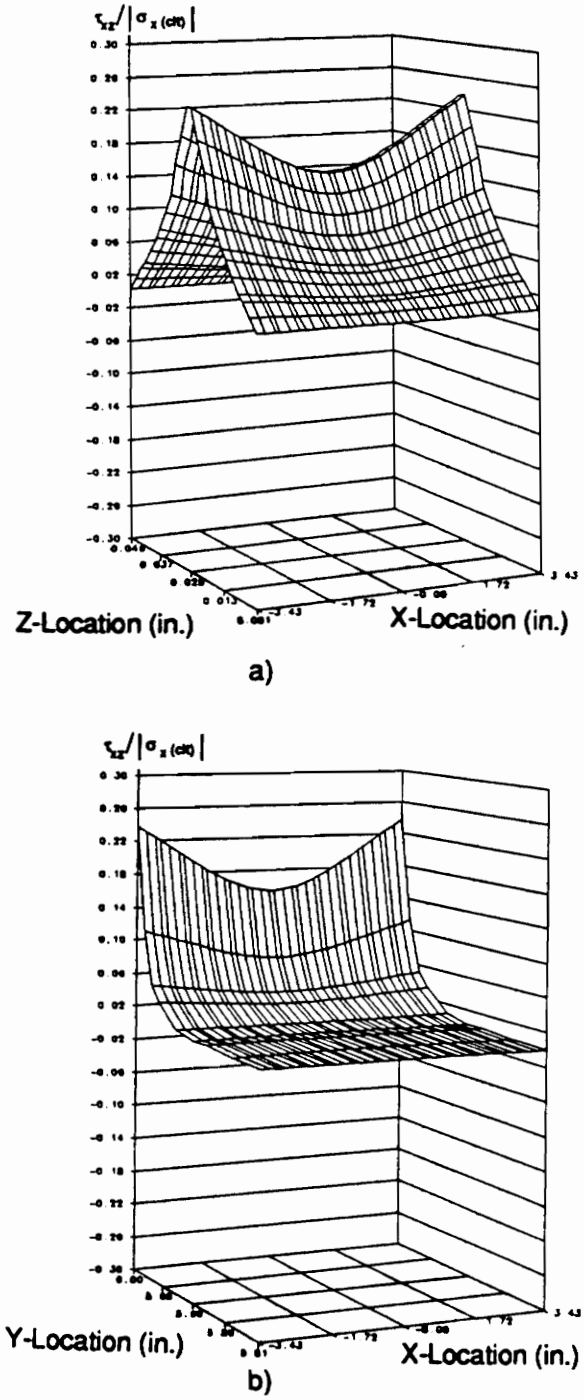

Figure 69. τ_{xz} for Local Straight Edge Model for $[\pm 15_{2n}]_s$ near Six-Inch Diameter Hole: a) Through-the-Thickness b) At the z = 0.025 in. Interface

effect of the hole on the deformation state for the smaller holes. The straight edge model near the one-inch diameter hole exhibits no in-plane curvature of the elements in Figure 63b), while those near the six-inch diameter hole in Figure 61b) are considerably bowed in the central portion of the model.

Because of the similarities in the interlaminar stress distributions for the local models near different diameter holes, the individual results are not presented, but a direct comparison of the results follows. The nearby hole affects all of the interlaminar stress distributions along the straight free edge, but its influence is clearest for the interlaminar shear stress (τ_{xz}) at the $z = 0.025$ in. interface. The in-plane distributions of τ_{xz} at the interface for the straight edge near the three- and one-inch diameter holes are similar to those near the six-inch diameter hole, except for the integration points nearest the free edge. The stresses over the localized region of interest for all three hole diameters are presented in Figure 70. Over this region, no hole effect is discernible for the plate with a one-inch diameter hole; as far as the straight edge interlaminar stress state is concerned, this plate does not have a hole. The three-inch diameter hole has some influence on the straight free edge interlaminar stress field, but not as marked as the six-inch diameter hole. Both of these holes depress the stress magnitudes symmetrically in the central region of the plate. The straight edge values near the six-inch diameter hole are markedly depressed in this region; at the centerline, τ_{xz} is nearly 30% and 25% lower than those values for the straight edges near the one- and three-inch diameter holes, respectively. Near the ends of this region, the plate with a six-inch diameter hole does not recover the same stress as the other plates. This is attributable to the fact that the same end-displacement was applied to the plates, regardless of hole size. Since the in-plane stiffness for a plate with the six-inch diameter hole is lower, its in-plane stresses will be lower. Since the transition from the internal stress state to the traction-free edge state is over the same distance for these laminates, lower in-plane stresses will require lower stress gradients, and therefore, lower interlaminar stresses arise. The changes in the distribution and magnitude of the interlaminar stresses increase with increasing hole size, which suggests that the presence of the hole near the free edge reduces the intralaminar and interlaminar stress fields along the straight free edge.

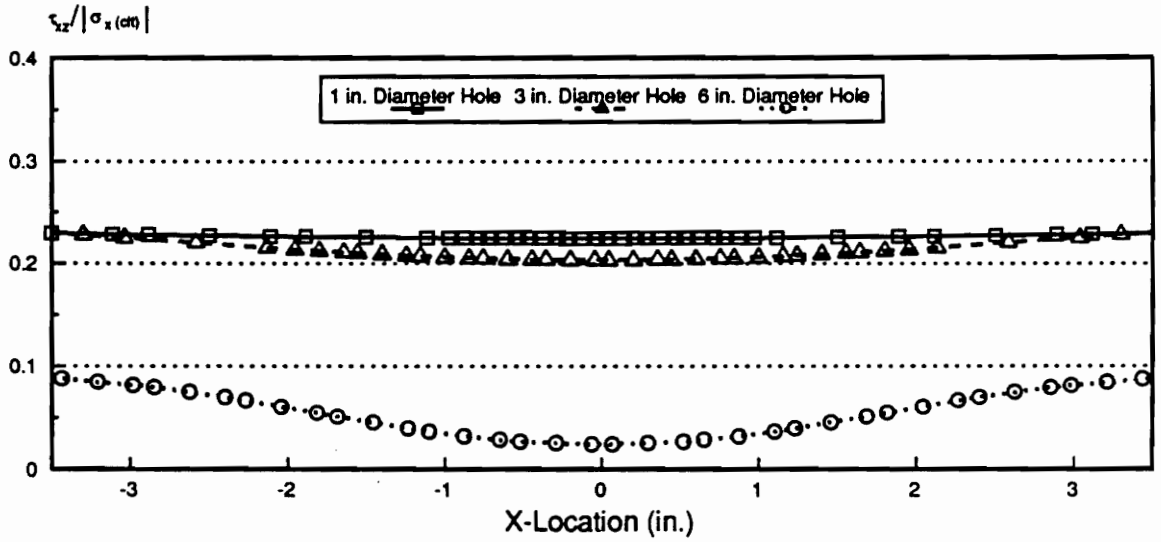

Figure 70. τ_{xz} **at Straight Edge for** $[\pm 15_{2n}]_s$ **near Different Hole Diameters:** a) At the z = 0.025 in. Interface

Extensive examination of the influence of the in-plane compliances of laminates on their respective interlaminar stress fields have been conducted to determine which laminates develop large interlaminar stresses. The intention of this study was not to do further work in this area, but rather to demonstrate that the global/local modeling technique is able to determine these stress fields for a general lamination sequence. Two $[\pm\Theta]_S$ laminates were considered prior to one with both of these angle of orientations: $[\pm\Theta_1/\pm\Theta_2]_S$. The first of these was a $[\pm 15_{2n}]_S$ stacking sequence and the second, $[\pm 45_{2n}]_S$, is considered next.

When the global deformation fields were cursorily examined earlier, it was determined that the $[\pm 45_{2n}]_S$ laminate exhibited greater in-plane deformations than the $[\pm 15_{2n}]_S$ laminate for the same applied end-shortening displacement. As seen when comparing the straight edge models in Figure 61b) and Figure 71b), the local model for the $[\pm 45_{2n}]_S$ laminate had a greater degree of deformation than the $[\pm 15_{2n}]_S$ laminate, both in-plane and out. At the center of the plate the outward in-plane bowing of the elements is greater, and there is more element expansion through the laminate thickness for the $[\pm 45_{2n}]_S$ stacking sequence than the $[\pm 15_{2n}]_S$ laminate. Near the center of the straight edge model, however, there is less thickening, as the six-inch diameter hole relieves the intralaminar stress and therefore, the interlaminar strain and stress state at the edge of the laminate. τ_{xz} is the dominant interlaminar stress component and is maximum at the interface between the plies, since this laminate is member of the $[\pm\Theta]_S$ family.

Unlike the $[\pm 15_{2n}]_S$ laminate, the other interlaminar stress components are larger in magnitude for the $[\pm 45_{2n}]_S$ plate. Examination of the through-the-thickness distribution of σ_z in Figure 72a) reveals that it is nonzero and maximum along the mid-plane of the laminate. Its reported peak values are small, however, less than 5% of the normalization stress. The interlaminar shear stress (τ_{yz}) is also small, reaching maximum absolute magnitude of 6% of the normalization stress, shown in Figure 72b). At the interface between the $\pm 45°$ layers, τ_{yz} exhibits opposing gradients. Averaging these integration point stress values to determine the interfacial values yields a near zero stress at the interface. Both of these stress components have variations in their magnitudes over this region that are suggestive of a hole effect along the straight edge.

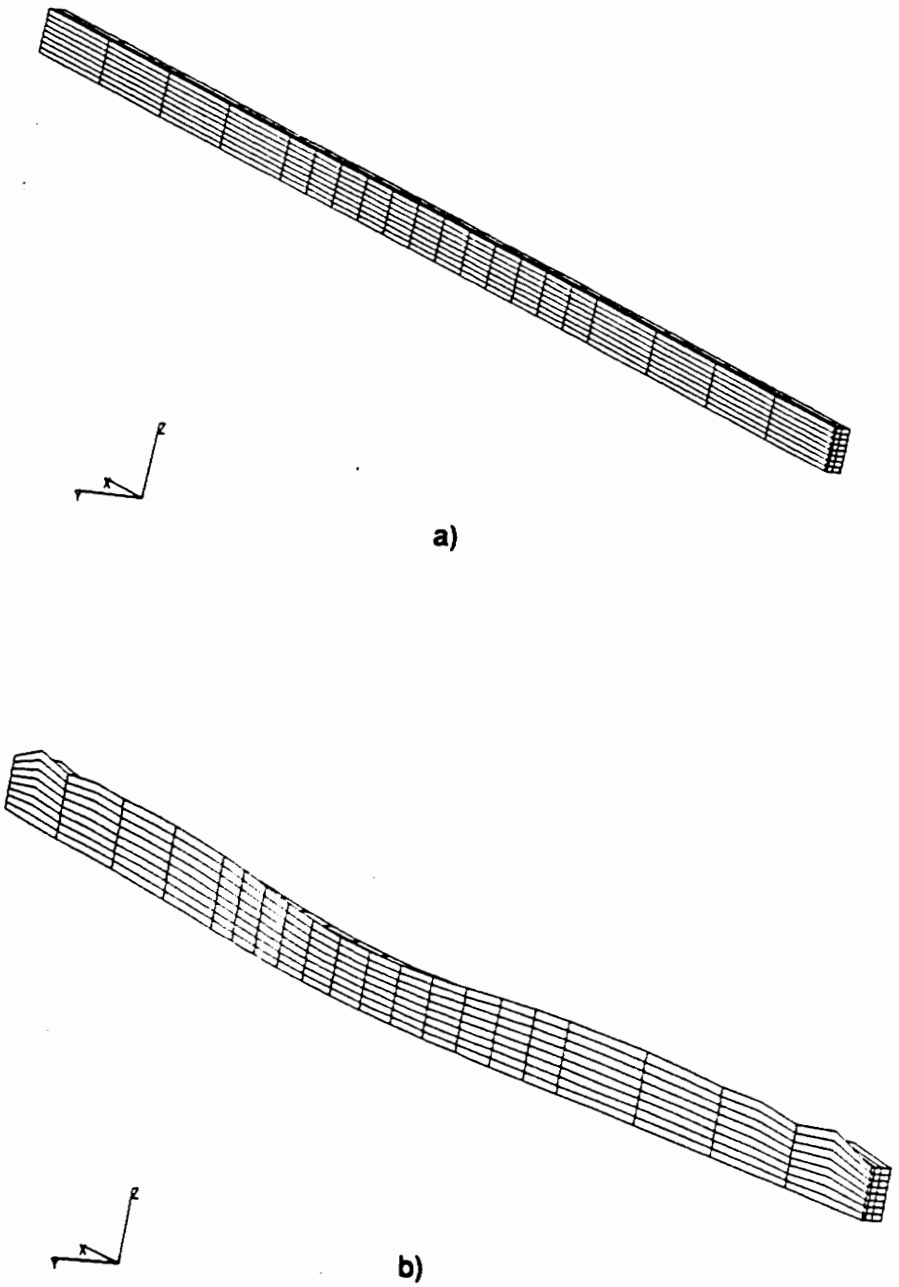

Figure 71. Straight Edge Models for $[\pm 45_{2n}]_s$ near Six-Inch Diameter Hole: a) Undeformed b) Deformed

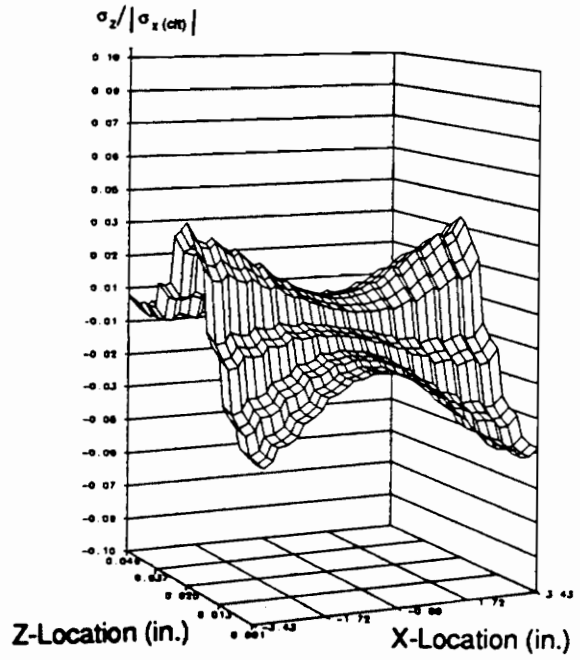

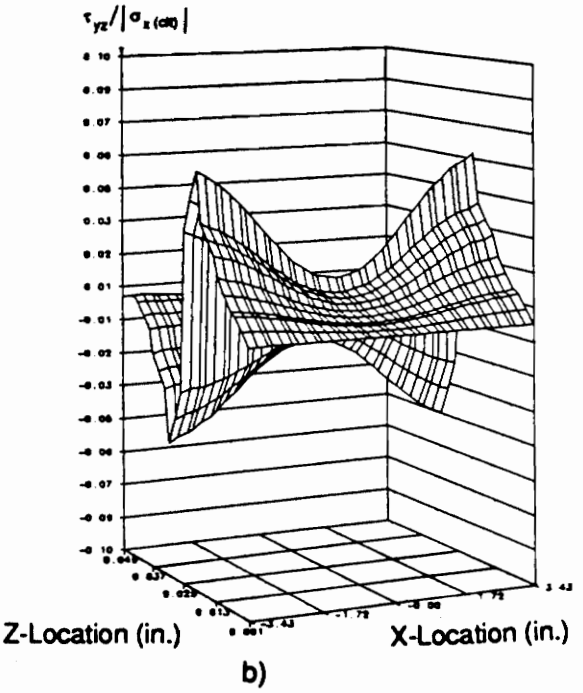

Figure 72. Through-the-Thickness Stresses at Straight Edge for $[\pm 45_{2n}]_s$ laminate near Six-Inch Diameter Hole: a) σ_z b) τ_{yz}

Figure 73a) is the through-the-thickness interlaminar shear stress (τ_{xz}) distribution for the $[\pm 45_{2n}]_S$ laminate with a six-inch diameter hole, while the in-plane τ_{xz} distribution at the interface between the $\pm 45°$ layers for this laminate is presented in Figure 73b). One of the most noticeable features of the distributions in both of these figures is the symmetric decrease in magnitude of the stress about the centerline of the hole, which reaches a minimum magnitude at the centerline of the hole. This reduction is stronger than that found for the $[\pm 15_{2n}]_S$ laminate and is attributable to the higher compliance of the $[\pm 45_{2n}]_S$ laminate. For each location in the localized region, the through-the-thickness distribution of τ_{xz} for this laminate is similar to that for the previous stacking sequence examined, but with greater extremes in value. The in-plane distribution of τ_{xz} at the $z = 0.025$ in. interface in Figure 73b) reflects the same information: its character is similar to the $[\pm 15_{2n}]_S$ laminate with a larger peak magnitude for the $[\pm 45_{2n}]_S$ laminate, and the stress relief effect due to the hole is stronger. These stresses vary from 0.5 times the normal in-plane stress of classical lamination theory to 0.15 at the center of the model.

A laminate composed of $\pm 15°$ and $\pm 45°$ ply groups would be expected to exhibit characteristics of both of its ply groups. The undeformed and deformed models for the $[\pm 15_n/\pm 45_n]_S$ laminate are found in Figure 74a) and b). The through-the-thickness enlargement of the elements nearest the free edge appears less severe than the $[\pm 15_{2n}]_S$ laminate, but more severe than the $[\pm 45_{2n}]_S$ laminate. Bowing of the elements along the straight edge away from the center of the hole is clearly discernible for this lamination sequence, but is not as severe as that seen in Figure 71b) for the $[\pm 45_{2n}]_S$ laminate, and more than for the $[\pm 15_{2n}]_S$ laminate in Figure 64b). With higher displacement scaling factors than used here, deformations between the ply groups could be seen in the x-z and y-z planes. Because there is both a Poisson's ratio mismatch between the groups of layers and shear coupling for each group and between each group, the deformation field is complex and all three interlaminar stress components are expected to be nonzero for at least part of the boundary layer region.

Examination of the through-the-thickness stress distributions near the straight edge for each component indicates which interfacial locations merit detailed study. All three of the through-the-

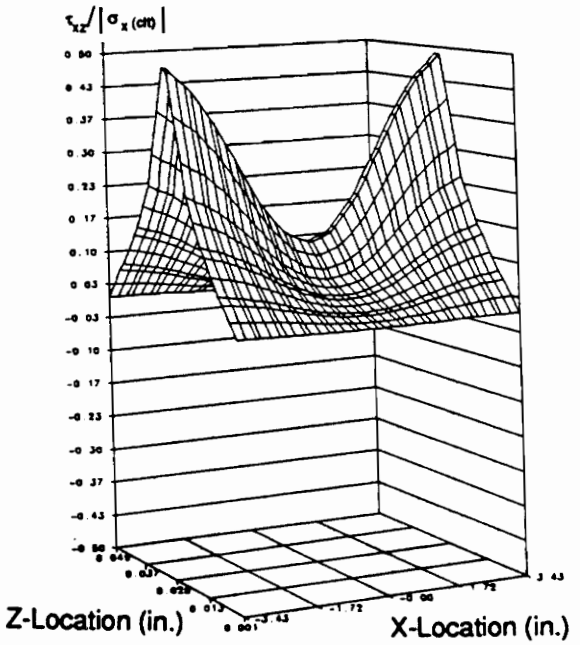

a)

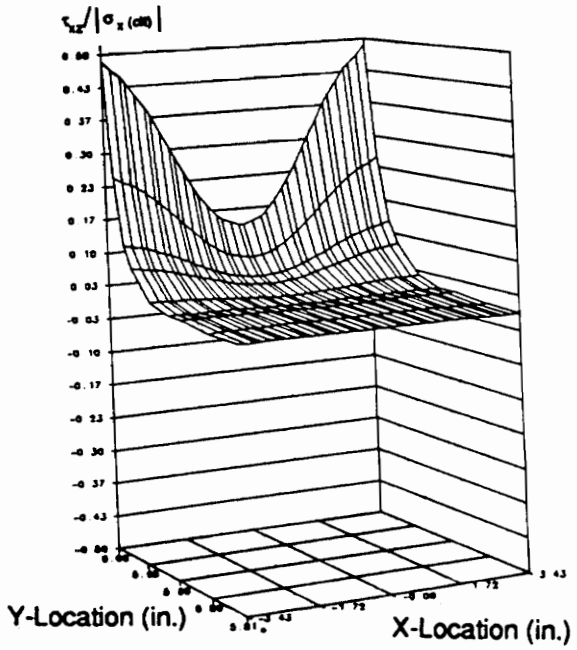

b)

Figure 73. τ_{xz} **at Straight Edge for** $[\pm 45_{2n}]_s$ **near Six-Inch Diameter Hole:** a) Through-the-Thickness b) At the z = 0.025 in. Interface

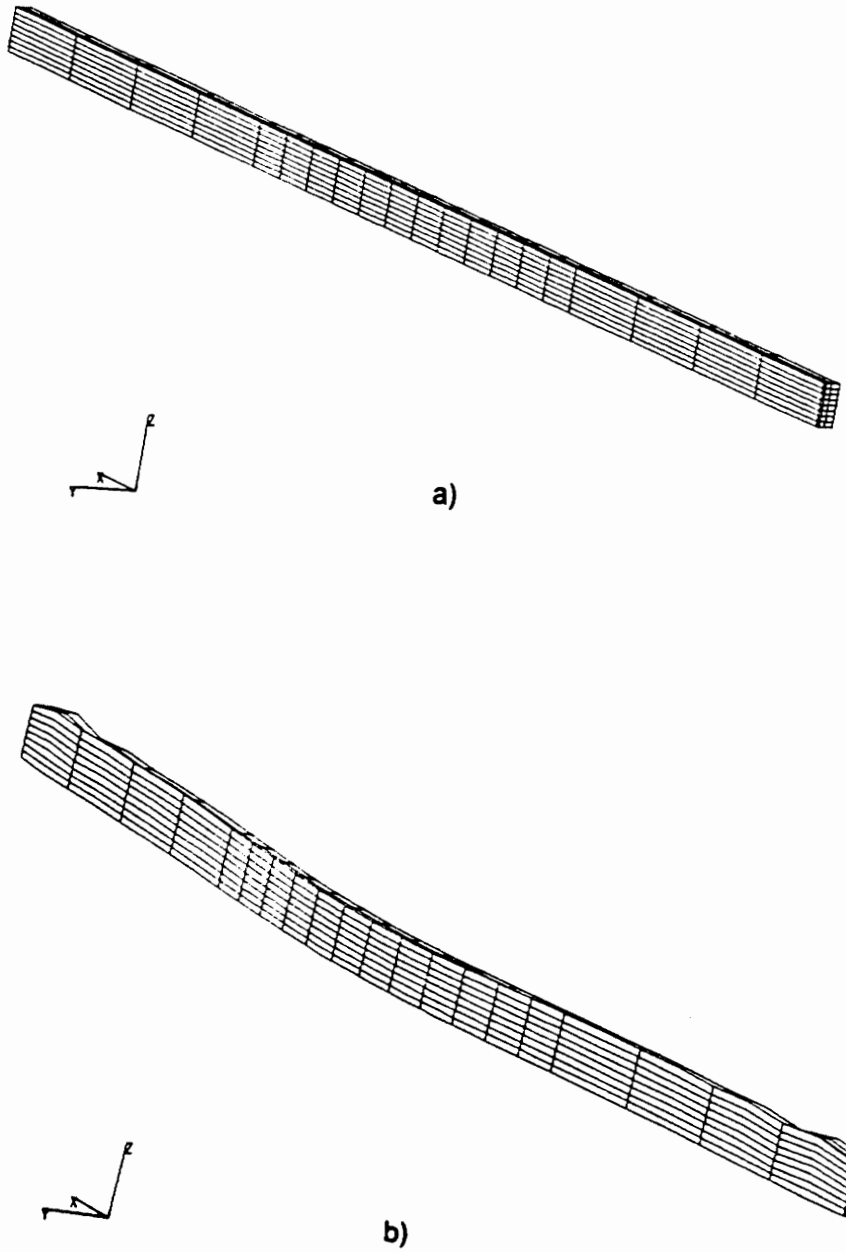

Figure 74. **Straight Edge Models for $[\pm 15_n/\pm 45_n]_s$ near Six-Inch Diameter Hole:** a) Undeformed b) Deformed

thickness stress distributions are presented in Figure 75a), b) and c). From Figure 75a), the locations of interest for the the interlaminar normal stress were identified as the laminate mid-plane, and the interface between the $\pm 45°$ layers. Because the Poisson's ratio mismatch between the $\pm 15°$ and $\pm 45°$ orientations is not as strong as that between 0° and 90° layers, this stress component is lower in magnitude than for the cross-plies. The largest stress magnitudes were along the mid-plane and reached a maximum of less than 5% of the normalization stress. Reductions in the peak magnitudes of the stress attributable to the presence of the nearby six-inch diameter hole were determined to be greatest at the laminate mid-plane and diminished quickly through the laminate.

The presence of steps in the through-the-thickness σ_z distribution is unsettling. Because of the dominance of x-z plane shearing and the fact that a 20-node element can only adequately predict a linear stress distribution, more compliant elements or a greater number of elements might have eliminated these steps. Recent work reported by Zahlan (1990) raised the possibility that more than two 20-node elements through a material layer are required some loading conditions. The use of two 20-node elements per ply is not an inherent assumption of this global/local analysis technique. Since the main thrust of the present work was to develop and verify this technique for general laminates, these steps are noted as a limitation of the element selection and not of the technique itself.

From Figure 75b), the interface of interest for τ_{yz} was identified as the interface between the -15° and 45° layers. Throughout this figure, the stress field exhibited several sign reversals, but at all locations its magnitude was small, less than 2% of the normalization stress. The presence of the hole has a moderate effect on the through-the-thickness distribution of this component which will be discussed later.

The remaining stress component to be considered is τ_{xz}. Because this laminate is composed entirely of off-axis plies, it is expected that this component would be dominant, and it is. A near zero stress can be found near the mid-plane and top of the laminate in Figure 75c). Also in this figure it is seen that high stress gradients appear on either side of each interface through the laminate thickness

at z = 0.0125 in., z = 0.025 in., and z = 0.0375 in. At the z = 0.0375 in. interface (between the ± 15° layers), the reported peak stress reached 30% of the normalization stress, while at the z = 0.0125 in. interface (between the ± 45° layers), it reached 4% of the normalization stress. The ± 15° layers have a higher in-plane stiffness than the ± 45° layers and will therefore resist the same end-shortening displacement to a greater degree, resulting in larger interlaminar stresses. Because stronger shear coupling also exists between these layers, the sharper and stronger peak at this interface is not unexpected. In addition, the stress reduction because of the nearby hole is strongest at this interface and decreases in influence as the z-location of the interfaces approaches the laminate mid-plane. It can also be seen that the shear stress values at the interface between the material layer groups are negative, while at the interfaces inside the layer groups the stresses are tensile. These sign reversals are consistent with the change in sign of the localized in-plane coefficient of mutual influence through the laminate thickness.

Previous interlaminar free edge stress distributions for the cross-ply and angle-ply laminates were affected by the presence of the nearby hole in a symmetric fashion about the centerline of the hole. However, two of the three in-plane stress distributions presented have asymmetric distributions. These are shown in Figure 76a) and b), which are the in-plane distributions of the interlaminar normal stress at the integration points nearest the mid-plane and at the ± 45° interface, respectively. As the z-location increases from the mid-plane, σ_z decreases in value from 2.3% of the in-plane normal stress predicted by classical lamination theory (Figure 76a) to 1.0% at the far edges of this localized region (Figure 76b). From the through-the-thickness distribution in Figure 75a), steps in the interlaminar normal stress were noted for this laminate, so these reported values are somewhat suspect. The in-plane distributions for one of the interlaminar shear stress components (τ_{yz}) is presented in Figure 76c) and can be seen to have a symmetric distribution about the centerline of the hole at this interfacial location, although there is a strong asymmetry predicted for this stress component at other locations through the laminate. A peak magnitude of nearly 1% of the normalization stress was predicted by the analyses.

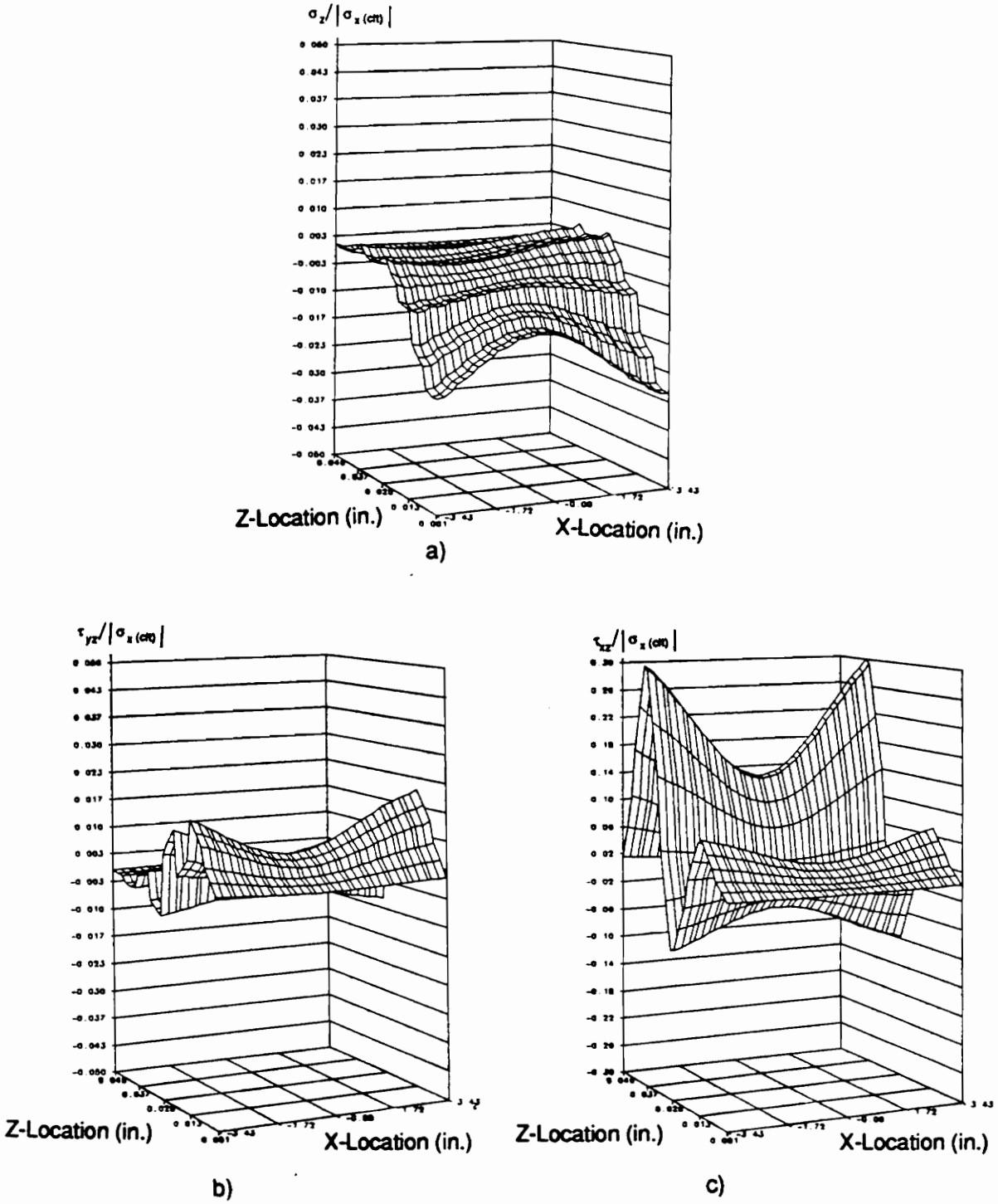

Figure 75. Through-the-Thickness Stresses for Straight Edge Model for $[\pm 15_n/\pm 45_n]_s$ near Six-Inch Diameter Hole: a) σ_z b) τ_{yz} c) τ_{xz}

Both of these stress components are small in magnitude throughout this laminate, and do not arise in-plane until the final row of elements at the free edge. The asymmetric distributions of these stresses were unexpected and could possibly be due to the changing load path around the hole and how this manifests itself in transverse shear through the laminate, or possibly the difficulty in satisfying the traction-free boundary conditions with classical displacement-based finite elements. Further mesh refinement, or even the selection of higher-order elements, would be advisable in this region, before firm statements can be made about the origin of this effect.

The interlaminar shear stress (τ_{xz}) in-plane distributions at the three ply interfaces are presented in Figure 77a), b), and c) in order of increasing z-location. For each of these distributions, there are large gradients in the elements nearest the free edge, suggesting again the existence of a stress singularity. Comparing these three distributions, their shapes and magnitudes change through the laminate. At the $\pm 45°$ and $\pm 15°$ interfaces (Figure 77a) and Figure 77c), respectively), the character of these curves for a given x-location is similar to that for the $[\pm 45_{2n}]_s$ and $[\pm 15_{2n}]_s$ laminates investigated earlier. The stronger interlaminar effect for the $\pm 15°$ plies is clearly discernible, as is the greater influence the hole. Since shear coupling between the plies is dependent on the order and magnitude of the ply angles at the interface, the effect in a given $\pm\Theta$ group will be dependent on the value of Θ. At $z = 0.025$ in., the plies above and below this interface are -15° and +45°, respectively. The shear coupling between these plies is opposite to the other interfaces, which is reflected in Figure 77b). This is the only interface whose distribution is not symmetric about the centerline of the hole for this stress component, so it would appear that the change in the load path around the hole and through the laminate thickness appears to affect the -15°/45° interface more than the other interfaces. Since the interlaminar normal stress at the mid-plane is directly dependent on those effects at the $z = 0.0125$ in. interface, and partially on those effects at the $z = 0.025$ in. interface, its asymmetry could be attributable to the -15°/45° interface.

The complex stress state of the $[\pm 15_n/\pm 45_n]_s$ laminate was examined in detail to demonstrate two issues. As this lamination sequence is a mixture of the other angle-ply lamination sequences under consideration, the resulting stress field should resemble the other stress fields but still contain the

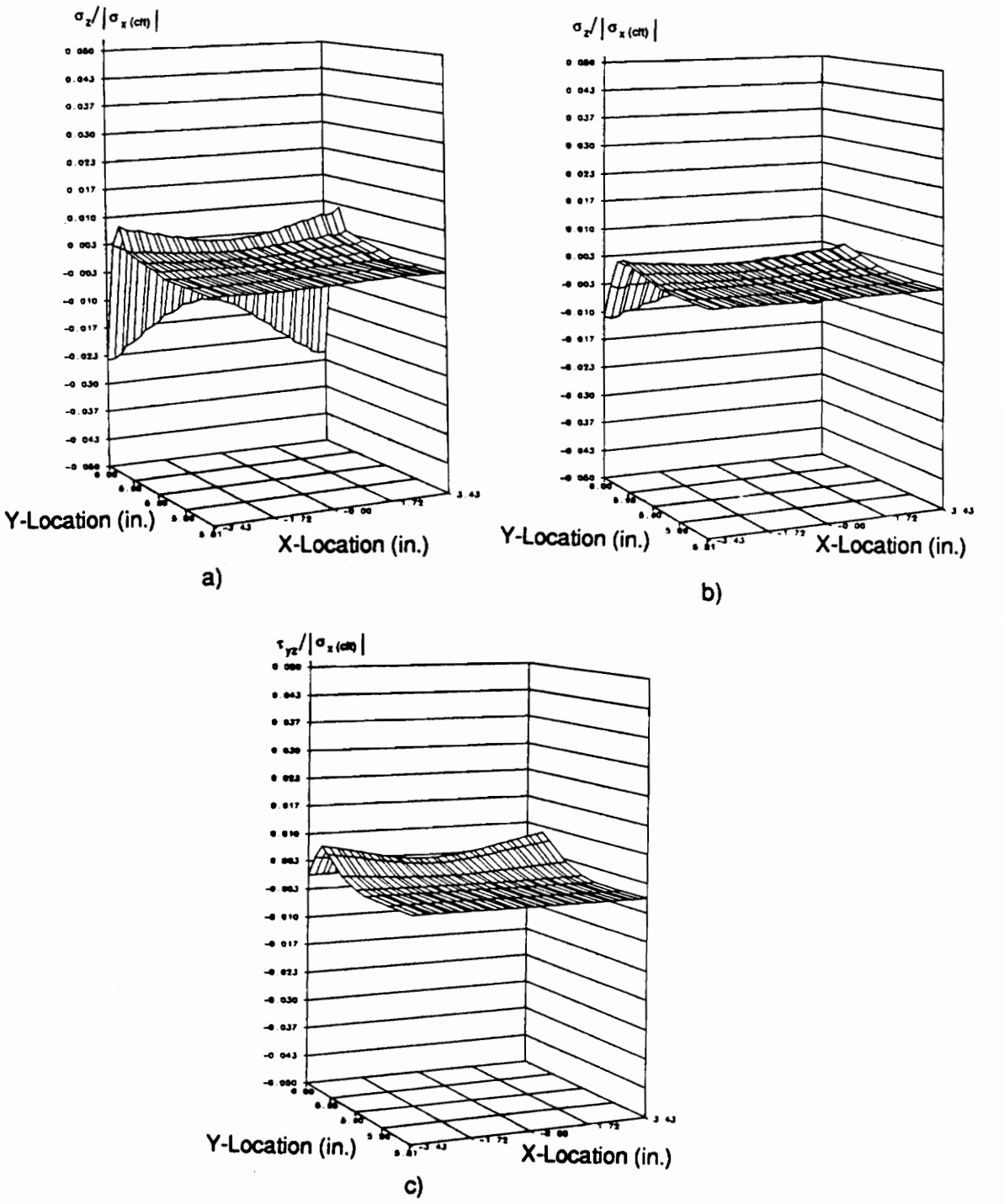

Figure 76. Stress Distributions for $[\pm 15_n/\pm 45_n]_s$ near Six-Inch Diameter Hole: a) σ_z at Mid-plane b) σ_z at z = 0.0125 in. c) τ_{yz} at z = 0.0125 in.

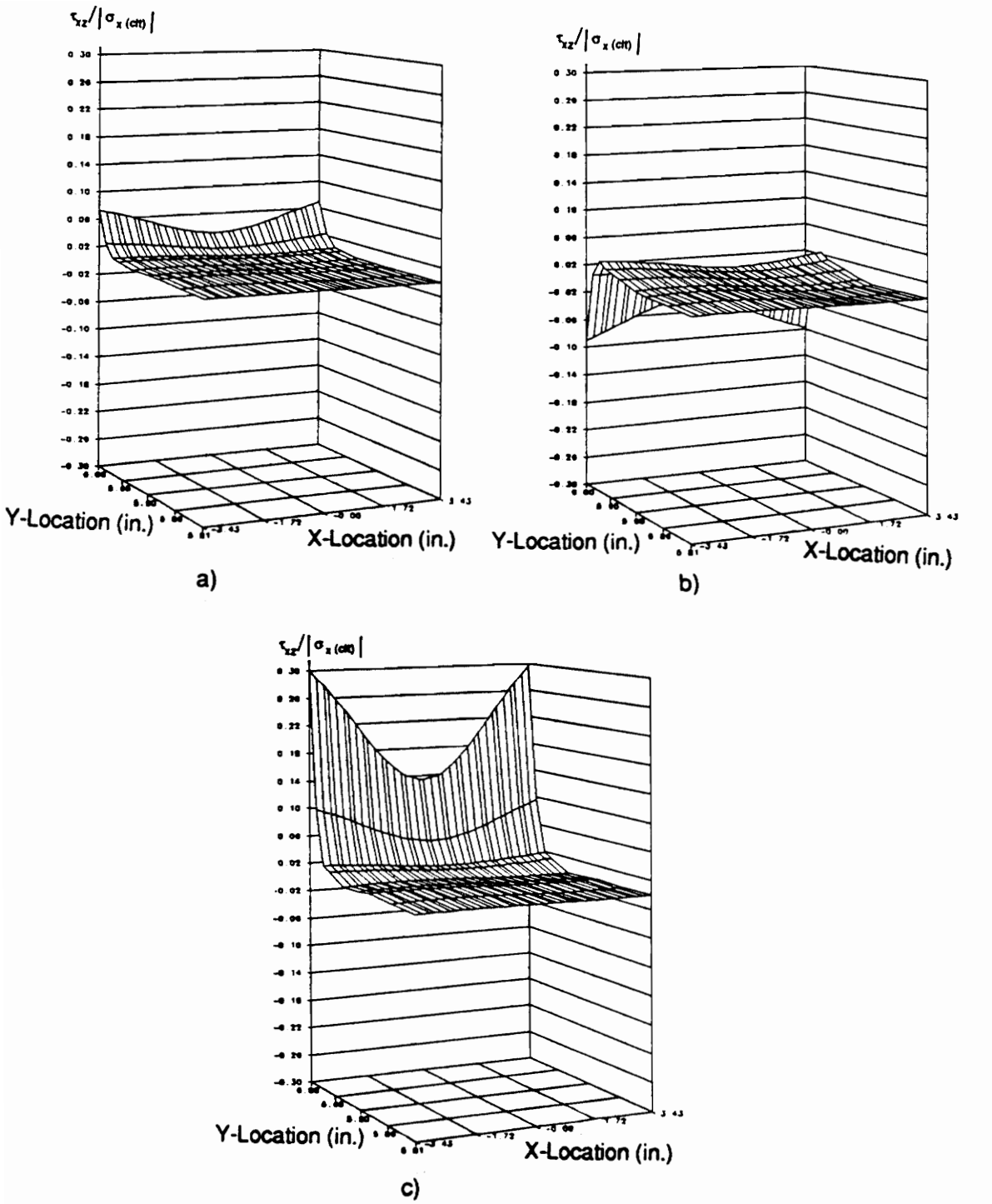

Figure 77. τ_{xz} **for Straight Edge Model for** $[\pm 15_n/\pm 45_n]_s$ **near Six-Inch Diameter Hole:** a) At z = 0.0125 in. b) At z = 0.025 in. c) At z = 0.0375 in.

effect of the Poisson's ratio mismatch not found in simpler lamination sequences. Trust in the global/local method is then gained before consideration of quasi-isotropic laminates. Quasi-isotropic laminates are used often in structural components, because their in-plane response is nearly isotropic in nature. Like the $[\pm 15_n/\pm 45_n]_S$ stacking sequence, quasi-isotropic laminates exhibit both shear coupling and Poisson's effects through their thickness due to the different layers that comprise the laminate. It will be clearly demonstrated with this global/local analysis that the interlaminar stress fields can be fairly complex, and not necessarily negligible.

The undeformed and deformed local straight edge models for the $[0_n/\pm 45_n/90_n]_S$ laminate with a six-inch diameter hole are presented in Figure 78a) and b). The deformed view of this local model hints at the complex interlaminar strain state that exists. Because of the proximity of the six-inch diameter hole to the straight edge, the elements in the central area of the model bow outward away from the hole. Along the free edge, those elements which form the 90° plies immediately above the laminate mid-plane are severely compacted, with less compaction in the central portion of the model near the hole. Those elements nearest the top free surface represent the 0° layer and are greatly contracted toward the laminate mid-plane. With the displacement scaling selected, the final row of elements is contracted sharply downward, giving the illusion of a beveled edge.

Examination of the through-the-thickness interlaminar stress distributions for this lamination sequence reveals the interfaces of interest for the interlaminar normal stress (σ_z) and the interlaminar shear stresses, τ_{yz} and τ_{xz}, in Figure 79a), b), and c), respectively. Considerable through-the-thickness variation for each stress component was predicted. The σ_z magnitudes are strongly negative at the mid-plane and increase in value with z-location, reaching a slightly positive value at the 0°/45° interface before becoming zero at the top of the laminate. The six-inch diameter hole at the center of the plate reduces the magnitude of this component symmetrically about the centerline of the hole throughout the laminate half-thickness, with its strongest effect at the laminate mid-plane. Locations of interest for σ_z are identified from the through-the-thickness distribution as the mid-plane and all the ply interfaces.

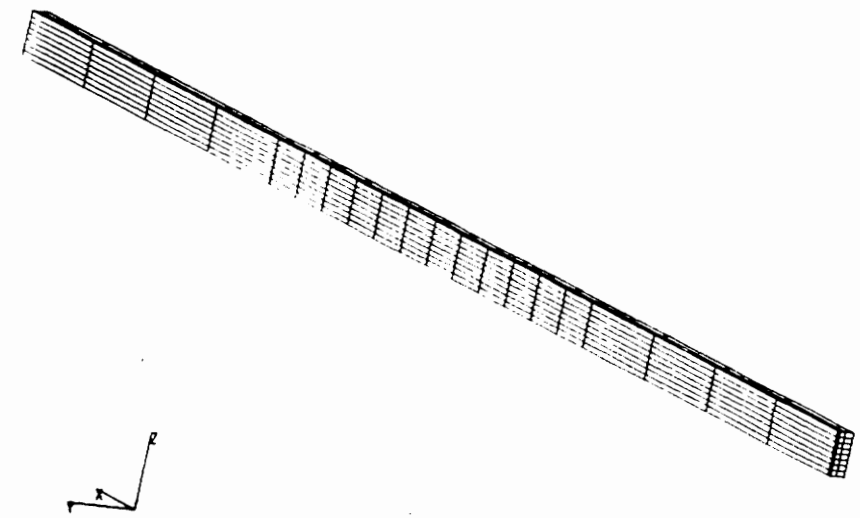

a)

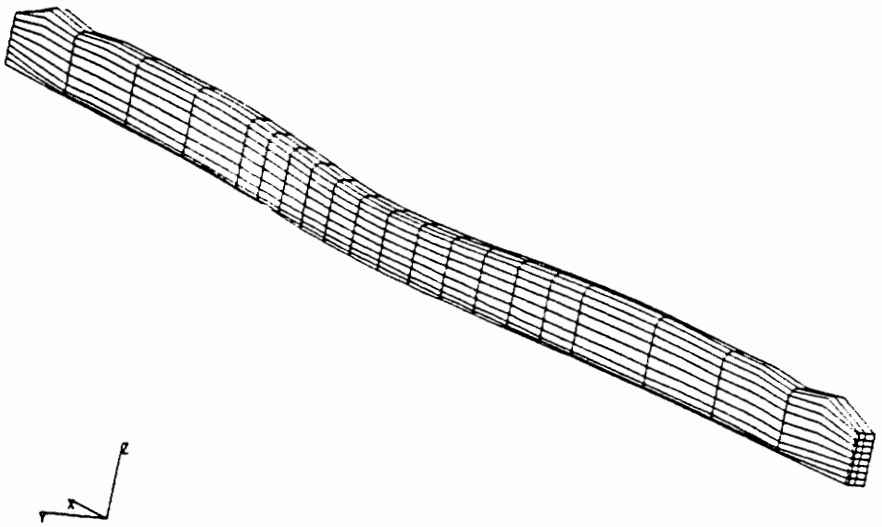

b)

Figure 78. Straight Edge Models for $[0_n/\pm 45_n/90_n]_s$ near Six-Inch Diameter Hole: a) Undeformed b) Deformed

As shown in Figure 79b), the magnitude of τ_{yz} changes from zero at the laminate mid-plane to a positive value at the -45°/90° interface, to a negative value at the 45°/0° interface, and back to zero at the top of the laminate. All of the ply interfaces will be investigated further. The reduction in the magnitude of the stress component attributable to the presence of the hole appears sharpest at the -45°/90° interface at z = 0.0125 in.

It would be expected that the interlaminar shear stress (τ_{xz}), which arises because of shear coupling, would be maximum through the laminate at the ± 15° interface, where shear coupling is also a maximum. In Figure 79c), this is seen to be the case. At the other ply interfaces, there are peaks in the stress which are smaller in magnitude. This stress component is zero at the mid-plane and top of the laminate. Two smaller peaks exist at the -45°/90° interface and the 0°/45° interface which are opposite in character to those at the ±45° interface. Again, the effect of the nearby hole is to reduce the magnitude of the stresses symmetrically about the centerline of the hole, and this reduction is strongest at the interfacial location of the maximum stress. All interfaces are to be examined in further detail for this component.

In Figure 80a), the mid-plane interlaminar normal stress distribution for the quasi-isotropic laminate resembles that for the cross-ply laminates. At the edges of the localized area, this component is reported to be 22% of the normalization stress, while stress reduction because of the nearby hole causes the stress to drop to 8% of the normalization stress. At the mid-plane, this stress reduction is symmetric about the centerline of the hole. In Figure 80b), the distribution at z = 0.0125 in., which is the -45°/90° interface, is presented. The shape of the predicted character of σ_z at this location is similar to that at the mid-plane but reduced in magnitude, with the peak stress at this location slightly more than half that found at the mid-plane. Again the presence of the hole in the laminate alters the stress distribution symmetrically about the centerline of the hole, and causes this stress to drop from 12% to 5% of the normalization stress. Figure 80c) is the in-plane σ_z distribution at the interface between the ±45° layers (z = 0.025 in.). At this interface, there is a reversal in the sign of the peak stress value, and a further reduction in magnitude compared to the previously mentioned interfaces. The positive value here would suggest expansion of the layers, however, the

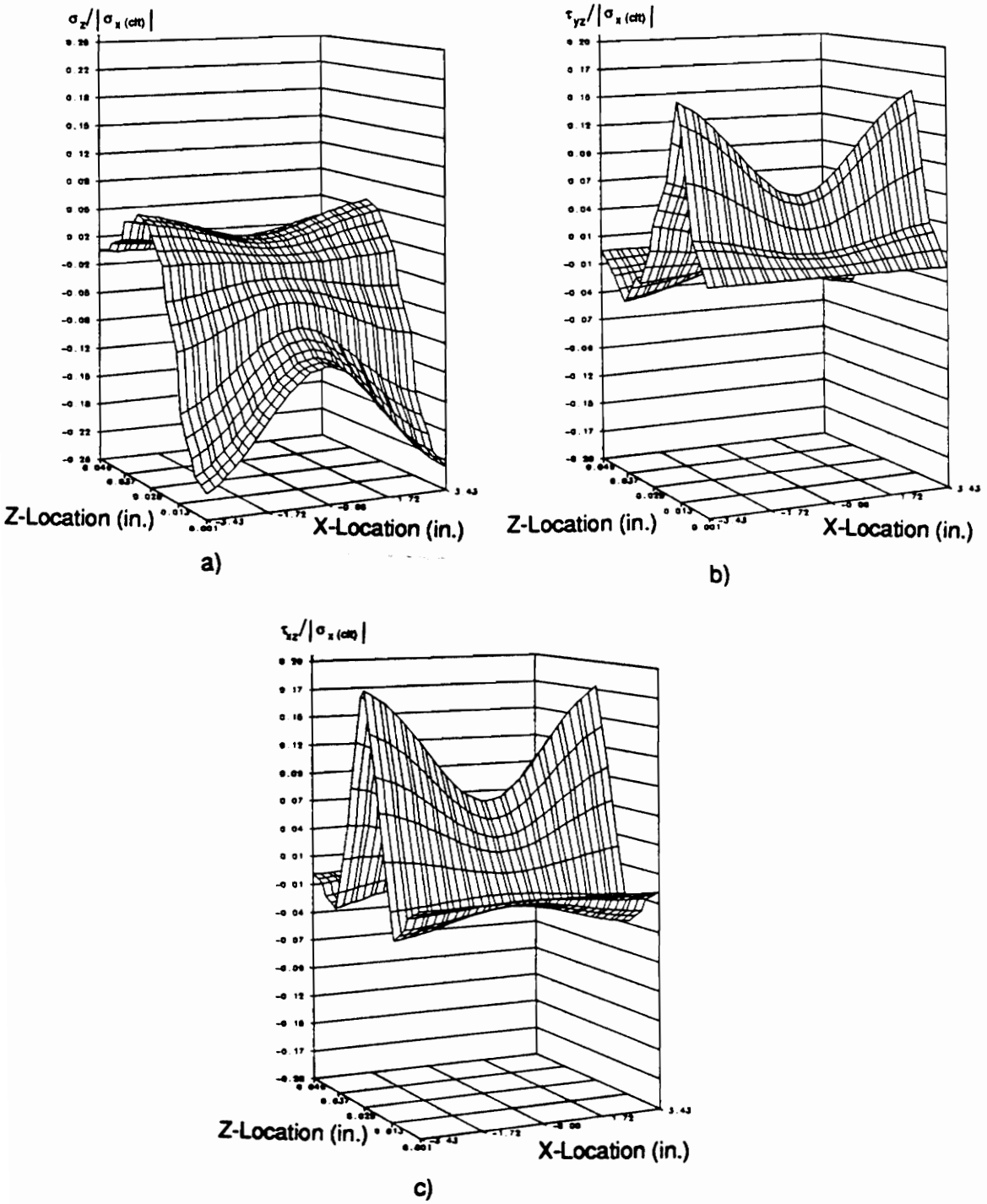

Figure 79. Through-the-Thickness Stresses for $[0_n/\pm 45_n/90_n]_s$ near Six-Inch Diameter Hole: a) σ_z b) τ_{yz} c) σ_{xz}

magnitude of the stresses here is nearly 25% of the mid-plane values. This suggests that while there are tensile values, the deformation state may not strongly reflect this expansion because of the strong element contraction found at the the mid-plane. The stress distribution for the final interface of interest, the 0°/45° interface at z = 0.0375 in., is presented in Figure 80d). The in-plane distribution here is similar to the z = 0.025 in. interface with slight tensile stresses at the free edge. As was shown in the through-the-thickness σ_z distribution, the magnitude of the stresses is reduced and the effect of the nearby hole is very small at this interface.

Figure 81a), b) and c) contain the interfacial in-plane distributions of the interlaminar shear stress (τ_{yz}) for the $[0_n/\pm 45_n/90_n]_s$ laminate near a six-inch diameter hole at z = 0.0125 in., z = 0.025 in., and z = 0.0375 in., respectively. The decay in magnitude of the stresses through the laminate half-thickness is evident from a cursory examination of these distributions. In Figure 81a), the distribution of τ_{yz} at the -45°/90° interface is presented. The reduction in stress due to the nearby hole appears symmetric over the centerline of the hole, with a 55% reduction from the maximum value presented. Of all the interfaces under consideration, this one has the highest magnitude for this component. The interlaminar effect is confined to one laminate thickness in depth from the free edge with high stress gradients over this region. However, those elements closest to the free edge contain stress values which appear quite different in character. The row of elements closer to the global/local boundary has stress values which would appear to grow without bound, but those nearest the free edge have a moderate slope. The possibility remains that an insufficient number of elements through a particular ply was used for this loading situation and mesh refinement studies should be completed prior to any firm conclusions.

The next interface under consideration is the ±45° interface at z-location z = 0.0125 in. The stresses at this interface are presented in Figure 81b). Comparing this figure to the previous one reveals the change in character of this stress component through the laminate thickness. The previous interface under consideration had steeper stress gradients through the boundary layer which were also opposite in sign over the row of elements closest to the free edge. The maximum values are lower, reaching a high of 0.7% times the normalization stress at the far edges of the localized region as

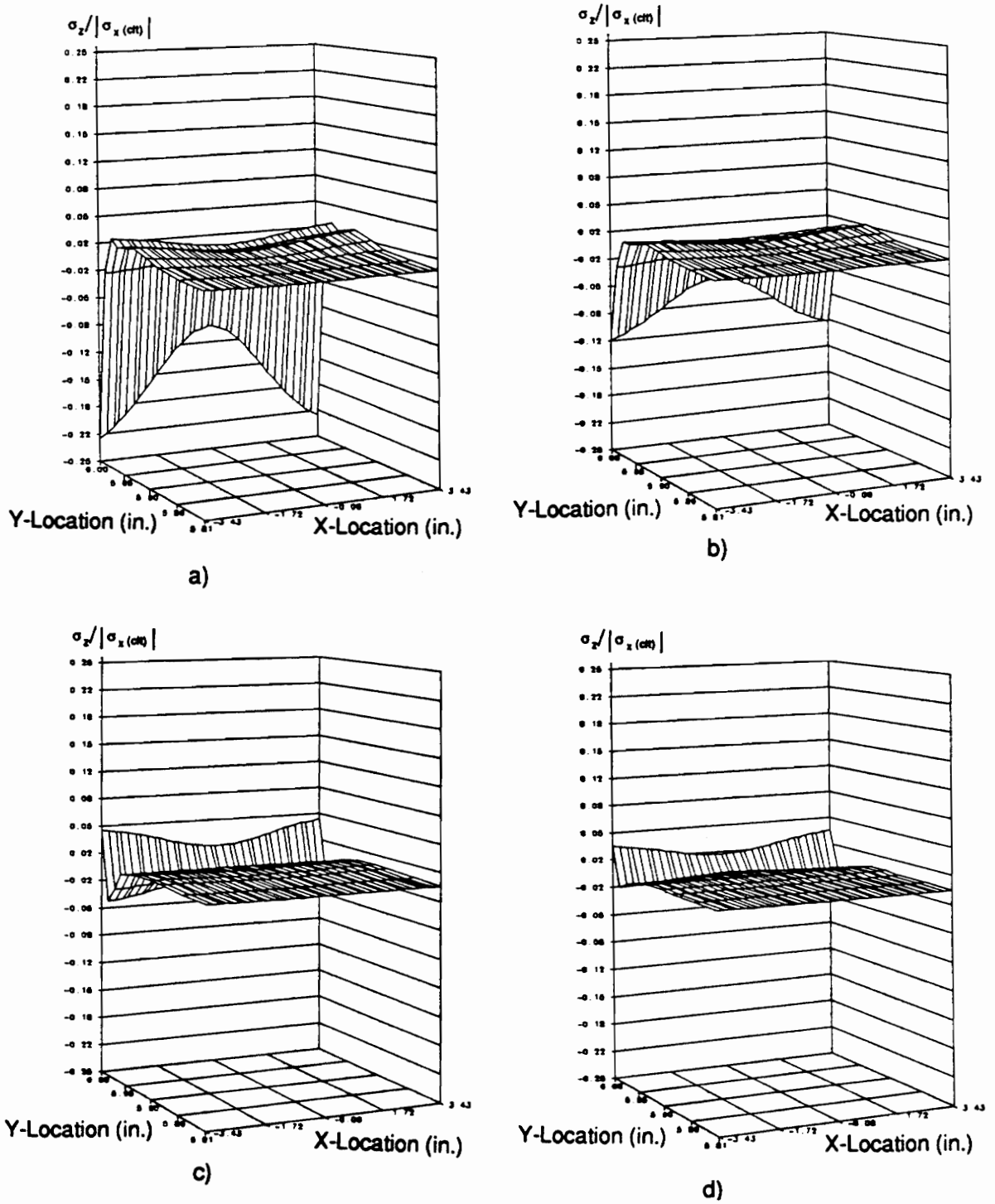

Figure 80. σ_z **for** $[0_n/\pm 45_n/90_n]_s$ **near Six-Inch Diameter Hole:** a) At Mid-plane b) At z = 0.0125 in. c) At z = 0.025 in. d) At z = 0.0375 in.

opposed to 0.15%. Again the stress reduction in the central region of the plate due to the nearby hole is evident. While not visible from the viewing angle selected, this reduction is not symmetric about the centerline of the hole.

Figure 81c) contains the in-plane stress distribution of τ_{yz} at the 45°/0° interface. A zero stress is reported until the final row of elements at the free edge, which exhibit steep negative gradients. From the viewing angle selected, it can be seen that there is a stress reduction effect attributable to the nearby six-inch diameter hole. However, it is not visible that this reduction in stress is not symmetric about the hole centerline. The shape of this distribution is different from the other interfaces in this laminate.

The final interlaminar straight edge stress component to be presented is τ_{xz}. Figure 82a) contains the in-plane distribution for this component at $z = 0.0125$ in., or at the -45°/90° ply interface. While there is some shear coupling between the 90° and -45° plies, this stress is zero over much of the local model at this interface. The rapid growth of this component over the row of elements closest to the free edge would suggest that either further discretization or the use of elements which satisfy the traction-free boundary condition exactly would alter its reported shape and magnitude. At the far edges of the localized region, a maximum magnitude of 2% of the normalization stress is realized. The view of the hole effect is obscured by the choice of viewing angle, but careful examination of Figure 82a) suggests that there is some reduction in this stress component.

At $z = 0.025$ in., or the $\pm 45°$ interface, τ_{xz} is much larger in magnitude than the previous interface and exhibits a shape not unlike the $[\pm 45_{2n}]_S$ laminate. Shear coupling is strongest between the $\pm 45°$ layers than the other layers in this laminate, and therefore is the interface where the largest magnitudes of this stress component occur. Nonzero stress values are found only within one laminate thickness of the free edge, showing that the global/local analysis technique used to compute these results determined correctly that the expected interlaminar influence is confined to this region. From this figure, the strong influence of the nearby hole is seen to reduce this stress component

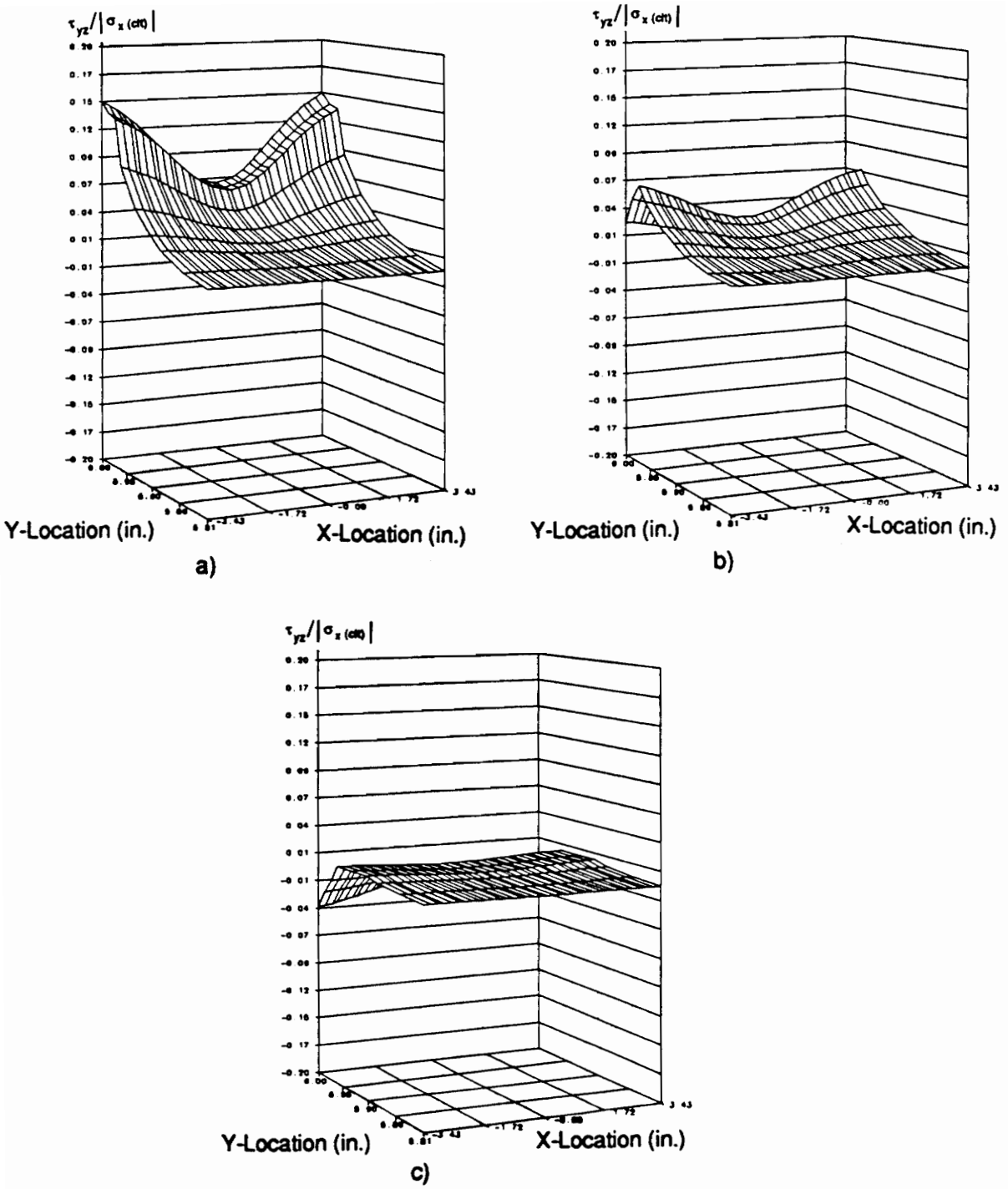

Figure 81. τ_{yz} for $[0_n/\pm 45_n/90_n]_s$ near Six-Inch Diameter Hole: a) At z = 0.0125 in. b) At z = 0.025 in. c) At z = 0.0375 in.

symmetrically about the centerline of the hole from a peak value of 17% to 8% of the normalization stress.

The remaining interface to be considered is that between the 0°/-45° plies. The in-plane values for τ_{xz} at this interface are presented in Figure 82c). As for the first interface considered for this stress component, the magnitudes reported here are small. Like the 90°/-45° interface, τ_{xz} is nonzero only over the final row of elements along the straight free edge. It is interesting to note that there is an asymmetric distribution about the centerline of the hole which is visible in this figure.

Examination of the interlaminar stress fields along the straight edge for the quasi-isotropic lamination sequence suggested quite definitively that while its in-plane response is isotropic, there is a strong interlaminar response. The interlaminar normal stress exists through the laminate thickness as does both of the interlaminar shear stresses. It was interesting to note that asymmetric distributions about the centerline of the hole were found for several locations for this laminate and all of the stress components. Further examination would be required before firm conclusions of the origin of their asymmetric nature could be made.

5.3.2.3 Verification of Global/Local Modeling Technique for the Curved Edge

An unsuccessful attempt was made to verify the local curved edge model stress fields with a complete three-dimensional model of the $[\pm 15_{2n}]_s$ plate with a six-inch diameter hole. The validity of the results generated by the global/local finite element analysis procedure is therefore determined by a comparison of the trends in the interlaminar stress fields found with the global/local analysis technique to those described in the literature which were performed with other methods. Dana (1974) was one of the first investigators to apply three-dimensional finite element analysis to the determination of interlaminar stress distributions around holes in composite laminates. Tensile loads were applied to thick and thin $[\mp 45]_s$ laminates with holes. While the thickness ratios are not identical between this and the present work, similar interlaminar stress variations about holes

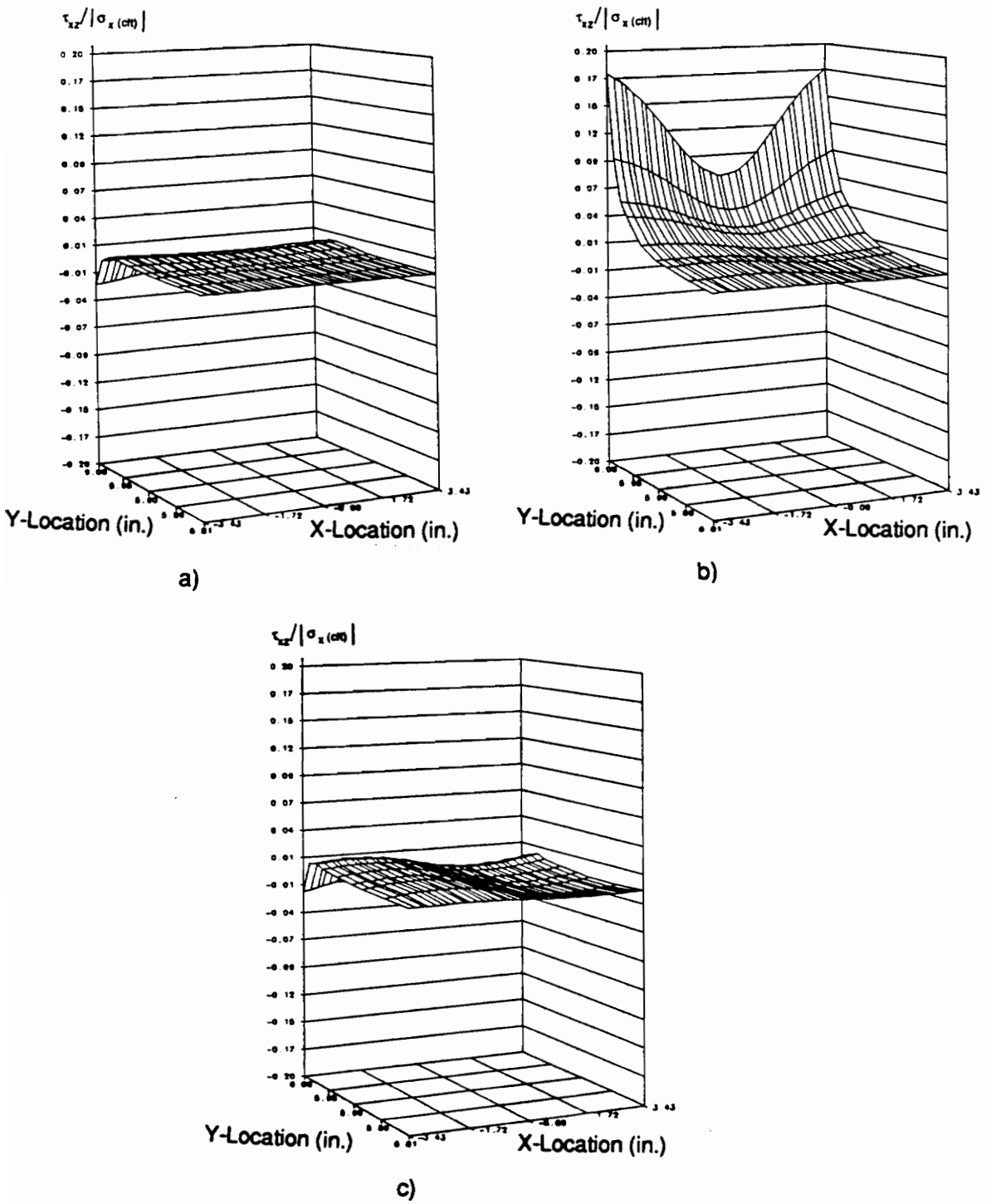

Figure 82. **Interlaminar Stress Distributions for $[0_n/\pm 45_n/90_n]_S$ near Six-Inch Diameter Hole:** a) τ_{xz} at z = 0.0125 in. b) τ_{xz} at z = 0.025 in. c) τ_{xz} at z = 0.0375 in.

in thin laminates were predicted. It was found that while the far-field laminate stacking sequence influenced the global stress state, the local interlaminar stress state was affected also by the effective lamination orientation around the hole. The effective stacking sequence relative to the hole surface changes around the hole because the global lamination sequence will be intersected at different angles by the curved edge. Even for laminates possessing only one type of interlaminar effect for the global lamination sequence, either Poisson's ratio mismatch or shear coupling, all three interlaminar stresses existed around the hole. Stress distributions through the laminate thickness were compared qualitatively for those angular positions presented. Agreement was good, but not exceptional. Because Dana's work was completed during the early 1970's, its efforts were limited by the available computational power, and the element discretization both in-plane and out are considerably coarser than the present study. Dana used three linear elements through plies, which was found by Vidussoni (1988) to be less accurate than two quadratic elements. Zahlan (1990) concluded that several quadratic elements are required through a ply thickness to determine the stress field, casting further shadows on these results. Burns et al (1985) also used three linear elements through a ply thickness to investigate a broader range of laminate orientations with holes. Comparison of these results to the present work is difficult because only thick laminates were considered. The fact that the global/local modeling technique for the cross-ply composite laminate was as accurate as could be expected, the belief is that any errors in the global/local angle-ply or quasi-isotropic laminate modeling will come about because of discretization problems, not the global/local analysis procedure since similar trends were found by other researchers.

5.3.2.4 Curved Free Edge Model Results

When the local curved free edge models were generated for the angle-ply and quasi-isotropic laminates, the entire region around the curved edge was modeled. To give the reader an understanding of the computational effort involved with these local models, initially undeformed and deformed views are presented for each of the $[\pm 15_{2n}]_S$ laminates in Figure 64 through Figure 66. From these

figures it is obvious that these models obscure the view of the hole edge, so several of the curved free edge models were cut in half and only the angular positions between 0° and 180° are presented. Each of these local models had its z-direction dimension multiplied by a factor of five to clearly reveal the through-the-thickness displacement and stress contour information. Any of the presented z-direction displacements were scaled by a factor of 100, while the in-plane displacements were scaled by a factor of 10.

Figure 64a) and b) contains the undeformed and deformed view of the entire curved edge model for a $[\pm 15_{2n}]_S$ laminate with a six-inch diameter hole. As noted previously, this model is extensive, with a large number of nodes and elements. The deformed global model had a rectangle of nodes bordering the curved edge region which exhibited both convexity and concavity, as shown in Figure 50b). These nodes are the global/local interfaces for the curved edge angle-ply local models, and it is these boundary conditions were applied to the local model and caused the hole to become noncircular, as seen in Figure 64b) for the local model. While the global model could only predict the noncircularity of the hole, the thickening and compaction around the hole was predicted by the local three-dimensional finite element model and presented for the deformed half-model view in Figure 83. The redistribution of the global compressive load because of the interruption of the global load path was manifested in the three-dimensional displacement or strain field in the local model. Furthermore, examination of this view reveals that the out-of-plane deformation field around holes in this laminate varies with angular position. This change in deformation appears to exhibit no symmetry about $\theta = 90°$ along the curved free edge and is irregular enough to be attributable to more than just the redistribution of the load path around the hole. Near the local x-axis, there is a strong compaction in those elements nearest the mid-plane of the laminates, while near $\theta = 90°$ there is both thickening and compaction of the elements through the laminate thickness. The three-dimensional character of this deformation state is not straightforward, as it is both a function of the change in load path and the effective stacking sequence around the hole. This precludes a strong reliance on intuition about the expected behavior around holes for angle-ply

laminates. Besides, if the deformation state is considered to be relatively complex, then the interlaminar stress state cannot be expected to straightforward either.

In Figure 84, all three interlaminar stress components through the laminate half-thickness are presented between $\theta = 0°$ and 180° at those integration points nearest the curved edge of the hole for the $[\pm 15_{2n}]_S$ laminate with a six-inch diameter hole. The interlaminar normal stress is nonzero around the hole, as seen in Figure 84a). Although there is no global Poisson's ratio mismatch for a $[\pm 15_{2n}]_S$ laminate, there is a change in the effective Poisson's ratio between the plies around the curved free edge of the hole. Those edges not locally parallel or perpendicular to the global axes will experience local stacking stacking sequences other than $[\pm\Theta]_S$. At $\theta = 0°$ and 90°, the localized lamination sequence will be a member of the $[\pm\Theta]_S$ family, and σ_z will be zero at the free edge through the thickness. At $\theta = 45°$ and 135°, the localized lamination sequence will be a $[\mp\Theta]_S$ laminate which also has no Poisson's ratio mismatch. Examination of Figure 84a) reveals that at these angular positions, the through-the-thickness distribution contains lines of zero stress. For other locations around the hole, σ_z is maximum at the mid-plane and decays to zero at the top free surface with an anti-symmetric distribution about $\theta = 90°$.

Figure 85 is a view of the deformed half-model with superimposed σ_z stress contours. The change in the sign of the stress contours near $\theta = 90°$ over a small area in this figure was also shown in the through-the-thickness distribution in the previous figure. This method of presenting the stress contours on the deformed view of the model offers further insight into the stress state that exists around the hole. Those angular positions where there is enlargement of the hole edge are where there are concentrations of positive interlaminar normal stress contours, while those locations where the hole edge is compacted are where there are many negative contours. At $\theta = 0°$ and 180°, there is compression of the elements both due to the in-plane and interlaminar effects. At the angular positions near $\theta = 90°$, the in-plane load causes expansion of the hole edge, while the localized Poisson's ratio mismatch causes both enlargement and compression of the elements nearest the hole edge. Further understanding of the complex interlaminar stress state around the hole requires examination of the other stress components.

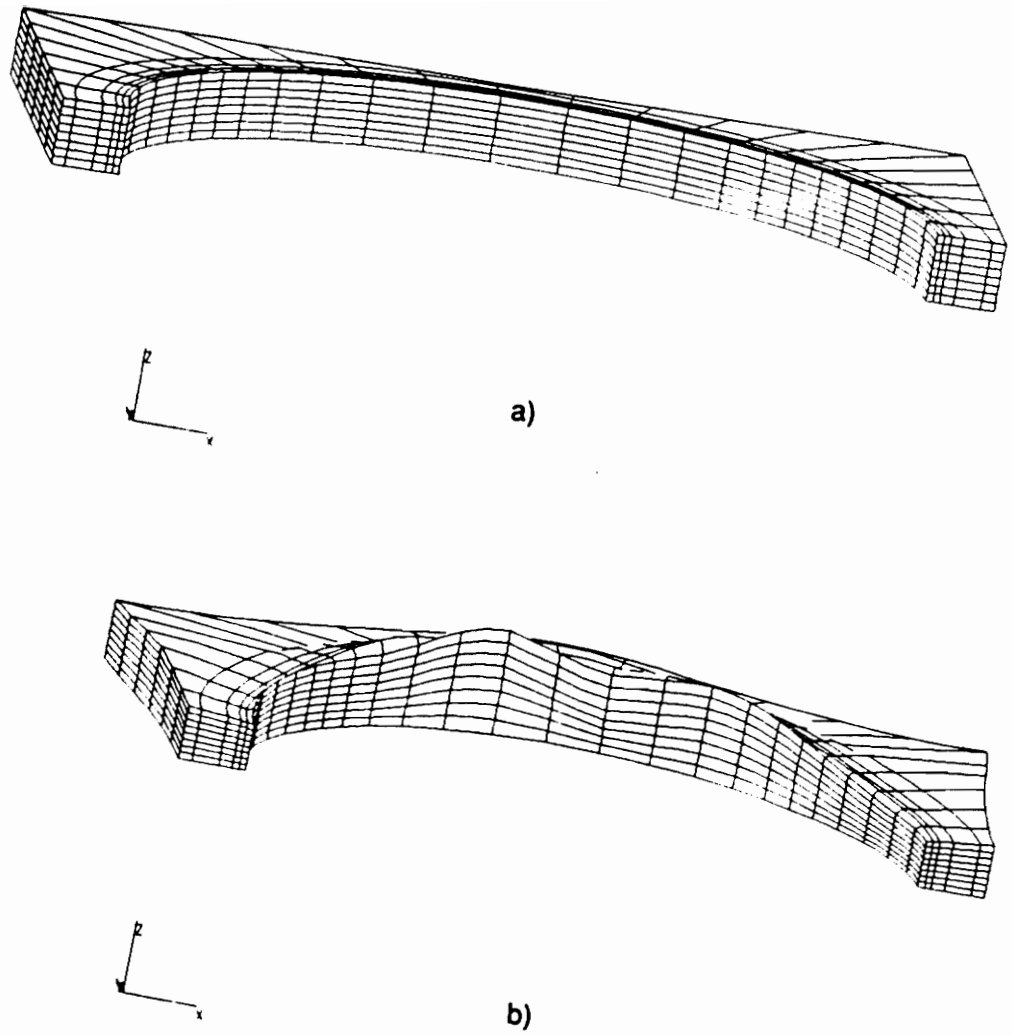

Figure 83. Partial Curved Edge Models for $[\pm 15_{2n}]_s$ around Six-Inch Diameter Hole: a) Undeformed b) Deformed

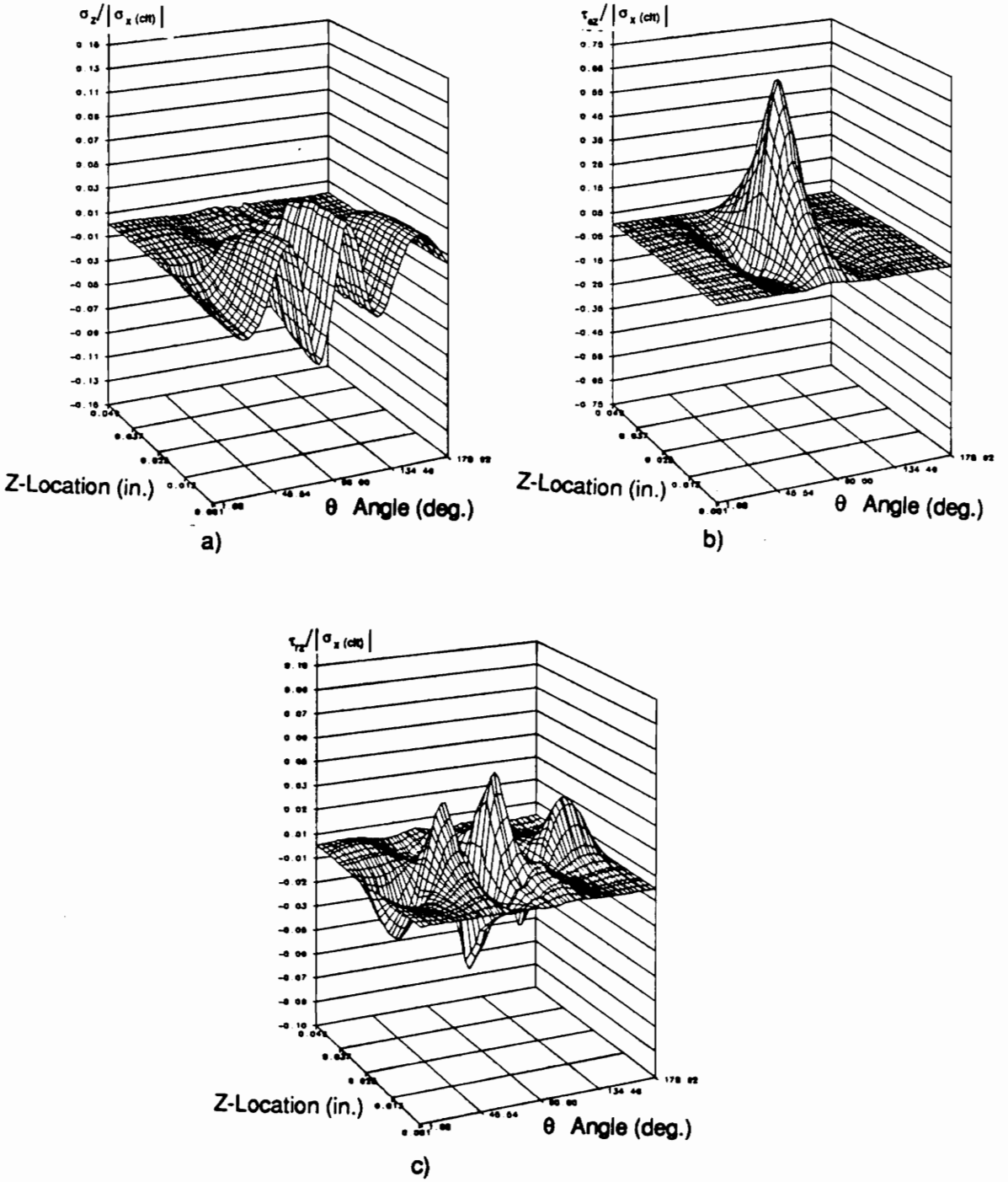

Figure 84. Through-the-Thickness Stresses for Partial Curved Edge Model for $[\pm 15_{2n}]_s$ around Six-Inch Diameter Hole: a) σ_z b) $\tau_{\theta z}$ c) τ_{rz}

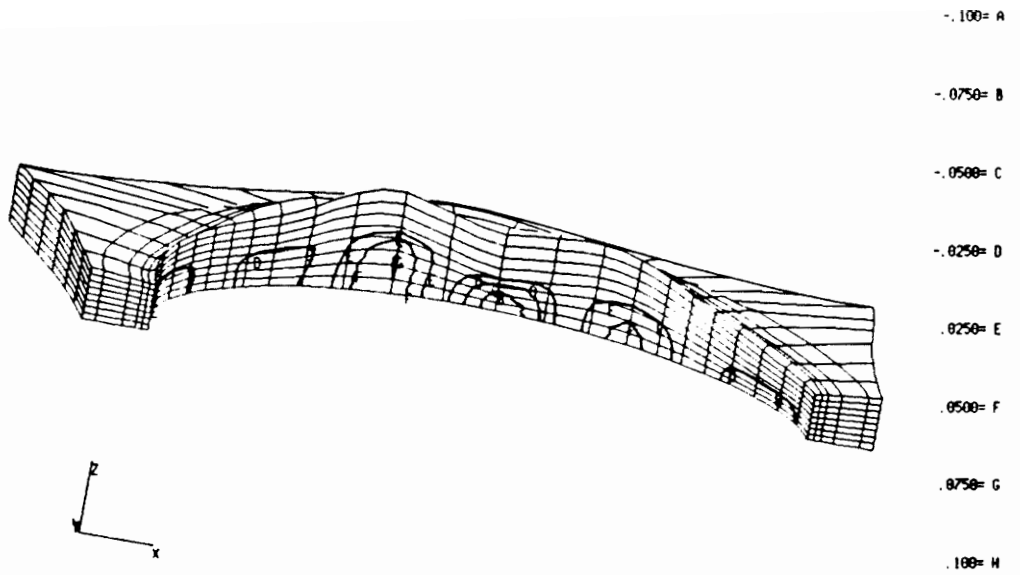

Figure 85. σ_z **Contours for Partial Curved Edge Model for** $[\pm 15_{2n}]_s$ **around Six-Inch Diameter Hole**

The through-the-thickness distribution of the interlaminar shear stress ($\tau_{\theta z}$) is presented in Figure 84b), while the stress contours for this stress component are found in Figure 86. The dominant feature of the through-the-thickness distribution was the highly concentrated stress peak found at $\theta = 90°$. This high concentration of stress is reflected in the stress contour distribution as well. Because of the changing load path around the hole, high stresses are found in the global x-direction at this position, and consequently, large interlaminar stresses are not unexpected in this area. These large stress values reflect the strong tendency for the plies to move past one another in the plane parallel to the z-axis in this region. Examination of the deformed half-model reveals that at the same positions where the elements are moving most relative to another in the deformed grid, the stress contours for $\tau_{\theta z}$ are highly concentrated.

The remaining interlaminar shear stress τ_{rz} through-the-thickness distribution is presented in Figure 84c), and its stress contours are shown in Figure 87 on the deformed half-model. This is the stress component which reflects the tendency of the hole diameter change through the laminate. From Figure 84c), the magnitudes of this stress component at this radial location are small, with a complex shape which varies greatly with angular position and height in the laminate. This radial location is inside the laminate, but close to the hole edge where equilibrium considerations require that this stress component reach a value of zero although displacement-based finite elements cannot enforce this condition exactly. Because of the proximity of these integration points to the hole edge, the predicted stresses should be smaller in magnitude. The change in sign and magnitude with angular position mimics that of the interlaminar normal stress. For those locations identified earlier where the effective lamination sequence is symmetric and balanced, τ_{rz} is zero through the local model thickness; at intermediate values of θ, maxima and minima exist at the interface between the plies. Examination of the deformed model with superimposed stress contours reveals that the concentrated stress contours are centered on the interface at angular positions where the local model is changing from expansion to compaction in the z-direction or from compaction to expansion. As the laminate changes its z-direction movement, those elements on either side of the interface would cause the hole diameter to either reduce or expand, if permitted to move freely. Since dis-

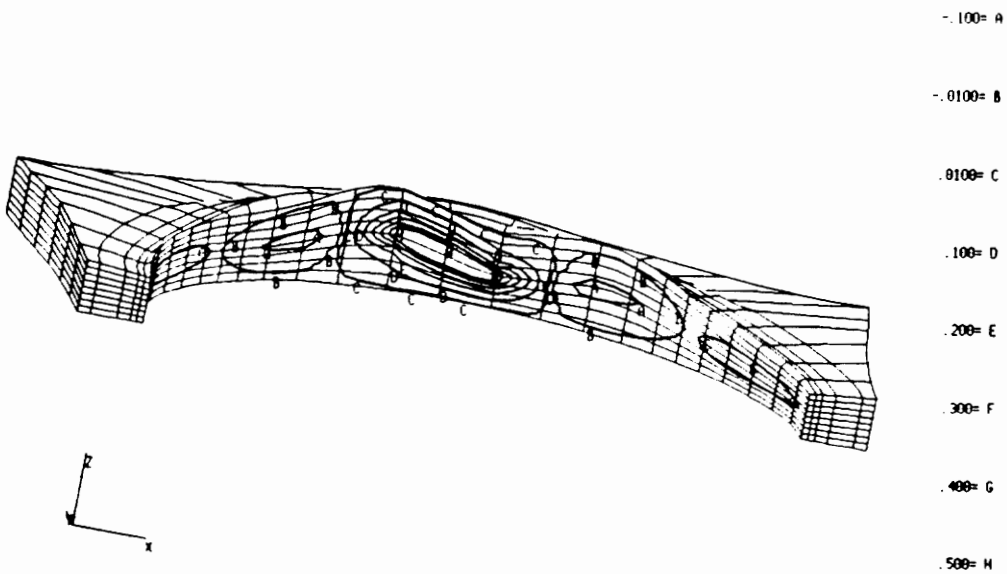

Figure 86. $\tau_{\theta z}$ **Contours for Partial Curved Edge Model for** $[\pm 15_{2n}]_s$ **around Six-Inch Diameter Hole**

placement compatibility must be enforced, this interlaminar stress component arises to constrain this motion.

The influence of the different diameter holes on the interlaminar stress field around the hole is considered for the $[\pm 15_{2n}]_S$ laminate for a six-, three-, and one-inch diameter hole in a 12 in. wide plate. From the through-the-thickness stress distributions for the interlaminar stresses around the six-inch diameter hole in Figure 84, locations of interest for each of the interlaminar stresses were identified. Incidentally, the distributions for the smaller diameter holes are not presented individually, but as compared to the other holes since their through-the-thickness distributions were similar. The peak location and its magnitude changed as a function of the hole diameter for the stress fields, as determined by this global/local technique.

Maximum values of the interlaminar normal stress were were predicted to exist at the integration points nearest the laminate mid-plane. Examination of σ_z for these three laminates reveals some interesting effects associated with the change in hole diameter (Figure 88) at the laminate mid-plane. The six-inch diameter hole stress distribution for this component is generally lower in magnitude than for the smaller holes, indicating that some redistribution of the load has occurred or that the stiffness of the plate is greatly reduced by the presence of this large hole. The stresses for the three-inch diameter hole are coincident with those for the six-inch diameter hole at the following angular locations: $0° < \theta < 25°$, $75° < \theta < 105°$, and $155° < \theta < 180°$. However, the peak magnitude is largest for the three-inch diameter hole and its exact location is shifted further away from $\theta = 90°$ than the six-inch diameter hole. Because of the reduced net section of the plate with the six-inch diameter hole, its compliance is less than the plate with a three-diameter hole. However, the three-inch diameter hole is near enough to the straight free edge that some of the stress field is relieved. In the previous chapter, the three-inch diameter hole was identified as being closer to a 'critical' hole diameter for the cross-ply stacking sequence and the geometric dimensions of the plate. It is also so identified for the angle-ply laminates. The distribution for the one-inch diameter hole does not resemble those for the other sized holes as closely. The location of the peak magnitude was shifted further from $\theta = 90°$ than the three- and six-inch diameter holes. Between

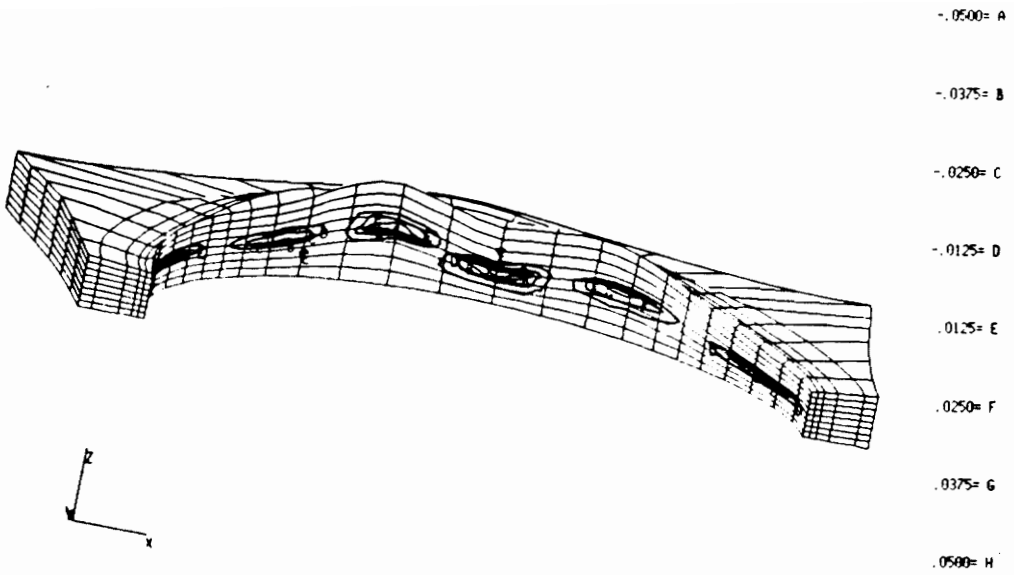

Figure 87. τ_{rz} **Contours for Partial Curved Edge Model for** $[\pm 15_{2n}]_s$ **around Six-Inch Diameter Hole**

$0° < \theta < 45°$ and $135° < \theta < 180°$, the stresses for the one-inch diameter hole did not track those for the larger holes. Since the one-inch diameter hole which has no effect on the straight edge displacement or stress field, then the distribution of stress could not be expected to be very similar to the distribution of stress for holes which interact with the straight free edge. There are, however, fewer elements in the one-inch diameter curved edge model, and there is a possibility that the local model nodal discretization could have been further refined to produce a fully converged solution. Further examination of more finely discretized models would determine which of these are dominating the stresses presented here.

The next component under consideration is the interlaminar shear stress ($\tau_{\theta z}$). From the through-the-thickness distributions in Figure 84b), its location of interest in the laminate was identified as the $z = 0.025$ in. interface. $\tau_{\theta z}$ stresses for all three hole diameters are presented in Figure 89a) and can be seen to be quite similar in character. The three-inch diameter hole had the largest stress at the centerline of the hole, which was roughly 10% larger than the peak found for the six-inch diameter hole, while the one-inch diameter hole had the lowest value, nearly 70% smaller than that for the three-inch diameter hole. With the six-inch diameter hole displacement field interacting with the nearby straight edge, and the one-inch diameter hole having no interaction at all, the three-inch diameter hole could possibly be close to a critical hole size for this plate. Again the one-inch diameter hole does not have the same sharp character in its distribution as the other holes, raising the possibility of a less than fully converged local model.

The peak magnitudes for τ_{rz} are ten times less than those for the previously considered interlaminar shear stress and on the same order as the interlaminar normal stress, as can be seen by comparing Figure 89a) and b) and and Figure 88. Figure 89b) contains the stress values found for all three local models at $z = 0.025$ in. From the through-the-thickness distribution for the remaining interlaminar stress (τ_{rz}) in Figure 84c), the stress distribution is seen to contain interesting variations. Near $\theta = 90°$, all exhibit both a negative and a positive peak and passes through zero at $\theta = 90°$. The location of the peak stresses near $\theta = 90°$ is closest to $\theta = 90°$ for the six-inch diameter hole, and shifts further away with decreasing hole diameter. The exact location and magnitude of

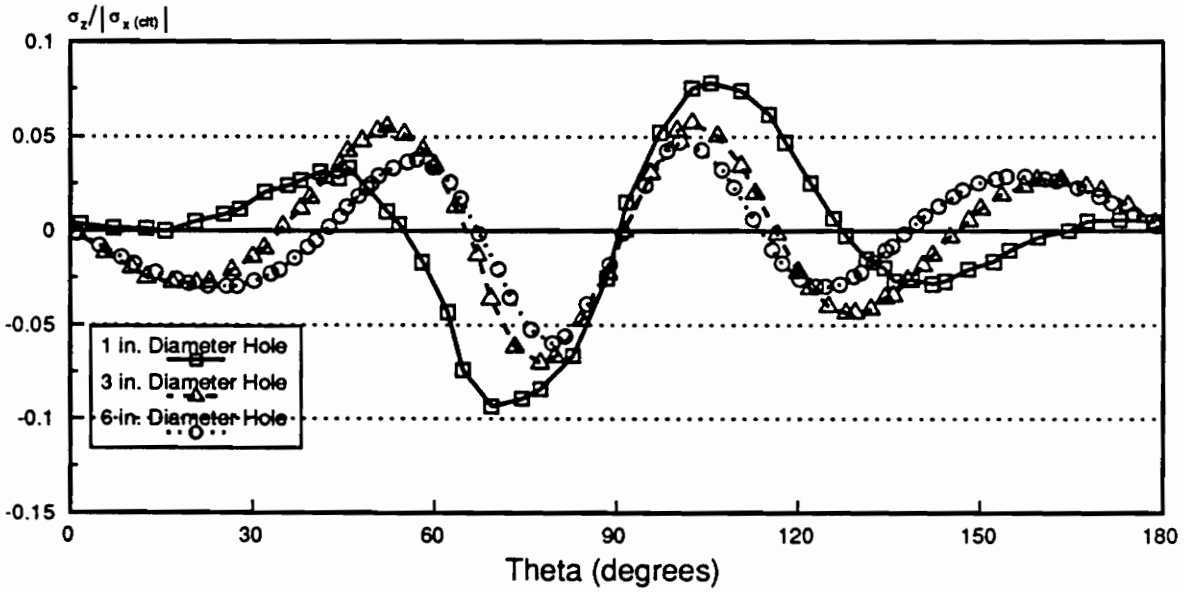

Figure 88. σ_z **around Hole for** $[\pm 15_{2n}]_s$ **for Different Holes Diameters:** a) At Mid-plane

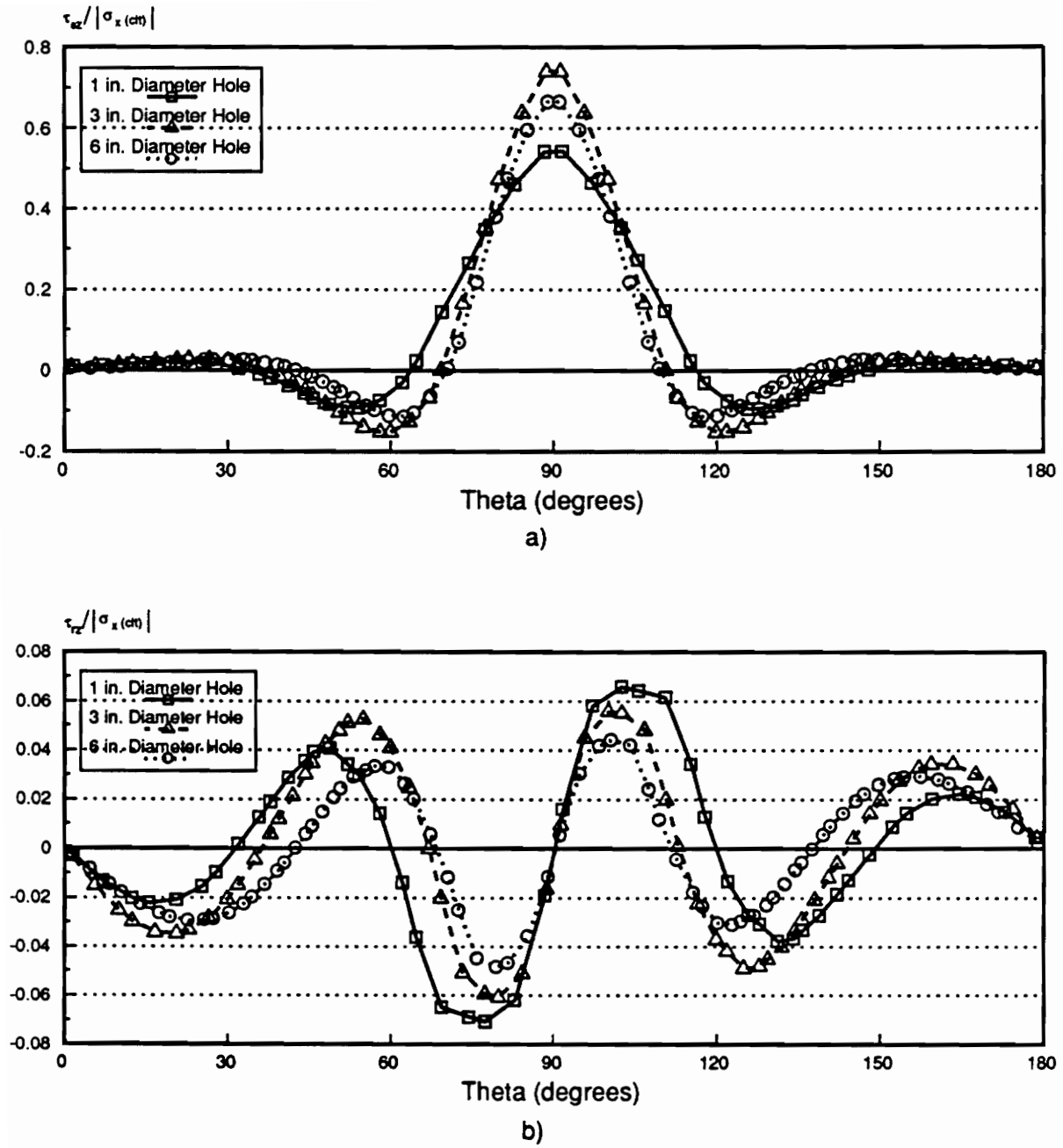

Figure 89. **Interlaminar Shear Stress Distributions at the Curved Free Edge for Different Hole Diameters:** a) $\tau_{\theta z}$ at z = 0.025 in. b) τ_{rz} at z = 0.025 in.

the apex of this curve for the one-inch diameter hole is difficult to determine exactly because of its rounded nature. With increasing hole diameter, the maximum stress in this region increases in magnitude. Considering the stresses near $\theta = 60°$ next, the effect of the change in hole diameter is less clear. The six-inch diameter hole has the lowest magnitude in this region, while the three-inch diameter hole has the largest. If the angular position of this peak stress for the three-inch diameter hole is taken as a reference, then the six-inch hole has its peak nearer $\theta = 90°$ with the one-inch diameter hole closer to $\theta = 0°$.

For the $[\pm 15_{2n}]_S$ laminate, the influence of increasing hole diameter in a finite-width plate is similar to the cross-ply laminates. The three- and six-inch diameter holes had the same distribution shape, while the six-inch diameter hole has a lower peak stress magnitude, suggesting that stress relief because of the presence of the nearby straight edge did occur. Deviations from the shape of the stresses for the other holes were found for the one-inch diameter hole. Because of its small size, it has no influence on the interlaminar stress fields at the free edge, and therefore no stress relief. However, firm conclusions about its exact nature should not be made until a further study with different levels of in-plane nodal discretization are completed. Such a study would be more tractable with the global/local method than with a full three-dimensional finite element analysis.

To further understand the interlaminar stress state in laminated plates, a $[\pm 45_{2n}]_S$ laminate with a six-inch diameter hole was modeled with this two-dimensional to three-dimensional global/local analysis technique. Most of the previous investigations of the interlaminar stress states at the straight free edge or around holes have included at least one $[\pm 45_{2n}]_S$ laminate, so a wide body of information about the predicted stress states are available. While the entire local model was used during the analysis, only the partial deformed model is presented in Figure 90b). The in-plane compressive global loading causes the plate to expand in thickness, but the elements near the hole edge at times expand and contract depending on the localized displacement state. Near $\theta = 0°$ and 180°, the elements within one laminate thickness of the hole edge undergo strong compaction toward the laminate mid-plane. As the elements under consideration are further from this region, the degree of compaction lessens until the elements begin to expand. Unlike the $[\pm 15_{2n}]_S$ laminate,

this change in thickness is smooth and gradual. The ply angles are originally perpendicular to each other, and while their local effective lamination sequence will change as a function of the angular position, their relative orientation to one another remains 90° apart. The interlaminar effects due to the Poisson's ratio mismatch and the shear coupling between the layers can be described as functions of sin(θ) and cos(θ), so that relative ply orientation along the interface will cause the sines to be evaluated as cosines for the different plies. Since sine and cosine are smooth functions, the resulting deformation state would be expected to reflect this character.

While the deformation state found for this laminate is smooth, the interlaminar stress state is not necessarily so. The through-the-thickness distributions of all three interlaminar stresses are presented in Figure 91a), b) and c). Examination of Figure 91a), reveals that the interlaminar normal stress has a complex distribution which is maximum at the laminate mid-plane, which is consistent with that found for the other laminates considered. Near $\theta = 90°$ where the in-plane stresses are high and changing over small distances, there are nonzero stresses near the interface between the plies. This is not consistent with previous results and may be attributed to the difficulty of matching the traction-free boundary condition at the edge with classical displacement-based elements at this location. Examination of the σ_z stress contours on the deformed half-model in Figure 92b) concisely reveals that the negative stresses are concentrated in the elements which are nearest the mid-plane, while the positive stresses are found predominantly in the elements modeling the 45° ply. At the 'edges' of the partial model near $\theta = 0°$ and 180°, no stress contours are found farther away than one laminate thickness from the curved edge of the model. Demonstrating again that the global/local modeling procedure has correctly determined the expected extent of the interlaminar stress state around the hole.

The through-the-thickness $\tau_{\theta z}$ stresses are shown in Figure 91b), while the stress contours around the hole are in Figure 93. This stress component exhibits smooth changes in magnitude and shape as a function of angular position around the curved free edge. The through-the-thickness distribution of $\tau_{\theta z}$ has its peak values near $\theta = 90°$ where the in-plane stress components are also large, with smaller peaks near $\theta = 0°$ or 180°. At $\theta = 45°$ and $\theta = 135°$, this stress is zero through the

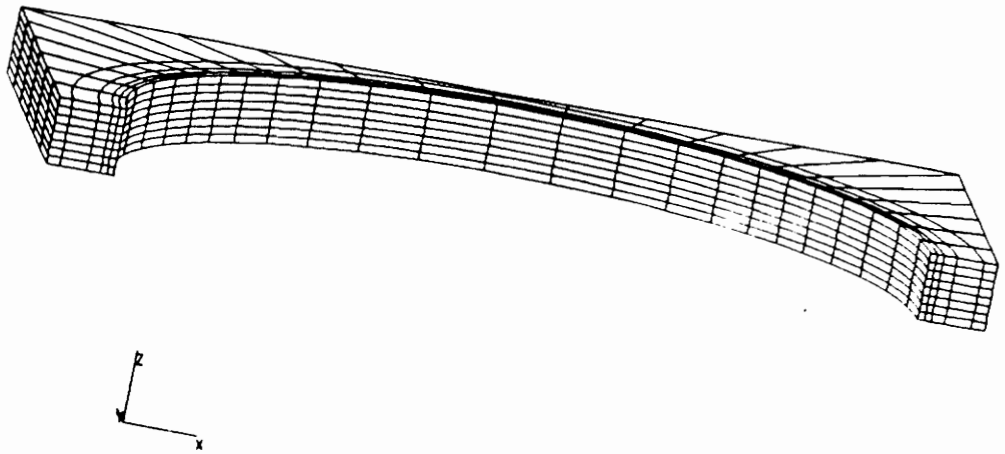

a)

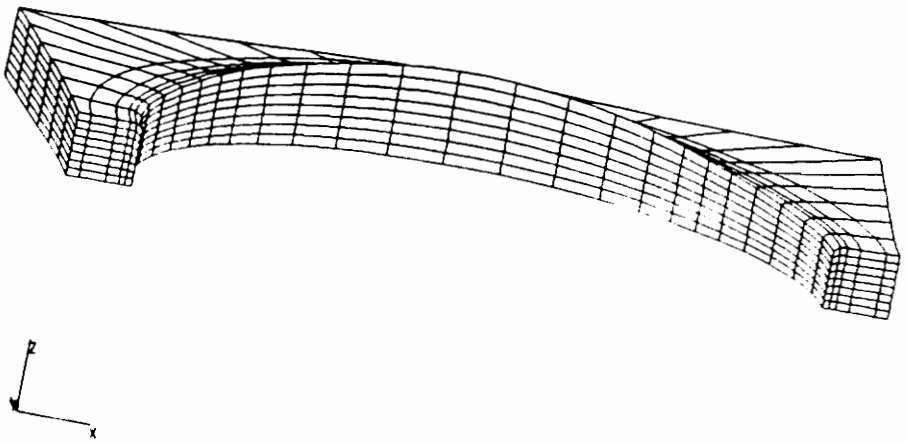

b)

Figure 90. **Partial Curved Edge Models for $[\pm 45_{2n}]_s$ around Six-Inch Diameter Hole:** a) Undeformed b) Deformed

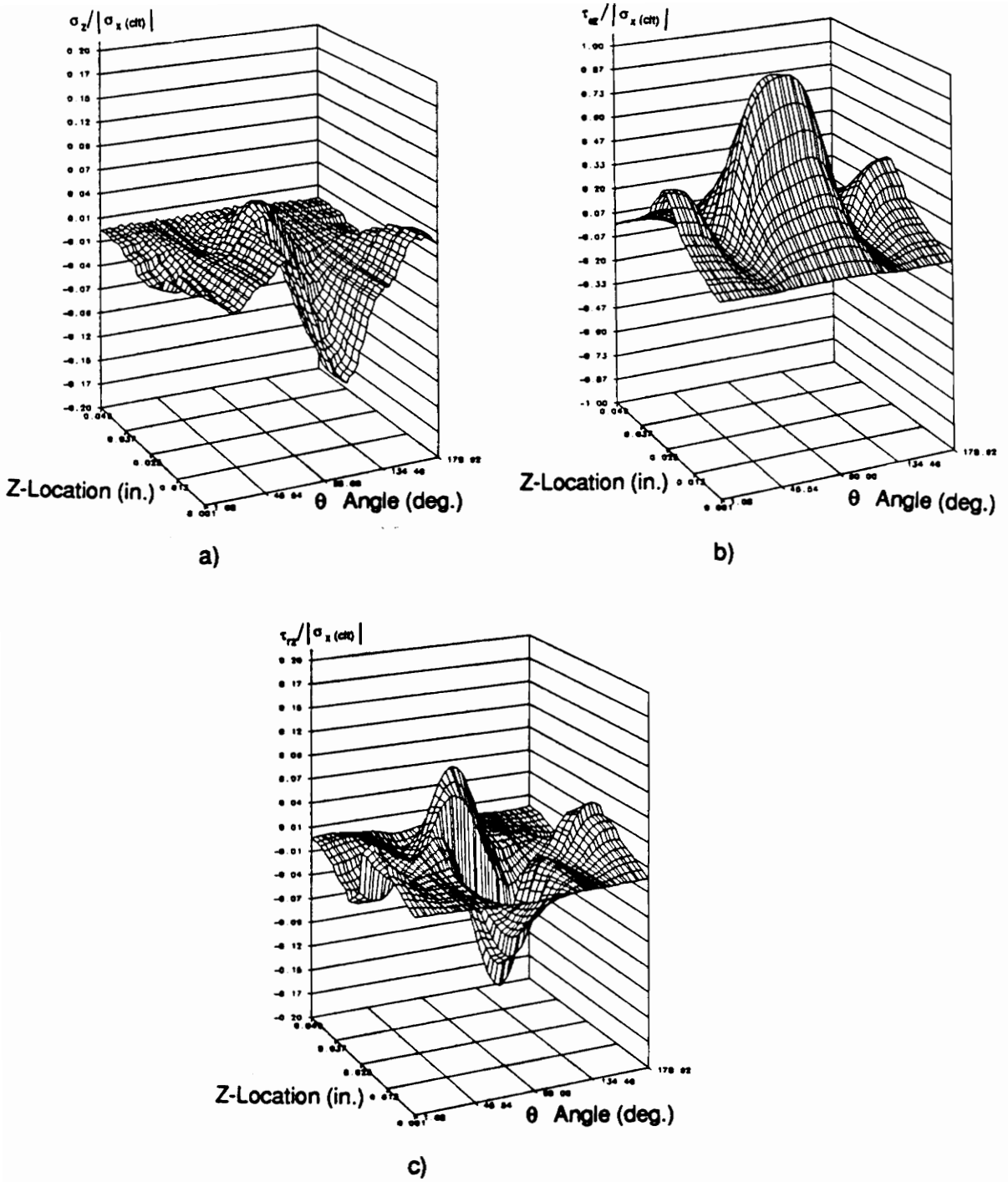

Figure 91. Through-the-Thickness Stresses for Partial Curved Edge Model for $[\pm 45_{2n}]_s$ near Six-Inch Diameter Hole: a) σ_z b) $\tau_{\theta z}$ c) τ_{rz}

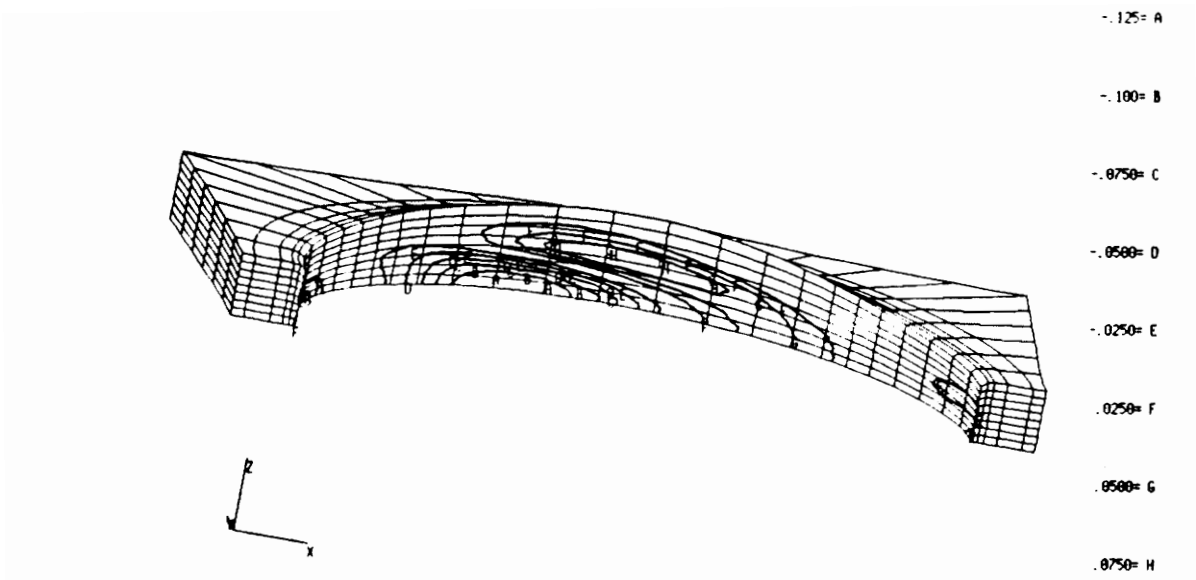

Figure 92. σ_z **Contours for Partial Curved Edge Model for** $[\pm 45_{2n}]_s$ **around Six-Inch Diameter Hole**

laminate. These locations are where the effective stacking sequence becomes a cross-ply laminate, which will exhibit no shear coupling between the plies. In addition, the deformed half-model has the largest concentration of stress contours in the region where the deformations are the largest. As seen in Figure 93, those elements near $\theta = 90°$ at the ply interface must shear in the tangential direction as the elements in the 45° ply expand in thickness while those in the -45° ply contract, which is also the location of the peak stress magnitudes.

In Figure 94, the dominant feature is the strong difference in value for τ_{rz} for those integration points above and below the interface. Because of the high value of $\tau_{\theta z}$ over the laminate, the tendency for the layers to slide past one another at the hole edge is large, and is greatest in the region near 90°. To restrain this motion, the hole must change in diameter through its thickness, which results in significant differences in τ_{rz} on either side of the interface. Near the plate where the in-plane loading and interlaminar effects are in opposition to each other, the difference in stress values are opposite for the interface near those elements modeling the region of the plate where these reinforce one another. The jump in value across the interface is largest near $\theta = 90°$, because the stress field in this region has greater stress values for the other components, and therefore, larger differences for τ_{rz} result. Near $\theta = 45°$ and 135°, this stress component is zero through the laminate thickness which are also the locations where the effective stacking sequence is a cross-ply laminate and the other interlaminar shear stress ($\tau_{\theta z}$) is zero. Examination of the partial model with the stress contours indicates the same information and trends.

When the straight edge stress states were examined for a $[\pm 15_n/\pm 45_n]_s$ plate with a six-inch diameter hole, a complex interlaminar stress state was determined. This is attributable to the Poisson's ratio mismatch between the groups of oriented plies and shear coupling at the center of each group and between the groups of plies. All three of the interlaminar stress components were examined in some detail. Studies of the interlaminar stress state around the six-inch hole for such a lamination sequence is difficult to interpret. As for the other laminates studied, the interlaminar stress state around the hole is dependent on the global stacking sequence, the effective stacking sequence around the hole, the global applied load, and the localized load path around the hole. Even

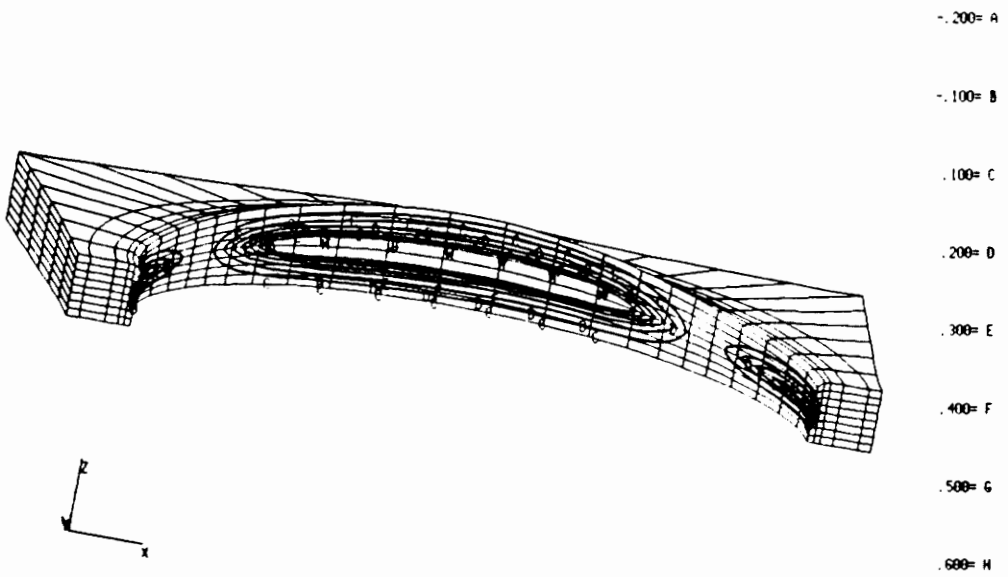

Figure 93. $\tau_{\theta z}$ **Contours for Partial Curved Edge Model for** $[\pm 45_{2n}]_s$ **around Six-Inch Diameter Hole**

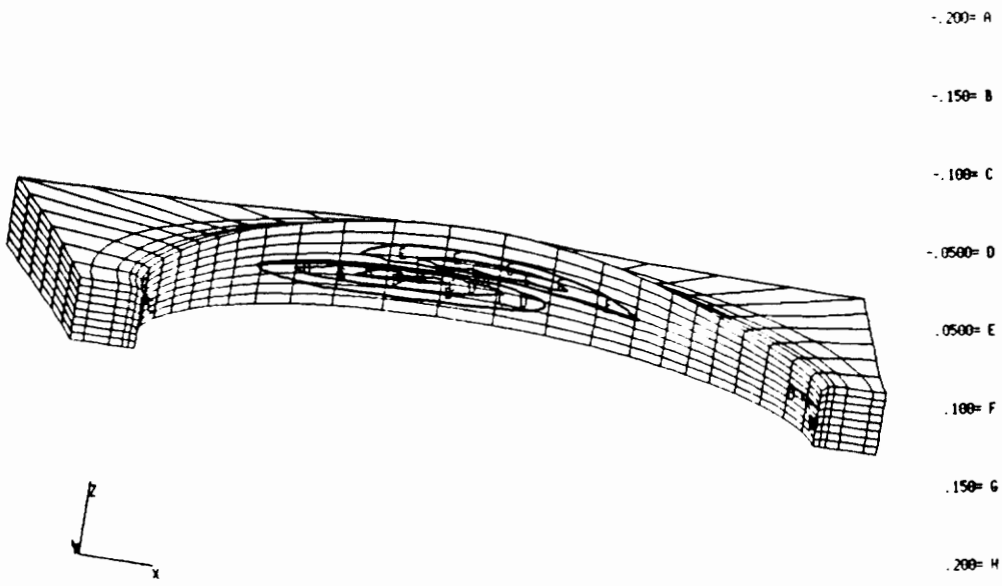

Figure 94. τ_{rz} **Contours for Partial Curved Edge Model for** $[\pm 45_{2n}]_s$ **around Six-Inch Diameter Hole**

those laminates whose global orientation exhibited but one type of interlaminar effect had a fully coupled interlaminar stress state around the hole and all three interlaminar stresses became significant. Obviously, if the global stacking sequence will cause several interlaminar mechanisms between its layers, the interlaminar stress state around the curved free edge of the hole will be extremely complex and difficult to interpret. All three of the interlaminar stresses will be expected to exhibit intricate distributions.

To gain an understanding of the behavior of the interlaminar stresses around the hole, first the local deformation fields were examined. Figure 95a) and b) are the undeformed and deformed partial models for this stacking sequence and hole diameter. When a global compressive loading is applied, the plate will expand through its thickness for a positive laminate through-the-thickness Poisson's ratio, which is the case for this laminate and all of the other laminates under consideration and is seen in this figure. As determined for several of the other stacking sequences, those elements nearest the hole edge at $\theta = 0°$ and 180° will deform toward the laminate mid-plane. As θ increases, this compaction lessens and reaches zero at $\theta = 45°$. When $45° < \theta < 135°$, the elements nearest the hole edge can experience compaction and enlargement through the laminate thickness. Following the top row of elements nearest the hole edge in Figure 95b) reveals this effect for this layer of elements, while the deformation of the normals to the plies suggests that this deformation state is not constant through the laminate.

The trends in the deformation field are reflected in the through-the-thickness distribution of the interlaminar normal stress, which is presented in Figure 96a). The through-the thickness distributions for the interlaminar shear stresses ($\tau_{\theta z}$ and τ_{rz}) are found in Figure 96b) and c). As expected, all of the stress components are complex. The interlaminar normal stress has a complex variation through the thickness along the hole edge, because each angular position now experiences Poisson's ratio mismatches at three interfaces for those positions away from $\theta =$ 0°, 90° and 180°. Concentration of the stress at these different z-locations in the laminate is shown for the stress contours in Figure 97. At $\theta = 0°$ and 180°, the through-the-thickness distribution is seen to be similar to the straight edge for this laminate, while at $\theta = 45°$ and 135°, there is no interlaminar normal stress

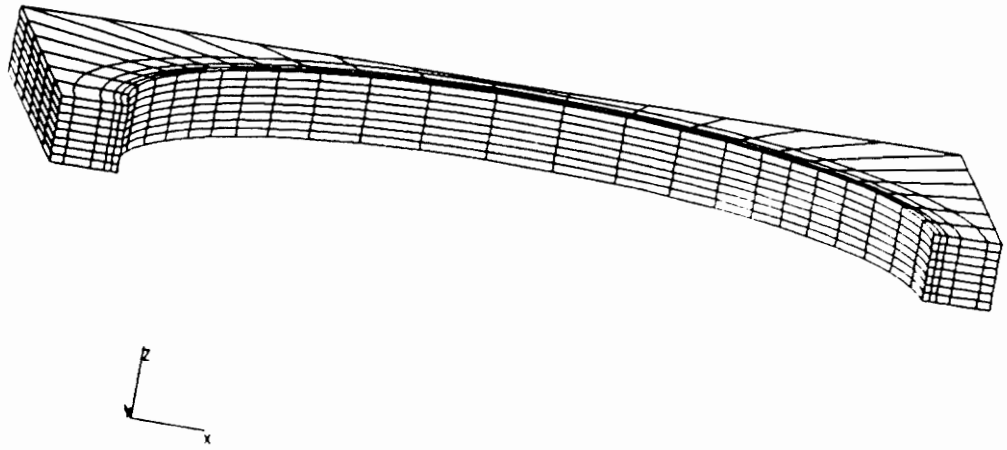

a)

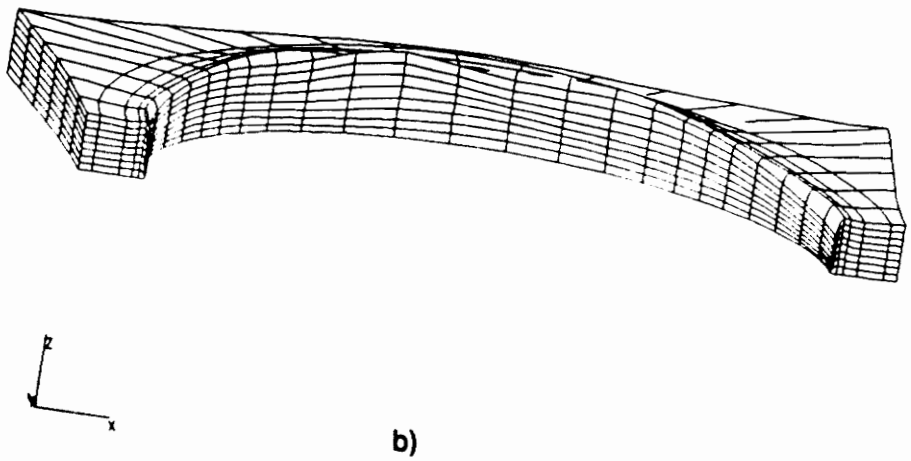

b)

Figure 95. Partial Curved Edge Models for $[\pm 15_n/\pm 45_n]_s$ around Six-Inch Diameter Hole: a) Undeformed b) Deformed

through the laminate. Examination of the stress contours superimposed on the deformed grid suggests that those areas with the greatest change in thickness are those with the largest stress gradients, which is not unexpected. At $\theta = 0°$ and 180°, the largest concentration of negative stresses are found along the mid-plane in the region with the strongest element compaction. Near $\theta = 90°$, some element expansion was found as well as some positive stress values at the 15°/-45° interface. Examination of both the through-the-thickness stress distributions and stress contours for this stress component clearly indicates that the stress distribution is not symmetric about the hole centerline. A cursory examination of the stress contours of the $[\pm 15_{2n}]_S$ and $[\pm 45_{2n}]_S$ laminates show that the distribution for the $[\pm 15_n/\pm 45_n]_S$ laminate is made considerably more complex by the enforcement of compatibility between the 15°/-45° layers.

Examination of the through-the-thickness interlaminar shear stress ($\tau_{\theta z}$) in Figure 96b) reveals that its distribution resembles more closely a combination of those for the $[\pm 15_{2n}]_S$ and $[\pm 45_{2n}]_S$ laminates. The $[\pm 15_{2n}]_S$ laminate had a highly concentrated stress near $\theta = 90°$, and this concentration can be found at the interface for the $\pm 15°$ layers of the $[\pm 15_n/\pm 45_n]_S$ plate, but shifted slightly toward $\theta = 0°$. The $[\pm 45_{2n}]_S$ laminate, on the other hand, had a more gradual stress distribution as a function of angular position, and this relative smoothness can be seen in the stress distribution for the $[\pm 15_n/\pm 45_n]_S$ laminate. At the 15°/-45° interface, this interlaminar shear stress is negative in value and shifted away from $\theta = 90°$ toward $\theta = 180°$. While this is not clear from the through-the-thickness distribution, it can be seen in the stress contours on the deformed partial model in Figure 98. For the $[\pm 45_{2n}]_S$ laminate, there were additional stresses near $\theta = 0°$ and 180°. This character was determined at the $\pm 45°$ interface for the $[\pm 15_n/\pm 45_n]_S$ laminate.

For both of the previous angle-ply lamination sequences, the τ_{rz} distribution around the hole and through-the-thickness was complex in shape and difficult to describe. As expected, this stress component is no less so for the $[\pm 15_n/\pm 45_n]_S$ laminate. Its through-the-thickness and stress contours around the hole are found in Figure 96c) and Figure 99, respectively. The through-the-thickness distributions resemble none of the distributions shown for the previous lamination sequences considered and are difficult to interpret. As the effective stacking sequence changes around

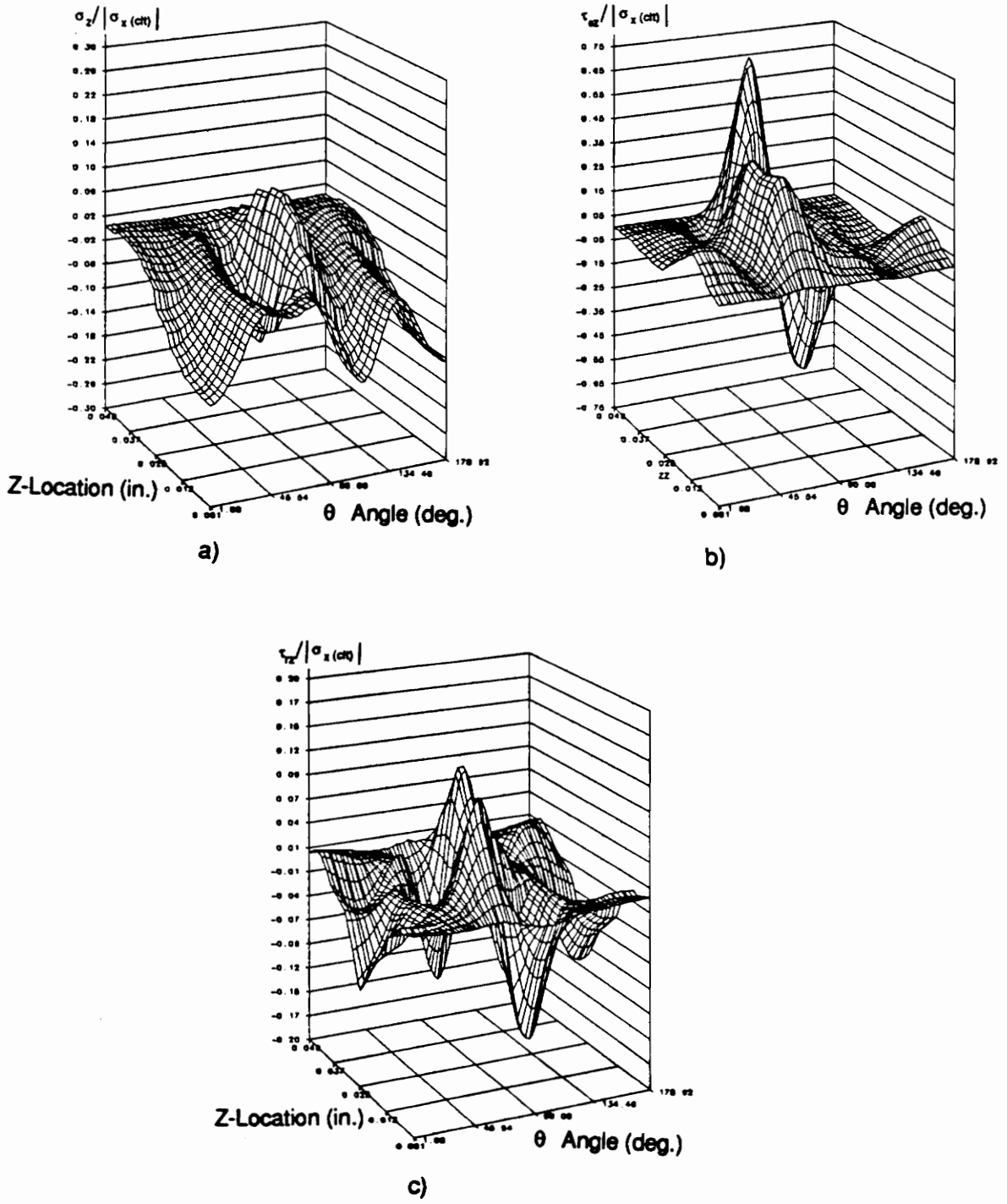

Figure 96. **Stresses for Partial Curved Edge Model for $[\pm 15_n/\pm 45_n]_s$ around Six-Inch Diameter Hole** Hole: Through-the-Thickness a) σ_z b) $\tau_{\theta z}$ c) τ_{rz}

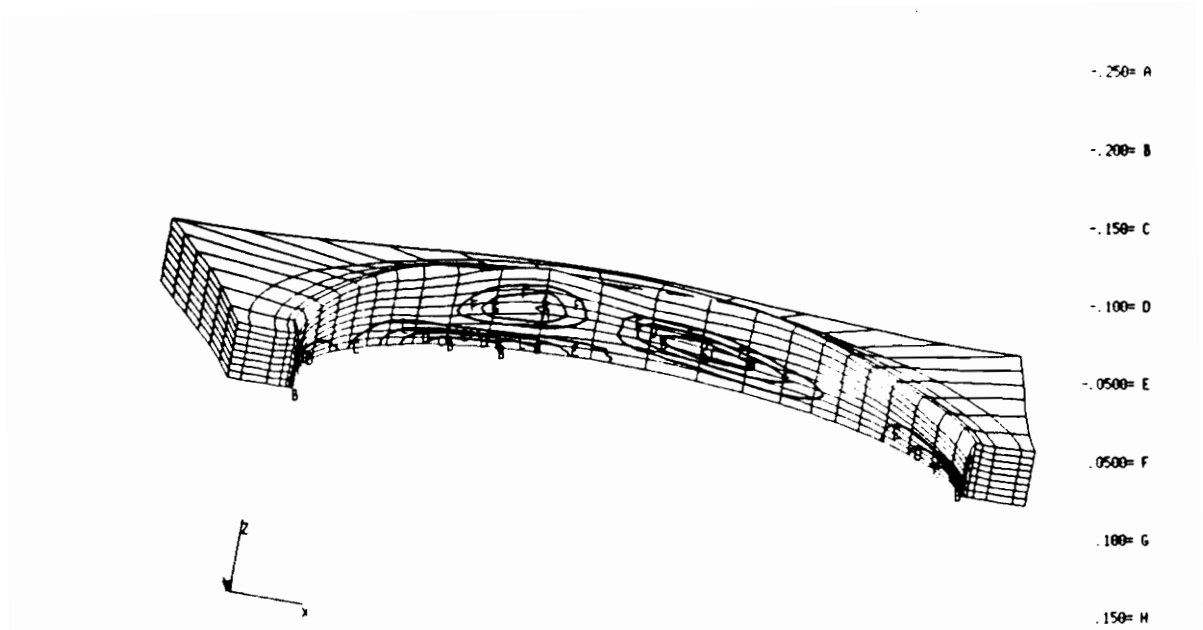

Figure 97. σ_z **Contours for Partial Curved Edge Model for** $[\pm 15_n/\pm 45_n]_s$ **around Six-Inch Diameter Hole**

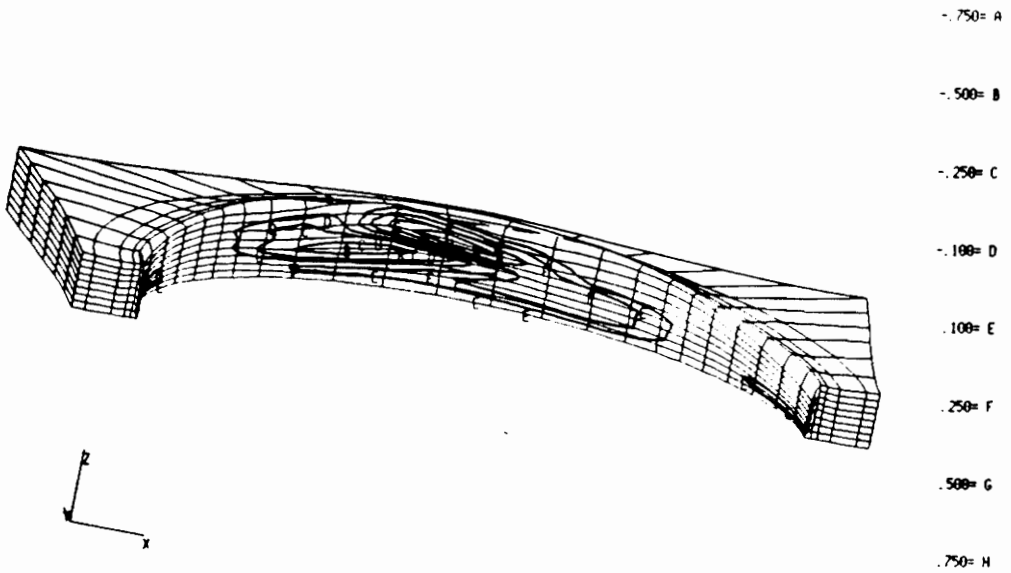

Figure 98. τ_{oz} Contours for Partial Curved Edge Model for $[\pm 15_n/\pm 45_n]_s$ around Six-Inch Diameter Hole

the hole, strains are developed at each interface to maintain compatibility of the layers. Each angular location which has concentrations of stress contours corresponds to a position which has considerable deformation along the row of elements along the top of the plate. However, the location of the stress concentrations through the laminate thickness changes with angular position. Several of the peaks found in the through-the-thickness distributions are seen to be at slightly different angular positions and at different heights in the laminate. Most of the strong peaks were at the $\pm\Theta$ interfaces, while the 15°/-45° interface experienced a lower stress magnitude over a larger region around the hole. While it is not clear from the deformed partial model stress contours, it appears that the distributions were somewhat anti-symmetric about $\theta = 90°$. The positive values were at the $\pm 45°$ interface on one side of $\theta = 90°$ and at the $\pm 15°$ interface on the other side of $\theta = 90°$. Likewise, the negative shear values were found on either side of $\theta = 90°$ for the different interfaces.

The $[\pm\Theta_1/\pm\Theta_2]_s$ lamination sequence study of interlaminar effects around holes is difficult to interpret because all of the three interlaminar stresses exist and have strong gradients around the hole at several interfaces. Each interface around the hole is affected by Poisson's ratio mismatch between the ply groups, and shear coupling within and between the ply groups for most of the curved edge. The resulting interlaminar stress distributions are difficult to interpret at best, and will be for any laminate with several ply interfaces through its thickness.

Quasi-isotropic laminates are similar to the $[\pm 15_n/\pm 45_n]_s$ laminate since there are several ply interfaces where Poisson's ratio mismatch and shear coupling can possibly occur. For a $[0_n/\pm 45_n/90_n]_s$ plate with a six-inch diameter hole, each ply interface then becomes of interest. The undeformed and deformed partial models for this laminate are presented in Figure 100a) and b). Around the hole, thickening of the model due to the in-plane loading is gradual and smooth. However, the deformations in the boundary layer around the hole enforces compaction of the elements for all angular positions which varies in intensity. Close examination of the deformed model reveals that at the laminate mid-plane all of the elements are compacted. In the $\pm 45°$ layers, there is both expansion and contraction, and in the 0° layers, enlargement of the elements can be detected

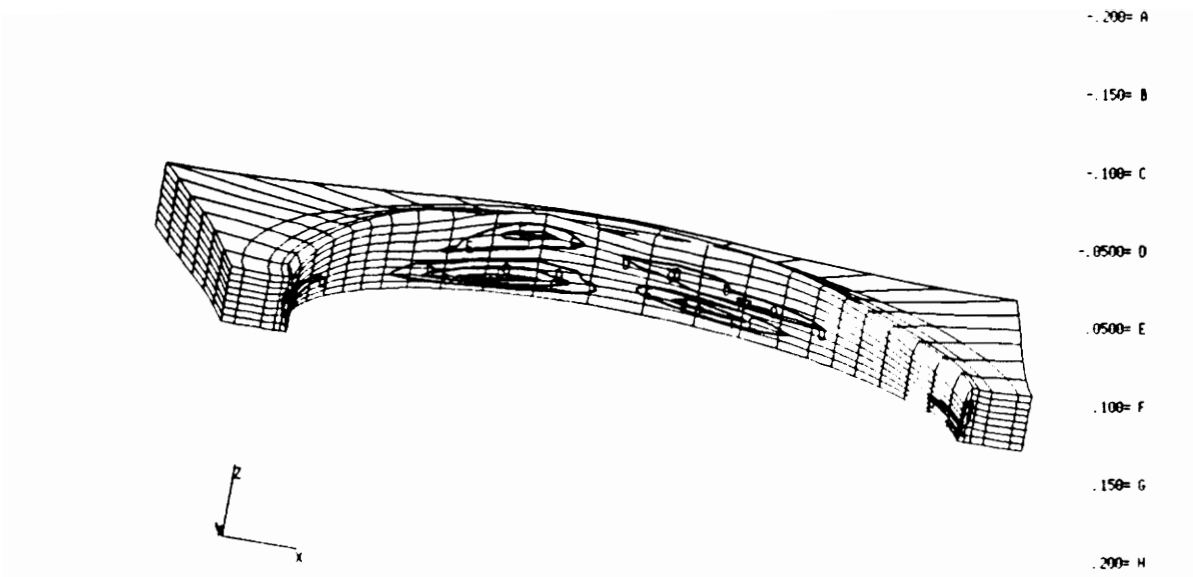

Figure 99. τ_{rz} Contours for Partial Curved Edge Model for $[\pm 15_n/\pm 45_n]_s$ around Six-Inch Diameter Hole

around the hole edge. Sliding of the elements relative to one another in the x-y plane occurs at several locations around and through the laminate. Definitive changes in the hole diameter through the laminate can be seen at the 0° and 90° locations because of the cut in the local model.

In Figure 101, the through-the-thickness distributions for all three interlaminar stress components are presented. Figure 101a) is the interlaminar normal stress distribution, while the two interlaminar shear stresses, τ_{yz} and τ_{xz}, are in Figure 101b) and c), respectively. From Figure 101a), the interlaminar normal stress can be seen to be large and mostly negative, except in the $\pm 45°$ plies. Maximum magnitudes were found near the laminate mid-plane. Figure 102 is a view of the partial deformed model with σ_z contours superimposed. The positive stresses are confined to the $\pm 45°$ plies and near $\theta = 90°$. However, the magnitudes of these positive stresses are small in comparison to the negative stresses found throughout the curved edge region. As a consequence, there is no expansion of the elements around the hole attributable to the interlaminar strain state. There is, however, a lessening of the compaction of elements around the hole. At $\theta = 0°$ and 180°, the elements are strongly compressed toward the laminate mid-plane, while the through-the-thickness stress distribution indicates significant stress values only in the 90° layers at these locations.

Figure 101b) is the through-the-thickness $\tau_{\theta z}$ stress distribution. At the 0°/45° interface, the peak magnitudes are slightly larger than those for the $\pm 45°$ interface and considerably larger than at the -45°/90° interface. This change in value is attributable to the amount of load carried by the respective layers. For the same end-shortening, the 0° layers will experience a higher in-plane stress than the |45°| or the 90° layers, and so its interlaminar stress values are expected to have larger magnitudes. Furthermore, the location for all of these peaks is near $\theta = 90°$, which is a location of concentrated in-plane stress for even the global model. The deformed partial model with the stress contours in Figure 103 reveals the location of some of these peaks more clearly through the laminate. At $\theta = 0°$ and 180°, the sign of the stresses is opposite in this figure. This shows that the sliding of elements is in the opposite direction. Near $\theta = 135°$, the compaction of the elements is

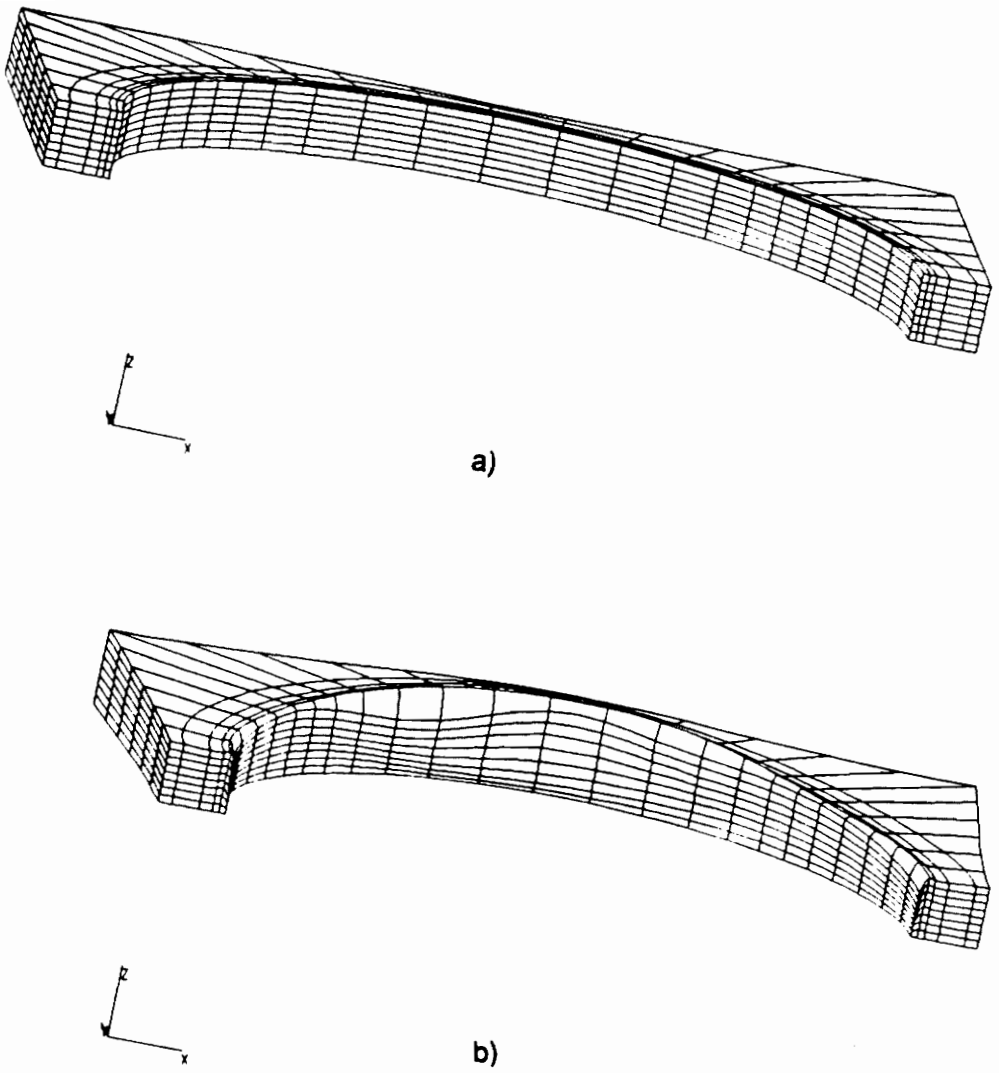

Figure 100. Partial Curved Edge Model for $[0_n/\pm 45_n/90_n]_s$ around Six-Inch Diameter Hole: a) Undeformed b) Deformed

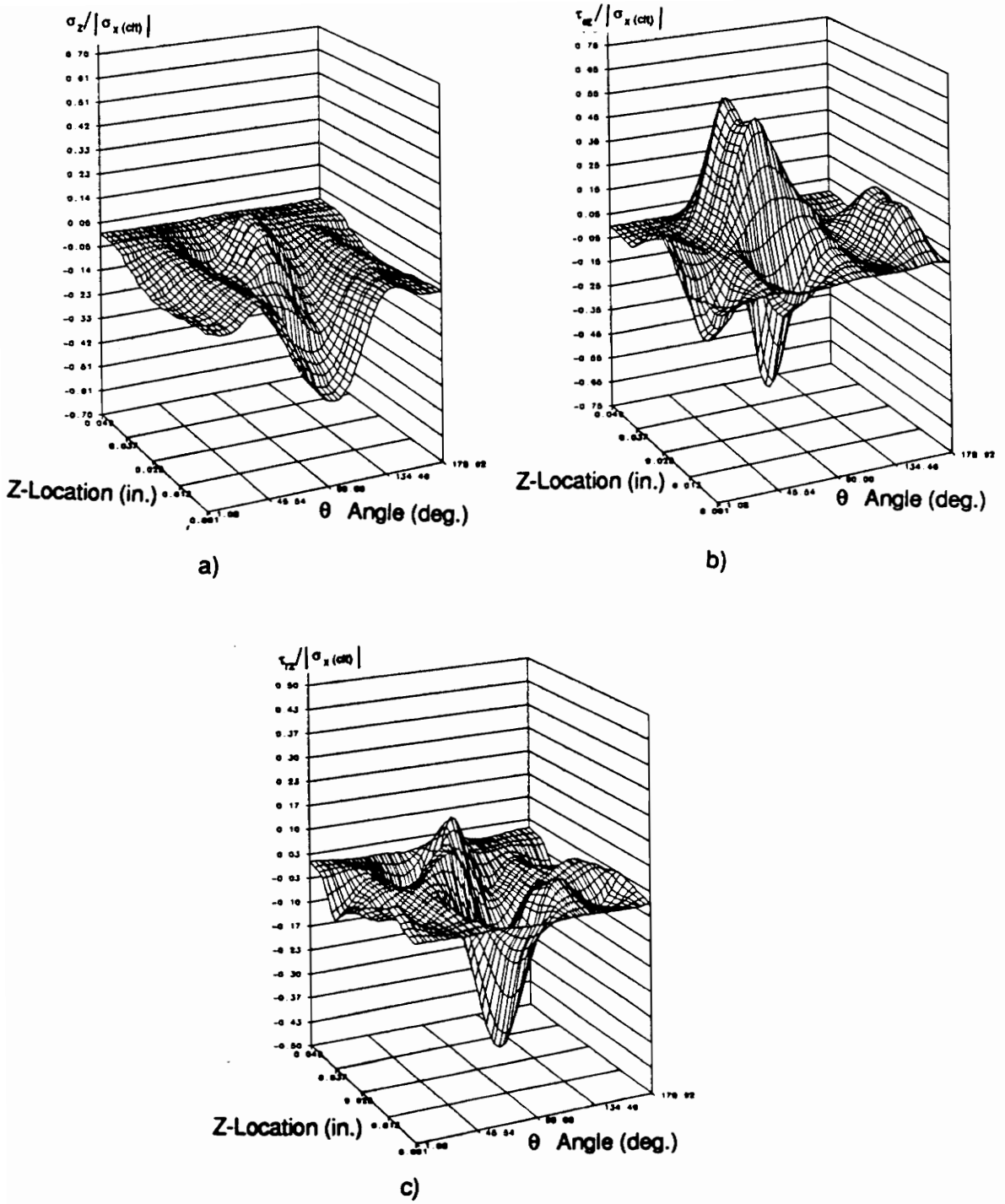

Figure 101. Stresses for Partial Curved Edge Model for Quasi-isotropic Laminate around Six-Inch Diameter Hole Hole: Through-the-Thickness a) σ_z b) $\tau_{\theta z}$ c) τ_{rz}

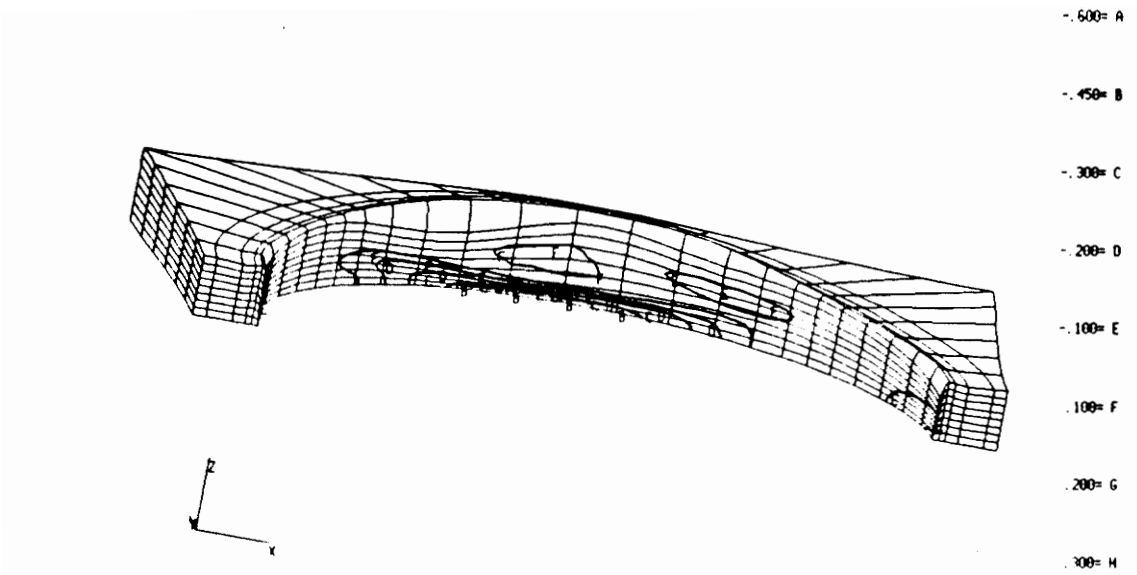

Figure 102. σ_z **Contours for Partial Curved Edge Model for Quasi-isotropic Laminate around Six-Inch Diameter Hole**

strong and results in the shearing of elements in one direction. However, near $\theta = 90°$, the elements are experiencing less compaction and the sign of the stresses is opposite.

Figure 101c) is the through-the-thickness stress distribution for the remaining interlaminar stress component, τ_{rz}. This stress distribution is difficult to interpret. Its magnitudes are larger for this laminate than any of the other lamination sequences considered in this study. On either side of $\theta = 90°$, the stresses peak and change direction in the $\pm 45°$ layers. In the 90° layers, there are large values in those same locations where the element compaction is greatest. Obviously, those elements are shifting through the laminate and changing the hole diameter slightly. As can be seen in Figure 104, this areas are coincident with those where the thickening and contraction of the elements through the laminate thickness are changing.

5.4 Conclusions for In-Plane Compression of Angle-Ply and Quasi-Isotropic Laminates

Several conclusions can be drawn from the analyses discussed, both about the state of stress around large holes in thin laminates and to the application of two-dimensional to three-dimensional global/local stress analysis in laminated composites. Considerable savings in computer time and storage can be achieved by using a global/local approach for analysis of laminated composites. It should be noted that use of the global/local method made the analysis of a thin laminated plate possible, as the full three-dimensional model would not converge.

During this study several conclusions were drawn about interlaminar stress and strain states for angle-ply and quasi-isotropic laminates. Interlaminar stress fields for straight and curved free edges were studied for varying stacking sequences and hole size.

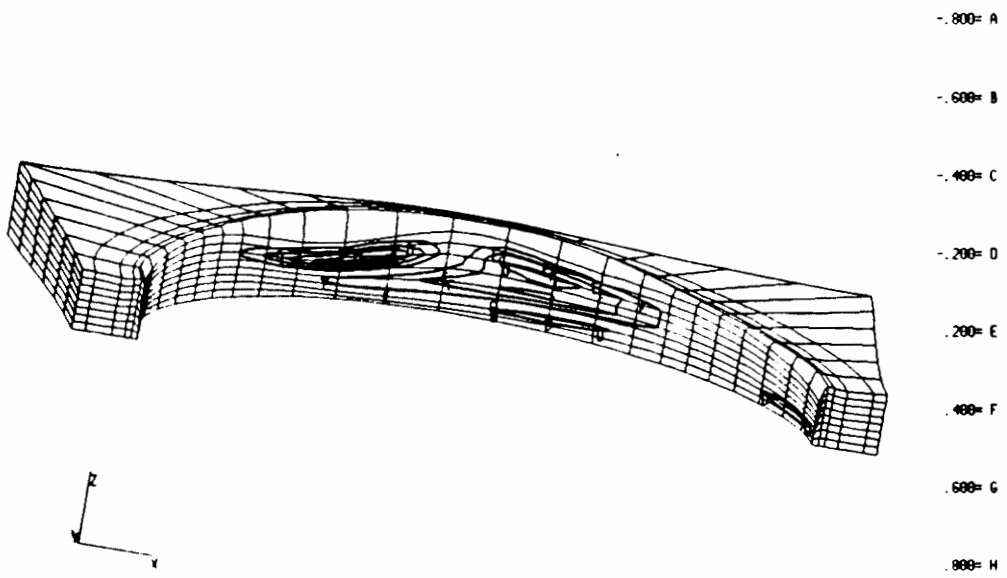

Figure 103. $\tau_{\theta z}$ **Contours for Partial Curved Edge Model for Quasi-isotropic Laminate around Six-Inch Diameter Hole**

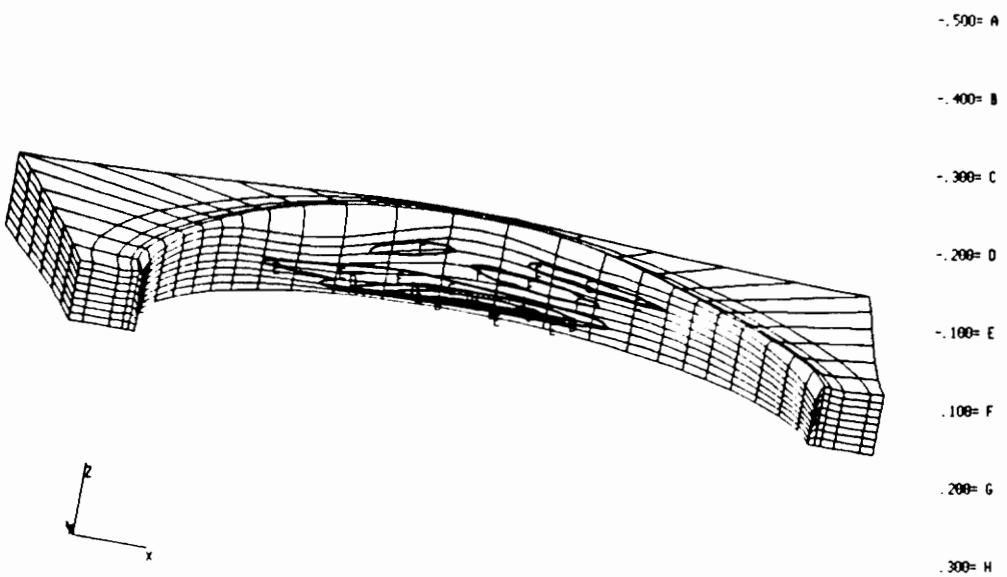

Figure 104. τ_{rz} **Contours for Partial Curved Edge Model for Quasi-isotropic Laminate around Six-Inch Diameter Hole**

Interlaminar stress fields in laminates with off-axis plies are more complex and dependent on stacking sequence than cross-ply laminates, because of the wider range of possible ply angle combinations, and therefore, interlaminar effects. Angle-ply laminates of the $[\pm\Theta]_S$ orientation do not experience a Poisson's ratio mismatch between the layers, but do have coupling between extension and shearing. The degree of shear coupling present, in turn, is dependent on the angle Θ in the laminate stacking sequence.

For a common end-shortening, because the compliances for the laminates considered can vary greatly, different in-plane stress levels result, which influence the interlaminar stress state. The $[\pm 15_{2n}]_S$ laminates studied are less compliant than the $[\pm 45_{2n}]_S$ laminate. Interlaminar stress fields along straight edges in proximity to a hole arise because of shear coupling for $[\pm\Theta]_S$ laminates. The $[\pm 15_{2n}]_S$ lamination sequence has a stronger shear coupling effect than the $[\pm 45_{2n}]_S$ laminates, which was reflected in the interlaminar stress fields.

Combining $\pm\Theta$ layer groups together to form a $[\pm\Theta_1/\pm\Theta_2]_S$ laminate immediately changes the interlaminar stress state to one resembling quasi-isotropic laminates. Between each group of layers, there is a Poisson's ratio mismatch, while shear coupling can occur at every layer interface. At a straight edge, the interlaminar normal stresses will be maximum at the mid-plane. At a nearby interface, the interlaminar shear stress τ_{yz} will be maximum. The interfacial location of the maximum τ_{xz} is dependent on the exact stacking sequence considered.

The effect of a hole on the nearby straight edge, if there was an effect, was to reduce magnitude of the interlaminar stresses for all laminates and hole diameters considered. The one-inch diameter hole appears to have no effect on the straight edge for all of the stacking sequences under consideration, while the six-inch diameter hole greatly influences the distribution character. The three-inch diameter hole stresses were determined to be a combination of those for the one- and six-inch diameter holes.

The interlaminar stress distribution around holes is more complex, and less intuitive. Like the stresses near the straight edge, it is dependent on the stacking sequence. However, as the angular position around the hole changes, so does the effective stiffness and stacking sequence. This affects the interlaminar stress fields greatly, and is why, although no interlaminar normal stress develops for $[\pm\Theta]_s$ stacking sequences at the straight edge, it does around the hole. The local Poisson's ratio mismatch and shear coupling change in value, which affects the stress fields. Some of the lamination sequence distributions are less complex than others, but intuition can lead the analyst astray.

The effect of the different hole sizes on the interlaminar distribution around holes is more involved and highly lamination sequence dependent. General comments are that the three- and six-inch diameter stress distributions resembled each other closely. The locations of stress peaks were generally shifted slightly and not at the same location as for the cross-ply laminates. In portions of the plate farther from the straight edge, the distributions could be coincident, but nearer to it there were more deviations. The three-inch diameter hole exhibited larger peak values for most of the stress components than the six-inch diameter hole, and this would suggest that a critical hole size exists in the laminate somewhere near three inches. It is believed that conclusive statements about the effect of the one-inch diameter hole in the hole region are premature until the issue of whether the deviations in the stress distributions are because of the lack of stress relief, or merely a discretization deficiency.

6.0 Conclusions - Global/Local Analysis

The two-dimensional to three-dimensional global/local finite element analysis technique presented was applied to several laminates with holes under compressive loading. Cross-ply, angle-ply and quasi-isotropic stacking sequences were modeled with three different hole diameters. Plate length-to-thickness ratio was 180, plate width-to-thickness was 120, and hole diameter-to-thickness values were 60, 30 and 10. Interlaminar stress fields at the straight edge near the hole and around the hole were examined in detail. Few previous investigations have involved these aspect ratio ranges, in part due to the prohibitive computational requirements of three-dimensional finite element analysis. Considerable saving in computer time and storage was achieved by using a global/local approach for analyses of laminated plates. The numerical results that were presented could have been more detailed and accurate through the use of more refined meshes, but the purpose of this study was to develop and verify the applicability of the procedure to the analysis of laminated composites structures. One of the primary goals of this global/local analysis method is to reduce the resource requirements of detailed analyses by performing several moderate analyses rather than one extremely large analysis.

For the cross-ply laminates, comparison between a complete three-dimensional model and local models of a plate for a specific hole diameter and stacking sequence was excellent along the straight free edge, and reasonable along the curved edge for all interlaminar stress components. Better

agreement is believed possible with an improved in-plane distribution of elements in certain locations around the hole. The global/local analyses were able to determine the effects of clustered, dispersed, and reversed plies from the same in-plane displacement field on the three-dimensional interlaminar stress field. Conclusions about the hole effect in a finite plate on the interlaminar stress fields at a nearby straight edge and around the holes were made, and presented at the conclusion of that chapter.

The global/local displacement application procedure for the straight edge cross-ply models proved to be a special case where prior knowledge of the strain field ($\gamma_{xz} = 0$) allowed the free edge boundary layer to cross the boundary of the local model. All symmetry planes were exploited to reduce both the straight and curved edge models to their smallest possible form. Care must be taken in the displacement procedure to not inhibit boundary layer development with kinematically inadmissible displacements along the symmetry planes, and the 'cut' through the boundary layer.

For laminates with off-axis plies, the three-dimensional nature of the strain and stress fields preclude the application of constant displacements in any direction through the boundary layer as was permissible in one plane for the cross-ply laminates. Thus, the straight edge models had to extend from one end of the plate to the other. The error in attempting to reduce the size of the local angle-ply models by cutting a boundary layer was explored. In order to model the global load application conditions with the reduced local models, assumptions about the displacement field were made at the cuts. However, the only possible assumption was kinematically inadmissible and inaccurate displacement and strain fields developed. The local curved free edge models for the cross-ply and angle-ply laminates are similar in character. However, the cross-ply laminates under in-plane loading contain several symmetry planes which were exploited that do not exist for the other laminates or for more general loading conditions. Thus, the size of the angle-ply models around the hole are nearly four times that of the cross-ply laminates.

An attempt was made to correlate the global/local analyses of an angle-ply laminate to a complete three-dimensional model. However, examination of the displacement fields from the analysis indi-

cate that this model had not converged. Trends from previous analyses indicate that the interlaminar stress fields at the straight free edge and around the hole are reasonable and at least as accurate as those analyses. The fact that the three-dimensional model was not as tractable as believed is a sign that the global/local analysis technique can be applied to more intricate problems to assist in the analysis and design of structures.

Cautions and general comments about the global/local analysis procedure should be made. Application of the global/local technique proved to be successful when some basic rules are followed. The global analysis must model the global response accurately. Generally, the global/local interfaces should be located in regions with relatively uniform stress fields, making an extremely fine global grid unnecessary, and its exact placement was found not extremely critical as long as it is outside the region of local influence. Of course, the global/local interfaces should be as close to the local effect as possible to reduce the model size without overconstraining the development of the three-dimensional displacement or stress fields. With proper mesh design, the model size and computer resources can be kept low. A requirement on the local model is that it determines the local effect accurately. Certain short-cuts are permissible, but are dependent on the three-dimensional displacement fields. Through the global/local method, it is possible to tailor problem size to the accuracy required, and to more specifically model local effects in thin laminated plates. When applying such a technique, care must be taken by the analyst, to have an understanding of both the two-dimensional and three-dimensional finite element analyses limitations and capabilities, and the two-dimensional stress state, if not the three-dimensional stress state. Without such an understanding, an inappropriate assumption might be made and the global/local analysis would yield inappropriate displacement and stress fields.

Global/local analyses can drastically improve the efficiency of computerized structural analysis and can provide sizable savings by circumventing the need to perform expensive analyses of non-critical regions. In addition, the design of the Testbed and the work of the Computational Mechanics Branch assisted the present effort tremendously by having specialists create modular processors which take advantage of local memory management schemes, utilize sparse matrix storage, and

contain efficient solution techniques. The result is a tool which minimizes the effort of the structural analyst in determining structural response, thus permitting more complicated analyses, that were previously intractable, to be completed.

7.0 References

Barker, Richard M., Jon R. Dana and Charles W. Pryor, Jr., "Stress Concentrations Near Holes in Laminates", Journal of the Engineering Mechanics Division, 1974, pp. 477-488.

Barlow, John, "Optimal Stress Locations in Finite Element Models," International Journal for Numerical Methods in Engineering, Vol. 10, 1976, pp. 243-251.

Barlow, John, "More on Optimal Stress Points - Reduced Integration, Element Distortions and Error Estimation," International Journal for Numerical Methods in Engineering, Vol. 28, 1989, pp. 1487-1504.

Bradford, L. G., S. B. Dong, D. A. C. Nicol and R. A. Westman, Application of Global-Local Finite Element Method to Fracture Mechanics, September, 1976.

Burns, S. W., C. T. Herakovich and J. G. Williams, "Compressive Failure of Notched Angle-Ply Composite Laminates: Three-Dimensional Finite Element Analysis and Experiment," Virginia Tech Center for Composite Materials and Structures Report 85-11.

Clough, Ray W. and Edward L. Wilson, "Dynamic Analysis of Large Structural Systems with Local Nonlinearities," Computer Methods in Applied Mechanics and Engineering, Vol. 17/18, 1979, pp. 107-129.

Dana, Jon Ramon, Three-Dimensional Finite Element Analysis of Thick Laminated Composites -- Including Interlaminar and Boundary Effects near Circular Holes, Virginia Polytechnic Institute and State University, Ph.D. Dissertation, 1974.

Dana, J. R. and R. M. Barker, "Three-Dimensional Analysis for Stress Distribution Near Circular Holes in Laminated Composites," Report VPI-E-74-18, Virginia Polytechnic Institute and State University, 1974.

Dong, S. B., "Global-Local Finite Element Methods," State-of-the-Art Surveys in Finite Element Technology, A. K. Noor, W. D. Pilkey, editors, ASME, Ch. 4, 1983, pp. 451-474.

Dong, Stanley B., "Global Functions in Global-Local Finite Element Analysis of Localized Stresses in Prismatic Structures," Proceedings of NASA Workshop on Computational Methods in Structural Mechanics and Dynamics: June 1985, W. J. Stroud, J. M. Housner, J. A. Tanner, R. J. Hayduk, editors, NASA CP-3034-Part 1, 1989, pp. 134-150.

Goetschel, D. B., S. B. Dong and R. Muki, "A Global Local Finite Element Analysis of Axisymmetric Scattering of Elastic Waves," Journal of Applied Mechanics, Vol. 49, 1982, pp. 129-135.

Gong, Yaonan, "Local Global Structural Analysis by Transition Elements," Computers and Structures, Vol. 30, No. 4, 1988, pp. 831-836.

Griffin, O. Hayden, Jr. and Jack C. Roberts, "Numerical/Experimental Correlation of Three-Dimensional Thermal Stress Distributions in Graphite/Epoxy Laminates," Journal of Composite Materials, Vol. 17, 1983, pp. 539-548.

Griffin, O. Hayden, Jr., "Three-Dimensional Thermal Stresses in Angle-Ply Composite Laminates," Journal of Composite Materials, Vol. 22, 1988, pp. 53-70.

Han, Tao-Yang and John F. Abel, "Adaptive Substructuring Techniques in Elasto-Plastic Finite Element Analysis," Computers and Structures, Vol. 20, No. 1-3, 1985, pp. 181-192.

Hirai, Itio, Bo Ping Wang and Walter D. Pilkey, "An Efficient Zooming Technique for Finite Element Analysis," International Journal for Numerical Methods in Engineering, Vol. 20, 1984, pp. 1671-1683.

Hirai, Itio, Yoshihiro Uchiyama, Yoji Mizuta and Walter D. Pilkey, "An Exact Zooming Method," Finite Elements in Analysis and Design, Vol. 1, 1985, pp. 61-69.

Hsu, Peter W. and Carl. T. Herakovich, "Edge Effects in Angle-Ply Laminates," Journal of Composite Materials, Vol. 11, 1977, pp. 422-428.

Jara-Almonte, C. C. and C. E. Knight, "The Specified Boundary Stiffness/Force SBSF Method For Finite Element Subregion Analysis," International Journal for Numerical Methods in Engineering, Vol. 26, 1988, pp. 1-11.

Jones, Robert M., Mechanics of Composite Materials, Hemisphere Publishing Corporation, New York, 1975.

Kardestuncer, H., editor-in-chief, Finite Element Handbook, McGraw-Hill Book Company, 1987.

Kassapoglou, Christos and Paul A. Lagace, "Closed Form Solutions for the Interlaminar Stress Field in Angle-Ply and Cross-Ply Laminates," Journal of Composite Materials, Vol. 21, 1987, pp. 292-308.

Kelley, F. S., "Mesh Requirements for the Analysis of a Stress Concentration by the Specified Boundary Displacement Method," Computers in Engineering, Vol. 3, 1982, pp. 39-42.

Knight, Norman F. Jr., William H. Greene and W. Jefferson Stroud, "Nonlinear Response of Blade-Stiffened Graphite-Epoxy Panel with a Discontinuous Stiffener -- Work In Progress," Proceedings of NASA Workshop on Computational Methods in Structural Mechanics and Dynamics: June, 1985, W. J. Stroud, J. M. Housner, J. A. Tanner, R. J. Hayduk, (editors), NASA CP-3034-Part 1, 1989, pp. 51-66.

Knight, N. F. Jr., R. E. Gillian, S. L. McCleary, C. G. Lotts, E. L. Poole, A. L. Overman and S. C. Macy, CSM Testbed Development and Large-Scale Structural Applications, NASA TM 4072, April, 1989.

Liao, C. L., J. N. Reddy, and S. P. Engelstad, "A Solid-Shell Transition Element for Geometrically Non-linear Analysis of Laminated Composite Structures," International Journal for Numerical Methods in Engineering, Vol. 26, 1988, pp. 1843-1854.

Lotts, C. G., W. H. Greene, S. L. McCleary, N. F. Knight, S. S. Paulson and R. E. Gillian, Introduction to the Computational Structural Mechanics Testbed, NASA-TM 89096, September 1987.

Noor, Ahmed, K. and Jeanne M. Peters, "Nonlinear Analysis via Global-Local Mixed Finite Element Approach," International Journal for Numerical Methods in Engineering, Vol. 15, 1980, pp. 1363-1380.

Noor, Ahmed K., "Global-Local Methodologies and Their Application to Nonlinear Analysis," Finite Elements in Analysis and Design, Vol. 2., 1986, pp. 333-346.

Owen D. R. J. and Z. H. Li, "A Refined Analysis of Laminated Plates by Finite Element Displacement Methods, Computers and Structures, Vol. 26, No. 6., 1987, pp. 907-917.

Pagano, N. J., "On the Calculation of Interlaminar Normal Stress in Composite Laminate," Journal of Composite Materials, Vol. 8, 1974, pp. 65-82.

Pagano, N. J. and R. Byron Pipes, "The Influence of Stacking Sequence on Laminate Strength," Journal of Composite Materials, Vol. 5, 1971, pp. 50-57.

Pipes, R. Byron and N.J. Pagano, "Interlaminar Stresses in Composite Laminates Under Uniform Axial Extension," Journal of Composite Materials, Vol. 4, 1970, pp. 538-548.

Poole, Eugene L. and A. L. Overman, The Solution of Linear Systems of Equations With a Structural Analysis Code on the NAS CRAY-2, NASA CR 4159, December, 1988.

Ransom, J. B. and N. F. Knight, Jr., Global-Local Stress Analysis of Composite Laminates, NASA TM 101622, June, 1989.

Ransom, Jonathan, Global/Local Stress Analysis of Composite Structures, NASA TM 101640, August, 1989.

Reddy, J. N., An Introduction to the Finite Element Method, McGraw-Hill Publishing Company, 1984.

Reddy, J. N., "On Computation Schemes for Global-Local Stress Analysis," Proceedings of NASA Workshop on Computational Methods in Structural Mechanics and Dynamics June 19-21, 1985, W. J. Stroud, J. M. Housner, J. A. Tanner, R. J. Hayduk, (editors), NASA CP-3034-Part 1, 1989, pp. 123-134.

Reddy, J. N., "On Refined Computational Models of Composite Laminates," International Journal for Numerical Methods in Engineering, Vol. 37, 1989, pp. 361-382.

Renieri, Gary D. and Carl T. Herakovich, "Nonlinear Analysis of Laminated Fibrous Composites," Report VPI-E-76-10, Virginia Polytechnic Institute and State University, June 1976.

Rybicki, E. F., "Approximate Three-Dimensional Solution for Symmetric Laminates Under In-Plane Loading," Journal for Composite Materials, Vol. 5, 1971, pp. 354-360.

Rybicki, E. F. and D. W. Schmueser, "Effect of Stacking Sequence and Lay-Up Angle on Free Edge Stresses Around a Hole in a Laminate Under Tension," Journal of Composite Materials, Vol. 12, 1978, pp. 300-313.

Salamon, Nicholas J., "An Assessment of the Interlaminar Stress Problem in Laminated Composites", Journal of Composite Materials Supplement, Vol. 14, 1980, pp. 177-194.

Schwartz, David J., "Practical Analysis of Stress Raisers in Solid Structures," Proceedings of Fourth International Conference on Vehicle Structural Mechanics, 1981, pp. 227-231.

Spilker, R. L. and S. C. Chou, "Edge Effects in Symmetric Composite Laminates: The Importance of Satisfying the Traction Free Edge Condition," Journal of Composite Materials, Vol. 14, 1980, pp. 2-19.

Stanley, Gary and Shahram Nour-Omid, The Computational Structural Mechanics Testbed Generic Structural Element Processor Manual, NASA CR-181732, March 1990.

Stanton, E. L., L. M. Crain and T. F. Neu, "A Parametric Cubic Modelling System for General Solids of Composite Materials, International Journal for Numerical Methods in Engineering, Vol. 11, 1977, pp. 653-670.

Stewart, Caroline B., The Computational Structural Mechanics Testbed User's Manual, NASA CR-100644, January, 1989.

Sun, C. T. and K. M. Mao, "A Global-Local Finite Element Method Suitable for Parallel Computations," Computers and Structures Vol. 29, No. 2, 1988, pp. 309-315.

Surana, Karan S., "Transition Finite Elements for Three-Dimensional Analysis," International Journal for Numerical Methods in Engineering, Vol. 15, 1980, pp. 991-1020.

Surana, Karan S., "Geometrically Non-linear Formulation for the Three-Dimensional Sold-Shell Transition Finite Elements," Computers and Structures, Vol. 15, 1982, pp. 549-566.

Thompson, Danniella M., O. H. Griffin, Jr. and Marco A. Vidussoni, "Cross-ply Laminates with Holes in Compression: Straight Free Edge Stresses Determined by 2-D to 3-D Global/Local Finite Element Analysis," Journal of Composites Science and Technology, Vol. 12, No. 4, December 1990, pp. 206-216.

Thompson, D. Muheim, and O. Hayden Griffin, Jr., "2-D to 3-D Global/Local Finite Element Analysis of Cross-Ply Composite Laminates," Journal of Reinforced Plastics and Composites, Vol. 9, No. 5, 1990, pp. 492-502.

Vidussoni, M.A., "Global/Local Finite Element Analysis of Laminated Composites", M.S. Thesis, Virginia Polytechnic and State University, Blacksburg, Virginia, July, 1988.

Wang, A.S.D. and F.W. Crossman, "Some New Results on Edge Effects in Symmetric Composite Laminates," Journal of Composite Materials, Vol.11, 1977, pp. 92-106.

Zahlan, N. and F. J. Guild., "Computer Aided Design of Thermoplastic Composite Structures", Composite Materials Design and Analysis -- Proceedings of Second International Conference on Computer Aided Design in Composite Material Technology -- Brussels, Eds. W.P. deWilde, W. R. Blain, Computational Mechanics Publications, United Kingdom, 1990, pp. 297-333.

Zienkiewicz, O. C., The Finite Element Method, Third Edition, McGraw-Hill Book Company, 1986.

Appendix A. Element Extrapolation Functions

A.1 Introduction

The determination of stress distributions from three-dimensional h-version finite elements with a local element-level extrapolation technique is presented in this appendix. This approach is applicable for the extrapolation of stresses or strains when the distribution is unknown across a structure and thus across the elements which represent this structure. A set of Lagrangian interpolating polynomials is used to extrapolate information from the Gaussian integration points to the nodal points on an element-by-element basis. Barlow (1976, 1989) has reported that the most accurate stresses for a displacement-based formulation element are calculated at the integration points. Most finite element models have element boundaries along geometric and/or material boundaries. Thus, the most accurate stresses are not obtained at these interfaces of interest, but rather at points within the elements. The stress extrapolation technique used in the present study extends that reported by Owen and Li (1987) for a 2x2x2 integration rule with an 8-node displacement-based three-dimensional element. This technique does not improve on the information available at the integration points, but presents it in a continuous manner at any location within the element. Generally, if a stress distribution varies widely across an element, more elements or higher order

elements should be used, rather than the extrapolation functions. Stresses can then be determined at nodal points or anywhere else in the element by using a weighted average of those stresses determined at the integration points over the element.

The type of integration scheme that is used affects the nature of the extrapolation functions. Many finite element models use displacement-based elements with reduced integration schemes. The reduced schemes soften the response of the displacement-based finite elements, which are inherently stiff in their response. Results generated are often closer to the exact solution, and are computationally less demanding than with full integration. However, the maximum element field order that can be adequately extrapolated for an integration scheme is dictated by the number of points in a particular direction. When the N-direction of the integration scheme has four (4) points, the maximum field order in the N-direction is a cubic, while three (3) points allows for a quadratic, and two (2) points a linear field. Thus, a reduced integration scheme with less integration points and the use of these extrapolation functions, has an upper bound on the order of the extrapolated stress field. On the other hand, using a higher-order integration scheme than necessary for a particular element or loading situation will only increase the computation time, and not the degree of accuracy of the results. If a higher-order stress distribution is expected, then a higher-order element with its corresponding integration scheme should be used. Following the development of these functions, two-dimensional examples are reported, since visualization of the functions is possible in two dimensions, but not in three dimensions with the available resources.

A.2 Development of Extrapolation Functions

The present approach uses Lagrangian interpolating polynomials constructed so the i^{th} polynomial, associated with integration point i, has a value of unity at that integration point and a value of zero at all other integration points. These polynomials are similar to the polynomials used to interpolate

geometry and displacements of a Lagrangian element, and for a 2x2x2 integration scheme, the form of the extrapolation functions is a more general form of the shape functions associated with an 8-node brick displacement-based element. The values, stresses in the present case, are then interpolated (or extrapolated) using the relationship

$$f\Big|_{(x,y,z)} = \sum_{i=1}^{N} f(x_i,y_i,z_i)\overline{\psi}_i\Big|_{(x,y,z)}$$

where f is the interpolated value at a point (x,y,z). N is the number of integration points, while $f(x_i,y_i,z_i)$ is the value at integration point i, associated with the function $\overline{\psi}_i$. These functions $\overline{\psi}_i$ are then evaluated at the point (x,y,z) for each function associated with an integration point.

These $\overline{\psi}_i$ polynomials can easily be constructed by the approach described by Reddy (1984). This approach is based on the fact that the interpolation function derived particular to any integration point should be zero at all but the i^{th} point and have the value of one at that point. The function is obtained by constructing a polynomial whose degree is sufficient to pass through all the integration points, and whose roots coincide with the desired extrapolation function. Such a function for a 2x2x2 integration rule, which is equal in all three coordinate directions, is of the form:

$$F(x_i, y_i, z_i) = \frac{(x+g)(x-g)(y-g)(y+g)(z-g)(z+g)}{(x-x_i)(y-y_i)(z-z_i)}$$

For a particular integration scheme, this function F is then evaluated at each integration point i to create a function ψ_i. For the 2x2x2 integration scheme, point i is located, in turn, at positions $(\pm g, \pm g, \pm g)$, where g is the coordinate of the integration point in the local element coordinate system, to determine the functions ψ_i. If the integration scheme is a 2x2x3 integration rule, for example, which is not equal in all directions, then the function F is of the form:

$$F(x_i, y_i, z_i) = \frac{(x+g)(x-g)(y-g)(y+g)(z-h)(z+h)}{(x-x_i)(y-y_i)(z-z_i)}$$

For the 2x2x3 integration scheme, point i is located at positions $(\pm g, \pm g, \pm h)$ and $(\pm g, \pm g, 0)$. For each set of extrapolation functions the function ψ_i is then normalized to have a value of one at the integration point i creating $\bar{\psi}_i$.

The development of an extrapolation function for one of the integration points in a particular integration scheme is presented. For the 2x2x3 integration scheme, for example, an integration point has the following coordinates: (-g,g,h). Evaluating the function F with this coordinate,

$$\psi(x,y,z) = F(-g,g,h) = \frac{(x+g)(x-g)(y-g)(y+g)(z-h)(z+h)}{(x+g)(y-(g))(z-(h))}$$

Simplifying the above expression yields,

$$\psi(x,y,z) = (x-g)(y+g)(z+h)$$

In order to determine the normalization constant, evaluate ψ at that same point,

$$\text{const} = \psi(-g,g,h) = (-2g)(2g)(2h) = -8g^4h$$

The function, $\bar{\psi}$, becomes,

$$\bar{\psi}(x,y,z) = \frac{-(x-g)(y+g)(z+h)}{8g^4h}$$

The remainder of the polynomials for the same integration scheme are then constructed. To determine a value at the node with the natural coordinates (1,1,1), the following summation is performed over the element.

$$f(1,1,1) = \sum_{i=1}^{N} f(x_i,y_i,z_i)\bar{\psi}_i\Big|_{(1,1,1)}$$

Reddy's approach was used to construct the interpolation functions for several integration schemes: 2x2x2, 2x2x3, 3x3x2, 3x3x3, 3x3x4, 4x4x2, 4x4x3, and 4x4x4. A graphical presentation of these

functions is provided for all of the above integration schemes in two-dimensions in Figure 105 through Figure 109. Functions for 2x2, 2x3, 2x4, 3x3, 3x4, and 4x4 planar schemes are presented. Because of the symmetry planes that exist through the center of an element plane, only those functions whose character is unique need be presented. Those functions presented are located in the first quadrant of the local element coordinate system. The equations for the three-dimensional extrapolation functions are presented, in their entirety, in Table 10 through Table 29, respectively. All of these sets of extrapolation functions are available for the family of Serendipity elements with 8, 16, 20, 24, and 32 nodes, which were implemented in the CSM Testbed by the author, for all of the integration schemes.

A.3 Examples

The capability of these functions to extrapolate various field orders in three-dimensions is difficult to present graphically. Accepting this limitation, this capability can be demonstrated for a plane of locations at a constant z-value with fields that are invariant in the z-dimension. The field xy^2 is the highest in-plane order field that can be extrapolated for the 2x2x3 integration points. In Figure 110 the exact distribution of xy^2, the representation of xy^2 by the integration points (sampling points), the extrapolation over the element of the information from the integration points, and finally the error of the extrapolation functions in determining the function is presented. In this case, the error is zero across the element.

The 2x2x3 integration scheme cannot successfully determine the x^2y^2 field, as shown in Figure 111. The amount of information at the sampling points is insufficient to determine the character of the field in the y-direction throughout the element. The error in attempting to use such an integration and its associated extrapolation function set is evident in this figure. However, a 3x3 integration scheme and its extrapolation functions can extrapolate a sampling point distribution that

is x^2y^2, as can be seen in Figure 112. Each of the sets of functions can determine information over an element for field orders that are less than their maximum capability. The maximum element field order for an integration scheme is dictated by the number of points in a particular direction, as mentioned previously.

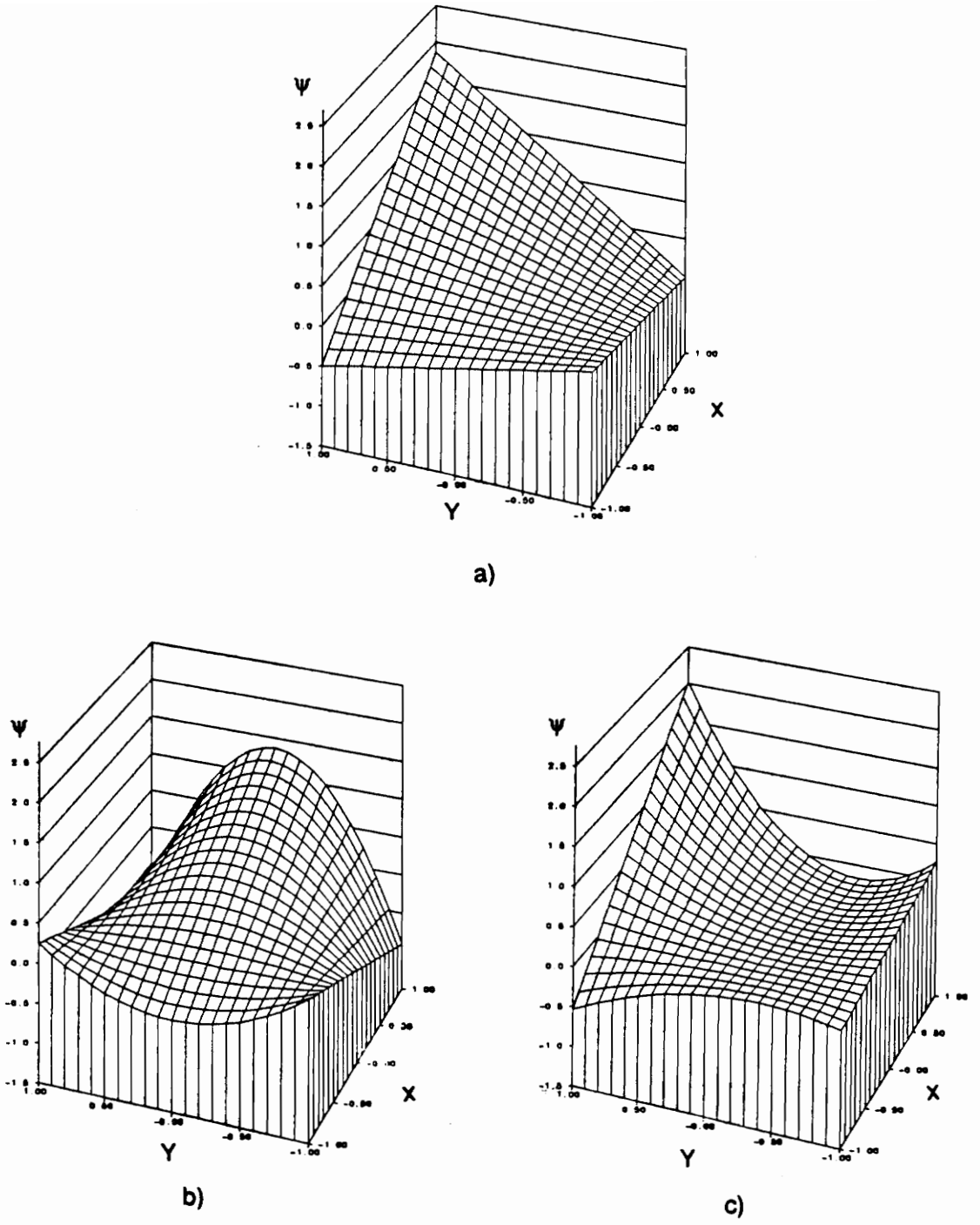

Figure 105. **Extrapolation functions for 2x2 and 2x3 integration sequences along z = constant:** a) Function for corner point (2x2) b) Function for mid-point (2x3) b) Function for corner point (2x3)

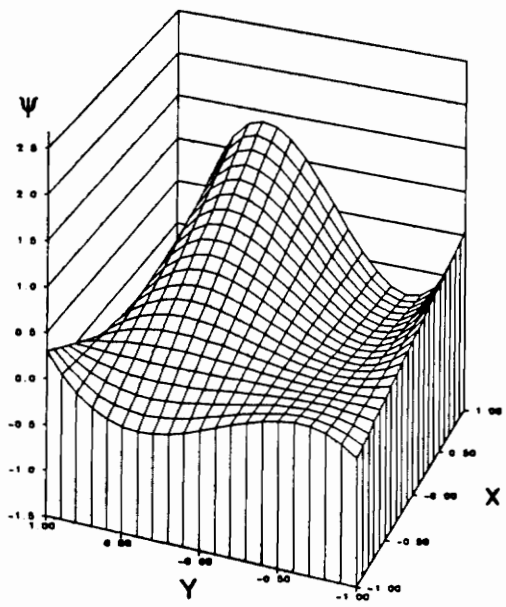

a)

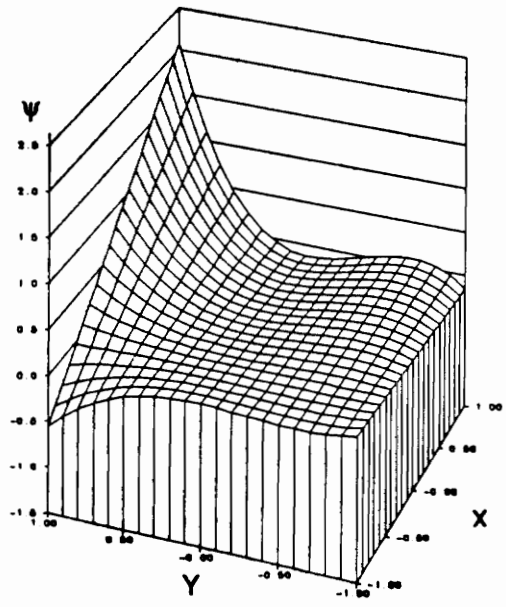

b)

Figure 106. Extrapolation functions for 2x4 integration sequence along z = constant: a) Function for mid-point b) Function for corner point

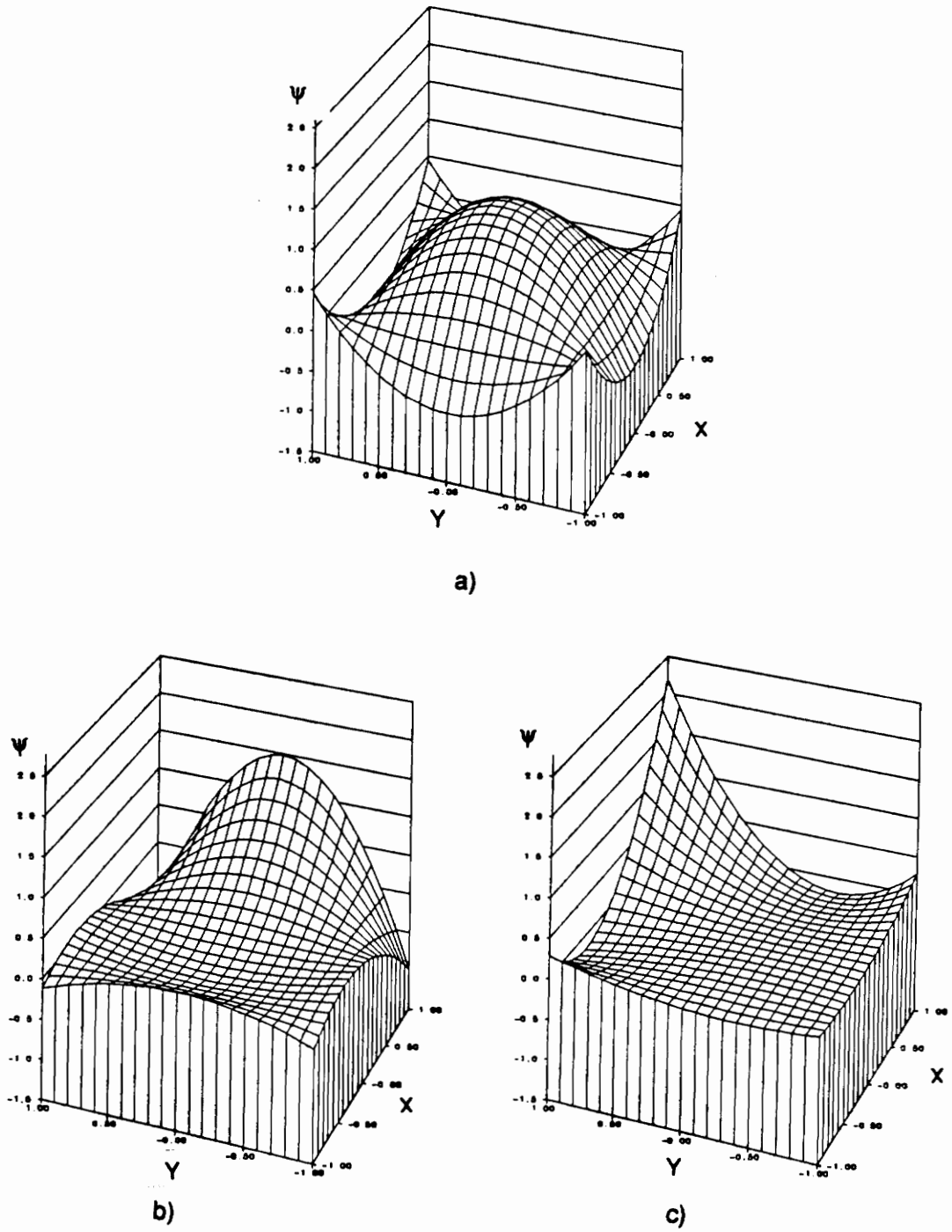

Figure 107. Extrapolation functions for 3x3 integration sequence along z = constant: a) Function for center point b) Function for mid-point c) Function for corner point

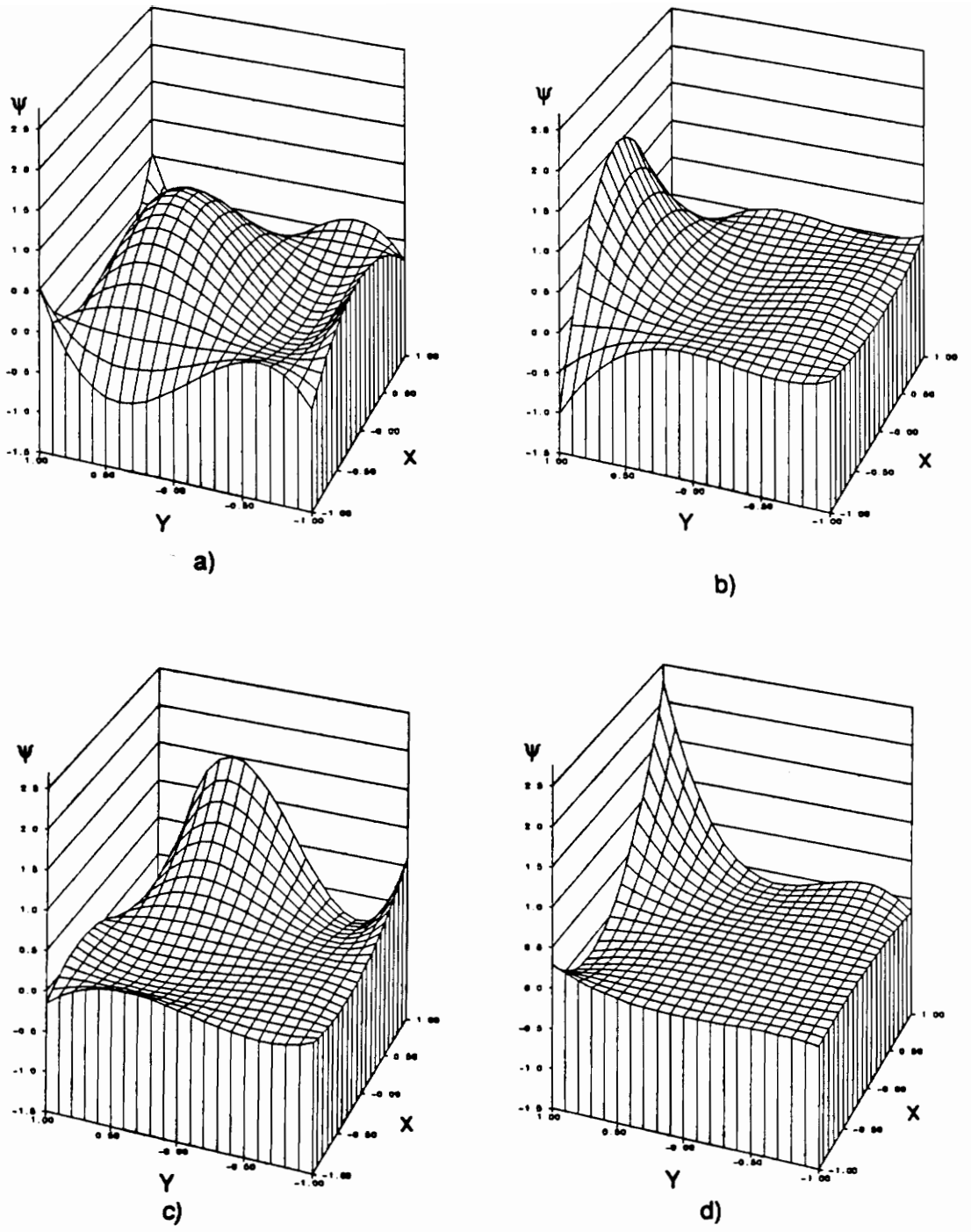

Figure 108. Extrapolation functions for 3x4 integration sequence along z = constant: a) Function for an interior point b) Function for a mid-point along quadratic edge c) Function for a mid-point along cubic edge d) Function for a corner point

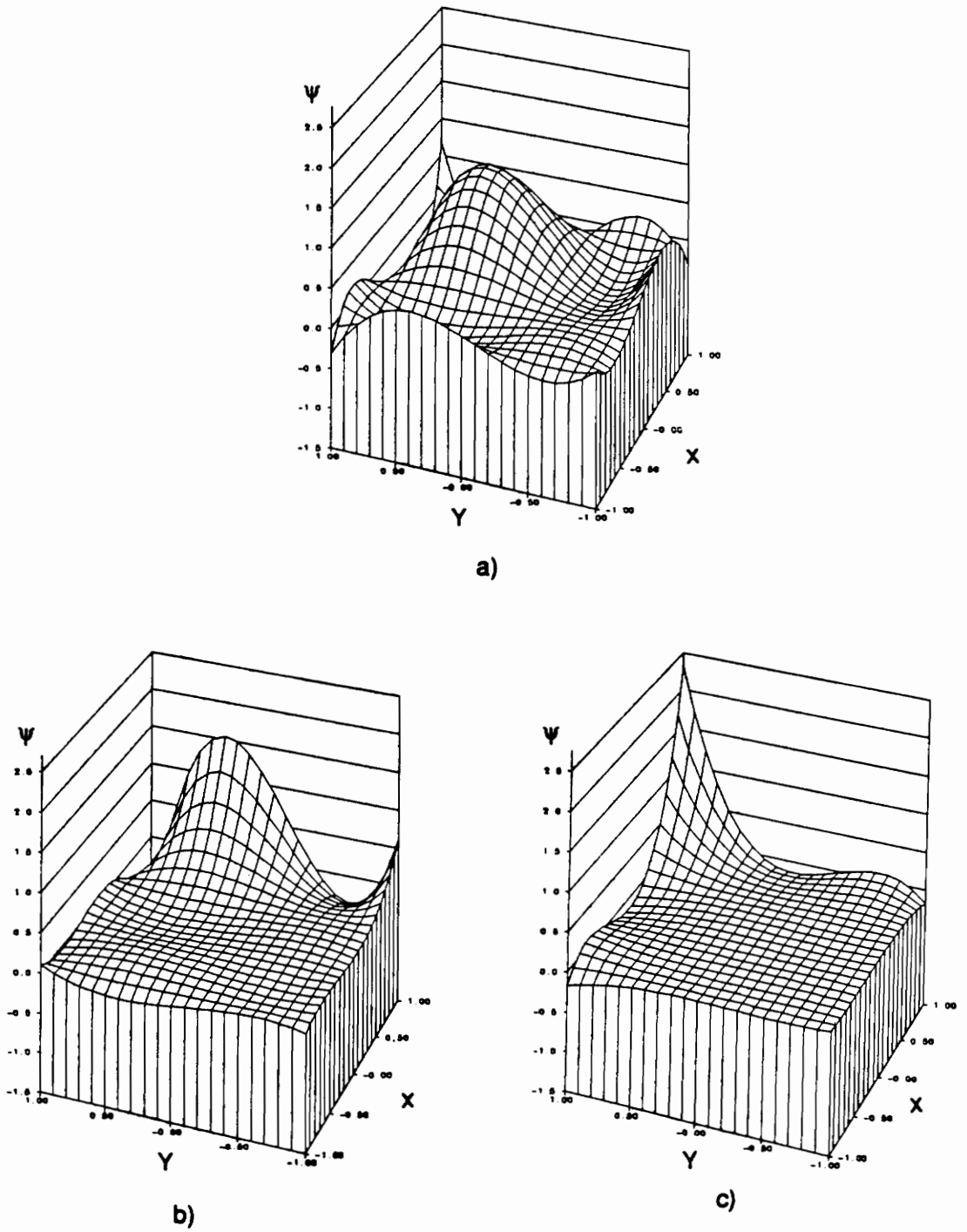

Figure 109. Extrapolation functions for 4x4 integration sequence along z = constant: a) Function for an interior point b) Function for a mid-point c) Function for a corner point

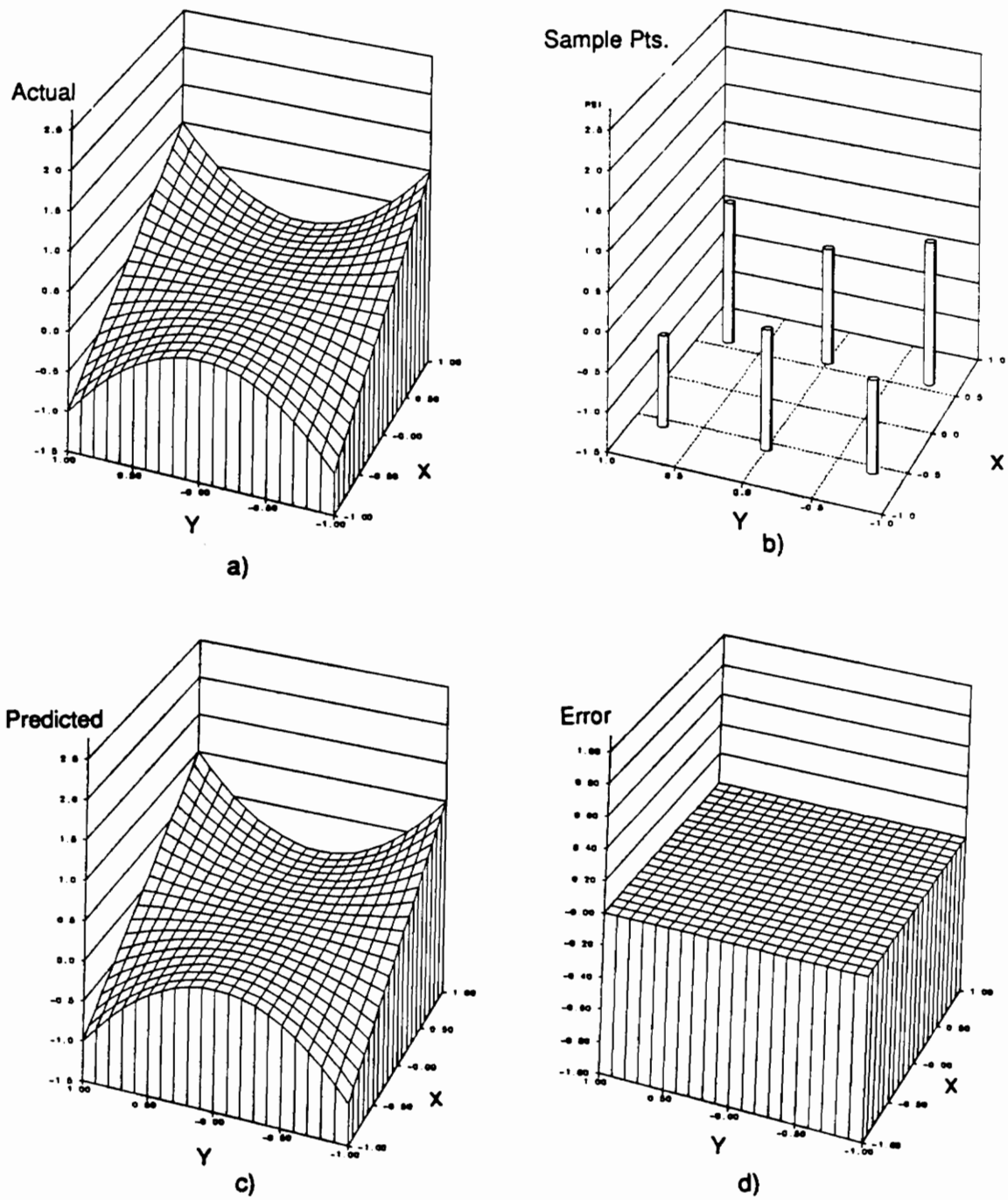

Figure 110. Extrapolation with 2x3 functions of xy^2: a) Actual Function b) Sampling Points c) Extrapolated Function d) Error

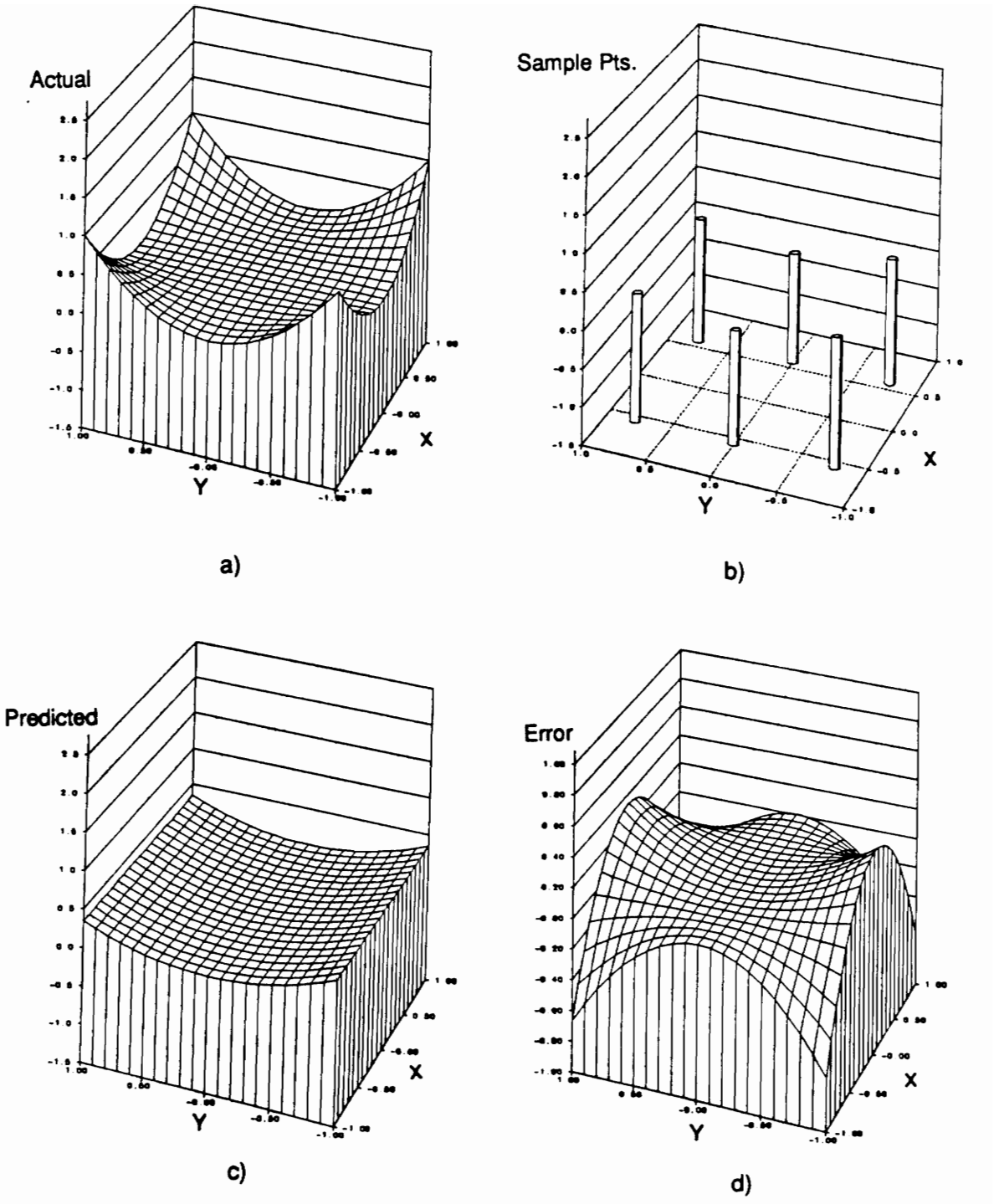

Figure 111. Extrapolation with 2x3 functions of x^2y^2: a) Actual Function b) Sampling Points c) Extrapolated Function d) Error

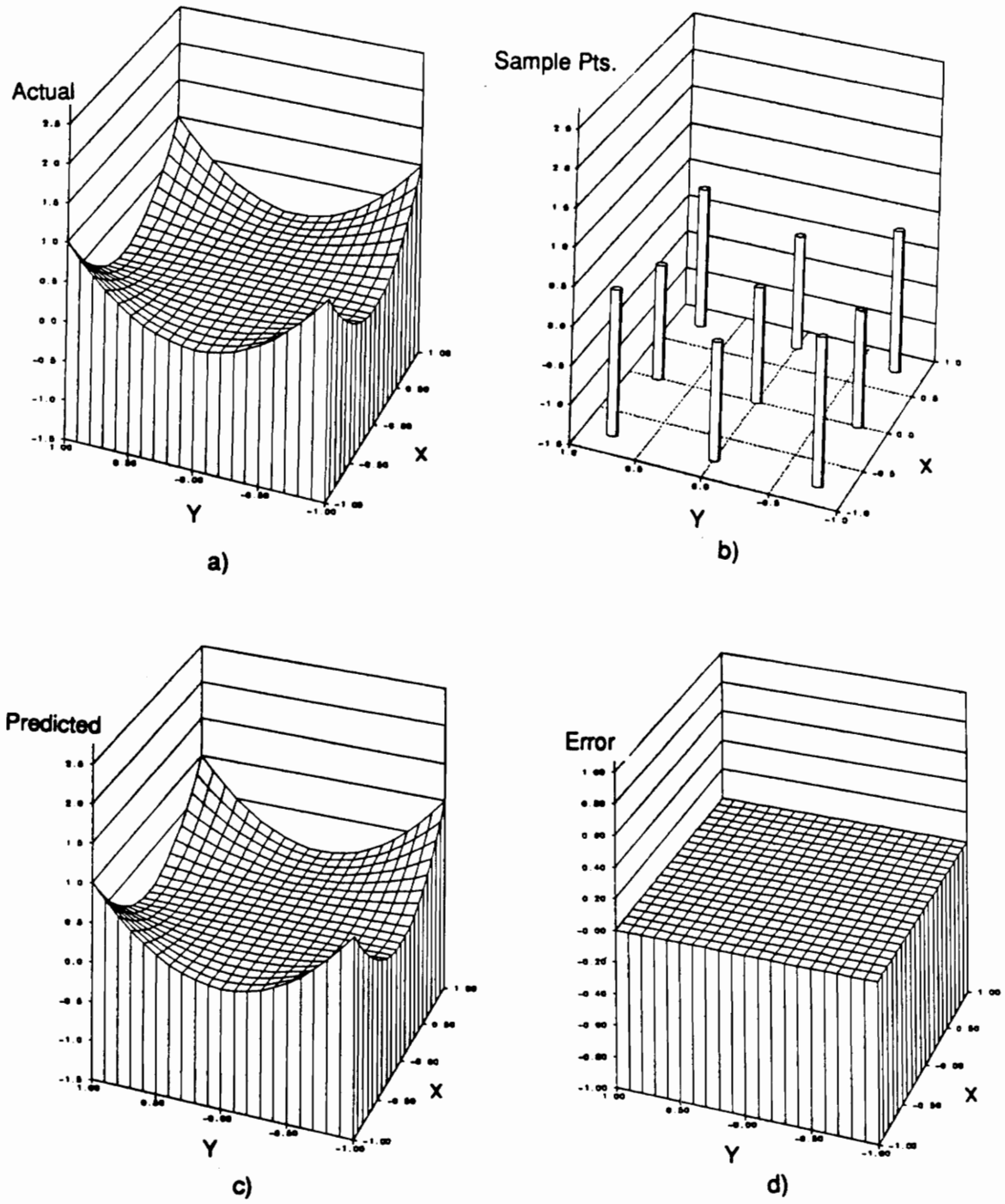

Figure 112. **Extrapolation with 3x3 functions of x^2y^2:** a) Actual Function b) Sampling Points c) Extrapolated Function d) Error

Table 10. Extrapolation Functions for 2x2x2 Integration Rule

Coordinate	Extrapolation Function
(-g,-g,-g)	$\frac{-(x-g)(y-g)(z-g)}{8g^3}$
(-g,g,-g)	$\frac{(x-g)(y+g)(z-g)}{8g^3}$
(g,-g,-g)	$\frac{(x+g)(y-g)(z-g)}{8g^3}$
(g,g,-g)	$\frac{-(x+g)(y+g)(z-g)}{8g^3}$
(-g,-g,g)	$\frac{(x-g)(y-g)(z+g)}{8g^3}$
(-g,g,g)	$\frac{-(x-g)(y+g)(z+g)}{8g^3}$
(g,-g,g)	$\frac{-(x+g)(y-g)(z+g)}{8g^3}$
(g,g,g)	$\frac{(x+g)(y+g)(z+g)}{8g^3}$
$g = 0.57735\ 02691\ 89626$	

Table 11. Extrapolation Functions for 2x2x3 Integration Rule

Coordinate	Extrapolation Function
(-g,-g,-h)	$\frac{(x-g)(y-g)z(z-h)}{8g^2h^2}$
(-g,g,-h)	$\frac{-(x-g)(y+g)z(z-h)}{8g^2h^2}$
(g,-g,-h)	$\frac{-(x+g)(y-g)z(z-h)}{8g^2h^2}$
(g,g,-h)	$\frac{(x+g)(y+g)z(z-h)}{8g^2h^2}$
(-g,-g,0)	$\frac{-(x-g)(y-g)(z-h)(z+h)}{4g^2h^2}$
(-g,g,0)	$\frac{(x-g)(y+g)(z-h)(z+h)}{4g^2h^2}$
(g,-g,0)	$\frac{(x+g)(y-g)(z-h)(z+h)}{4g^2h^2}$
(g,g,0)	$\frac{-(x+g)(y+g)(z-h)(z+h)}{4g^2h^2}$
(-g,-g,h)	$\frac{(x-g)(y-g)z(z+g)}{8g^2h^2}$
(-g,g,h)	$\frac{-(x-g)(y+g)z(z+g)}{8g^2h^2}$
(g,-g,h)	$\frac{-(x+g)(y-g)z(z+g)}{8g^2h^2}$
(g,g,h)	$\frac{(x+g)(y+g)z(z+g)}{8g^2h^2}$
$g = 0.57735\ 02691\ 89626 \quad h = 0.77459\ 66692\ 41483$	

Table 12. Extrapolation Functions for 3x3x2 Integration Rule for Integration Points along z = -g

Coordinate	Extrapolation Function
(-h,-h,-g)	$\frac{-x(x-h)y(y-h)(z-g)}{8gh^4}$
(-h,0,-g)	$\frac{x(x-h)(y-h)(y+h)(z-g)}{4gh^4}$
(h,h,-g)	$\frac{-x(x-h)y(y+h)(z-g)}{8gh^4}$
(0,-h,-g)	$\frac{(x-h)(x+h)y(y-h)(z-g)}{4gh^4}$
(0,0,-g)	$\frac{-(x-h)(x+h)(y-h)(y+h)(z-g)}{2gh^4}$
(0,h,-g)	$\frac{(x-h)(x+h)y(y+h)(z-g)}{4gh^4}$
(h,-h,-g)	$\frac{-x(x+h)y(y-h)(z-g)}{8gh^4}$
(h,0,-g)	$\frac{x(x+h)(y-h)(y+h)(z-g)}{4gh^4}$
(h,h,-g)	$\frac{-x(x+h)y(y+h)(z-g)}{8gh^4}$
g = 0.57735 02691 89626 h = 0.77459 66692 41483	

Table 13. Extrapolation Functions for 3x3x2 Integration Rule for Integration Points along $z = g$

Coordinate	Extrapolation Function
(-h,-h,g)	$\frac{x(x-h)y(y-h)(z+g)}{8gh^4}$
(-h,0,g)	$\frac{-x(x-h)(y-h)(y+h)(z+g)}{4gh^4}$
(h,h,g)	$\frac{x(x-h)y(y+h)(z+g)}{8gh^4}$
(0,-h,g)	$\frac{-(x-h)(x+h)y(y-h)(z+g)}{4gh^4}$
(0,0,g)	$\frac{(x-h)(x+h)(y-h)(y+h)(z+g)}{2gh^4}$
(0,h,g)	$\frac{-(x-h)(x+h)y(y+h)(z+g)}{4gh^4}$
(h,-h,g)	$\frac{x(x+h)y(y-h)(z+g)}{8gh^4}$
(h,0,g)	$\frac{-x(x+h)(y-h)(y+h)(z+g)}{4gh^4}$
(h,h,g)	$\frac{x(x+h)y(y+h)(z+g)}{8gh^4}$
$g = 0.57735\ 02691\ 89626$ $h = 0.77459\ 66692\ 41483$	

Table 14. Extrapolation Functions for 3x3x3 Integration Rule for Integration Points along z = -h

Coordinate	Extrapolation Function
(-h,-h,-h)	$\frac{x(x-h)y(y-h)z(z-h)}{8h^6}$
(-h,0,-h)	$\frac{-x(x-h)(y-h)(y+h)z(z-h)}{4h^6}$
(-h,h,-h)	$\frac{x(x-h)y(y+h)z(z-h)}{8h^6}$
(0,-h,-h)	$\frac{-(x-h)(x+h)y(y-h)z(z-h)}{4h^6}$
(0,0,-h)	$\frac{(x-h)(x+h)(y-h)(y+h)z(z-h)}{2h^6}$
(0,h,-h)	$\frac{-(x-h)(x+h)y(y+h)z(z-h)}{4h^6}$
(h,-h,-h)	$\frac{x(x+h)y(y-h)z(z-h)}{8h^6}$
(h,0,-h)	$\frac{-x(x+h)(y-h)(y+h)z(z-h)}{4h^6}$
(h,h,-h)	$\frac{x(x+h)y(y+h)z(z-h)}{8h^6}$
h = 0.77459 66692 41483	

Table 15. Extrapolation Functions for 3x3x3 Integration Rule for Integration Points along $z = 0$

Coordinate	Extrapolation Function
(-h,-h,0)	$\frac{-x(x-h)y(y-h)(z-h)(z+h)}{4h^6}$
(-h,0,0)	$\frac{x(x-h)(y-h)(y+h)(z-h)(z+h)}{2h^6}$
(-h,h,0)	$\frac{-x(x-h)y(y+h)(z-h)(z+h)}{4h^6}$
(0,-h,0)	$\frac{(x-h)(x+h)y(y-h)(z-h)(z+h)}{2h^6}$
(0,0,0)	$\frac{-(x-h)(x+h)(y-h)(y+h)(z-h)(z+h)}{h^6}$
(0,h,0)	$\frac{(x-h)(x+h)y(y+h)(z-h)(z+h)}{2h^6}$
(h,-h,0)	$\frac{-x(x+h)y(y-h)(z-h)(z+h)}{4h^6}$
(h,0,0)	$\frac{x(x+h)(y-h)(y+h)(z-h)(z+h)}{2h^6}$
(h,h,0)	$\frac{-x(x+h)y(y+h)(z-h)(z+h)}{4h^6}$
$h = 0.77459\ 66692\ 41483$	

Table 16. Extrapolation Functions for 3x3x3 Integration Rule for Integration Points along $z = h$

Coordinate	Extrapolation Function
(-h,-h,h)	$\frac{x(x-h)y(y-h)z(z+h)}{8h^6}$
(-h,0,h)	$\frac{-x(x-h)(y-h)(y+h)z(z+h)}{4h^6}$
(-h,h,h)	$\frac{x(x-h)y(y+h)z(z+h)}{8h^6}$
(0,-h,h)	$\frac{-(x-h)(x+h)y(y-h)z(z+h)}{4h^6}$
(0,0,h)	$\frac{(x-h)(x+h)(y-h)(y+h)z(z+h)}{2h^6}$
(0,h,h)	$\frac{-(x-h)(x+h)y(y+h)z(z+h)}{4h^6}$
(h,-h,h)	$\frac{x(x+h)y(y-h)z(z+h)}{8h^6}$
(h,0,h)	$\frac{-x(x+h)(y-h)(y+h)z(z+h)}{4h^6}$
(h,h,h)	$\frac{x(x+h)y(y+h)z(z+h)}{8h^6}$
$h = 0.77459\ 66692\ 41483$	

Table 17. Extrapolation Functions for 3x3x4 Integration Rule for Integration Points along z = -m

Coordinate	Extrapolation Function
(-h,-h,-m)	$\frac{x(x-h)y(y-h)(z-m)(z-n)(z+n)}{8h^4m(n-m)(n+m)}$
(-h,0,-m)	$\frac{-x(x-h)(y-h)(y+h)(z-m)(z-n)(z+n)}{4h^4m(n-m)(n+m)}$
(-h,h,-m)	$\frac{x(x-h)y(y+h)(z-m)(z-n)(z+n)}{8h^4m(n-m)(n+m)}$
(0,-h,-m)	$\frac{-(x-h)(x+h)y(y-h)(z-m)(z-n)(z+n)}{4h^4m(n-m)(n+m)}$
(0,0,-m)	$\frac{(x-h)(x+h)(y-h)(y+h)(z-m)(z-n)(z+n)}{2h^4m(n-m)(n+m)}$
(0,h,-m)	$\frac{-(x-h)(x+h)y(y+h)(z-m)(z-n)(z+n)}{4h^4m(n-m)(n+m)}$
(h,-h,-m)	$\frac{x(x+h)y(y-h)(z-m)(z-n)(z+n)}{8h^4m(n-m)(n+m)}$
(h,0,-m)	$\frac{-x(x+h)(y-h)(y+h)(z-m)(z-n)(z+n)}{4h^4m(n-m)(n+m)}$
(h,h,-m)	$\frac{x(x+h)y(y+h)(z-m)(z-n)(z+n)}{8h^4m(n-m)(n+m)}$
h = 0.77459 66692 41483 m = 0.86113 63115 94053 n = 0.33998 10435 84856	

Table 18. Extrapolation Functions for 3x3x4 Integration Rule for Integration Points along z = -n

Coordinate	Extrapolation Function
(-h,-h,-n)	$\frac{-x(x-h)y(y-h)(z-m)(z+m)(z-n)}{8h^4n(n-m)(n+m)}$
(-h,0,-n)	$\frac{x(x-h)(y-h)(y+h)(z-m)(z+m)(z-n)}{4h^4n(n-m)(n+m)}$
(-h,h,-n)	$\frac{-x(x-h)y(y+h)(z-m)(z+m)(z-n)}{8h^4n(n-m)(n+m)}$
(0,-h,-n)	$\frac{(x-h)(x+h)y(y-h)(z-m)(z+m)(z-n)}{4h^4n(n-m)(n+m)}$
(0,0,-n)	$\frac{-(x-h)(x+h)(y-h)(y+h)(z-m)(z+m)(z-n)}{2h^4n(n-m)(n+m)}$
(0,h,-n)	$\frac{(x-h)(x+h)y(y+h)(z-m)(z+m)(z-n)}{4h^4n(n-m)(n+m)}$
(h,-h,-n)	$\frac{-x(x+h)y(y-h)(z-m)(z+m)(z-n)}{8h^4n(n-m)(n+m)}$
(h,0,-n)	$\frac{x(x+h)(y-h)(y+h)(z-m)(z+m)(z-n)}{4h^4n(n-m)(n+m)}$
(h,h,-n)	$\frac{-x(x+h)y(y+h)(z-m)(z+m)(z-n)}{8h^4n(n-m)(n+m)}$
h = 0.77459 66692 41483 m = 0.86113 63115 94053 n = 0.33998 10435 84856	

Table 19. Extrapolation Functions for 3x3x4 Integration Rule for Integration Points along z = n

Coordinate	Extrapolation Function
(-h,-h,n)	$\frac{x(x-h)y(y-h)(z-m)(z+m)(z+n)}{8h^4n(n-m)(n+m)}$
(-h,0,n))	$\frac{-x(x-h)(y-h)(y+h)(z-m)(z+m)(z+n)}{4h^4n(n-m)(n+m)}$
(-h,h,n)	$\frac{x(x-h)y(y+h)(z-m)(z+m)(z+n)}{8h^4n(n-m)(n+m)}$
(0,-h,n)	$\frac{-(x-h)(x+h)y(y-h)(z-m)(z+m)(z+n)}{4h^4n(n-m)(n+m)}$
(0,0,n))	$\frac{(x-h)(x+h)(y-h)(y+h)(z-m)(z+m)(z+n)}{2h^4n(n-m)(n+m)}$
(0,h,n)	$\frac{-(x-h)(x+h)y(y+h)(z-m)(z+m)(z+n)}{4h^4n(n-m)(n+m)}$
(h,-h,n)	$\frac{x(x+h)y(y-h)(z-m)(z+m)(z+n)}{8h^4n(n-m)(n+m)}$
(h,0,n))	$\frac{-x(x+h)(y-h)(y+h)(z-m)(z+m)(z+n)}{4h^4n(n-m)(n+m)}$
(h,h,n)	$\frac{x(x+h)y(y+h)(z-m)(z+m)(z+n)}{8h^4n(n-m)(n+m)}$
h = 0.77459 66692 41483 m = 0.86113 63115 94053 n = 0.33998 10435 84856	

Table 20. Extrapolation Functions for 3x3x4 Integration Rule for Integration Points along $z = m$

Coordinate	Extrapolation Function
(-h,-h,m)	$\dfrac{-x(x-h)y(y-h)(z+m)(z-n)(z+n)}{8h^4m(n-m)(n+m)}$
(-h,0,m)	$\dfrac{x(x-h)(y-h)(y+h)(z+m)(z-n)(z+n)}{4h^4m(n-m)(n+m)}$
(-h,h,m)	$\dfrac{-x(x-h)y(y+h)(z+m)(z-n)(z+n)}{8h^4m(n-m)(n+m)}$
(0,-h,m)	$\dfrac{(x-h)(x+h)y(y-h)(z+m)(z-n)(z+n)}{4h^4m(n-m)(n+m)}$
(0,0,m)	$\dfrac{-(x-h)(x+h)(y-h)(y+h)(z+m)(z-n)(z+n)}{2h^4m(n-m)(n+m)}$
(0,h,m)	$\dfrac{(x-h)(x+h)y(y+h)(z+m)(z-n)(z+n)}{4h^4m(n-m)(n+m)}$
(h,-h,m)	$\dfrac{-x(x+h)y(y-h)(z+m)(z-n)(z+n)}{8h^4m(n-m)(n+m)}$
(h,0,m)	$\dfrac{x(x+h)(y-h)(y+h)(z+m)(z-n)(z+n)}{4h^4m(n-m)(n+m)}$
(h,h,m)	$\dfrac{-x(x+h)y(y+h)(z+m)(z-n)(z+n)}{8h^4m(n-m)(n+m)}$
$h = 0.77459\ 66692\ 41483$ $m = 0.86113\ 63115\ 94053$ $n = 0.33998\ 10435\ 84856$	

Table 21. Extrapolation Functions for 4x4x2 Integration Rule for Integration Points along z = -g

Coordinate	Extrapolation Function
(-m,-m,-g)	$\frac{-(x-m)(x-n)(x+n)(y-m)(y-n)(y+n)(z-g)}{8gm^2(n-m)^2(n+m)^2}$
(-m,-n,-g)	$\frac{(x-m)(x-n)(x+n)(y-m)(y+m)(y-n)(z-g)}{8gmn(n-m)^2(n+m)^2}$
(-m,n,-g)	$\frac{-(x-m)(x-n)(x+n)(y-m)(y+m)(y+n)(z-g)}{8gmn(n-m)^2(n+m)^2}$
(-m,m,-g)	$\frac{(x-m)(x-n)(x+n)(y+m)(y-n)(y+n)(z-g)}{8gm^2(n-m)^2(n+m)^2}$
(-n,-m,-g)	$\frac{(x-m)(x+m)(x-n)(y-m)(y-n)(y+n)(z-g)}{8gmn(n-m)^2(n+m)^2}$
(-n,-n,-g)	$\frac{-(x-m)(x+m)(x-n)(y-m)(y+m)(y-n)(z-g)}{8gn^2(n-m)^2(n+m)^2}$
(-n,n,-g)	$\frac{(x-m)(x+m)(x-n)(y-m)(y+m)(y+n)(z-g)}{8gn^2(n-m)^2(n+m)^2}$
(-n,m,-g)	$\frac{-(x-m)(x+m)(x-n)(y+m)(y-n)(y+n)(z-g)}{8gmn(n-m)^2(n+m)^2}$
(n,-m,-g)	$\frac{-(x-m)(x+m)(x+n)(y-m)(y-n)(y+n)(z-g)}{8gmn(n-m)^2(n+m)^2}$
(n,-n,-g)	$\frac{(x-m)(x+m)(x+n)(y-m)(y+m)(y-n)(z-g)}{8gn^2(n-m)^2(n+m)^2}$
(n,n,-g)	$\frac{-(x-m)(x+m)(x+n)(y-m)(y+m)(y+n)(z-g)}{8gn^2(n-m)^2(n+m)^2}$
(n,m,-g)	$\frac{(x-m)(x+m)(x+n)(y+m)(y-n)(y+n)(z-g)}{8gmn(n-m)^2(n+m)^2}$
(m,-m,-g)	$\frac{(x+m)(x-n)(x+n)(y-m)(y-n)(y+n)(z-g)}{8gm^2(n-m)^2(n+m)^2}$
(m,-n,-g)	$\frac{-(x+m)(x-n)(x+n)(y-m)(y+m)(y-n)(z-g)}{8gmn(n-m)^2(n+m)^2}$
(m,n,-g)	$\frac{(x+m)(x-n)(x+n)(y-m)(y+m)(y+n)(z-g)}{8gmn(n-m)^2(n+m)^2}$
(m,m,-g)	$\frac{-(x+m)(x-n)(x+n)(y+m)(y-n)(y+n)(z-g)}{8gm^2(n-m)^2(n+m)^2}$

m = 0.86113 63115 94053 n = 0.33998 10435 84856 g = 0.57735 02691 89626

Table 22. Extrapolation Functions for 4x4x2 Integration Rule for Integration Points along z = g

Coordinate	Extrapolation Function
(-m,-m,g)	$\frac{(x-m)(x-n)(x+n)(y-m)(y-n)(y+n)(z+g)}{8gm^2(n-m)^2(n+m)^2}$
(-m,-n,g)	$-\frac{(x-m)(x-n)(x+n)(y-m)(y+m)(y-n)(z+g)}{8gmn(n-m)^2(n+m)^2}$
(-m,n,g)	$\frac{(x-m)(x-n)(x+n)(y-m)(y+m)(y+n)(z+g)}{8gmn(n-m)^2(n+m)^2}$
(-m,m,g)	$-\frac{(x-m)(x-n)(x+n)(y+m)(y-n)(y+n)(z+g)}{8gm^2(n-m)^2(n+m)^2}$
(-n,-m,g)	$-\frac{(x-m)(x+m)(x-n)(y-m)(y-n)(y+n)(z+g)}{8gmn(n-m)^2(n+m)^2}$
(-n,-n,g)	$\frac{(x-m)(x+m)(x-n)(y-m)(y+m)(y-n)(z+g)}{8gn^2(n-m)^2(n+m)^2}$
(-n,n,g)	$-\frac{(x-m)(x+m)(x-n)(y-m)(y+m)(y+n)(z+g)}{8gn^2(n-m)^2(n+m)^2}$
(-n,m,g)	$\frac{(x-m)(x+m)(x-n)(y+m)(y-n)(y+n)(z+g)}{8gmn(n-m)^2(n+m)^2}$
(n,-m,g)	$\frac{(x-m)(x+m)(x+n)(y-m)(y-n)(y+n)(z+g)}{8gmn(n-m)^2(n+m)^2}$
(n,-n,g)	$-\frac{(x-m)(x+m)(x+n)(y-m)(y+m)(y-n)(z+g)}{8gn^2(n-m)^2(n+m)^2}$
(n,n,g)	$\frac{(x-m)(x+m)(x+n)(y-m)(y+m)(y+n)(z+g)}{8gn^2(n-m)^2(n+m)^2}$
(n,m,g)	$-\frac{(x-m)(x+m)(x+n)(y+m)(y-n)(y+n)(z+g)}{8gmn(n-m)^2(n+m)^2}$
(m,-m,g)	$-\frac{(x+m)(x-n)(x+n)(y-m)(y-n)(y+n)(z+g)}{8gm^2(n-m)^2(n+m)^2}$
(m,-n,g)	$\frac{(x+m)(x-n)(x+n)(y-m)(y+m)(y-n)(z+g)}{8gmn(n-m)^2(n+m)^2}$
(m,n,g)	$-\frac{(x+m)(x-n)(x+n)(y-m)(y+m)(y+n)(z+g)}{8gmn(n-m)^2(n+m)^2}$
(m,m,g)	$\frac{(x+m)(x-n)(x+n)(y+m)(y-n)(y+n)(z+g)}{8gm^2(n-m)^2(n+m)^2}$

m = 0.86113 63115 94053 n = 0.33998 10435 84856 g = 0.57735 02691 89626

Table 23. Extrapolation Functions for 4x4x3 Integration Rule for Integration Points along z = -h

Coordinate	Extrapolation Function
(-m,-m,-h)	$\frac{(x-m)(x-n)(x+n)(y-m)(y-n)(y+n)z(z-h)}{8g^2m^2(n-m)^2(n+m)^2}$
(-m,-n,-h)	$\frac{-(x-m)(x-n)(x+n)(y-m)(y+m)(y-n)z(z-h)}{8g^2mn(n-m)^2(n+m)^2}$
(-m,n,-h)	$\frac{(x-m)(x-n)(x+n)(y-m)(y+m)(y+n)z(z-h)}{8g^2mn(n-m)^2(n+m)^2}$
(-m,m,-h)	$\frac{-(x-m)(x-n)(x+n)(y+m)(y-n)(y+n)z(z-h)}{8g^2m^2(n-m)^2(n+m)^2}$
(-n,-m,-h)	$\frac{-(x-m)(x+m)(x-n)(y-m)(y-n)(y+n)z(z-h)}{8g^2mn(n-m)^2(n+m)^2}$
(-n,-n,-h)	$\frac{(x-m)(x+m)(x-n)(y-m)(y+m)(y-n)z(z-h)}{8g^2n^2(n-m)^2(n+m)^2}$
(-n,n,-h)	$\frac{-(x-m)(x+m)(x-n)(y-m)(y+m)(y+n)z(z-h)}{8g^2n^2(n-m)^2(n+m)^2}$
(-n,m,-h)	$\frac{(x-m)(x+m)(x-n)(y+m)(y-n)(y+n)z(z-h)}{8g^2mn(n-m)^2(n+m)^2}$
(n,-m,-h)	$\frac{(x-m)(x+m)(x+n)(y-m)(y-n)(y+n)z(z-h)}{8g^2mn(n-m)^2(n+m)^2}$
(n,-n,-h)	$\frac{-(x-m)(x+m)(x+n)(y-m)(y+m)(y-n)z(z-h)}{8g^2n^2(n-m)^2(n+m)^2}$
(n,n,-h)	$\frac{(x-m)(x+m)(x+n)(y-m)(y+m)(y+n)z(z-h)}{8g^2n^2(n-m)^2(n+m)^2}$
(n,m,-h)	$\frac{-(x-m)(x+m)(x+n)(y+m)(y-n)(y+n)z(z-h)}{8g^2mn(n-m)^2(n+m)^2}$
(m,-m,-h)	$\frac{-(x+m)(x-n)(x+n)(y-m)(y-n)(y+n)z(z-h)}{8g^2m^2(n-m)^2(n+m)^2}$
(m,-n,-h)	$\frac{(x+m)(x-n)(x+n)(y-m)(y+m)(y-n)z(z-h)}{8g^2mn(n-m)^2(n+m)^2}$
(m,n,-h)	$\frac{-(x+m)(x-n)(x+n)(y-m)(y+m)(y+n)z(z-h)}{8g^2mn(n-m)^2(n+m)^2}$
(m,m,-h)	$\frac{(x+m)(x-n)(x+n)(y+m)(y-n)(y+n)z(z-h)}{8g^2m^2(n-m)^2(n+m)^2}$

m = 0.86113 63115 94053 n = 0.33998 10435 84856 h = 0.77459 66692 41483

Table 24. Extrapolation Functions for 4x4x3 Integration Rule for Integration Points along $z = 0$

Coordinate	Extrapolation Function
(-m,-m,0)	$\frac{-(x-m)(x-n)(x+n)(y-m)(y-n)(y+n)(z-h)(z+h)}{4g^2m^2(n-m)^2(n+m)^2}$
(-m,-n,0)	$\frac{(x-m)(x-n)(x+n)(y-m)(y+m)(y-n)(z-h)(z+h)}{4g^2mn(n-m)^2(n+m)^2}$
(-m,n,0)	$\frac{-(x-m)(x-n)(x+n)(y-m)(y+m)(y+n)(z-h)(z+h)}{4g^2mn(n-m)^2(n+m)^2}$
(-m,m,0)	$\frac{(x-m)(x-n)(x+n)(y+m)(y-n)(y+n)(z-h)(z+h)}{4g^2m^2(n-m)^2(n+m)^2}$
(-n,-m,0)	$\frac{(x-m)(x+m)(x-n)(y-m)(y-n)(y+n)(z-h)(z+h)}{4g^2mn(n-m)^2(n+m)^2}$
(-n,-n,0)	$\frac{-(x-m)(x+m)(x-n)(y-m)(y+m)(y-n)(z-h)(z+h)}{4g^2n^2(n-m)^2(n+m)^2}$
(-n,n,0)	$\frac{(x-m)(x+m)(x-n)(y-m)(y+m)(y+n)(z-h)(z+h)}{4g^2n^2(n-m)^2(n+m)^2}$
(-n,m,0)	$\frac{-(x-m)(x+m)(x-n)(y+m)(y-n)(y+n)(z-h)(z+h)}{4g^2mn(n-m)^2(n+m)^2}$
(n,-m,0)	$\frac{-(x-m)(x+m)(x+n)(y-m)(y-n)(y+n)(z-h)(z+h)}{4g^2mn(n-m)^2(n+m)^2}$
(n,-n,0)	$\frac{(x-m)(x+m)(x+n)(y-m)(y+m)(y-n)(z-h)(z+h)}{4g^2n^2(n-m)^2(n+m)^2}$
(n,n,0)	$\frac{-(x-m)(x+m)(x+n)(y-m)(y+m)(y+n)(z-h)(z+h)}{4g^2n^2(n-m)^2(n+m)^2}$
(n,m,0)	$\frac{(x-m)(x+m)(x+n)(y+m)(y-n)(y+n)(z-h)(z+h)}{4g^2mn(n-m)^2(n+m)^2}$
(m,-m,0)	$\frac{(x+m)(x-n)(x+n)(y-m)(y-n)(y+n)(z-h)(z+h)}{4g^2m^2(n-m)^2(n+m)^2}$
(m,-n,0)	$\frac{-(x+m)(x-n)(x+n)(y-m)(y+m)(y-n)(z-h)(z+h)}{4g^2mn(n-m)^2(n+m)^2}$
(m,n,0)	$\frac{(x+m)(x-n)(x+n)(y-m)(y+m)(y+n)(z-h)(z+h)}{4g^2mn(n-m)^2(n+m)^2}$
(m,m,0)	$\frac{-(x+m)(x-n)(x+n)(y+m)(y-n)(y+n)(z-h)(z+h)}{4g^2m^2(n-m)^2(n+m)^2}$

$m = 0.86113\ 63115\ 94053 \quad n = 0.33998\ 10435\ 84856 \quad h = 0.77459\ 66692\ 41483$

Table 25. Extrapolation Functions for 4x4x3 Integration Rule for Integration Points along z = h

Coordinate	Extrapolation Function
(-m,-m,h)	$\frac{(x-m)(x-n)(x+n)(y-m)(y-n)(y+n)z(z+h)}{8g^2m^2(n-m)^2(n+m)^2}$
(-m,-n,h)	$\frac{-(x-m)(x-n)(x+n)(y-m)(y+m)(y-n)z(z+h)}{8g^2mn(n-m)^2(n+m)^2}$
(-m,n,h)	$\frac{(x-m)(x-n)(x+n)(y-m)(y+m)(y+n)z(z+h)}{8g^2mn(n-m)^2(n+m)^2}$
(-m,m,h)	$\frac{-(x-m)(x-n)(x+n)(y+m)(y-n)(y+n)z(z+h)}{8g^2m^2(n-m)^2(n+m)^2}$
(-n,-m,h)	$\frac{-(x-m)(x+m)(x-n)(y-m)(y-n)(y+n)z(z+h)}{8g^2mn(n-m)^2(n+m)^2}$
(-n,-n,h)	$\frac{(x-m)(x+m)(x-n)(y-m)(y+m)(y-n)z(z+h)}{8g^2n^2(n-m)^2(n+m)^2}$
(-n,n,h)	$\frac{-(x-m)(x+m)(x-n)(y-m)(y+m)(y+n)z(z+h)}{8g^2n^2(n-m)^2(n+m)^2}$
(-n,m,h)	$\frac{(x-m)(x+m)(x-n)(y+m)(y-n)(y+n)z(z+h)}{8g^2mn(n-m)^2(n+m)^2}$
(n,-m,h)	$\frac{(x-m)(x+m)(x+n)(y-m)(y-n)(y+n)z(z+h)}{8g^2mn(n-m)^2(n+m)^2}$
(n,-n,h)	$\frac{-(x-m)(x+m)(x+n)(y-m)(y+m)(y-n)z(z+h)}{8g^2n^2(n-m)^2(n+m)^2}$
(n,n,h)	$\frac{(x-m)(x+m)(x+n)(y-m)(y+m)(y+n)z(z+h)}{8g^2n^2(n-m)^2(n+m)^2}$
(n,m,h)	$\frac{-(x-m)(x+m)(x+n)(y+m)(y-n)(y+n)z(z+h)}{8g^2mn(n-m)^2(n+m)^2}$
(m,-m,h)	$\frac{-(x+m)(x-n)(x+n)(y-m)(y-n)(y+n)z(z+h)}{8g^2m^2(n-m)^2(n+m)^2}$
(m,-n,h)	$\frac{(x+m)(x-n)(x+n)(y-m)(y+m)(y-n)z(z+h)}{8g^2mn(n-m)^2(n+m)^2}$
(m,n,h)	$\frac{-(x+m)(x-n)(x+n)(y-m)(y+m)(y+n)z(z+h)}{8g^2mn(n-m)^2(n+m)^2}$
(m,m,h)	$\frac{(x+m)(x-n)(x+n)(y+m)(y-n)(y+n)z(z+h)}{8g^2m^2(n-m)^2(n+m)^2}$

m = 0.86113 63115 94053 n = 0.33998 10435 84856 h = 0.77459 66692 41483

Table 26. Extrapolation Functions for 4x4x4 Integration Rule for Integration Points along z = -m

Coordinate	Extrapolation Function
(-m,-m,-m)	$\frac{(x-m)(x-n)(x+n)(y-m)(y-n)(y+n)(z-m)(z-n)(z+n)}{8m^3(n-m)^3(n+m)^3}$
(-m,-n,-m)	$-\frac{(x-m)(x-n)(x+n)(y-m)(y+m)(y-n)(z-m)(z-n)(z+n)}{8m^2n(n-m)^3(n+m)^3}$
(-m,n,-m)	$\frac{(x-m)(x-n)(x+n)(y-m)(y+m)(y+n)(z-m)(z-n)(z+n)}{8m^2n(n-m)^3(n+m)^3}$
(-m,m,-m)	$-\frac{(x-m)(x-n)(x+n)(y+m)(y-n)(y+n)(z-m)(z-n)(z+n)}{8m^3(n-m)^3(n+m)^3}$
(-n,-m,-m)	$-\frac{(x-m)(x+m)(x-n)(y-m)(y-n)(y+n)(z-m)(z-n)(z+n)}{8m^2n(n-m)^3(n+m)^3}$
(-n,-n,-m)	$\frac{(x-m)(x+m)(x-n)(y-m)(y+m)(y-n)(z-m)(z-n)(z+n)}{8mn^2(n-m)^3(n+m)^3}$
(-n,n,-m)	$-\frac{(x-m)(x+m)(x-n)(y-m)(y+m)(y+n)(z-m)(z-n)(z+n)}{8mn^2(n-m)^3(n+m)^3}$
(-n,m,-m)	$\frac{(x-m)(x+m)(x-n)(y+m)(y-n)(y+n)(z-m)(z-n)(z+n)}{8m^2n(n-m)^3(n+m)^3}$
(n,-m,-m)	$\frac{(x-m)(x+m)(x+n)(y-m)(y-n)(y+n)(z-m)(z-n)(z+n)}{8m^2n(n-m)^3(n+m)^3}$
(n,-n,-m)	$-\frac{(x-m)(x+m)(x+n)(y-m)(y+m)(y-n)(z-m)(z-n)(z+n)}{8mn^2(n-m)^3(n+m)^3}$
(n,n,-m)	$\frac{(x-m)(x+m)(x+n)(y-m)(y+m)(y+n)(z-m)(z-n)(z+n)}{8mn^2(n-m)^3(n+m)^3}$
(n,m,-m)	$-\frac{(x-m)(x+m)(x+n)(y+m)(y-n)(y+n)(z-m)(z-n)(z+n)}{8m^2n(n-m)^3(n+m)^3}$
(m,-m,-m)	$-\frac{(x+m)(x-n)(x+n)(y-m)(y-n)(y+n)(z-m)(z-n)(z+n)}{8m^3(n-m)^3(n+m)^3}$
(m,-n,-m)	$\frac{(x+m)(x-n)(x+n)(y-m)(y+m)(y-n)(z-m)(z-n)(z+n)}{8m^2n(n-m)^3(n+m)^3}$
(m,n,-m)	$-\frac{(x+m)(x-n)(x+n)(y-m)(y+m)(y+n)(z-m)(z-n)(z+n)}{8m^2n(n-m)^3(n+m)^3}$
(m,m,-m)	$\frac{(x+m)(x-n)(x+n)(y+m)(y-n)(y+n)(z-m)(z-n)(z+n)}{8m^3(n-m)^3(n+m)^3}$

$m = 0.86113\ 63115\ 94053 \quad n = 0.33998\ 10435\ 84856$

Table 27. Extrapolation Functions for 4x4x4 Integration Rule for Integration Points along z = -n

Coordinate	Extrapolation Function
(-m,-m,-n)	$\frac{-(x-m)(x-n)(x+n)(y-m)(y-n)(y+n)(z-m)(z+m)(z-n)}{8m^2n(n-m)^3(n+m)^3}$
(-m,-n,-n)	$\frac{(x-m)(x-n)(x+n)(y-m)(y+m)(y-n)(z-m)(z+m)(z-n)}{8mn^2(n-m)^3(n+m)^3}$
(-m,n,-n)	$\frac{-(x-m)(x-n)(x+n)(y-m)(y+m)(y+n)(z-m)(z+m)(z-n)}{8mn^2(n-m)^3(n+m)^3}$
(-m,m,-n)	$\frac{(x-m)(x-n)(x+n)(y+m)(y-n)(y+n)(z-m)(z+m)(z-n)}{8m^2n(n-m)^3(n+m)^3}$
(-n,-m,-n)	$\frac{(x-m)(x+m)(x-n)(y-m)(y-n)(y+n)(z-m)(z+m)(z-n)}{8mn^2(n-m)^3(n+m)^3}$
(-n,-n,-n)	$\frac{-(x-m)(x+m)(x-n)(y-m)(y+m)(y-n)(z-m)(z+m)(z-n)}{8n^3(n-m)^3(n+m)^3}$
(-n,n,-n)	$\frac{(x-m)(x+m)(x-n)(y-m)(y+m)(y+n)(z-m)(z+m)(z-n)}{8n^3(n-m)^3(n+m)^3}$
(-n,m,-n)	$\frac{-(x-m)(x+m)(x-n)(y+m)(y-n)(y+n)(z-m)(z+m)(z-n)}{8mn^2(n-m)^3(n+m)^3}$
(n,-m,-n)	$\frac{-(x-m)(x+m)(x+n)(y-m)(y-n)(y+n)(z-m)(z+m)(z-n)}{8mn^2(n-m)^3(n+m)^3}$
(n,-n,-n)	$\frac{(x-m)(x+m)(x+n)(y-m)(y+m)(y-n)(z-m)(z+m)(z-n)}{8n^3(n-m)^3(n+m)^3}$
(n,n,-n)	$\frac{-(x-m)(x+m)(x+n)(y-m)(y+m)(y+n)(z-m)(z+m)(z-n)}{8n^3(n-m)^3(n+m)^3}$
(n,m,-n)	$\frac{(x-m)(x+m)(x+n)(y+m)(y-n)(y+n)(z-m)(z+m)(z-n)}{8mn^2(n-m)^3(n+m)^3}$
(m,-m,-n)	$\frac{(x+m)(x-n)(x+n)(y-m)(y-n)(y+n)(z-m)(z+m)(z-n)}{8m^2n(n-m)^3(n+m)^3}$
(m,-n,-n)	$\frac{-(x+m)(x-n)(x+n)(y-m)(y+m)(y-n)(z-m)(z+m)(z-n)}{8mn^2(n-m)^3(n+m)^3}$
(m,n,-n)	$\frac{(x+m)(x-n)(x+n)(y-m)(y+m)(y+n)(z-m)(z+m)(z-n)}{8mn^2n(n-m)^3(n+m)^3}$
(m,m,-n)	$\frac{-(x+m)(x-n)(x+n)(y+m)(y-n)(y+n)(z-m)(z+m)(z-n)}{8m^2n(n-m)^3(n+m)^3}$

m = 0.86113 63115 94053 n = 0.33998 10435 84856

Table 28. Extrapolation Functions for 4x4x4 Integration Rule for Integration Points along $z = n$

Coordinate	Extrapolation Function
(-m,-m,n)	$\frac{(x-m)(x-n)(x+n)(y-m)(y-n)(y+n)(z-m)(z+m)(z+n)}{8m^2n(n-m)^3(n+m)^3}$
(-m,-n,n)	$\frac{-(x-m)(x-n)(x+n)(y-m)(y+m)(y-n)(z-m)(z+m)(z+n)}{8mn^2(n-m)^3(n+m)^3}$
(-m,n,n)	$\frac{(x-m)(x-n)(x+n)(y-m)(y+m)(y+n)(z-m)(z+m)(z+n)}{8mn^2(n-m)^3(n+m)^3}$
(-m,m,n)	$\frac{-(x-m)(x-n)(x+n)(y+m)(y-n)(y+n)(z-m)(z+m)(z+n)}{8m^2n(n-m)^3(n+m)^3}$
(-n,-m,n)	$\frac{-(x-m)(x+m)(x-n)(y-m)(y-n)(y+n)(z-m)(z+m)(z+n)}{8mn^2(n-m)^3(n+m)^3}$
(-n,-n,n)	$\frac{(x-m)(x+m)(x-n)(y-m)(y+m)(y-n)(z-m)(z+m)(z+n)}{8n^3(n-m)^3(n+m)^3}$
(-n,n,n)	$\frac{-(x-m)(x+m)(x-n)(y-m)(y+m)(y+n)(z-m)(z+m)(z+n)}{8n^3(n-m)^3(n+m)^3}$
(-n,m,n)	$\frac{(x-m)(x+m)(x-n)(y+m)(y-n)(y+n)(z-m)(z+m)(z+n)}{8mn^2(n-m)^3(n+m)^3}$
(n,-m,n)	$\frac{(x-m)(x+m)(x+n)(y-m)(y-n)(y+n)(z-m)(z+m)(z+n)}{8mn^2(n-m)^3(n+m)^3}$
(n,-n,n)	$\frac{-(x-m)(x+m)(x+n)(y-m)(y+m)(y-n)(z-m)(z+m)(z+n)}{8n^3(n-m)^3(n+m)^3}$
(n,n,n)	$\frac{(x-m)(x+m)(x+n)(y-m)(y+m)(y+n)(z-m)(z+m)(z+n)}{8n^3(n-m)^3(n+m)^3}$
(n,m,n)	$\frac{-(x-m)(x+m)(x+n)(y+m)(y-n)(y+n)(z-m)(z+m)(z+n)}{8mn^2(n-m)^3(n+m)^3}$
(m,-m,n)	$\frac{-(x+m)(x-n)(x+n)(y-m)(y-n)(y+n)(z-m)(z+m)(z+n)}{8m^2n(n-m)^3(n+m)^3}$
(m,-n,n)	$\frac{(x+m)(x-n)(x+n)(y-m)(y+m)(y-n)(z-m)(z+m)(z+n)}{8mn^2(n-m)^3(n+m)^3}$
(m,n,n)	$\frac{-(x+m)(x-n)(x+n)(y-m)(y+m)(y+n)(z-m)(z+m)(z+n)}{8mn^2(n-m)^3(n+m)^3}$
(m,m,n)	$\frac{(x+m)(x-n)(x+n)(y+m)(y-n)(y+n)(z-m)(z+m)(z+n)}{8m^2n(n-m)^3(n+m)^3}$

$m = 0.86113\ 63115\ 94053 \quad n = 0.33998\ 10435\ 84856$

Table 29. Extrapolation Functions for 4x4x4 Integration Rule for Integration Points along z = m

Coordinate	Extrapolation Function
(-m,-m,m)	$\frac{-(x-m)(x-n)(x+n)(y-m)(y-n)(y+n)(z+m)(z-n)(z+n)}{8m^3(n-m)^3(n+m)^3}$
(-m,-n,m)	$\frac{(x-m)(x-n)(x+n)(y-m)(y+m)(y-n)(z+m)(z-n)(z+n)}{8m^2n(n-m)^3(n+m)^3}$
(-m,n,m)	$\frac{-(x-m)(x-n)(x+n)(y-m)(y+m)(y+n)(z+m)(z-n)(z+n)}{8m^2n(n-m)^3(n+m)^3}$
(-m,m,m)	$\frac{(x-m)(x-n)(x+n)(y+m)(y-n)(y+n)(z+m)(z-n)(z+n)}{8m^3(n-m)^3(n+m)^3}$
(-n,-m,m)	$\frac{(x-m)(x+m)(x-n)(y-m)(y-n)(y+n)(z+m)(z-n)(z+n)}{8m^2n(n-m)^3(n+m)^3}$
(-n,-n,m)	$\frac{-(x-m)(x+m)(x-n)(y-m)(y+m)(y-n)(z+m)(z-n)(z+n)}{8mn^2(n-m)^3(n+m)^3}$
(-n,n,m)	$\frac{(x-m)(x+m)(x-n)(y-m)(y+m)(y+n)(z+m)(z-n)(z+n)}{8mn^2(n-m)^3(n+m)^3}$
(-n,m,m)	$\frac{-(x-m)(x+m)(x-n)(y+m)(y-n)(y+n)(z+m)(z-n)(z+n)}{8m^2n(n-m)^3(n+m)^3}$
(n,-m,m)	$\frac{-(x-m)(x+m)(x+n)(y-m)(y-n)(y+n)(z+m)(z-n)(z+n)}{8m^2n(n-m)^3(n+m)^3}$
(n,-n,m)	$\frac{(x-m)(x+m)(x+n)(y-m)(y+m)(y-n)(z+m)(z-n)(z+n)}{8mn^2(n-m)^3(n+m)^3}$
(n,n,m)	$\frac{-(x-m)(x+m)(x+n)(y-m)(y+m)(y+n)(z+m)(z-n)(z+n)}{8mn^2(n-m)^3(n+m)^3}$
(n,m,m)	$\frac{(x-m)(x+m)(x+n)(y+m)(y-n)(y+n)(z+m)(z-n)(z+n)}{8m^2n(n-m)^3(n+m)^3}$
(m,-m,m)	$\frac{(x+m)(x-n)(x+n)(y-m)(y-n)(y+n)(z+m)(z-n)(z+n)}{8m^3(n-m)^3(n+m)^3}$
(m,-n,m)	$\frac{-(x+m)(x-n)(x+n)(y-m)(y+m)(y-n)(z+m)(z-n)(z+n)}{8m^2n(n-m)^3(n+m)^3}$
(m,n,m)	$\frac{(x+m)(x-n)(x+n)(y-m)(y+m)(y+n)(z+m)(z-n)(z+n)}{8m^2n(n-m)^3(n+m)^3}$
(m,m,m)	$\frac{-(x+m)(x-n)(x+n)(y+m)(y-n)(y+n)(z+m)(z-n)(z+n)}{8m^3(n-m)^3(n+m)^3}$
m = 0.86113 63115 94053 n = 0.33998 10435 84856	

Vita

The author was born on June 20, 1965 in Winnipeg, Manitoba, Canada. She attended the University of Manitoba in Winnipeg for one year, and then transferred to the Aerospace Engineering Department at Texas A&M University in College Station, Texas in August 1984. After three years of study, she graduated Cum Laude with a Bachelor of Science in Aerospace Engineering in May 1987.

In September 1987, she entered the Master of Science program (thesis) in Engineering Mechanics at Virginia Polytechnic Institute and State University. During that time she was both a Graduate Teaching Assistant and Graduate Research Assistant in the Engineering Science and Mechanics Department, and completed a internship at NASA Langley Research Center with the Computational Structural Mechanics Group in the Structural Mechanics Branch.

The author plans to continue her studies at Virginia Polytechnic and State University upon the completion of her Master of Science requirements in the Engineering Mechanics program.